



Identification and characterization of Mass Transport Deposits from seismic data. Application to the Amazon River Mouth basin

Pauline Le Bouteiller

► To cite this version:

Pauline Le Bouteiller. Identification and characterization of Mass Transport Deposits from seismic data. Application to the Amazon River Mouth basin. Earth Sciences. Sorbonne Université, 2018. English. NNT : 2018SORUS481 . tel-02613626

HAL Id: tel-02613626

<https://theses.hal.science/tel-02613626>

Submitted on 20 May 2020

HAL is a multi-disciplinary open access archive for the deposit and dissemination of scientific research documents, whether they are published or not. The documents may come from teaching and research institutions in France or abroad, or from public or private research centers.

L'archive ouverte pluridisciplinaire **HAL**, est destinée au dépôt et à la diffusion de documents scientifiques de niveau recherche, publiés ou non, émanant des établissements d'enseignement et de recherche français ou étrangers, des laboratoires publics ou privés.

Sorbonne Université

Ecole doctorale Géosciences Ressources Naturelles et Environnement

Institut des Sciences de la Terre de Paris

Identification and characterization of Mass Transport

Deposits from seismic data

Application to the Amazon River Mouth basin

Par Pauline Le Bouteiller

Thèse de doctorat en Géosciences

Dirigée par :

Pr. Christian Gorini

Dr. Florence Delprat-Jannaud

Dr. Jean Charléty

Dr. Didier Granjeon

Présentée et soutenue publiquement le 5 décembre 2018

Devant un jury composé de :

Pr. AlRegib, Ghassan	Georgia Institute of Technology	Rapporteur
Dr. Cattaneo, Antonio	Ifremer	Rapporteur
Pr. Migeon, Sébastien	Sorbonne Université	Examineur
Dr. Coléou, Thierry	CGG	Examineur
Dr. Viana, Adriano	Petrobras	Examineur
Dr. Charléty, Jean	IFP Energies nouvelles	Encadrant
Dr. Delprat-Jannaud, Florence	IFP Energies nouvelles	Promotrice
Pr. Gorini, Christian	Sorbonne Université	Directeur de thèse

Contents

Remerciements	7
Summary	9
1 Introduction	11
1.1 Context and motivations	11
1.1.1 Interest for better understanding sedimentary basins on continental margins	11
1.1.2 Mass transport: one sedimentary process in sedimentary basins . . .	12
1.2 Main questions and objectives of the PhD	13
1.3 Mass transport deposits, mass transport events	15
1.3.1 Mass transport deposit: a geological object	15
1.3.2 Pre-conditioning and triggering factors	16
1.3.3 Transport processes	22
1.3.4 Depositional and post-depositional processes (PDP)	28
1.4 Approaching MTDs through seismic data acquisition and interpretation . .	29
1.4.1 Seismic data acquisition and processing	29
1.4.2 Seismic facies and interpretation	31
1.4.2.1 Model-driven seismic facies: seismic stratigraphy	32
1.4.2.2 Data-based-only seismic facies	32
1.4.2.3 Seismic geomorphology	35
1.5 Data and settings of the case study	35
1.5.1 Regional setting: the Amazon River basin geological history	36
1.5.2 Gravitational processes in the Amazon basin	39
1.5.3 Data used for this PhD project	43
1.6 Challenges	45
1.6.1 Diversity of mass transport processes, diversity of MTD characters .	45
1.6.2 Making the most of seismic data	47
1.6.3 Making the most of prior information	52
1.7 Organization of the next chapters	53
2 Retrieving MTDs in seismic data: a specific setting with varied object expressions	55
2.1 Introduction	55
2.2 Object recognition in a seismic image: related work	55
2.2.1 Seismic data representation	56

2.2.1.1	Seismic attributes and seismic facies numerical representation	56
2.2.1.2	Texture analysis and seismic textural attributes	57
2.2.2	Comparing seismic patches: similarity quantification	61
2.2.3	Highlighting regions of interest in a seismic image: segmentation . .	63
2.2.3.1	Segmenting an object with geometrical methods	63
2.2.3.2	A local approach: classifying pixels	67
2.2.3.3	A specific kind of local approach: learning abstract high-level representations for segmentation	75
2.2.4	Synthesis	78
2.3	Recovering MTDs as heterogeneous geobodies from seismic data - ARTICLE	80
2.4	Discussion	114
2.4.1	Handling seismic data: balancing computer power constraints and orientation representativity	115
2.4.2	MTD depiction in the four studied datasets	116
2.4.3	How much variation is there among the detected MTDs?	121
2.4.4	Highlights of the mixed approach for our objective	124
2.4.4.1	Comparison with a model-driven approach	124
2.4.4.2	Comparison with data-driven or mixed approaches	127
2.5	Conclusion	129
3	Interpretation of MTD properties: properties of mass transport events	131
3.1	Introduction	131
3.1.1	Assessing the responsibility of physical processes for MTD characters	131
3.1.2	Dealing with multiple heterogeneous causal factors in geoscience . .	133
3.1.3	Organization of this chapter	138
3.2	Creation of seismic facies groups for MTD description	138
3.3	Development of the methodology - ARTICLE	141
3.4	Outlook on the knowledge base automation	197
3.5	Conclusion	198
4	Implications of our methods for interpretation schemes and for sedimentary basin understanding	199
4.1	Relationship between the two objectives of identification and interpretation	199
4.1.1	Objects and their contours	200
4.1.2	Objects and their internal facies	203
4.1.3	Qualitative and binary MTD descriptors	204
4.2	How have we made the most of seismic data and prior information?	205
4.2.1	Mixing a-priori expertise and new objective methods	205
4.2.2	Adaptability of the method to any kind of seismic data	206
4.2.3	Point-by-point practical solutions	207
4.3	Implications for sedimentary basin understanding	208
4.3.1	Facies-based approach	208
4.3.2	Object-based approach	211
4.4	Conclusion	211

5	Conclusion and perspectives	213
5.1	Main contributions of this PhD	213
5.1.1	Methodological contributions	213
5.1.2	The Amazon case study	216
5.2	Perspectives	217
5.2.1	A more accurate and flexible Identification	217
5.2.2	Transferring Identification methods	219
5.2.3	An automated, comprehensive knowledge-based system	220
5.2.4	Suggestions for advances on the Amazon case study	220
5.3	Conclusion	222
A	Generative Topographic Mapping for clustering a dataset	223
A.1	GTM: the model	223
A.2	Using the GTM latent representation for clustering	226
A.3	Choice of parameters	227
A.4	Magnification factors	228
B	Segmentation quality assessment	229
C	Supplementary material for section 3.3	233
D	List of oral and written communications	236
	List of Figures	239
	List of Tables	247

Remerciements

First of all, I would like to thank all members of my jury who accepted to review my work and take part in the defence. I am grateful for their beneficial comments and remarks on the manuscript, as well as for their interest and the discussions that took place during the defence.

Au terme de ces trois années, je tiens à remercier mes encadrants de thèse. Merci à Christian Gorini, mon directeur de thèse, pour son enthousiasme indéfectible pour le projet, ses idées ambitieuses et ses encouragements. Merci à Florence Delprat-Jannaud, promotrice IFPEN, pour sa confiance, ses conseils toujours avisés et le temps précieux qu'elle m'a accordé. Merci à Didier Granjeon, co-promoteur IFPEN, pour son suivi attentif et attentionné. Merci à Jean Charléty, encadrant IFPEN, pour les inestimables et constructifs échanges "de fond" durant les développements du projet de thèse, et pour le non moins inestimable temps passé à des corrections en tout genre ou préparation d'événements. Merci à vous tous de m'avoir suivie et soutenue chacun à votre manière.

Tous mes remerciements aussi à Sara Lafuerza pour son intérêt, son partage d'expérience et son implication dans le projet "base de connaissances". Merci Sara pour tes encouragements et ta disponibilité !

Merci aussi à Noalwenn, ainsi que Karine, qui ont chacune prêté leurs yeux d'expertes pour relire une première version d'article avec efficacité. Merci à Tadeu pour son aide déterminante dans la rédaction d'un article.

Parmi les expériences de la thèse, une des plus incroyables a été une campagne en mer de 5 semaines pendant ma première année. Je remercie particulièrement Sylvie Leroy qui m'a permis d'y participer, les chefs de mission Daniel Aslanian, Maryline Moulin et Mikaël Evain, ainsi que toute l'équipe scientifique et les membres de l'équipage. Un grand merci à mes encadrants de m'avoir permis de vivre cette expérience inoubliable.

J'ai aussi eu la chance de participer à des congrès/séminaires. Chacun a été source de découvertes passionnantes... et compliquées ! Et de rencontres et discussions enrichissantes. Chaque congrès m'a vraiment remotivée. Merci en particulier à Christian d'avoir eu cela à coeur, et à Florence et Jean pour les opportunités proposées, les entraînements etc.

La vie quotidienne à l'IFPEN m'a aussi fait rencontrer quantité de personnes formidables. Sans pouvoir citer tout le monde, je remercie du fond du coeur les habitants des Tilleuls, et Jamila, Djamela et Meriem; mais aussi les personnels de ménage et de la cantine que je n'ai jamais vus sans sourires. Du côté de Jussieu et de l'ED, merci à Dovy et Sandrine pour leur aide.

Un grand merci aux amis sans qui rien n'est possible ! Merci aux thésards des Tilleuls, à mes co-bureau, Raphaëlle puis Marianne et Dan-Dan. J'ai adoré partager le bureau avec vous ! Merci à Claire pour son amitié présente, à l'IFPEN comme à Jussieu. Merci Jean, Cédric, Damaris, Sophie, Adriana, Martina, Sebastian, Richard, Anouk, Virginie, Arthur, Rita, Alexandre, Juan-Pablo, Nikolaos, Vasilis, Camille, Juliette... A Anabel et Hamza, Chakib, Imane, Zaineb, Omar, Nicolas S, Aurélien, Christopher, Chahir, Bertrand, Zadi... Merci à Nicolas P, à Cyril, Malik et Bernard... quels talents ! Merci aux thésards Amazonie, Alberto et Juliana et puis à leur forêt vierge de tomates cerises. A Ikenna, Célia, Roohollah, Layla, Julien, Marie, Benjamin, Quentin, Sylvain, Vincent, Maxime... Merci aux copains en thèse et à ceux qui n'y sont pas, à Frantz et Niko, à Mathilde, aux Islandais, aux Suisses et aux Finlandais, à Yoyo, Hélo. Merci à tout l'EVOG pour tous ces lundis soirs, à Martin, Matthieu et Thibault pour tous ces mercredis soirs musicaux ;), à toutes les GA (tellement!), et puis à Madeleine, Amélie, Alix, Céline.

Merci à mes parents, veilleurs d'une écoute et d'un soutien vital, et à mes frère et soeurs &cie, parce qu'après moult doutes et péripéties, et somme toute en bonne partie grâce à vous, finalement je rallie le clan ;)

Enfin, bien sûr, merci Alex de me tirer vers le haut.

Summary

Within sedimentary basins, gravity-driven mass transport events play a key role in the delivery of sediments from continental shelves to the deep ocean. Current investigations intend to better understand the processes involved during a mass transport event, both for a better characterization of the sedimentary basin history and for present-day geohazard assessments.

Special attention is given to the nature and potential of seismic data as invaluable information source. From seismic data, both quantitative analyses and qualitative elements are commonly extracted for interpretation purposes on a studied area. We observe a need to integrate seismic data-extracted information and existing expertise on seismic interpretation of mass transport deposits (MTDs), into formalized interpretation schemes.

In the same time, ways to investigate data and take advantage of organized knowledge are tremendously developed and evolve rapidly. Current artificial intelligence, learning algorithms and knowledge-based systems allow to apprehend, use and mine large or complex datasets efficiently.

This PhD project is a way to be at the crossing of seismic interpretation and statistical learning in their recent developments for image segmentation and knowledge mining. The project contributes to investigations on mass transport processes by concentrating on the deposits generated by a mass transport event, approached through information available in seismic data. To carry on the project, we rely on a seismic dataset acquired offshore the Amazon River Mouth basin, in Brazil.

Two main lines of research are followed and presented in this report, corresponding to the two objectives of the PhD: (1) to locate MTDs in seismic data, in position and extension, while preserving the variety of their characters; (2) to characterize physical processes acting over geological times, responsible for location, geometry and internal heterogeneities of these MTDs.

The first objective is tackled by proposing a methodology for detecting heterogeneous

objects within seismic data, considered as images. The main associated challenges are how to deal with 3D seismic images and, within them, the heterogeneity of the internal characters of MTDs. Our methodology provides a specific seismic data representation that is coupled to little prior input on MTD positions, needed to guide the procedure but for which uncertainty is admitted and taken into account. It finally produces a 3D identification of MTDs. The workflow relies on a probabilistic approach, enabling to keep track of uncertainties. Our methodology is applied to a 3D seismic data volume of the Amazon basin, showing consistent detection results, although with overall volume under-estimation.

The second objective is treated by building a methodology producing interpretations hypotheses on physical processes involved in mass transport events. The methodology is based on literature-extracted elements, organized into a graph, whose nodes and edges carry the existing interpretation knowledge. The graph is then used as an inference engine, where the observed features of MTDs give rise to hypotheses on processes playing in the MTD history. We provide an application of our methodology, showing that it allows to recover consistent interpretation hypotheses. The knowledge base that is built for the methodology provides a framework for an explicit procedure where different interpretation paths are gathered and considered equally before inferring the most likely ones.

The two methodologies that we propose have proven effective for our case study. They enable the retrieval of more varied properties than in model-driven-only methods, and more interpretable results than in data-driven-only methods. Improvements for the next future include using more efficient computing schemes for better taking into account structural orientations, and enhancing the knowledge base by extending its content and implementing it on dedicated automated tools.

Both methodologies can be used independently from one another, or combined into a global workflow. This PhD contributes to prove that it is possible to combine data-driven and knowledge- or model-driven information in efficient ways for seismic interpretation.

Chapter 1

Introduction

This chapter gives the context and objectives of this PhD. We introduce our object of study: mass transport deposits, and their generating mass transport events. We then introduce seismic data and its potential for interpreting buried sedimentary systems. We also present the case study that will be used for applications in the next chapters. Finally, we highlight the main challenges that are addressed in this PhD.

1.1 Context and motivations

1.1.1 Interest for better understanding sedimentary basins on continental margins

Sedimentary basins on continental passive margins are submarine areas located at the transition between continental and oceanic crusts, where sediments generated by inland erosion and transported by rivers are deposited and accumulate. These basins comprise, from continent to ocean, the continental shelf ending with the shelf-break, the continental slope, and the deep ocean basin, where a deep-sea fan may form at the bottom of the slope (Figure 1.1).

Interests in these natural environments are diverse: on the one hand, they are a unique source of information on the geological history of their surrounding settings, through the study of sedimentary records. On the other hand, submarine basins and ancient submarine basins are the main supply of natural resources on Earth: mineral resources, water, and hydrocarbons.

Offshore hydrocarbon exploration and production has grown as one key activity for world-wide energy production. Renewable energies such as wind, wave- and tide-related, or geothermic energies, are also increasingly developed in coastal or offshore areas. These developments go along with transport infrastructures and submarine cables for telecom-

munications or energy transport (see for example the [Submarine Cable Map website](#)¹).

Meanwhile, coastal and offshore environments are subject to natural and industrial risks: gradual erosion and sea-level rise shifting the shoreline inland; tsunamis and storms threatening infrastructures and cities; slope instabilities jeopardizing seafloor-anchored infrastructures; pollution of soils, waters and air.

The development of human activity in sedimentary basins has therefore motivated private companies and institutions to study these environments with scientific approaches. Data of many kinds are acquired there, comprising samples (water samples, cores, produced hydrocarbons) and geophysical data such as bathymetric, magnetic, gravimetric and seismic data. Data processing and interpretation is then conducted, as well as numerical modeling to simulate the physical processes acting in the formation and evolution of a sedimentary basin.

1.1.2 Mass transport: one sedimentary process in sedimentary basins

Among sediment deposition processes, gravity-driven mass transport is one that contributes to the reorganization of the basin deposits. Continental margin settings count a significant amount of mass transport deposits in their sedimentary records ([Shipp *et al.* \(2011\)](#), [Posamentier & Martinsen \(2011\)](#)), on their slopes and in the deep basin. Such submarine mass transport deposits can be up to two order of magnitude bigger than terrestrial ones (e.g., [Masson *et al.* \(2006\)](#)). They constitute a critical portion of basin sediments that remain to be better understood, considering two interests: the present description of

¹[TeleGeography \(2018\)](#)

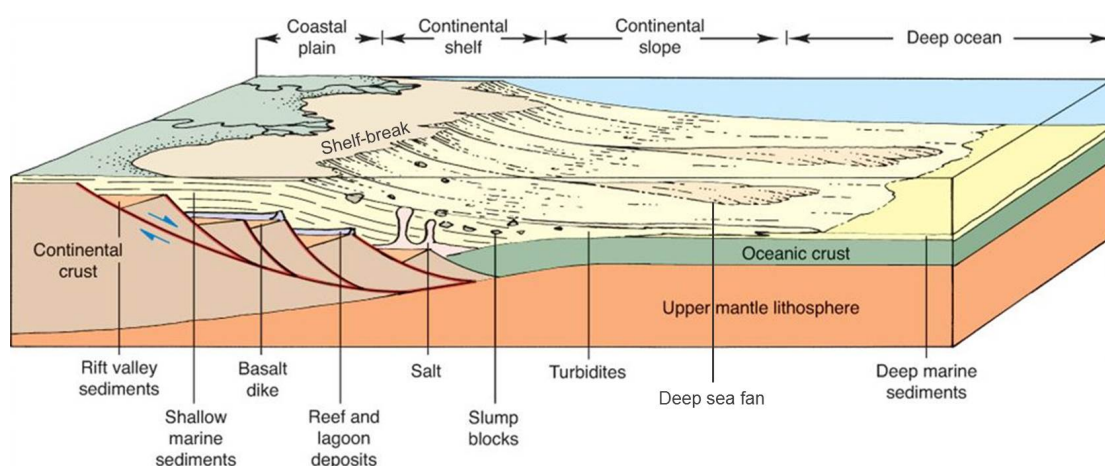


Figure 1.1: Main features of a passive continental margin. Tilted fault blocks, dikes, salt (or evaporites), reef and lagoon deposits, are signatures of the passive margin formation and past evolution. Shallow marine sediments, slump blocks, turbidites and deep marine sediments are continuing deposited sediments in the basin. Modified from [Christiansen & Hamblin \(2015\)](#).

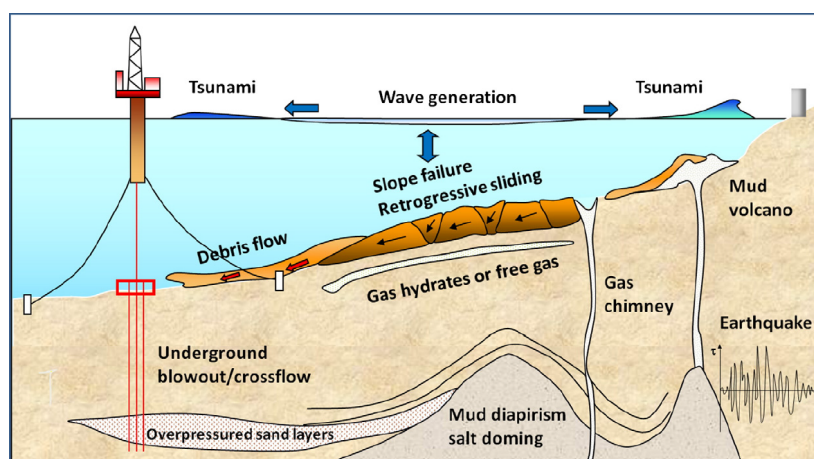


Figure 1.2: Various geohazards related to mass transport along a continental slope and their potential impacts on coastal to marine infrastructures. Among them: slope failures, impact of debris flows on infrastructure, dissociation of hydrates, shallow-gas pockets, overpressure, fluid escape features (gas chimneys, mud volcanoes), diapirism, seismicity, and highly destructive tsunamis. From [Vanneste *et al.* \(2014\)](#).

sedimentary structures and resources in a basin, and the reconstruction of its geological history.

Depending on their lithological content, mass transport deposits can constitute impermeable sedimentary bodies acting as potential seals for hydrocarbons; their own material may on the contrary have potential reservoir properties (e.g., [Posamentier & Martinsen \(2011\)](#)). Large mass transport deposits result from processes that modified the morphology of the basin. A mass transport event might also remove sediment from a region, creating an access to previously covered layers.

The characteristics of mass transport deposits within a basin are helpful to infer the evolution of deposition processes through time (e.g., [Ortiz-Karpf *et al.* \(2016\)](#), [Patruno & Helland-Hansen \(2018\)](#)). Their study should increase the understanding of seafloor stability during the basin history and thus at the present day, in order to assess the impact of geohazards on the basin environment (see Figure 1.2).

Lastly, although mass transport deposits are most-easily detected and interpreted when they are still on the seafloor, a lot of them are buried and 'hidden' within the basin sedimentary layers. Therefore, studying them requires specific approaches enabling the broader study of other buried geological elements, specifically those that have to be approached by indirect measurements such as geophysical data acquisition.

1.2 Main questions and objectives of the PhD

The project presented here falls within the scope of such research aiming at improving the understanding on sedimentary basins. In this theme, some investigations are led re-

garding gravity-driven mass movements in these basins. They address the problem of understanding the relationship between such mechanisms and the infilling and sedimentary geometries of a basin. Attention is also given to the impacts of external factors (for instance, climatic changes, oceanic circulations, chemical conditions, continental erosion or sedimentary influxes) on mass transport processes.

Among the possible approaches to deal with these questions, studying the record of mass movements in the basin stratigraphy, in particular mass transport deposits (MTDs), is an approach based on present-day observations enabling the inference of past evolutions. MTDs are geobodies, i.e. geometrically-closed objects within the sedimentary layering. Different kinds of data may be available to get access to these objects: if directly visible on the seafloor e.g. on bathymetric data, then the surface and morphology of the object is easy to derive, potentially with a detailed resolution. However, from bathymetric data only, one does not have access to the internal/bottom parts of the object.

For cases where the MTD is buried, core samples might be available; these data also give localized, precise information that do not necessarily generalize to the rest of the object. Among geophysical imaging methods, seismic reflection data provide a more global information on the object, as the image can cover the whole object and especially its internal material. Seismic data have been acknowledged as an invaluable source of information for 3D geomorphology studies of geological objects (e.g., [Posamentier *et al.* \(2007\)](#), [Frey-Martínez \(2010\)](#)). In this thesis we focus on this kind of data - although ultimately, merging information from several kinds of data such as mentioned above is necessary.

The questions driving this PhD project are the following:

What is the expression of MTDs in seismic data?

How can we relate the resulting seismic evidence of mass transport to the processes that made them?

These questions address several issues: the origins and actual processes of mass transports; the properties of the resulting deposits and their spatial positioning; the link between geological properties of MTDs and their seismic expression; and the methodology to handle seismic data and exploit seismic information.

Given these issues and the abundance and variety of traces of these mechanisms in the data available for this study, two main lines of research were chosen:

1. **Identification:** to locate MTDs in seismic data, in position and extension, while preserving the variety of their characters.
2. **Interpretation:** to characterize physical processes acting over geological times, responsible for location, geometry and internal heterogeneities of these MTDs.

Identification of objects means determining what features are associated to these objects (i.e. how to recognize and discriminate them), searching the seismic image numerically, and finding the positions and limits of the objects. *Interpretation* is about understanding the reasons: reasons why mass transport originally took place (process of trigger), reasons why deposits were placed in a certain way (process of deposit), reasons why the deposits have a certain seismic aspect (process of transport and deposit), reasons why the geometry of the region is shaped as it is (larger-scale gravity-driven evolution). Both *identification* and *interpretation* require to extract information from a seismic dataset in a relevant, efficient manner.

1.3 Mass transport deposits, mass transport events

1.3.1 Mass transport deposit: a geological object

As referred to in this report, a submarine mass transport is an event of 'en-masse' transport of sediments (Posamentier & Martinsen (2011)) following a mechanical rupture and with horizontal predominant displacement (as opposed to in-place collapse). It is also sometimes called submarine landslide or submarine mass failure; the latter terms are restrictive compared to 'mass transport' which usually encompasses the failure, transport and deposit, and which can occur with any kind of deformation, not restricted to sliding. The definition of a mass transport deposit (MTD) is given by its name: it is the deposit resulting from a mass transport event. The most downward portion of such sedimentary object (geobody) is called the 'toe region'. The upper portion is called either 'head' or 'tail', conversely. In this report we will use the term 'head' (see Figure 1.3). An accumulation of deposits from several mass transport events over a period of time is called a mass transport complex (MTC).

MTDs can have contrasting sizes. The head region of an MTD may be, or not, still attached to its source zone. In the MTD source zone, a 'headscarp' is sometimes visible; this

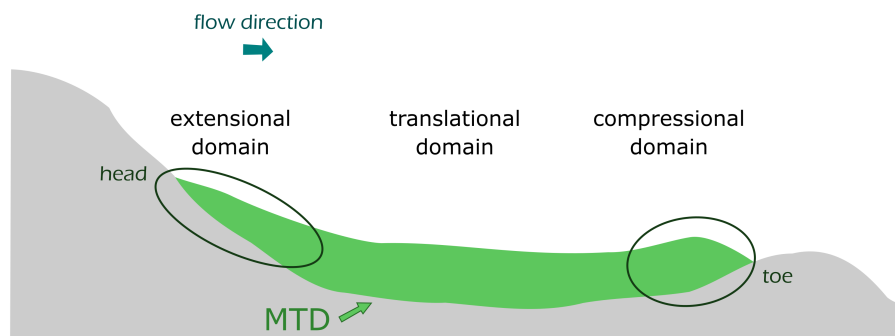


Figure 1.3: Schematic description of the three domains in an MTD. This scheme does not cover all kinds of MTDs.

scarp corresponds to the place from where the material was removed at the mass transport trigger. The headscarp may not be distinguishable anymore within the sedimentary layers.

The typical representation of an MTD (see Figure 1.3) proposes three main domains (e.g., Richardson *et al.* (2011), Reis *et al.* (2016)): (i) the extensional domain in the head region; (ii) the translational domain in the central region, corresponding to the largest part of the MTD; (iii) the compressional domain in the toe region. These three names refer to the major kinds of deformation that may be found in each domain. Note, however, that this model is only valid for certain kinds of MTDs: those that have developed keeping attached or close to their headscarp and subject to frontal confinement. Nevertheless, apart from MTDs, the model also applies to MTCs in some large-scale contexts (e.g., Moscardelli & Wood (2008)): then, upper-slope regions of the MTC shows predominantly extensional deformation while compression is evidenced in its downslope regions.

Figure 1.4 gives examples of observation of mass transport deposits: either direct observation of a modern subaerial MTD or indirect observation of a submarine, buried MTD, in marine seismic data offshore Japan.

Three stages associated to mass transports can be distinguished: (i) the trigger stage, to which are associated pre-conditioning and triggering factors (PTF); (ii) the transport stage, and (iii) the deposition stage, to which are associated depositional and post-depositional processes (PDP). A presentation of each stage, together with explanations on how forward models are able to reproduce the processes involved, is given here.

1.3.2 Pre-conditioning and triggering factors

A mass transport is generally due to a combination of environmental mechanisms acting over different temporal scales. In order to evaluate the likelihood of a landslide to occur,

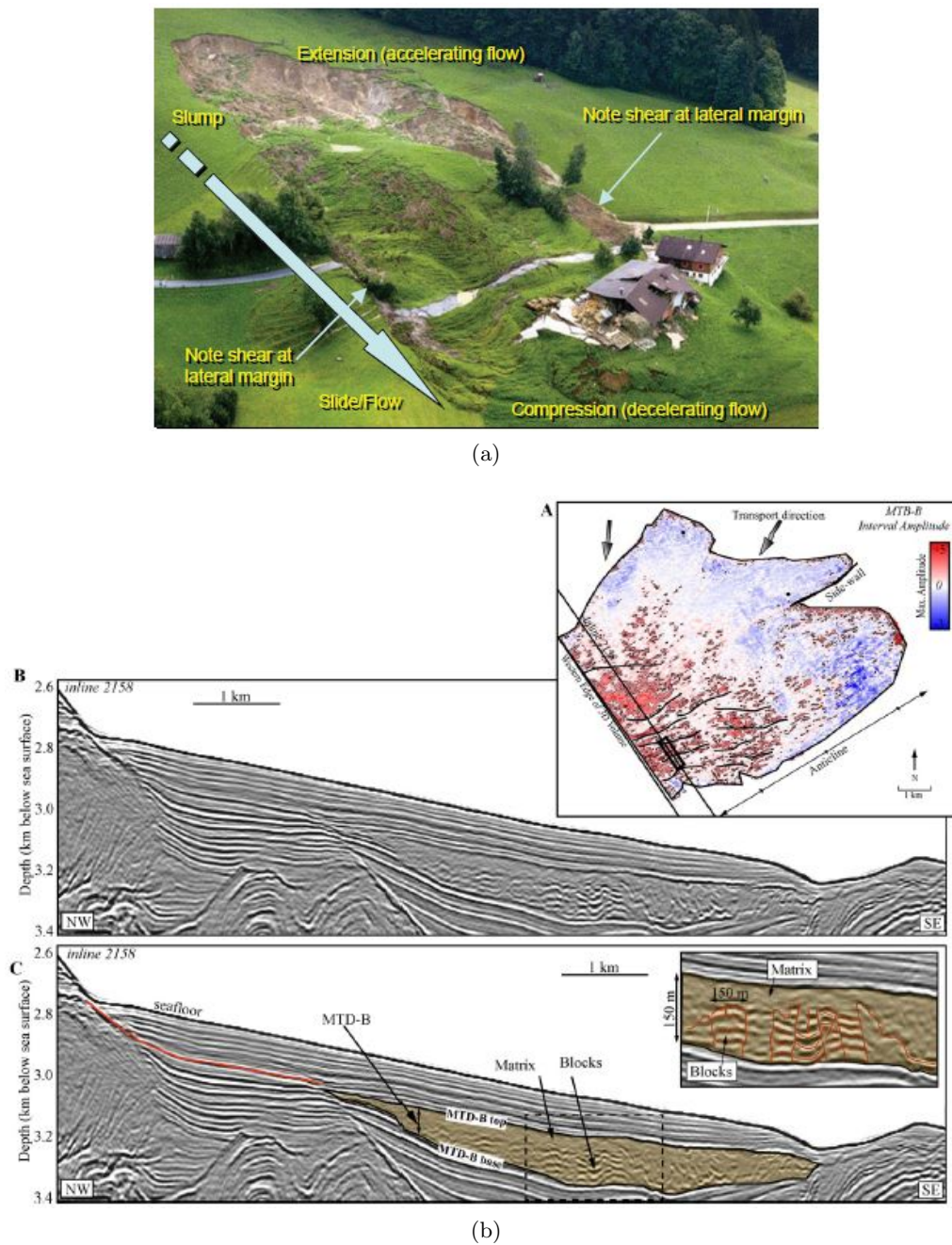


Figure 1.4: Mass transport examples. (a) Subaerial mass-transport in the Austrian Alps; extensional and compressional features are seen, as well as lateral shear. These features are also seen in submarine mass transports. From [Posamentier & Martinsen \(2011\)](#). (b) Map (A), seismic profile (B) and interpreted seismic profile (C): MTD in brown (interpreted preserved blocks inside), headscarp in red. On this profile the MTD toe is its right-most part. From [Moore & Sawyer \(2016\)](#).

geotechnics use the Factor of safety; this factor is the ratio between the shear strength of the material and the effective shear stress driving a possible de-stabilization. Both values depend on several parameters, that are in turn affected by pre-conditioning and triggering factors. In the present context, we will refer to the Flow factor F_f , defined by [Sawyer et al. \(2012\)](#) as the inverse of the Factor of safety:

$$F_f = \frac{\text{driving shear stress}}{\text{resistive shear strength}}$$

So that if $F_f < 1$, the material is likely to stay still; and if $F_f \geq 1$, the material is unstable; the higher F_f , the more likely a flow is to occur.

Assessment and prediction of this F_f is done via stability analysis methods.

'Limit equilibrium analysis' is the simpler among them; it computes a global value of F_f on a system with a pre-defined potential slip surface, generally a circular one. Methods of this kind (e.g. [Bishop \(1955\)](#), [Morgenstern & Price \(1965\)](#)) rely on the theory by [Terzaghi \(1942\)](#) (itself derived from the Mohr-Coulomb principle) which relates the resistive shear strength τ on the potential failure surface to the effective stress σ' , effective internal friction angle ϕ' , and effective cohesion c' of the material, as:

$$\tau = \sigma' \tan \phi' + c' ,$$

where $\sigma' = \sigma - u$

The effective stress corresponds to the total stress σ , minus the pore pressure u . A sudden increase in pore pressure on the surface may not be drained rapidly enough to prevent a decrease in shear strength τ , so that F_f is increased; pore pressure is therefore one of the critical elements acting in the stability of submarine slopes.

An empirical limit equilibrium analysis is presented by [Sawyer et al. \(2012\)](#), for studying mudflow transport behavior and associated deposit morphology. Their approach is based on laboratory experiments of subaqueous flows with different F_f values (see Figure 1.5). Their study results in the definition of three main domains of F_f , each associated to a set of characteristics of the final deposit:

- High F_f (6.23 in their case) leads to a thin and broad MTD, with the maximum thickness located at the slope change (material accumulation); the head of the MTD thins until a point.
- Medium F_f (3.05 and 3.53 in their case) leads to a retrogressive failure, which creates a hummocky surface on the top of the MTD; during the process, internal levees are formed on the edges (see Figure 1.5D), which may allow the transport to be continued further.

- Low F_f (1.38 in their case) leads to a short, thick deposit, made of blocks containing fractures.

These trends, resulting from an experimental study, illustrate the potentially strong impact of the initial conditions of a slope system on a mass transport event and its deposit.

A more precise analysis for slope instability can be done by numerically modeling the

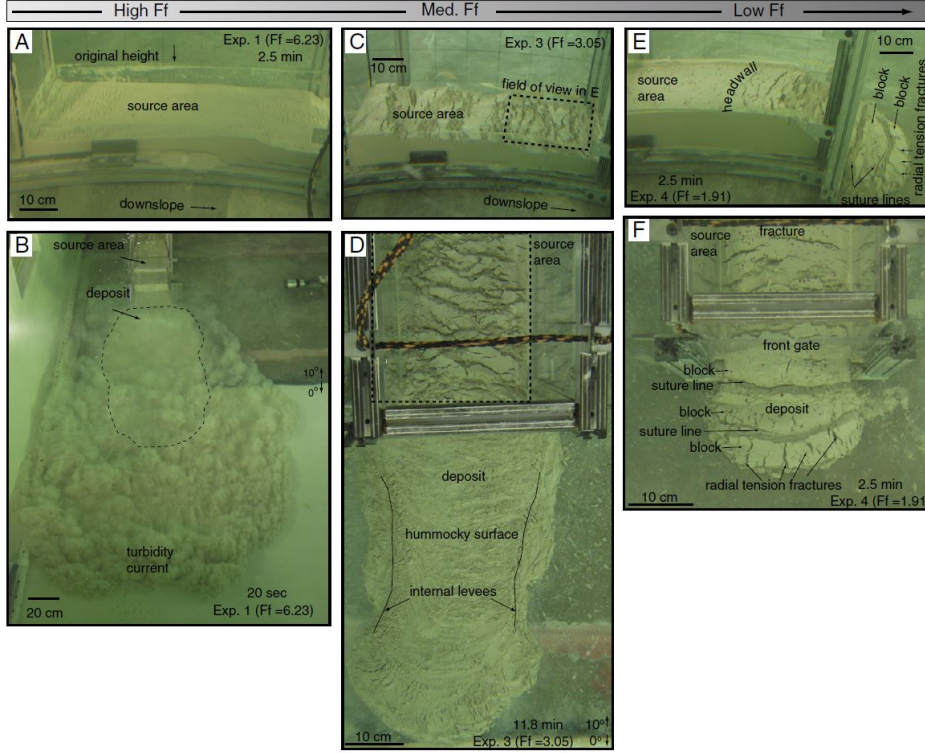


Figure 1.5: Mudflow features characteristic of Flow factor. A, C, E: lateral view of source area. B, D, F: top view of the basin area. From [Sawyer et al. \(2012\)](#).

whole slope system. This is proposed for instance by [Sultan et al. \(2001\)](#) in a 'pseudo-3D' approach (a 2D profile extended in the third dimension) with special attention to the pore pressure distribution. In 2D, [Chemenda et al. \(2009\)](#) model numerically the gradual alteration of rock properties with time. The advantage of complete numerical modeling is to assess the precise regions of highest deformation before the failure with little a priori on the type and position of the rupture surface (e.g., integrated approaches as by [Bouziat et al. \(2016\)](#) or [Busson et al. \(2018\)](#), and softwares like FLAC3D by [Itasca \(2018\)](#)). This solution is computationally more costly than Limit Equilibrium Analysis, as F_f is typically computed on every cell of the 2D or 3D mesh.

An intermediate solution is 'Limit Analysis'; based on mechanical principles and theorems, it allows to assess the stability of a slope structure without the need for an exhaustive computation of the structure as in numerical limit equilibrium models ([Drucker & Prager \(1952\)](#), [Optum CE \(2018\)](#)).

In any case, numerical stability analysis methods do not reproduce the moment subsequent to failure where solid rocks lose their cohesion and begin to be transported.

The literature records the following kinds of pre-conditioning and triggering factors (PTF).

PTF 1 - Geomorphology of the slope environment: gravity influence on the balance of forces

The morphology of a submarine sloping environment, and therefore its influence on the balance of gravity (which drives movement) vs. shear strength, is usually related to several factors:

- Geomorphological elements in a sedimentary basin may provide an initial steep pathway; for example, incisions of channels reaching the top of the continental shelf, incisions caused by a former mass transport, or caused by contouritic/bottom currents (e.g. [Miramontes et al. \(2016\)](#)), decrease the shear strength of a formation. On the contrary, a downslope buttress, initially or due to a previous mass transport, limits the available pathway and increases the region stability. Geomorphological elements also impact the fluid pore pressure distribution within the formation, as shown by [Lacoste et al. \(2012\)](#) through laboratory experiments.
- Tectonic- or isostasy-related uplift or subsidence may lead to a change in location of the basin depocenter (zone of thickest deposits) ([Nelson et al. \(2011\)](#)), thereby modifying the basin depositional environment.
- Change in sedimentation rate and sediment type may also lead to a change in the morphology of the basin, and/or a change in load affecting in-place sediments.

PTF 2 - Weak layer: locally low shear strength

Within sediments accumulation, the presence of a 'weak' layer (i.e. with low, or contrastingly low, shear strength), along which a mass transport would occur, can be related to several elements:

- The layer sediments themselves may have low shear strength. Examples include: evaporites; clayey mudstones of a condensed layer created by a flooding event; clayey mudstones of a contouritic deposit on a glaciated margin ([Leynaud et al. \(2009\)](#)); cohesionless sandy soils, which may be liquefied by an increase in pore pressure.
- A pore pressure increase in the layer may have occurred before its consolidation and burial; for instance, a too quick overloading of fine-grained unconsolidated sediments can prevent the pore fluid drainage ([Leynaud et al. \(2009\)](#)).

- A pore pressure increase in the layer may have occurred after its consolidation by contraction of the sediment matrix, for example if the compaction induced by burial is too quick to allow fluid drainage; horizontal compression may also occur in the basin due to lateral tectonics.
- A pore pressure increase in the layer may have occurred after its consolidation by pore fluid quantity increase. Examples include: instability of gas hydrates which, in precise temperature and pressure conditions, can release gas very suddenly (Mienert (2009)); or, generation and migration of hydrocarbons into a reservoir layer. An example of fluid migration is shown by Frey-Martínez *et al.* (2011) on the Ebro margin, where they suggest that the vertical stacking of submarine canyons created a preferential pathway for fluid migration, which led to overpressure concentration and mass transport triggering.

A weak layer that favors the trigger of mass transport is sometimes called 'décollement layer', especially when laterally expanded in the basin.

PTF 3 - Seismicity

Seismicity can trigger a mass transport by a single earthquake, if its magnitude is high enough or if the pre-conditioning factors are sufficient. Yet long-term seismicity can also progressively affect the environment geomorphology (impacting PTF 1) or the properties of the medium (possibly impacting PTF 2), so that mass transport is more and more likely to occur with time.

PTF 4 - Localized deformation

Volcanic activity can create localized stresses and deformations, which then impact PTF 1 and PTF 2. Creep is another kind of deformation process which is long-term and occurs within evaporite layers or diapirs, driving deformation of contiguous rocks (e.g., Type-3 failure scarps in Migeon *et al.* (2011)).

PTF 5 - Climatic impact

The most famous climate-related factor is the sea-level change. In their study case, Nelson *et al.* (2011) note that most MTDs were deposited during low sea-level periods, and where accurate age data are available, MTDs are connected to rapid sea-level rises or falls. Both low-stand periods and transitional periods are therefore regarded. The intermediate factor is unknown, however: a sea-level rise can induce slope instability if the rise changes the conditions of other PTFs. Although it is apparent from some studies (e.g., Maslin *et al.* (2005), Owen *et al.* (2007), Leynaud *et al.* (2009)), Urlaub *et al.* (2013) have shown that statistics on available known cases are not actually sufficient to prove this relationship.

Note that submarine mass transports differ from subaerial ones especially in that some

very large-scale submarine events - both in terms of volume and of runout distance (the distance overrun by the transported mass) - have been shown to occur on slopes as low as 1° . For instance, [Damuth & Embley \(1981\)](#) report transports of up to 300 km on slope angles of 0.3° to 0.6° . The triggering processes of such events are still under debate (e.g., [Elverhoi et al. \(2010\)](#), [Urlaub et al. \(2015\)](#), [Hühnerbach & Masson \(2004\)](#), [Hampton et al. \(1996\)](#)). On quasi-flat slopes, overpressures high enough to trigger instability may be generated by rapid sedimentation in environments close to river mouths (e.g., [Flemings et al. \(2008\)](#)), yet as highlighted by [Urlaub et al. \(2015\)](#), some submarine mass transports also occur in regions with low sedimentation rates. [Urlaub et al. \(2015\)](#) show that the presence of a highly-compressible sedimentary layer may allow to trigger very large submarine mass transports; such high compressibility may occur because of the presence of organic matter or because of a rapid break down of sediment structure (here the cement between grains).

Several factors are generally adding up to trigger a submarine landslide. Knowing the precise cause for one event is complex, as shown by the above-mentioned PTFs, which cannot all be called 'causes' for the trigger of a mass transport. For instance, is the climatic impact really a cause for trigger of a mass transport, or would it be rather the change in pore fluid distributions that a sea-level change implies?

One may rather consider to distinguish between long-term and short-term effects (e.g., [Richardson et al. \(2011\)](#)), although requiring to define what are 'long' vs. 'short' terms. In this view, short-term changes in the geomorphology, in the fluid overpressure distribution (thus involving fluid flow), in the seismicity are more adapted to be considered causal processes. To them, two other processes may be added: offshore events (punctual storms) and waves (e.g., [Hampton et al. \(1996\)](#)) which can destabilize a slope rapidly, and chemical effects within the sedimentary formation. This 'long-term' vs. 'short-term' distinction is yet to be quantified.

1.3.3 Transport processes

En masse transports and turbidity currents

Different kinds of transport processes can be classified according to their material and velocity properties; a complete classification of submarine mass transports based on macroscopic transport behavior was given by [Posamentier & Martinsen \(2011\)](#). It is illustrated on Figure 1.6. The authors distinguish, by decreasing order of mass cohesion and increasing order of flow velocity: creeps, slides, slumps, flows with plastic behavior, and flows with fluidal behavior. Falls are the quickest, less cohesive processes in their classification. 'Flows' can be '*en masse*' sediment transport which keep cohesion between grains (such as creeps, slides or slumps), or sediment transport where grains are mostly separated such

as turbulent flows (among which turbidity currents) (Posamentier & Martinsen (2011)). Nelson *et al.* (2011) introduce additional names for flows that have a brittle deformation: debris slides (corresponding to the 'slides' in Figure 1.6, but where sediments are divided in blocks), and flows with mixed plastic and laminar behavior: debris flows (suggesting the presence of a matrix and some blocks inside).

Turbidity currents are considered distinct from other mass transport kinds (Posamentier

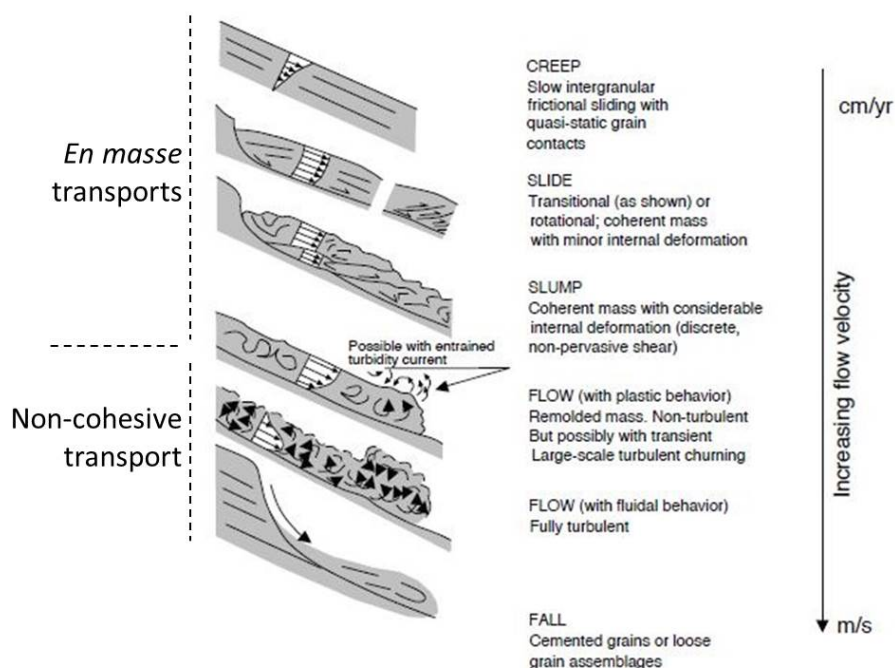


Figure 1.6: Schematic cross-sections illustrating gravity-driven deformational processes, including those that form mass-transport deposits. Modified from Posamentier & Martinsen (2011).

& Martinsen (2011), Nelson *et al.* (2011)), although transport properties vary continuously from cohesive mass transport to low-density turbidity current. Turbidity currents are not *en masse* transports (see Figure 1.6) and do not necessarily result from a rupture of the seafloor material. According to Mulder & Alexander (2001), their main particle-support mechanism is fluid turbulence, as opposed to particle interaction or matrix support which characterize other kinds of mass transport. Turbidity currents can occur simultaneously with, or because of, more cohesive mass transports (see for instance Figure 1.5 (B)). Nelson *et al.* (2011) describe how MTDs and turbidite systems interplay in several case studies of continental margins. They show that MTDs can dominate by far compared to turbidite systems, or on the contrary be almost absent from the sedimentary records, depending on the margin; both kinds of deposits can also be mixed at all spatial scales. This interplay is influenced by the combination of triggering factors. For example, Leynaud *et al.* (2009) show that statistics distinguish submarine mass movements on European continental margins depending on their latitude, i.e. if the margin is glaciated (rather subject to

large-scale slides) or non-glaciated (rather subject to turbidity currents).

Relationship to environmental factors and controls

Mass transport events are part of the more global sediment transfer from the continental shelf to the deep basin. The transport process is therefore linked to the location of the event within the sedimentary basin: on the higher slope, downslope, in the basin, or on the slopes of a deep-sea fan if there is one. This is why the above classification is able to describe the flow itself, but the interpretation of the flow characteristics depends on its environment.

Both analog and numerical models of mass transport have been developed to relate these flow characteristics with environmental factors. They are mostly based on a granular-medium assumption for the transported material. We here rely on studies from both subaerial and subaqueous modeling.

In this respect, one parameter of interest to reproduce by a model is the runout distance (or area). For subaerial mass transports, a few models give good estimates of this parameters. Mangeney-Castelnau *et al.* (2005) study the collapse of an initially cylindrical granular mass along a rough horizontal plane, comparing a numerical, depth-integrated, model, to laboratory experiments. They conclude that the area overrun by the transported mass is correlated to its initial potential energy; their model suggests that the effective friction angle of the basal surface depends on the initial aspect ratio of the moving mass. This global view illustrates the transfer of energy involved in a mass transport: a high initial potential energy is transformed into kinetic energy driving the movement, and eventually dissipated through internal, basal or upper friction with surrounding sediment or water. The SHALTOP numerical model (Mangeney *et al.* (2007)) has shown effective in reproducing the runout distance of some natural landslides (e.g., Favreau *et al.* (2010)); it is based on a depth-averaged thin-layer approximation for a continuous flow representation. The Flow-R empirical model (Horton *et al.* (2013)) provides regional susceptibility assessment of instability, based mainly on a digital elevation model and user-input features like planar curvature (computed feature) or land use. It also models the runout of debris flows. Transport propagation mainly relies on a multiple flow direction spreading algorithm (Holmgren (1994)), and a friction loss function determines the flow energy loss. This model is used in applications for geohazard assessment (e.g., Kappes *et al.* (2012)) at the regional scale. Both models were developed for subaerial conditions. Submarine mass transports have different characteristics.

Other modeling studies build relationships between the initial conditions of a submarine

mass transport and the qualitative type of transport. Via sandbox modelling, [Mourgues & Cobbold \(2006\)](#) classify 'gravity spreading' versus 'gravity gliding'. In gravity spreading, they find that the propagation of the spreading and of the extensional deformations (normal faults) depends on the fluid overpressure on a décollement layer. For medium overpressure, normal faults are closely spaced and bound rotated blocks. For higher overpressure, the propagation of the deformation is faster, and the blocks between faults are not rotated. In gravity gliding, both the fluid overpressure (on the décollement layer and within the sliding mass) and the basal surface properties (frictional behavior and shape) control the sliding.

Still with sandbox models, [Mourgues *et al.* \(2009\)](#) simulate the effect of pore fluid pressure increasing and reaching the lithostatic pressure. In this situation, they observe a local fluidization of the sand, and a ductile flow of this sand associated to local thickening of the deforming zone.

In a numerical slope stability analysis, 'deep gravity spreading' (i.e. rooting on a basal detachment surface) is distinguished from 'shallow slumping' by [Mourgues *et al.* \(2014\)](#). With illustrative experiments, the authors explore the relative effects of fluid overpressure in the basal layer, fluid overpressure in the material above, basal dip and upper slope angle, on the kind of flow likely to occur. Results (see Figure 1.7) show that for a low overpressure ratio λ_b^* in the basal layer, instabilities are driven only by a wedge surface slope angle (α) being higher than the material internal friction angle; in this case, shallow landsliding is naturally preferred: slides do not root in the basal detachment surface. But above a certain overpressure ratio threshold λ_b^{*m} in the basal layer, deformation can occur in the form of gravity spreading, triggered for higher overpressures if the surface slope angle is smaller; for large slope angles and high overpressures in the basal layer, both processes can be mixed (top-right corner of Figure 1.7). The threshold of basal overpressure λ_b^{*m} between the two domains depends on the surface slope angle, the basal slope angle, the internal friction angle of the wedge material and that (reduced) on the basal layer.

Another element impacting transport is the lithological content of the transported mass. [Elverhoi *et al.* \(2010\)](#) present laboratory experiments that demonstrate the impact of the initial clay-to-sand ratio on the separation of the flow into a lower dense flow and an upper turbidity current. As shown on the top of Figure 1.8, clay-rich flows remain cohesive longer, with a thick muddy matrix in laminar regime in the lower part supporting a turbulent flow. They are subject to hydroplaning and acceleration of their frontal part, which can produce large runout distances. More sand-rich flows (bottom of Figure 1.8) are less cohesive. Their lower layer is thinner than that of clay-rich flows and it is formed of sand rather than clay; most of the material is actually transported through turbulent current above. These sand-rich flows are subject to water intrusion and fluidization. They also have reduced erosive capacities compared to clay-rich flows.

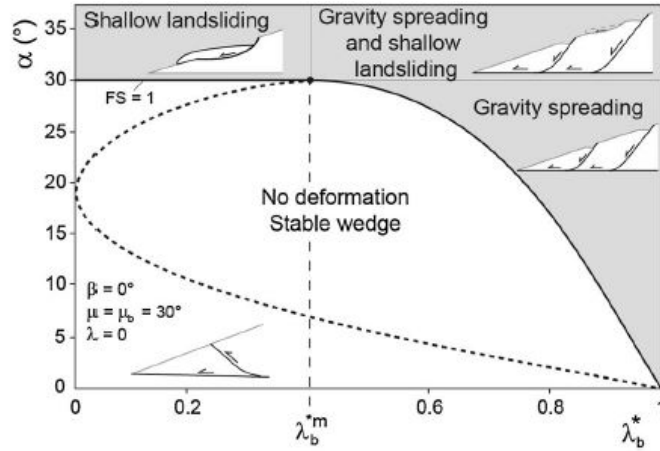


Figure 1.7: Solutions of the model of Mourgues *et al.* (2014) for sand-like material. α is the slope angle of the free surface; λ_b^* is the overpressure ratio of the basal detachment surface, with value zero if no overpressure and 1 if overpressure equals hydrostatic pressure. The dashed line represents the solution for a compressive state of stress. The black bold line represents the solution for a gravity-driven extensional state of stress (the one studied in this PhD project): this line is the limit where the Flow factor (inverse of the Factor of Safety FS here) is $F_f = 1$. The grey area shows domains of slope instability triggered by gravity only. From Mourgues *et al.* (2014).

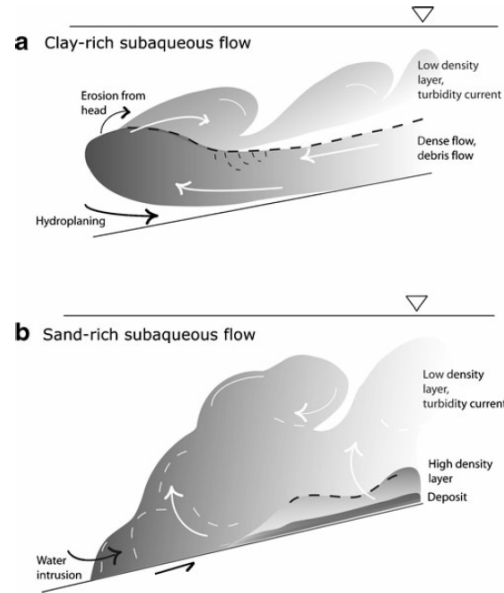


Figure 1.8: Sketches of subaqueous (a) clay-rich and (b) sand-rich debris flows, as observed in experiments. From Elverhoi *et al.* (2010). In their article, clay portion ranges from 5 to 25%, but the authors precise that these critical values may change depending on the kind of clay and the scale of the experiment / field data.

The afore-mentioned studies by Mourgues *et al.* and Elverhoi *et al.* highlight the role of pore pressure (at the initial stage and during transport), initial lithological content of the moving mass, slope angle, and basal surface properties during transport, on the type of deformation of the flow and its rheology.

Grain-to-grain interactions are also studied as part of transport processes; these affect in particular the occurrence of an instability of the front of a granular flow, called 'fingering'. The distribution of grain size in a granular flow is studied via analog (e.g. Goujon *et al.* (2007)) and numerical (e.g. Gray & Kokelaar (2010)) modeling. The internal distribution of grains, their relative friction coefficients, and their size compared to the size of heterogeneities on the gliding surface, have shown to have effects on the morphology of the MTDs. Narrowing, fingering effects can be found because of heterogeneities in size and frictional behavior of the grains (e.g. Goujon *et al.* (2007)). These studies were done for subaerial conditions; subaqueous conditions may modify the results as the density ratio between the ambient fluid and the grains changes; nevertheless, this phenomenon has also been observed in submarine environments (e.g., Moscardelli & Wood (2008)).

Finally, the precise dynamics of a mass transport (velocity change, variations of properties within the transported mass) are difficult to capture in a model. For example, local slope angle variations can modify these dynamics but cannot always be taken into account in models which are limited in resolution. For dense flows, the change in basal surface frictional energy has been shown to be related to the shape of the envelope of the seismic signal generated by the flow (e.g., Favreau *et al.* (2010), Durand *et al.* (2016)). Although effective mostly for low signal frequencies and far from its source, this relationship enables to approach the dynamic behavior of a dense mass transport. Again, to our knowledge, this relationship has only been shown for subaerial mass transport.

The existing global controls on mass transport processes therefore comprise various elements: initial morphology of the transported mass; morphology of the seafloor and of the décollement level if any; transported material properties: grain size and density, grain type proportions and dynamic distribution, frictional behavior, internal fluid pressure; underlying material properties: frictional behavior, fluid overpressure. Similarly to preconditioning and triggering factors, the actual controls in a real environment are complex to define as several usually interfere.

Mass transports, in turn, affect their proximal environment, by triggering: fluid migration in altered preferential pathways (Frey-Martínez *et al.* (2011)); development (enlarging) of gullies (canyons); further mass transport (case of retrogressive events); induced seismicity; water displacement, tsunami. These elements, however, are little seen in literature

concerning ancient, buried mass transport deposits.

Despite the number of models that exist and can partially explain the transport processes involved in a mass transport, two limits seem to remain: (i) the incapacity to model a trigger and transport on a quasi-flat slope, and (ii) the incapacity to simulate in a deterministic way the spatial variability inside the transport, which is later recovered in the heterogeneous internal geological facies of an MTD.

1.3.4 Depositional and post-depositional processes (PDP)

Depositional and post-depositional processes (PDP) concern the end of the transport, when the mass stabilizes; they also include the posterior evolution of the deposit, with burial-related and possibly chemical changes. The following processes are often referred to as potential impacts on the process of deposition.

PDP 1: Compression at the front of the flow (e.g., [Silva *et al.* \(2010\)](#));

PDP 2: Loss of mass, especially if a turbidity current is triggered by the mass transport (e.g. [Figure 1.5 \(B\)](#));

PDP 3: Turbidite deposition on top of the mass transport initial deposit;

PDP 4: Terminal dispersion: the flow dispersing and getting much wider and slower (e.g., [Moscardelli & Wood \(2008\)](#), [Richardson *et al.* \(2011\)](#));

PDP 5: Remobilization, i.e. part of the deposited material falling again (e.g., [Moore & Sawyer \(2016\)](#));

PDP 6: Compaction during burial due to post-deposition sedimentation

PDP 7: Fluid migration and associated changes to the sedimentary pile: possibly, volcano creation, or PDP 3 or PDP 4;

PDP 8: Regional deformation, impacting the morphology of the deposit, and possibly some other PDPs (e.g., [Omosanya & Alves \(2013\)](#));

Models either take these PDP into account together with the transport phase, or do not consider them at all. For example, compression is observed at the toe of mass transport deposits in analog modelling, while loss of mass is seldom considered. Post-depositional processes acting on MTDs are complex to model, given that they imply the whole sedimentary cover.

We have seen a few examples of models that relate one of the three stages of a mass transport to the final properties of an MTD. In the work of [Mourgues *et al.* \(2014\)](#), several parameters are shown to impact the kind of transport that will occur, when outside the stability zone (see [Figure 1.7](#)). In that of [Sawyer *et al.* \(2012\)](#), the value of F_f is

shown to impact the final depositional properties (see Figure 1.5). Each model brings in new elements on one aspect of a mass transport event. It is clear, however, that many different processes may be involved in the formation of one MTD character. This makes the modeling of a mass transport event very complex.

1.4 Approaching MTDs through seismic data acquisition and interpretation

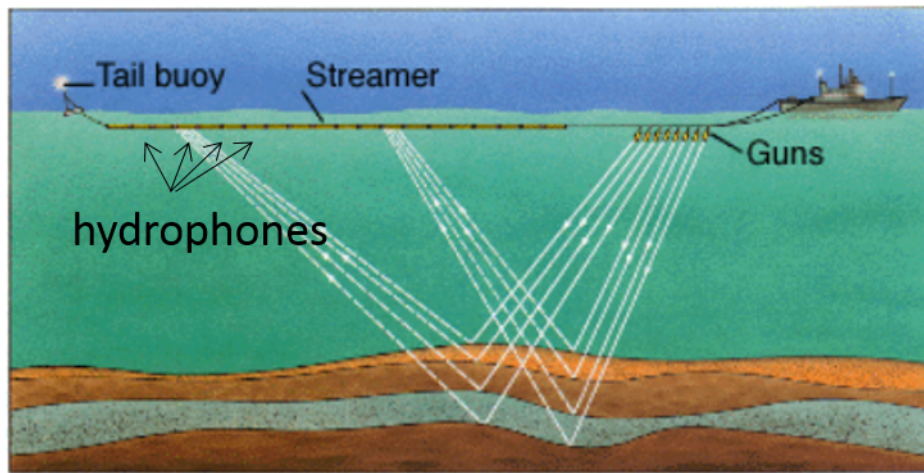
MTDs may be studied by forward models presented above. Some models are especially useful for geotechnical applications for instance. Ultimately though, data is needed to observe existing MTDs resulting from past events, understand how they were formed, and constrain model parameters. In this section, we present seismic data and its potential for sedimentary systems interpretations.

1.4.1 Seismic data acquisition and processing

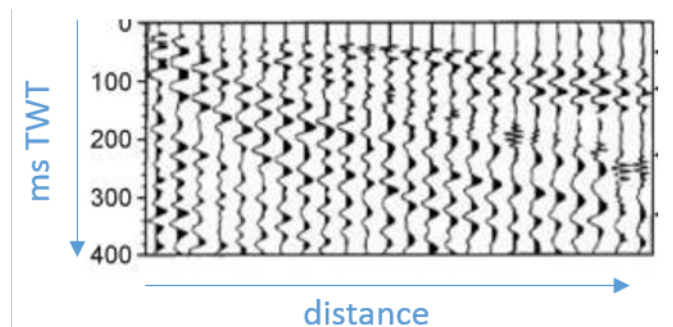
Seismic imaging allows to study the structure of sedimentary basins through the propagation of seismic waves. Seismic data such as the ones in use in this project are acquired by means of a source and receiver system. A source generates vibrations; the source is either vibrating trucks or explosive on land, or one or several air guns for offshore acquisitions. The wave travels through the underground medium, and its propagation undergoes changes due to varying properties of the medium. The receiver records the resulting total vibration at the place where it is set (e.g., at the sea surface) - see Figure 1.9a.

Each point on the map that is targeted by the acquisition is then given its several seismic response signals, corresponding to several distances (or 'offsets') between source and receiver: a set of seismic 'traces', each of which is a seismic signal in amplitude versus time; a trace is usually visualized vertically. The seismic signal reflects the surveyed medium properties, mainly rock heterogeneities and wave-propagation effects such as dispersion.

After a few processing steps, these traces are stacked into only one trace, allowing to improve the signal-to-noise ratio. The resulting data have one trace for each targeted point on the map (e.g. Figure 1.9b). In any case, several processing steps are applied on the seismic traces; they are then grouped to form 2D or 3D data. A '2D profile', or '2D line', is made of several adjacent traces that were acquired on a line. A '3D volume' or '3D cube' is made of several adjacent traces that were acquired in the two horizontal directions; sections of the cube along the two directions are called 'inlines' and 'crosslines' respectively, according to the data storage. The axes of the 2D / 3D data are then distances horizontally and time vertically. 2D profiles, generally acquired along rather long distances, provide a regional overview of the stratigraphy of a basin; and 3D cubes, generally limited in length, offer multi-directional information on a local scale.



(a)



(b)

Figure 1.9: Marine seismic acquisition: example for 2D data. (a) The acquisition ship drags a system of sources (air guns) and receivers (hydrophones on the streamer). Modified from the [Schlumberger Oilfield Glossary](#). (b) Display of seismic data (not depth-converted), positive amplitudes shaded for enhanced inter-trace continuity. Each trace results from the operation of stacking signals from all receivers. TWT: two-way traveltime. Modified from the [US EPA web archive](#).

Additional processings of seismic imaging include time-to-depth conversion, where the time data is converted into depth-interpreted data (so that the vertical axis is depth) thanks to the use of a velocity model. This conversion is not always done as it requires acquiring a velocity model and it demands extra processing time. A seismic dataset, in the end, consists in seismic amplitude data for every sample of every trace. Visualizing a vertical seismic section or profile gives as primary information some laterally-correlated amplitude peaks, called reflectors. These correspond to interfaces between layers of contrasting acoustic properties. Reflectors that correspond to 3D surfaces interpreted as representative of a given event in geological time are called 'horizons'.

Due to signal acquisition and processing, seismic data are limited in resolution. The resolution is the minimum spatial or temporal separation between two geological features (typically reflectors) for them to be well separated by seismic imaging. Both vertical and lateral resolutions depend on the dominant signal frequency and the wave velocity in the medium. The lateral resolution also depends on the depth; migration, one of the seismic processing steps, improves it, so that very often the lateral resolution is limited by the lateral sampling rate.

Typical wave velocities (c) in the subsurface range from 1500 m/s to over 6000 m/s. They most often increase with depth. The dominant frequency f of the output seismic signal ranges from 20 to 50 Hz. It decreases with depth. The dominant wavelength λ is related to c and f as:

$$\lambda = c/f$$

Vertical resolution depends on this wavelength: the minimum spatial separation between two reflectors to be identified is typically chosen as $\lambda/4$ (see for example the [SEG \(2018\)](#) webpage), i.e. from 10m to 63m. As for lateral resolution, it does not usually surpass a few meters. Seismic vertical resolution is thus relatively poor compared to cores or log measurements, for which centimeter variations are observed vertically. Geomorphologic structures visible on the seafloor surface can be described with fine precision by multi-beam echo-sounder data acquisitions. These kinds of data are advantageous for characterizing the fine scale (up to $10^{-1}m$) of the surface, in a local area. For buried geobodies, seismic data offer two advantages: (i) they give continuous information on the lateral extent of the MTD, and (ii) they give vertical information, i.e. on the internal content of the object (e.g. [Frey-Martínez \(2010\)](#)). A seismic section can actually be analyzed as an image. In particular, interpreters focus on the visual aspect of the seismic image in a local area, or patch (in 2D or 3D); this aspect is often called a 'seismic facies'.

1.4.2 Seismic facies and interpretation

Regions or patches of a seismic image that share common visual features can then be qualified with a seismic facies name. Note that such facies and seismic interpretation in

general are commonly determined for time data as well as for depth-converted data. Two kinds of approaches are mainly used to study seismic facies. Here we briefly present both approaches and we define seismic geomorphology.

1.4.2.1 Model-driven seismic facies: seismic stratigraphy

The first approach for studying seismic facies is related to seismic stratigraphy, a discipline that was initially highlighted by the works of [Mitchum Jr *et al.* \(1977\)](#). Since then, seismic stratigraphy has developed together with sequence stratigraphy, the latter being defined by [Catuneanu *et al.* \(2009\)](#) as the study of 'facies relationships and stratal architecture within a chronological framework'.

Figure 1.10a from [Bacchiana \(2008\)](#) gives a 3D sketch view of sedimentary deposits resulting from evolving depositional settings in a basin. Depositional settings evolve because of variations in the space available for sediments between the seafloor and the sea level - this space is called 'accommodation'. For a constant sediment influx and static seafloor, the depositional setting evolution depends on the eustasy, i.e. sea-level variations. The various shapes of 'systems tracts' in Figure 1.10a correspond to different moments in the eustatic cycle.

Seismic stratigraphy is based on the assumption that one seismic reflector corresponds to sediments deposited during a time interval of similar sedimentation conditions. Under this condition, the geometry of a set of reflectors corresponds to a specific depositional setting, as shown on Figure 1.11 ([Berton & Vesely \(2016\)](#)). On this figure, simple descriptions for seismic facies A to F are: oblique parallel clinoforms; oblique tangential clinoforms; sigmoidal clinoforms; discontinuous and dipping; discontinuous in several directions; parallel and flat. These geometries are classified according to reference geometries as shown in Figure 1.10b, in turn corresponding to various depositional settings such as sketched in Figure 1.10a - so that seismic facies are defined to be part of the highstand systems tract, transgressive systems tract, or other, defined in the stratigraphy model (Figure 1.10a).

1.4.2.2 Data-based-only seismic facies

In the previous approach, a prior, model-driven input (coming from stratigraphy), is provided to the definition of facies. Conversely, the second approach for defining seismic facies is a pure description of the patterns seen in the amplitude distribution with no a priori analysis. It can be similar to the 'sigmoidal clinoforms', 'discontinuous and dipping' descriptions mentioned before - although sticking to this low-level kind of description. However, it often also includes amplitude information, such as in 'parallel high-amplitude continuous reflectors', 'high-amplitude semi-continuous reflectors', 'low amplitudes' for example. These descriptive labels will be the final labels of the facies, with no association to a stratigraphic type. This distinction is inconspicuous; yet this second definition differs from the previous one where the final labels are necessarily part of the stratigraphic model.

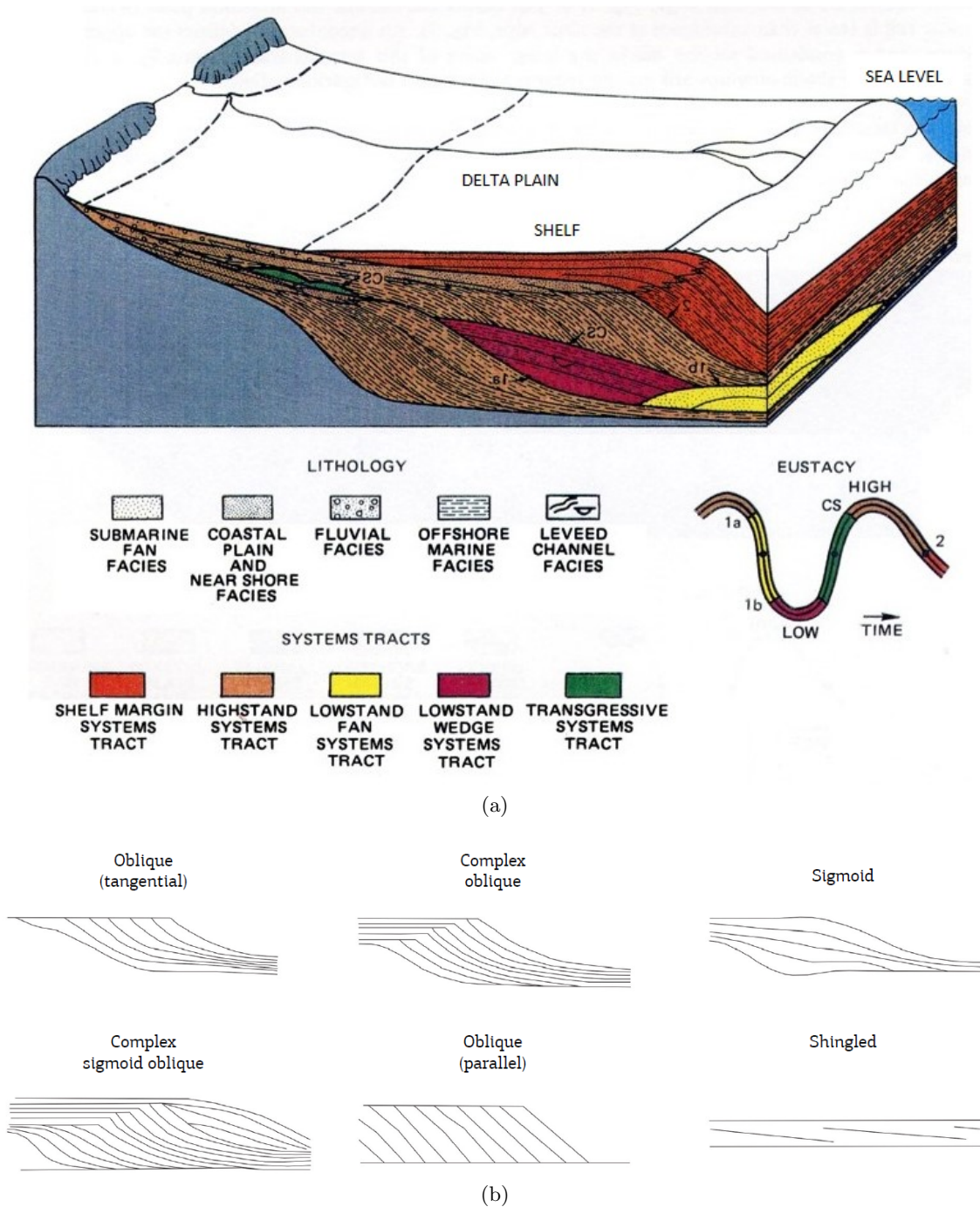
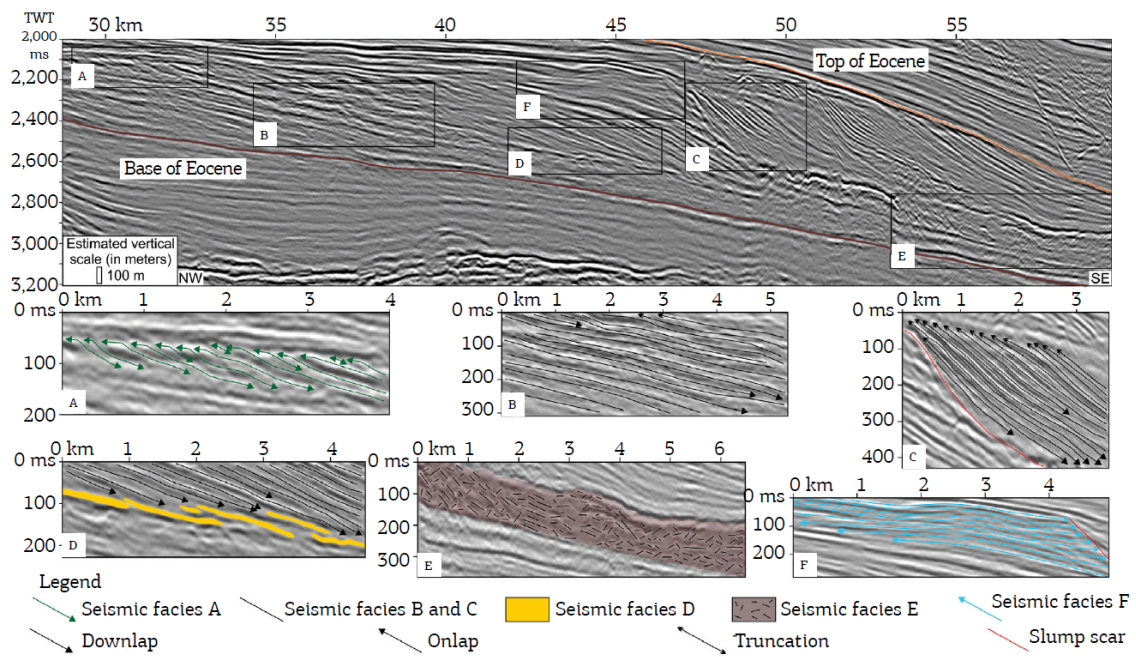


Figure 1.10: Sequence stratigraphy and stratal geometries. (a) Systems tract shapes and boundaries associated with eustatic cycles. Modified from [Bacchiana \(2008\)](#). (b) Several reference geometries used for seismic stratigraphy. From [Berton & Vesely \(2016\)](#) and [Mitchum Jr *et al.* \(1977\)](#).



TWT: two-way-time.

Figure 1.11: Seismic stratigraphic features on an example 2D seismic section, as interpreted by [Berton & Vesely \(2016\)](#): '(A) Seismic facies A, interpreted as shelf-margin deltas/shoreface deposits; (B) seismic facies B, interpreted as slope clinoforms with tangential (oblique) geometry; (C) seismic facies C, interpreted as slope clinoforms with sigmoidal geometry; (D) seismic facies D, interpreted as turbidites; (E) seismic facies E, interpreted as mass-transport deposits; (F) seismic facies F, interpreted as continental to shelfal deposits'. On the top image, the red and orange lines are horizons. From [Berton & Vesely \(2016\)](#).

In this way, the description of patterns does not necessarily rely on reflector geometry as understood by sequence stratigraphy; it may then be able to consider not only reflectors corresponding to iso-age formations, but also reflectors created by contrasts in e.g. lithologies or fluid content. For instance, in Figure 1.11, a unique stratigraphic seismic facies (E) has been created to depict mass transport deposits. In some cases, however, more precision is needed, either to detail the variations within a globally 'E-like' facies, or because the MTD does not appear as a uniform facies. Some examples will be given in section 1.6.1.

Facies may be created as a mutually exclusive facies set (i.e. one region is characterized by one facies only); one may also use non-exclusive facies sets, where one region is described by several facies. Further analyses then relate these non-semantically-meaningful seismic facies (e.g., homogeneous low amplitude values on a laterally large region of a 3D cube) with interpreted geological facies (e.g. open-marine deposition of pelagic sediments). Details on facies numerical definition will be given in section 2.2.1.1.

To sum up, seismic data analysis leads to defining seismic facies. These facies can themselves correspond to some geological characteristic of a depositional environment or be defined only via pure descriptions awaiting future interpretations. We will study further what kind of approach is more appropriate to our case study in chapter 2.

1.4.2.3 Seismic geomorphology

Seismic geomorphology is the discipline concerned with the 'extraction of geomorphic insights using predominantly three-dimensional seismic data' (Posamentier *et al.* (2007)). It is generally the name given to methods using seismic data (2D or 3D) for retrieving present-day- or paleo-landform features (SEG (2018)). Seismic facies analysis, for example, can be used in seismic geomorphology. Geomorphology itself describes the formation and evolution of landscapes (and submarine landscapes), thereby giving clues on the processes shaping a depositional environment. These processes are typically part of sediment deposition and erosion. Seismic data give access to information on buried sediments and, thus, on the past evolution of landscapes, giving rise to the name 'seismic geomorphology'. Studying MTDs with seismic data is therefore a contribution to seismic geomorphology.

1.5 Data and settings of the case study

In this PhD, we use for applications a set of seismic data that were acquired in the region of the Offshore Amazon River Mouth basin (Foz do Amazonas), hereafter called Amazon basin. In the current section, we present the geological settings of this data.

1.5.1 Regional setting: the Amazon River basin geological history

The Amazon River marine depositional system, fed by the discharge of the Amazon River, has been studied for several decades. The Amazon River, the biggest in the world in terms of water flow (mean water flow: $190\,000\text{ m}^3/\text{s}$), currently delivers the discharge of a transcontinental drainage basin of size $6.1\cdot 10^6\text{ km}^2$. This drainage basin spreads from the Andes mountains to the mouth of the Amazon River, on the Atlantic side of South America. The basin history is connected to that of the Andes mountains (Roddaz *et al.* (2005), Campbell *et al.* (2006), Figueiredo *et al.* (2009), Shephard *et al.* (2010), Hoorn *et al.* (2010), Espurt *et al.* (2009)), and to the regional/global-scale tectonics of the Brazilian continent. Figure 1.12 presents the main regional settings, with the data available for the study.

The Brazilian Equatorial Margin and its associated sedimentary basins initiated in the opening of the Atlantic Ocean. Dating back to before the Atlantic Ocean opening are major structures still having an important role in the geology of the basin: the Guiana and Brazilian shields (now bordering the Amazon River mouth on the Northern, resp. Southern sides), and pre-rifting-related grabens that, according to Soares Junior *et al.* (2011), eventually turned into the continental break-up of the margin. The Atlantic Ocean opening occurred in the early Cretaceous (Moulin *et al.* (2010), Soares Junior *et al.* (2011)).

Soares Junior *et al.* (2011) propose a place in the Gondwana and Pangea continents (earlier stage studied: late Triassic, i.e. 237 - 201 Ma), that corresponds to the Amazon Basin current position. By following the evolution of tectonic plates with time, they reconstruct the earliest structures of the Amazon basin as well as two other neighboring basins, in a forward manner. The Atlantic Ocean opening occurred in the early Cretaceous (after 145 Ma, Moulin *et al.* (2010), Soares Junior *et al.* (2011)); its Equatorial part was completely opened by the late Albian (100 Ma). This corresponds to the start of deposition of deep marine mudstones and siltstones; this depositional environment, lasting until the Paleocene, led to the sedimentary so-called Limoeiro Formation (Figueiredo *et al.* (2007), Reis *et al.* (2016)). Subsidence happened relatively late in the passive margin evolution: instead of occurring just after the rift phase (Albian), it took place at a late Paleocene – early Eocene stage (56 Ma, Soares Junior *et al.* (2011)). This period approximately coincides with a new phase in the sedimentological history of the Amazon basin, with the establishment of a carbonate platform (Wolff & Carozzi (1984)). The carbonate platform was then built in 4 cycles until middle Miocene (15 - 13 Ma) (to late Miocene (8 - 5 Ma) in the Northern part of the basin, see Cruz (2018)), with clastic deposition periods in between (Wolff & Carozzi (1984), Figueiredo *et al.* (2007), Cruz (2018)). During the 4th cycle, i.e. from early to middle Miocene (23 - 15 Ma), the carbonate platform was progressively destroyed (Wolff & Carozzi (1984)); shale deposition expanded and turned from a lagoonal to a marine deposition-type (Cruz (2018)).

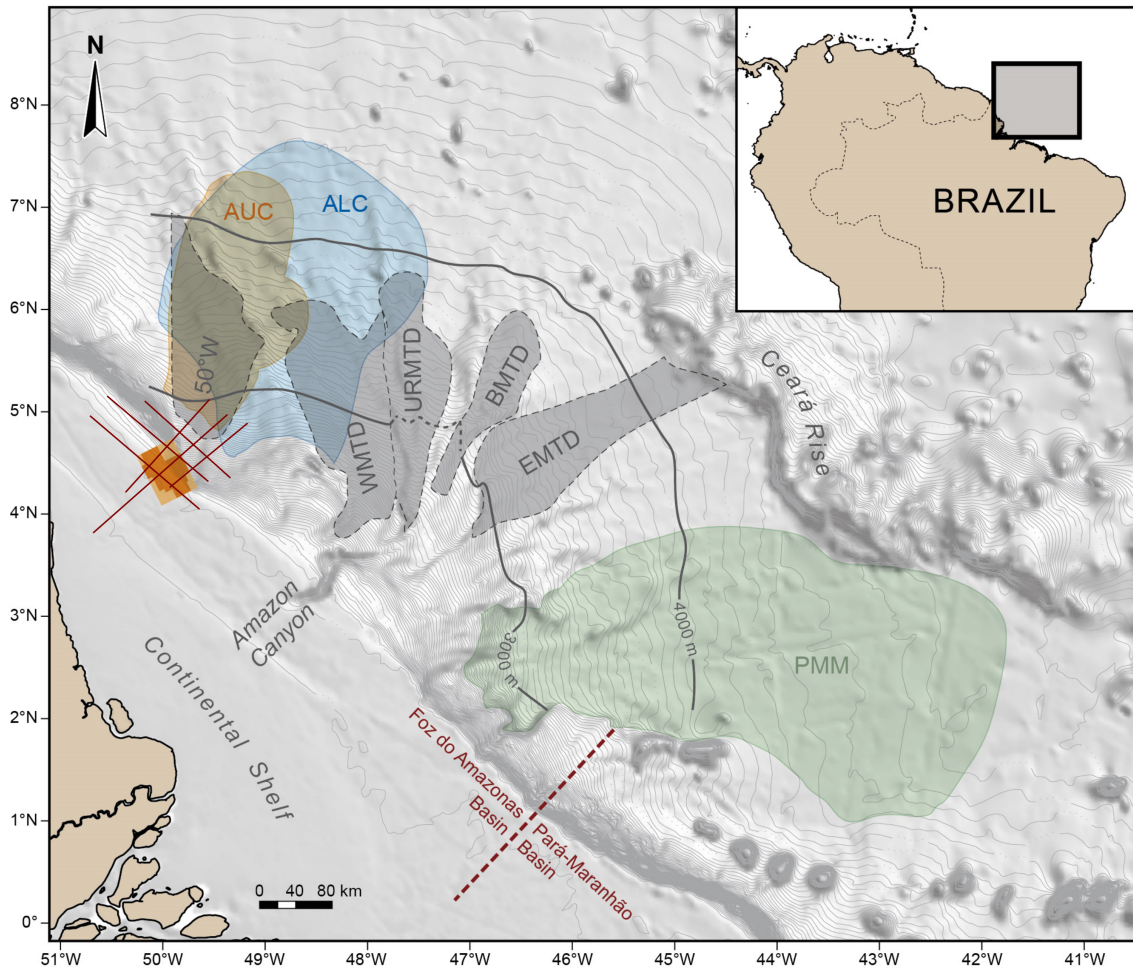


Figure 1.12: Bathymetric map of the Amazon basin with location of major previously-studied MTDs and seismic data. Modified from Reis *et al.* (2016) and Silva *et al.* (2016). The 50°W (Damuth & Embley (1981)), WMTD, EMTD (Western / Eastern MTDs, Damuth *et al.* (1988)) are superficial MTDs. URMTD and BMTD (Unit R / Buried MTDs, Damuth *et al.* (1988)) are buried. The Amapá and Pará-Maranhão Megaslides (ALC-AUC / PMM) were studied by Silva *et al.* (2010) and Reis *et al.* (2016). Amapá Lower Complex (ALC), the deepest mass transport complex of Amapá, is mapped in blue; Amapá Upper Complex (AUC), more recent, is mapped in orange, after Reis *et al.* (2016). The 3D seismic cube is mapped with available seismic data in dark orange and 2D seismic profiles are mapped in dark red.

After the setting of these early structures on the Brazilian Equatorial margin, the South American continent underwent major tectonic changes in its Northern part during the Miocene epoch.

On the continental side, an East-West tilt of the South American continent has been highlighted by Shephard *et al.* (2010): mantle-convection-driven subsidence (Eastwards) and the Andean uplift (Westwards) were the two main processes driving this tilt. By using coupled models of mantle convection and plate kinematics, they propose a continental evolution as follows. An initial subsidence formed the Amazonia 'mega-wetland', that existed from late Oligocene / early Miocene (Hoorn *et al.* (2010)) until middle to late Miocene. Meanwhile, the South American continent was driven westwards from 30 Ma on (early Oligocene) and over the subducted neighboring western plates. This westward motion of South America over subducted slabs induced a 'rebound', i.e., part of the plate was uplifted – and this uplift propagated eastwards. This would be the origin of the Andes formation. The Eastern subsidence rate decreased a little, and the continuous eastward-propagating uplift finally reached previously mega-wetland zones during the late Miocene (14 to 6 Ma). In the end, both subsidence and uplift induced an East-West tilt of the continent. This led to the establishment of the Amazon drainage and fluvial systems (Hoorn *et al.* (2010), Shephard *et al.* (2010)).

On the marine side, the depositional system also changed during the Miocene epoch, as observed in sedimentological records (exploration wells / 2D seismic data) in proximal and distal parts of the Amazon basin by Figueiredo *et al.* (2009) and Gorini *et al.* (2014). Sedimentation was first primarily carbonates on the shelf; the little amount of clastic sediment input, appearing at least in the early Miocene (18.3 to 15 Ma, according to Gorini *et al.* (2014)), was that from the (small) eastern Amazonian basin. Carbonate sedimentation terminated abruptly (9.5 to 8.3 Ma) on distal seismic lines from the Amazon paleo-canyon, but gradually on proximal seismic lines, especially on the North-West part of the shelf (Gorini *et al.* (2014)). The transcontinental Amazon River establishment dates back to the early- or mid-Tortonian (11.5, resp. 9.5 Ma) according to Figueiredo *et al.* (2009), resp. Gorini *et al.* (2014). With the fluvial system transporting sediments from the Andean erosion and through a large drainage basin, the clastic continental influx initiated the deposition of a deep-sea fan (Figueiredo *et al.* (2009)). The carbonate sedimentation probably stopped because of two combined processes: a very rapid sea-level rise after a major lowstand (carbonates not able to develop quickly enough), and the increased influx of clastic material (Gorini *et al.* (2014)). Since then, sedimentation rate kept increasing, two major increases occurring at around 5.6 and 3.8 Ma, the latter jointly with a widespread progradation. At 2.4 Ma, a third increase occurred, together with changes in drainage system (incisions in the shelf and rather basinwards deposits). From then on,

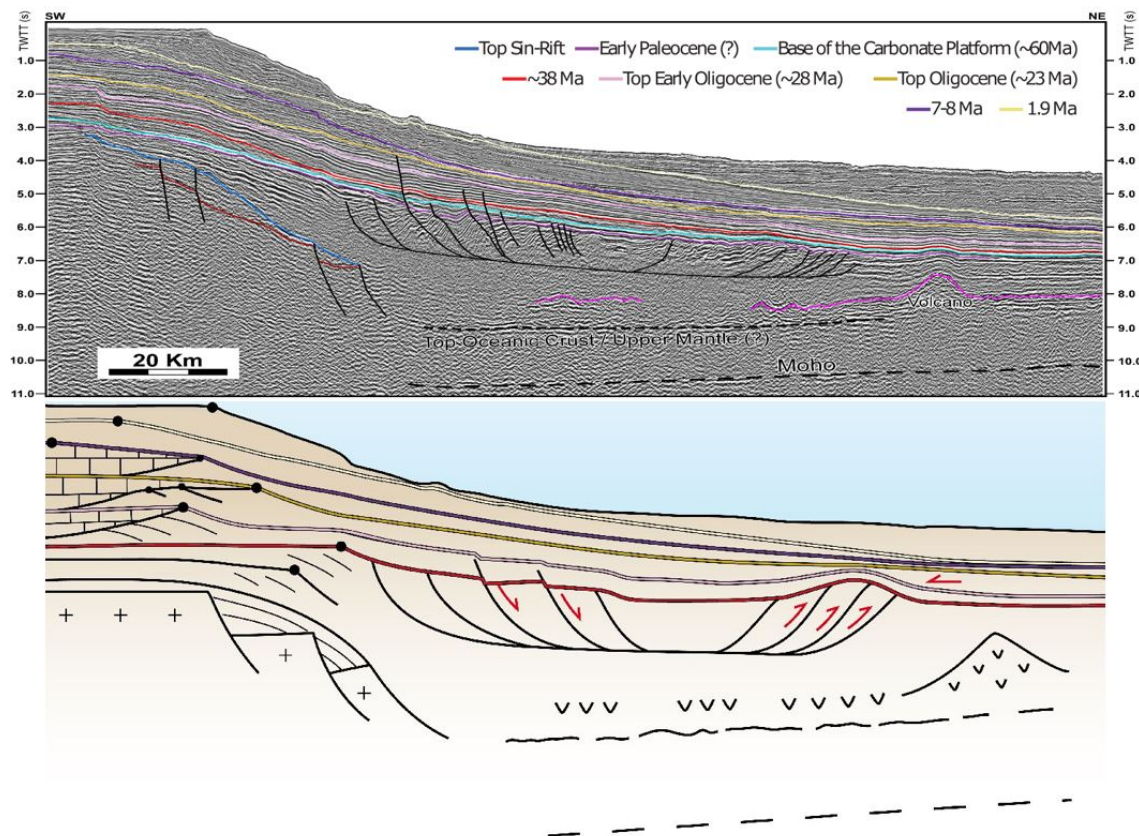


Figure 1.13: Interpretation of a 2D seismic profile across the Amazon basin: horizons corresponding to the main evolution stages of the basin. From Cruz (2018). The top sin-rift dates back to the late Cretaceous (100 - 66 Ma); above it is the Limoeiro Formation (deep marine mudstones and siltstones). The base of the carbonate platform dates back approximately to the early Eocene (60 to 56 Ma). The 7-8 Ma horizon corresponds to the end of the top of the carbonate platform, and base of siliciclastic sedimentation. The dark lines connecting the slope and basin regions within the Limoeiro Formation are examples of an extensional-compressional tectonic system.

400 ka cycles appeared in the deposits (highest eccentricity cycle), characteristic of high sedimentation rates in deltaic environments (Figueiredo *et al.* (2009), Gorini *et al.* (2014)).

The Ceará Rise is a relief offshore the Amazon basin (see Figure 1.12). The origin of this topographical high is still under debate. Figure 1.13 summarizes the main evolution stages of the Amazon basin, as interpreted by Cruz (2018) from a basin-scale 2D seismic profile.

1.5.2 Gravitational processes in the Amazon basin

In the Amazon basin, information on the presence/absence of mass transport signatures and their characteristics (source of detachment, mass-transport process, composition...) give clues to confirm or make hypotheses on the region geological history (subsidence and tectonics, sea level influence, South-American continent evolution...). More locally,

understanding the causes and effects of MTDs should give insights on the probability of presence of fluids, among which hydrocarbons, pressure effects, slope stability, seafloor topographic evolution, and other factors.

Multiple influences

The Amazon basin sedimentation has been subject to two kinds of influences:

- (A) Transform-fault-related controls: neighboring sedimentary basins along the Brazilian Equatorial margin have been impacted by tectonic movements linked to transform faults along the Atlantic dorsal (Darros de Matos (2000)). Silva *et al.* (1998) also mention the Saint-Paul's fracture zone as a control on the morphology of the Amazon basin. However, Cruz (2018) highlights that the Amazon basin itself might not be subject to such description, partly due to the large thickness of deposited sediments – which changes a lot the balance between geological controls on this part of the margin.
- (B) Compression-extension tectonic controls, linked to the Andean uplift and to specific subsidence effects on the margin

Focusing on the second influence (B), a lot of work has been done to connect the large-scale gravity tectonics to smaller-scale elements that are specific to the Amazon basin: a succession of submarine slides, which occurred accordingly since the establishment of a clastic sedimentation in the basin (Reis *et al.* (2016)). Two main aspects can then be distinguished regarding gravity-driven processes occurring in the Amazon basin:

1. Large-scale, tectonic-related gravitational processes, affecting the whole marine sedimentary sequence from the carbonate platform to the top. These processes are mostly driven by an extensional-compressional tectonic system, and are typically observed in the form of listric normal faults in the upper slope and fold-and-thrust belts in the middle-to-down slope (Reis *et al.* (2010); see also Figure 1.13). These faults and folds are thin-skinned and their possible causes and aspects have been discussed by several authors (Cobbold *et al.* (2004), Silva *et al.* (1998) for example).
2. Somewhat smaller-scale (because 'localized') gravity-driven events, namely, submarine slides (in the Amazon case, they are sometimes called 'megaslides' given their outstanding size), appearing mainly in the Miocene-to-present sedimentary series (Maslin *et al.* (2005), Silva *et al.* (2010)), in the form of Mass-Transport Deposits (MTDs). These 'smaller-scale' processes are still among the largest known submarine slides on Earth, covering areas of up to $10^3 km^2$ with estimated thicknesses of several $10^2 m$ (Reis *et al.* (2016)).

A study by Reis *et al.* (2010) shows that the 2 kinds of processes are strongly linked, notably through the trigger of MTDs along thrust belts. As such, MTDs may be seen as the dynamical counterpart of the slower, long-lasting, tectonic-related gravitational processes.

First aspect: large scale processes - analog models

Studying the Amazon basin extensional-compressional system, Cobbold *et al.* (2004) set up a sandbox model with production of fluid flow (air) through the sandbox material. They conclude that the upper slope features (listric normal faults) would be linked to the downslope features (folds and thrusts belts) by a common basal detachment within the Cenomanian-Turonian strata (i.e. in the Limoeiro Formation). They also show that fluid overpressure may be the most likely factor that induced small shear stresses on this level, also arguing that hydrocarbon generation most probably created this fluid overpressure rather than compaction. However, they do not assess the possibility of gas hydrates presence as a possible source of short-term fluid overpressure.

Still with a similar experimental apparatus, but focused on progradational delta more generally than just the Amazon region, Mourgues *et al.* (2009) observe that thrust belts could be created by high fluid pressures inducing a fine shear band (corresponding to the detachment level) where the sands used in the experiments behave like a fluid, with ductile flow. They also point out that old buried thrustbelts can be reactivated during progradation. These elements can be related to the Amazon basin: overpressured detachment levels seem to be a likely hypothesis according to several authors.

Second aspect: localized events

Inside these localized events, a first kind of MTDs are the ones that are observed on the Amazon Fan itself; the main trigger of these is subject to debate, as the slope there is very low (current slope: maximum 0.9° according to Reis *et al.* (2016); slopes followed by the transported masses: maximum 0.6° according to Damuth & Embley (1981)). Damuth & Embley (1981) suggest that they could be related to the channel-levee system in the fan; Maslin *et al.* (2005) argue instead that the climatic control drove these 'localized' MTDs, triggering them either by a gas-hydrate release, or by a sediment over-burdening. In any case, these authors study MTDs dating to the Quaternary (after 2.58 Ma), which are either buried or superficial, one of them (the '50°W') being further NW from the fan (see Figure 1.12).

The other kind of MTDs are even larger, and were exclusively produced on the NW and SE sides of the Amazon Fan. Several MTDs are seen almost stacked vertically, lead-

ing them to be called 'Mass Transport Complexes'. These large MTDs were described by Silva *et al.* (2010) and Reis *et al.* (2016) through 2D seismic data analysis. Due to their size, they are visibly related to the extensional-compressional system mentioned earlier, as extension (faults) and compression (folds and thrusts) are present inside the MTDs themselves.

Reis *et al.* (2016) distinguish 6 main megaslides on the NW side, calling them the 'Amapá Megalide Complex', with megaslide AM1 in the Amapá Lower Complex and AM2 to AM6 in the Amapá Upper Complex; and 4 on the Southern side, called the 'Pará-Maranhão Complex' (PM1 to PM4).

Reis *et al.* (2016) suggest that the AM1 megaslide, from a mixed carbonate-siliciclastic source, was formed in the late Miocene to early Pliocene from the platform that collapsed under its own weight (maybe triggered by seismicity), falling towards NW (as guided by the paleobathymetry). AM2 to AM6 and PM1 to PM4, from siliclastic origin only, were triggered in separate periods due to instability on a same specific horizon called 'H3' in the article, imprecisely dated back before the end of the carbonate production – the process of sliding was 'continuous' along this horizon (called a 'décollement' level), i.e., one megaslide was not formed by only one event. H3 is in lateral correlation with the base of all these megaslides. In Reis *et al.* (2016)'s interpretation, H3 could be a condensed section (formed during a major flooding of the zone, i.e. during a rapid sea-level rise), which impermeability and fluid overpressure led to these sliding events. One may note the possible correspondence between this H3 horizon and the basal detachment mentioned in the Limoeiro Formation by Cobbold *et al.* (2004) and Figueiredo *et al.* (2007).

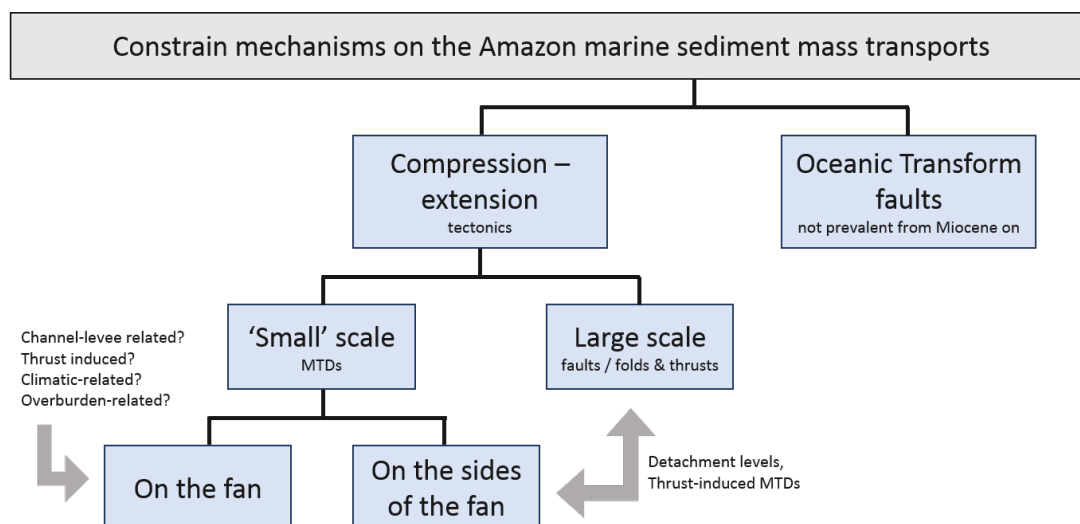


Figure 1.14: Synthetic schema of the main types of transport mechanisms in the Amazon River Mouth basin, according to the literature (Damuth & Embley (1981), Silva *et al.* (1998), Cobbold *et al.* (2004), Maslin *et al.* (2005), Figueiredo *et al.* (2007), Silva *et al.* (2010), Reis *et al.* (2016)).

Figure 1.14 summarizes the aspects discussed above about mass transports in the Amazon River Mouth Basin. From the literature, we highlight that:

- MTDs exist at different scales, and their aspect is sometimes influenced by the compression-extension environment;
- Compression patterns can be seen in seismic data, inside or nearby the head (front) of some MTDs; they appear as folds and thrusts, i.e. patterns oriented basinwards;
- Extension patterns can be seen in seismic data, usually not inside the tail (back) of MTDs; they can be a structural indicator for interpretation. The tail of MTDs can either be distinguished (by its thinner thickness), or not;
- A surface could be identified to correlate several MTDs (or their headscarp) or gravity-driven mechanisms; this surface could be an overpressured detachment level;
- The channel-levee system in the deep-sea fan could be related to MTDs on/near the fan.

Overall, the Amazon basin has several examples of different kinds of gravity-driven mechanisms. These elements make it an appropriate setting for the objectives of this PhD.

1.5.3 Data used for this PhD project

The seismic data used in this study consist in a 3D post-stack seismic cube BM-FZA-4-5 provided by CGG (Houston office). We also use three partial stacks: the near-offset, mid-offset and far-offset datasets. In each case, the cube is time-migrated (post-stack migration) but not depth-migrated. Its size is 60 x 43 km (2388 inlines, 1732 crosslines), with 25 m of intertrace. In the 60 x 43 km rectangle, data is available in parts only (see dark orange in Figure 1.12). The vertical sampling rate is 4 ms, and the seismic cube contains 2225 samples vertically, i.e. 8896 ms of record. The dominant frequency of the full-stack signal is 37 Hz, yielding a 10-20 m vertical resolution for velocity considered in [1500 to 3000 m/s]. The cube is on the current shelf break with dip-oriented inlines, at the junction of three major sedimentary domains: shelf, basin and deep-sea fan in its south-eastern part and further South-East (Figure 1.12). It is also situated at the beginning of the North-West sub-basin of the Amazon basin (Cruz (2018)), called Cassiporé sub-basin.

Additional 2D data are provided by Rio de Janeiro State University (UERJ). In the 2D seismic profiles, the inter-trace distance varies between 12.5 m and 200 m, and the vertical sampling rate is 4 ms. These seismic profiles are spaced of about 5 to 20 km; they have 10 to 12 s recorded and 20 m vertical resolution. Only part of them were used (see Figure 1.12).

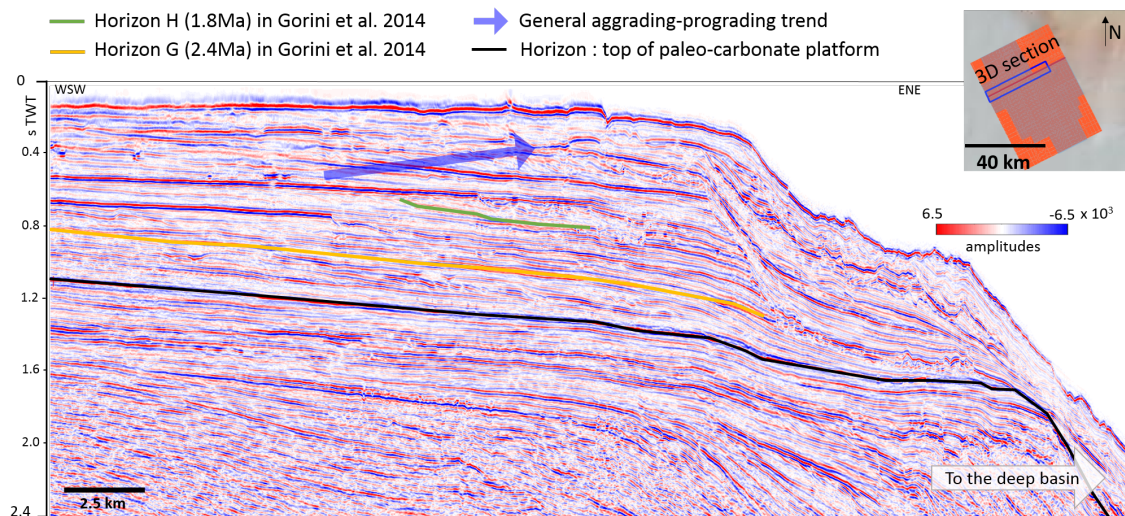


Figure 1.15: Seismic section extracted from the 3D cube. Most recent, upslope sedimentary series are shown, together with several horizons. Progradation is the deposition of sediments gradually further in the basinward direction; aggradation is the deposition of sediments that gradually builds upwards. No MTD is visible on this section.

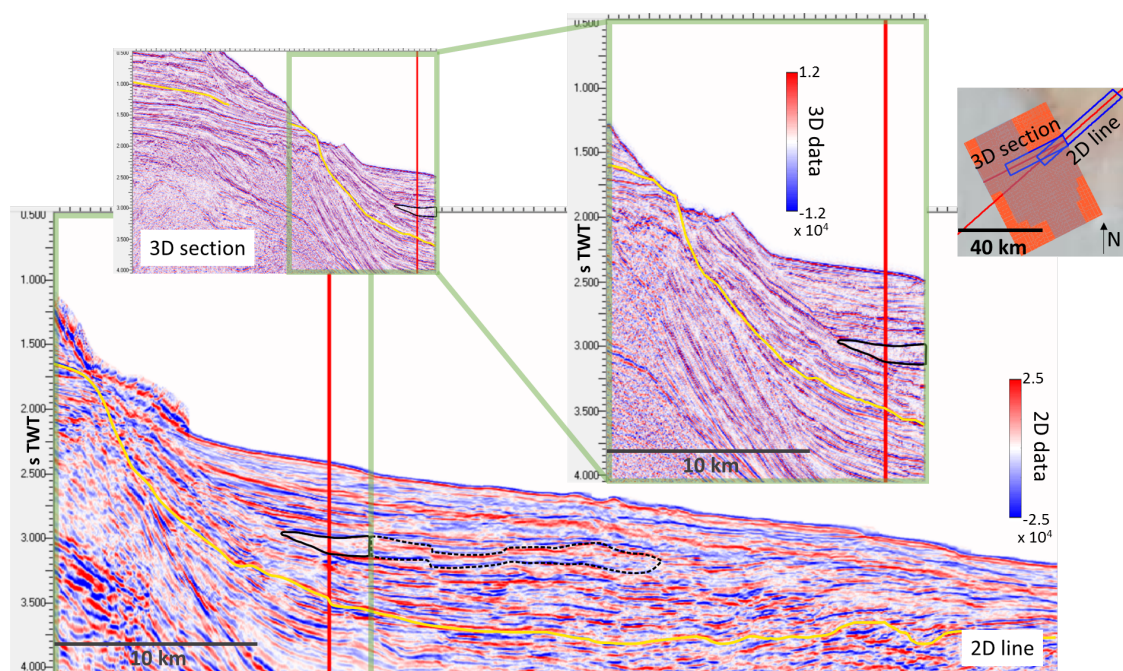


Figure 1.16: 2D seismic profile compared with a 3D section extracted from the 3D cube. Most recent, downslope sedimentary series are shown, together with horizon G (2.4 Ma) from Gorini *et al.* (2014) (yellow line). The top-left image displays the context of the 3D section extract shown on the right; this green-contoured extract corresponds spatially to the green-contoured region of the 2D section.

Figures 1.15 and 1.16 give examples of a section extracted from the 3D cube and a 2D profile, respectively. Some characteristic elements of the history of the Amazon basin are visible on the seismic data: the top of the carbonate platform, a few horizons and a prograding trend within the most-recent clastic units. Figure 1.16 shows how the two kinds of data are related; the 2D profile allows to hypothesize the continuation of the MTD part that is visible on the 3D-extracted section.

1.6 Challenges

Several challenges are addressed by the two objectives of this PhD. The diversity of mass transport processes and MTD characters, the nature of seismic data, and the nature of prior information, are discussed here.

1.6.1 Diversity of mass transport processes, diversity of MTD characters

In section 1.3, the three main stages of a mass transport event, as considered by a modeling approach, have been presented. Each of these stages may occur in various ways, so that the overall genesis of one MTD character (an observed feature on seismic data) depends on several different processes. Nevertheless, the diversity of these processes will have to be taken into account for our objectives.

Now, from a the point of view of data analysis, a variety of seismic visual characters are often used for MTD description. We here describe the most prominent of them.

Posamentier & Martinsen (2011) listed 6 seismic visual criteria for MTD characterization, illustrated on Figure 1.17. They include features that are seen from seismic vertical section views (internal chaotic to transparent facies, basal erosion, plowing of substrate, thrust faulting), another one from horizontal slices of a 3D seismic cube (irregularities), and another one from both (presence of 'clasts', i.e. blocks). Frey-Martínez (2010) gathered such features into 4 groups. Features of Figure 1.17 are included in the 3 first groups, related to the toe region, basal shear surface, and internal architecture; the last group is features related to the headscarp of the MTD, i.e. the place where the mass transport initiated. Bull *et al.* (2009) also proposed feature groups: one for the headscarp domain and one for the toe domain, and a larger one for the 'translational' domain, i.e. the main body of the MTD. This one contains sub-groups of features, concerning the MTD basal, upper and lateral surfaces, and its internal architecture.

Reis *et al.* (2016) noted such seismic characteristics of MTDs in the Amazon region, on 2D seismic profiles. Figure 1.18² shows examples of them on MTDs visible on the Amazon

²Figure with elements from the Virtual Seismic Atlas, VSA partnership (2018).

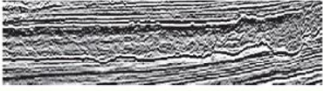




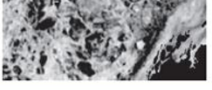
Internal chaotic to transparent seismic reflection character	
Basal grooving and/or deep erosional scour	
Plowing of sea-floor substrate and nearly vertical erosional lateral margins	
Presence of compressional thrust faulting (commonly ~ 15°) either near the flow terminus or lateral to the flow	
Irregular hummocks to featureless at upper boundary	
Presence of discrete 'clasts' within flow	

Figure 1.17: Seismic recognition criteria for MTDs; modified from [Posamentier & Martinsen \(2011\)](#).

seismic data, and MTDs from other places in the world as interpreted in the literature. Here we summarize their main features:

- **Chaotic facies** These are visible in almost every MTD, in the form of, either, middle to high frequency amplitude variations in all directions, or, in several directions but still containing one main direction (e.g. compressional patterns, Fig. 1.18h, similar to the thrust faulting in Figure 1.17) or a non-homogenous direction of pattern, as in Fig. 1.18c. On other images of the Figure, more contrast is necessary to visualize the chaotic facies of MTDs.
- **Transparent facies** These are very low amplitude regions (in absolute value), as in Fig. 1.18d.
- Internal preserved **slid blocks** (corresponding to 'clasts' mentioned by [Posamentier & Martinsen \(2011\)](#)), visible as preserved parallel reflectors locally; this element is only visible in the case of an MTD thick enough for the blocks to be distinct. An interpreted example of preserved block in a MTD is shown on Figure 1.4b.
- Close to the upslope limit of the MTD, signs of **previous stratification**; this is not seen on any of the examples here. [Reis et al. \(2016\)](#) suggest that these signs evidence a soft-deformation or slide-style of the mass transport at its beginning (see Figure 1.6).
- **Staircase-like geometries** on its basal surface, as it locally ramps up and down the stratigraphy. On Figure 1.18d, it is interpreted as an erosional feature. On Fig.

1.18d, the ramps are rather due to posterior extension processes and shifting of the sedimentary sequence.

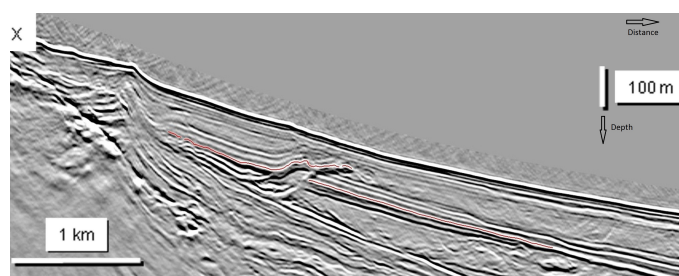
- **Strong amplitude reflector** at the base of the MTD. This might have different interpretations: in Fig. 1.18f and 1.18h, the strong reflector is warped and suggests that the mass transport followed an eroded surface, or eroded the basement itself (this is also mentioned in Figure 1.17); a flat base reflector might lead to other hypotheses, e.g. a condensed section deposited during a flooding event, or an overpressured surface. Note that the directions of the viewing section and of the transport are crucial to any interpretation of that kind.
- **Head scarp** at the upslope limit of the MTD. This element is not often visible. First, because only mass transports triggered in a fragile way can leave such an evidence; second, because it is often hidden by, and/or mixed with, posterior sedimentary deposits.

Note that, although not in line with the assumption of sequence stratigraphy (one reflector corresponding to sediment deposited during a same period of time), the facies and features presented here have been subject to a first analysis, which associated them to a geological label. Their definition has involved an initial interpretation. This interpretation is more local than the ones found by seismic stratigraphy. Among these elements, the chaotic facies is used by most interpreters as an MTD marker. Yet it is not the only one; all elements of the list are important to keep track of. MTDs also vary in size and shape.

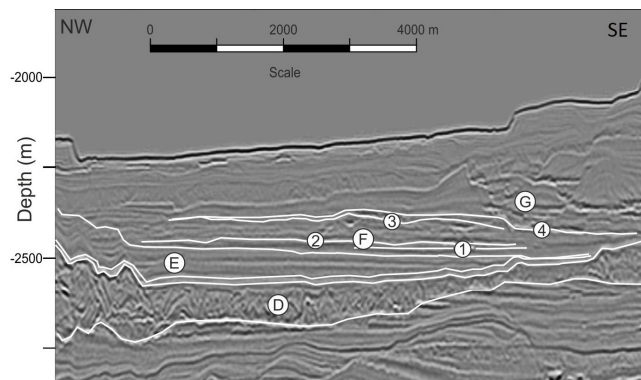
The variety of natural processes originating in MTD formation is such that MTDs are defined not by any common lithological content, nor by any regular seismic aspect, but by both stratigraphic and internal descriptions which may vary from one dataset to another (considering different data acquisition/processing schemes), or from one MTD to another. In this PhD, we have to cope with this variability of characters, both for identifying MTDs numerically in the seismic data and for interpreting their formation. How to use the information contained in seismic data to highlight this variability is also one of the underlying goals of the PhD.

1.6.2 Making the most of seismic data

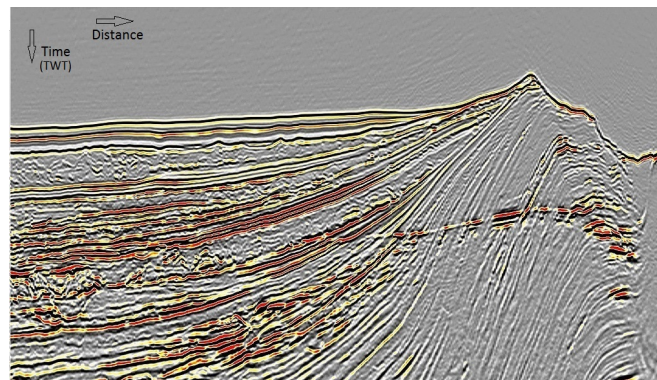
The process of interpreting seismic images relies on several standardized methods that link some seismic-extracted information to characteristics of the studied area. These include seismic stratigraphy and seismic facies interpretation, as presented previously in this chapter. Some processings may be run on the seismic data, manually or manually-driven within a seismic interpretation software. These include fault and horizon picking and 'attribute' computations to help facies definition (seismic attributes will be introduced



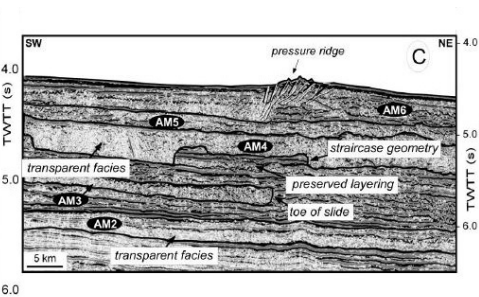
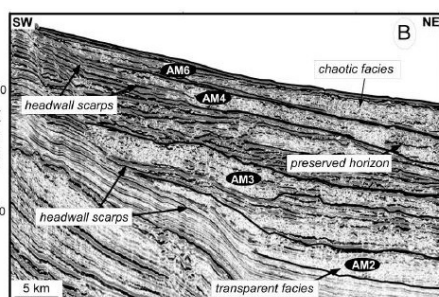
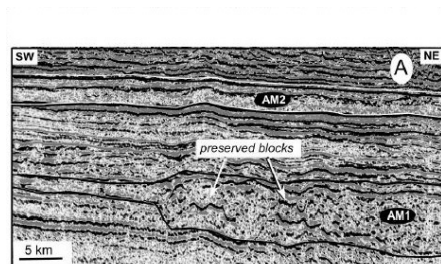
(a) A slide deposit on the flank of a salt diapir, Gulf of Mexico. Image by Henry Posamentier (2010).



(b) Post-avulsion evolution of a channel complex (in unit E). Image by Andrea Ortiz Karpf (2015).



(c) Mud volcano seismic section (part), lower Niger fan. Several MTDs on its flanks. Image by CGG Veritas (2010).

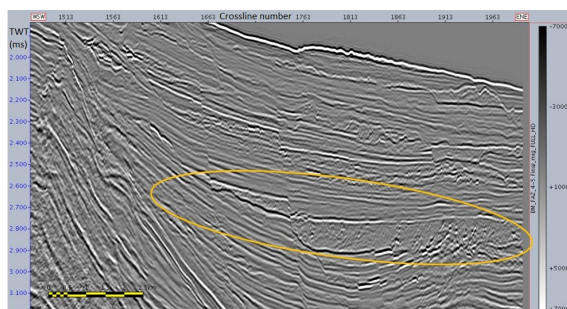


(d) Zoom-outs from 2D seismic lines illustrating internal facies of AMC megaslides. From Reis *et al.* (2016).

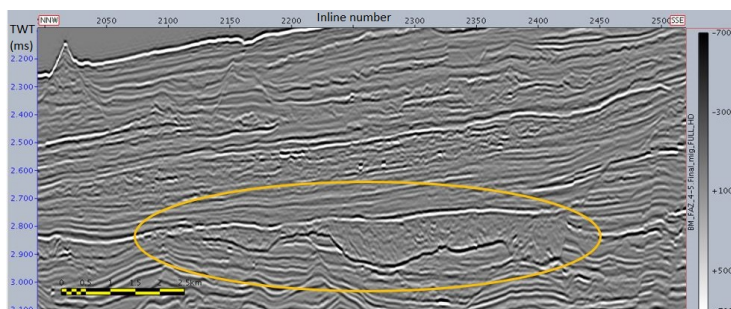
Figure 1.18: MTD seismic expression diversity in the literature: (a), (b), (c) (from the [VSA \(Virtual Seismic Atlas\) website](#)). MTD and extension processes diversity in the Amazon region: (d), (e), (f), (g), (h), (i), (j). Figure continued below.

further in the next chapter). Most of seismic interpretation is therefore rather model-driven, i.e. depending on several assumptions: available knowledge on the studied region, known correspondence with similar environments, chosen parameters, importance given to one part of the dataset, etc. This is what makes seismic interpretation results strong and reliable.

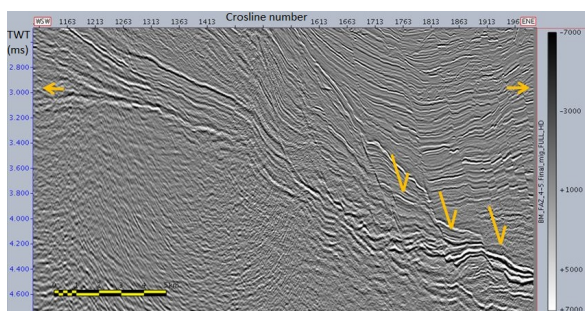
On the other hand, some limitations remain to the model-driven paradigm, particularly the time needed for repetitive tasks that may be quickly achieved through automation; this is particularly noticeable when it comes to using 3D seismic data. Another limit that arises is the need for high expertise and experience, which justifies the assumptions taken



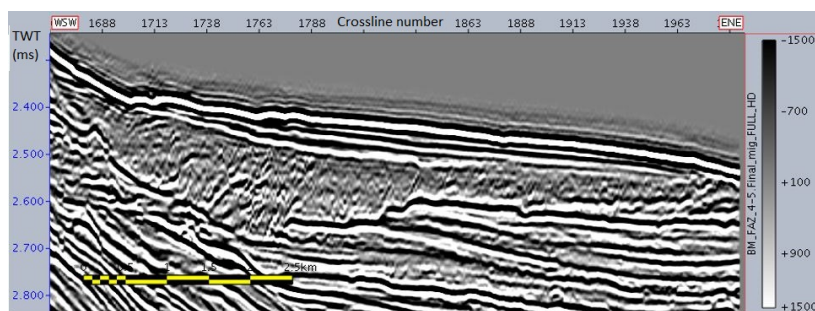
(e) (cont.) One MTD on inline IL2300 in the Amazon seismic cube.



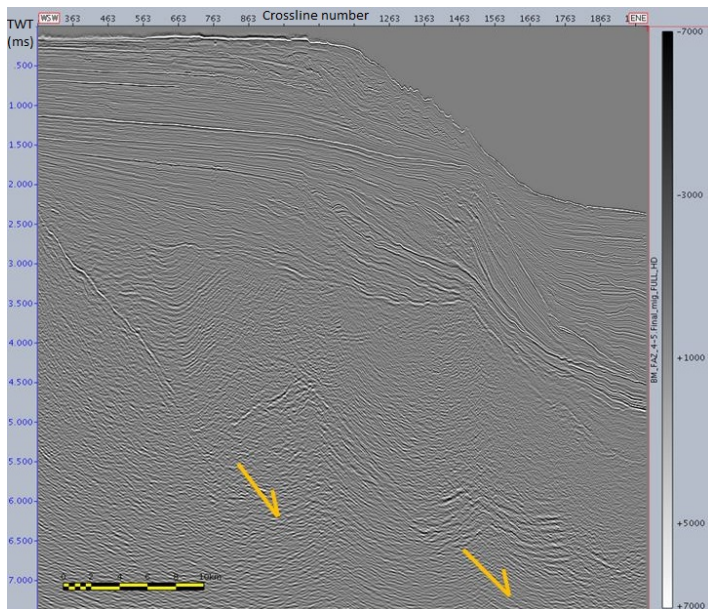
(f) (cont.) Same MTD as in (e), on crossline XL1800 in the seismic cube.



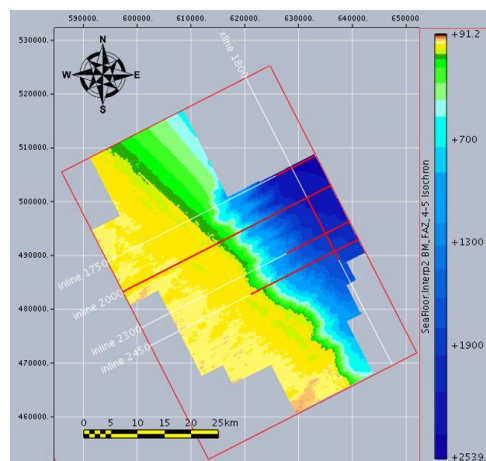
(g) (cont.) Extensional patterns, inline IL2450 in the seismic cube (top of carbonates, also affecting clastic units).



(h) (cont.) Compressional patterns in a MTD (inline IL1750) in the seismic cube (contrast exaggerated).



(i) (cont.) Extensional patterns visible deep in the seismic cube (inline IL2000).



(j) (cont.) Position of sections in the seismic cube. Map colored according to bathymetry.

Figure 1.19 (cont.): MTDs and extensional diverse seismic signatures.

in a model but may also jeopardize the objectivity of one interpretation. Therefore, new ways have to be explored to extract information from a seismic dataset.

From a seismic dataset, we need to extract semantic interpretations on geological objects, their shapes and sizes, their internal organization. These elements all relate to a certain geological 'structure'. Now how is such structure defined? Is there in seismic images a structure that naturally relates to the geological structure?

A simple analogy with natural images (e.g. photographs) could suggest to define 'structure' in an image as the set of objects separated by the most obvious borders (or most salient gradients) between them; objects are then represented as smooth regions between these borders. This corresponds to the piecewise-smooth component of the image. It is called the 'cartoon' or 'geometry' component, as opposed to the 'texture' component, which typically contains the detailed patterns of the image (e.g. [Le Guen \(2014\)](#)). In this framework, the image f is decomposed into its geometry component u and its texture component v such that $f = u + v$. As an example, a texture-geometry decomposition algorithm by [Le Guen \(2014\)](#) is here applied to two images: a reference, natural image, and a seismic image (Figure 1.19). The natural image application gives significant results. The geometry component shows the largest regions: the floor, the tablecloth, the clothes; the texture component enhances the details in each region (patterns on clothes, carpet). In the seismic image, however, such regions are not clearly defined by the algorithm. The geometry component highlights dark elongated regions which are actually the horizons, i.e. the borders of the geologically-meaningful regions; horizons of interest are not retrieved (Figure 1.19).

This illustrates the puzzle of defining numerically the 'structure' of a seismic image. Geological structures such as those defined in seismic stratigraphy (e.g. horizons on Figure 1.11) do not always correspond to the existing borders of regions visible in the seismic image. Indeed, while a geological structure can be the spatial arrangement of the lithology at the scale of a few meters, it can also mean the spatial arrangement of sedimentary layers that are several kilometer long or wide, and all other scales in between. The meaning behind the word 'structure' actually results from a choice of scale which is sometimes implicit. The seismic signal, on the other hand, is sensitive to acoustic impedance variations whatever the spatial scale (within the seismic resolution). A seismic image therefore reflects all of them, not necessarily following any model-defined geological structure.

Depending on the scale chosen, some will then call 'structure' of a seismic image the surfaces of interest for a certain geological duration and kind of processes, while denoting the remaining patterns 'textures'. But texture and structure are intrinsically mixed in a seismic image. In this project, we will choose to consider only a local definition of seismic 'texture', i.e. referring to the spatial arrangement of pixel intensities within a local area.

This inter-connection between spatial scales makes seismic images very different from natural images. Because of this, (i) the numerical definition of a structural model within a seismic dataset requires a lot of manual input, to pick most-important horizon and fault surfaces properly; (ii) the numerical definition of an object within a seismic image depends on the scale of study; and (iii) the numerical definition of seismic facies also depends on

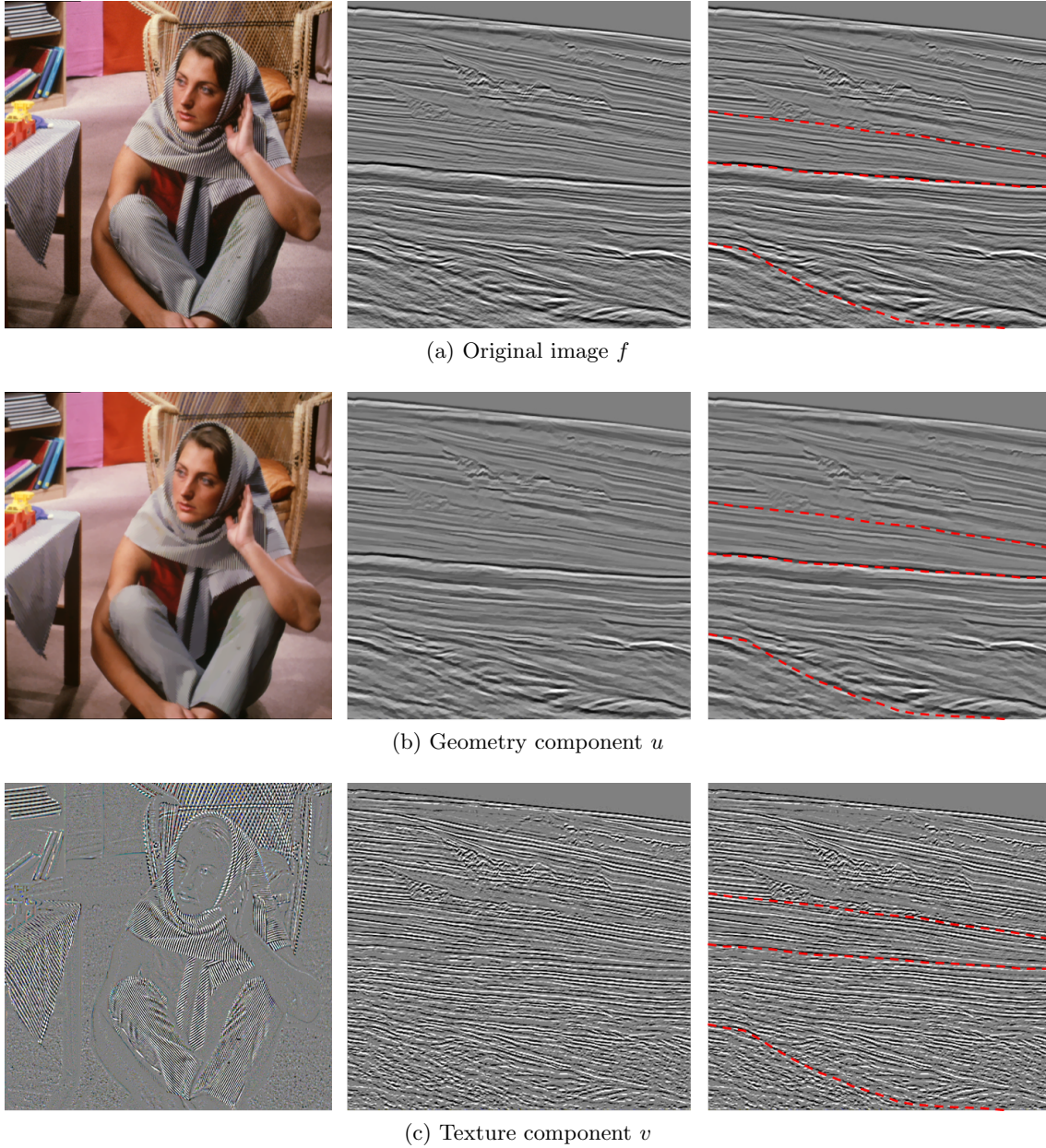


Figure 1.19: Texture - geometry decomposition ($f = u + v$) applied to a natural image (left) and to a seismic image (middle), with expected main geological region borders (right). The algorithm clearly yields a distinction between the geometry and texture parts of both natural and seismic images. However, the geometry component of the seismic image does not reveal the expected geological structure. Images obtained by applying algorithm and code from [Le Guen \(2014\)](#).

that scale. In particular, the size of the region/patch used to define a facies impacts this facies definition. For example, [Berton & Vesely \(2016\)](#) illustrate facies (E) on Figure 1.11 with a seismic patch of 350ms x 6.5km; zooming in this patch, however, one could get access to detailed variations of patterns, which could lead to define more precise facies based on smaller image patches.

The scale issue is also related to the seismic data quality. A poorly-resolved seismic dataset may not allow to spot small-scale or medium-scale surfaces of interest, for example. As 2D seismic profiles are often less well resolved than 3D data, they may not be used in the same way for studying MTDs as objects.

Finally, 3D seismic data contain invaluable information on the lateral variations of a surveyed area. How to use this information efficiently remains a challenge, as 3D data processing is computationally intensive.

Quantitative seismic interpretation, which relies on numerical results and quantified data-extracted elements, is therefore a time-consuming and complex task. Despite existing numerical helps for interpreters, the interpretation process could be further improved by developing numerical interactions between existing geological knowledge and the data itself. Bridging this gap requires a special care; it should allow to use data-driven information and geological knowledge more efficiently for interpretation.

1.6.3 Making the most of prior information

From seismic data acquisition to interpretation of mass transport processes, various steps of processing or modeling are involved. Each of them introduces uncertainty in the results. Apart from the inevitable uncertainties related to data quality and processing steps, we here emphasize that models, and projections of concepts on specific data, are always biased themselves. In this respect, we should remain conscious of the following major sources of uncertainty:

- **Intra-class object variability.** Among other geobodies, mass transport deposits can be considered as one class of objects. However, as mentioned in section 1.6.1, there is a huge variability inside this class. As a result, different kinds of MTDs may yield varied seismic signatures. The object itself may have different shapes and sizes, which prevents identification from relying on morphology alone for example. It may also be internally organized in a specific way that is more characteristic, e.g., of soft deformation than of fluidized flow. As a result, one often needs to spot several different parts of an MTD before clearly identifying it within a seismic volume.
- **Seismic facies representativity.** Although admittedly useful for geological facies estimation, seismic facies are not a perfect proxy either. As two very different

rocks (or rock geometries, or rock pore saturations...) may have equivalent acoustic impedances, their corresponding seismic facies can match. This has to be kept in mind: data representation is never uniquely representative.

- **Intra-interpreter group variability.** A manual delineation of e.g. fault surfaces or geobody delineation on a same geological data, done by different people, can yield different results. If these results are to be used as a reference prior information for a model, then how to select the best interpretation? Especially for underground studies where no outcrop and no well is used, the 'ground truth' is never known.

Considering these points, the prior input added to seismic information has to be used with care, in order to decrease its impact when too uncertain.

1.7 Organization of the next chapters

In this chapter, we have defined the main research questions driving this PhD. Our objects of study, mass transport and mass transport deposits, have been defined. We have described seismic data acquisition and primary interpretation methods. The data used for our case studies have been introduced. Finally, the most critical challenges associated to our objectives have been explained.

The next chapters of this report are organized as follows. Chapter 2 addresses the first objective of the PhD: to locate MTDs in seismic data, in position and extension, while preserving the variety of their characters (Identification). Chapter 3 is devoted to the second objective: to characterize physical processes acting over geological times, responsible for location, geometry and internal heterogeneities of these MTDs (Interpretation). In both chapters 2 and 3, some introductory elements are given with literature review and/or details on the material needed for the methods developed afterwards. The main contributions are given in an article, included in this document, followed by discussions and conclusions. Chapter 4 provides a synthesis on the developments of chapters 2 and 3 and on the contributions of this PhD; it assesses their limits and their advantages and suggests ways forward.

Chapter 2

Retrieving MTDs in seismic data: a specific setting with varied object expressions

2.1 Introduction

The first purpose of this PhD project is to identify MTDs in a seismic dataset. These sedimentary geobodies should then be considered as targets to retrieve, in any numerical or manual framework. We aim at identifying the position and 3D extension of MTDs, quickly but exhaustively, and in a way that the recovered geobodies may help for further geological interpretation of the region. We rely on numerical methods considering seismic data as 2D or 3D images to be interpreted.

In this chapter, section 2.2 first presents existing methods for object recognition in seismic images. Considering our objective, this consists in three parts: (i) how to represent the information of a seismic dataset (2.2.1), (ii) how to quantify the similarity of two seismic images (2.2.2), and (iii) based on the two previous points, how to extract new semantically-informative representations (2.2.3). A brief synthesis of the review is given in 2.2.4. After this review, the approach proposed to meet our objective is detailed in section 2.3, in the form of an article. A discussion is led in section 2.4, and section 2.5 concludes this chapter with opening remarks.

2.2 Object recognition in a seismic image: related work

What defines an 'object' in an image is what we perceive and interpret as being an object. This understanding implies going from the primary perception of the image to the final interpretation of the object. This global workflow is applied in numerical image analysis. A 'low-level' representation of the image data corresponds to primary perception, and

higher- and higher-level representations get closer and closer to a semantic interpretation. For instance in a picture, low-level features such as intensity, color, shape, texture, can highlight several zones: blue with plain texture / green with rough texture / dark with fluffy texture and straight shapes. These groups give no understanding of the image unless labels are attached to them (e.g. sky, grass, trees). Such labels are higher-level information; they are used for object recognition applications, such as content-based image retrieval, answering a request like 'image with landscape' in a search engine.

For object retrieval in seismic images, some strategy has to be created to bridge the gap between low-level representation (features extracted from the data) and high-level representation (i.e. our interpretation of the image).

This section gives an overview of existing methods for data representation, similarity quantification and image segmentation, leading to the choices we made for our developments.

2.2.1 Seismic data representation

Formally, data representation is a transformation from the data space to a feature space, i.e. where an image is replaced by a set of data features. This process is often based on the computation of descriptors of the image. Such representation is typically useful for further applications such as a segmentation procedure.

2.2.1.1 Seismic attributes and seismic facies numerical representation

In section 1.4, we have introduced seismic facies. Two approaches to define them have been presented: the first one is model-driven. It is guided by a guess on the visual aspect of a seismic patch given certain sediment depositional conditions (see Figures 1.10 and 1.11 on seismic stratigraphy). This facies representation is high-level, i.e. close to our interpretation. It is made possible thanks to the expertise of experimented interpreters (e.g. Mitchum Jr *et al.* (1977)). The drawback is the underlying assumption on the reflectors being representative of a unique time interval with similar depositional conditions, which is not always met. The second approach is only data-driven: facies are only defined through descriptions of the seismic patterns. This one is a low-level representation.

In any of the model-driven or data-driven approaches, translating these facies definitions to numerical ones starts from a low-level representation (corresponding to the data-driven case). It relies on combinations of local quantitative descriptors of the seismic image. Such a descriptor is called 'seismic attribute'; it is defined by Chopra & Marfurt (2007) as 'any measure of seismic data that helps us visually enhance or quantify features of interpretation interest'. Analyzing the values of seismic attributes in different regions of the seismic image then allows to define seismic facies as regions with specified values of attributes. For

instance, [Alves *et al.* \(2014\)](#) define facies based on three attributes: Contrast (C, related to the amplitude heterogeneity), Directionality (D, related to amplitude anisotropy) and Energy (E, related to the average signal power). They distinguish either 'low' or 'mid' or 'high' value for each attribute. Facies are defined as e.g. 'high C - high D - low E' or 'mid C - low D - high E' etc.

Seismic attributes are computed either on the 1D trace around a sample (or pixel of the seismic image), involving 1D signal features, or on the 2D/3D environment of the sample (vertically and laterally defining a window, or patch, around the pixel/voxel). They can be computed for every sample of the image (with overlap between the neighboring windows), or only some of them (e.g. with no overlap). Defining and computing seismic attributes corresponds to representing the seismic data in another domain: the attributes space.

Since the 70s (e.g., [Taner *et al.* \(1979\)](#)), an outstanding amount of seismic attributes have been designed so as to enhance specific geological features: they result from a 'feature engineering' process. [Pigott *et al.* \(2013\)](#) for instance highlight the advantages of Amplitude envelope, Chaos, Cosine of phase, Dip deviation, Instantaneous frequency, Instantaneous quality, Relative acoustic impedance, and Variance attributes for interpreting such geological features as concave and convex channels and clinoforms, bed continuity, gas presence, faults and fractures, lithologic change, porosity, sequence boundaries and unconformities, and terminations. The book by [Chopra & Marfurt \(2007\)](#) and the '[Attributes Revisited](#)' report ([RSI \(2003\)](#)) provide quite exhaustive reviews of such attributes. Choosing among them is thus governed by specific applications - among which, for example, defining stratigraphic facies; this choice can be challenging, as selecting part of the information introduces subjectivity in the interpretation. In any case, the authors, similarly to [Barnes \(2006\)](#), emphasize the need to limit the number of attributes used.

On the other hand, textural attribute sets, which were defined as a decomposition of the seismic image, yield a relatively exhaustive, thus non-biased, data representation. The following section summarizes the coupled evolution of textural analysis in image processing and in seismic facies analysis.

2.2.1.2 Texture analysis and seismic textural attributes

Texture analysis developed together with image analysis/processing and computer vision. It has been much used in other imaging fields such as medical imaging, textile or material defect detection, or fingerprint recognition (e.g., [Nailon \(2010\)](#), [Liu *et al.* \(2015\)](#), [Yazdi & Gheysari \(2008\)](#)). Initially, the statistical characterization of textures was intuited by the neuroscientist and psychologist Béla Julesz, who suggested that two images (or patches) having the same textural aspect for a human eye must have some N-th order statistic in

common. First-order statistics are statistics of the pixels distribution; 2nd-order statistics are statistics of pairs of pixels. Julesz’s first hypothesis was that 2nd-order statistics were sufficient to entirely describe distinguishable / undistinguishable textures (Julesz *et al.* (1973)); he then showed that higher orders were actually necessary (Julesz *et al.* (1978) – see also Portilla (2000)).

At the same time, for applied image analysis, Haralick *et al.* (1973) developed the ancestor of the Gray-Level Co-occurrence Matrices (GLCM), called Gray-Tone Spatial-Dependence Matrices. One GLCM describes joint statistics of gray levels (i.e. discretized intensity values) in an image, according to a spatial relationship between two pixels, defined by a specific vector:

$$GLCM_{\vec{v}}(i, j) = \text{card} \left\{ \begin{array}{l} (A, B) \text{ such that:} \\ GL(A) = i \\ GL(B) = j \\ \overrightarrow{AB} = \vec{v} \end{array} \right\}$$

where A, B are two pixels on the image, GL denotes their gray level, and \vec{v} is the vector defining the spatial relationship between two pixels.

Quantities extracted from this matrix thus provide 2nd-order attributes related to a specific scale and orientation, given by the norm and direction of the chosen vector (see e.g. Figure 2.1).

Seismic attributes were first based on 1D signal processing techniques, namely the analytic signal of each seismic trace: ‘instantaneous’ attributes (Taner *et al.* (1979), Bodine (1984)), ‘response’ attributes (Bodine (1984), Bodine (1986)).

In the 1980s, techniques coming from machine learning were introduced in seismic facies analysis: pattern recognition (Justice *et al.* (1985), Kubichek & Quincy (1985), Pitas & Kotropoulos (1992)), classification, clustering and segmentation (Love & Simaan (1985), Roberto *et al.* (1989)); some of these authors describe ‘texture attributes’, however not using the statistical definition from image analysis. Attributes were rather related to the analytic signal of a trace or the sub-horizontal length of a reflector, which were probably the most-relevant attributes for the data quality of that time.

A bit later on, spectral decomposition of the seismic signal enjoyed success (Peyton *et al.* (1998), Partyka *et al.* (1999)), as it allowed an interpreter to visualize different scales contained in seismic traces. Attributes *visualization* through appropriate color scales then gained significance, as also discussed in Marfurt *et al.* (1998). Seismic spectral decomposition is still much used; an RGB color blend can give an insightful visualization of the low-, mid- and high-frequency bands (see e.g. GeoTeric (2018)). Seismic ‘geometrical’ attributes were also introduced; they involve the neighborhood of a seismic trace. The dip and azimuth attributes are classified among them, as well as coherence and similarity-based attributes (Bahorich & Farmer (1995), Peyton *et al.* (1998)).

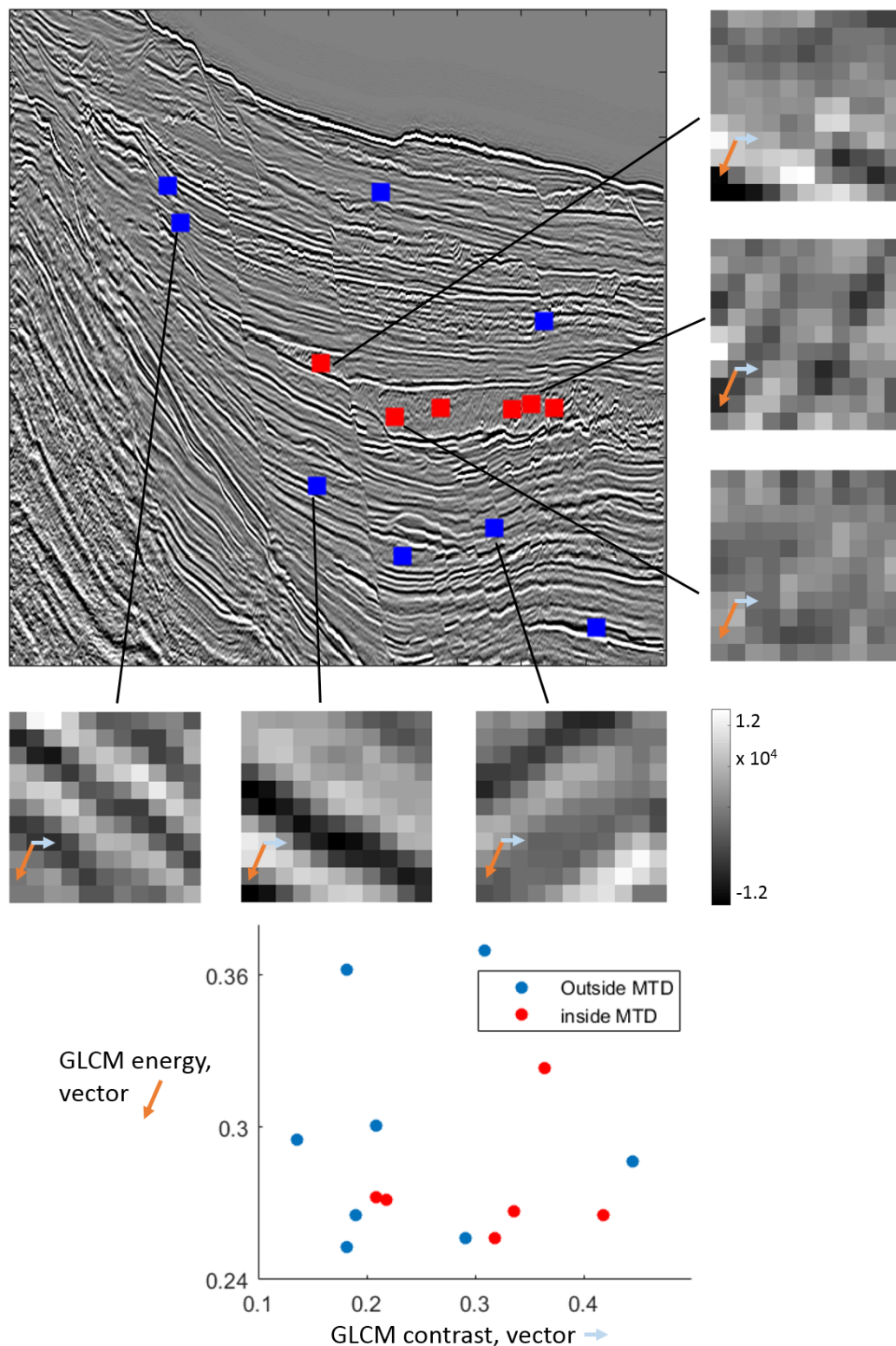


Figure 2.1: Example of GLCM attributes computed on several patches of a seismic image. Axes of the scatter plot correspond to GLCM contrast (abscissa) for a reference vector drawn in light blue, and GLCM energy (ordinate) for a reference vector drawn in orange.

In image processing, [Portilla \(2000\)](#) proposed to define a texture model based on statistics of paired coefficients of a steerable pyramid ([Simoncelli & Freeman \(23-26 Oct. 1995\)](#)), a specific transform of the image. Other approaches using 2D signal decomposition were already used, or appeared from that time (e.g. Gabor filters for texture segmentation in [Jain & Farrokhnia \(1990\)](#), wavelet transform for texture classification in [Unser \(1995\)](#), curvelet transform appearing in [Candès *et al.* \(2006\)](#)). On the other hand, new local texture descriptors were created: the Local Binary Pattern (LBP, [Ojala *et al.* \(2002\)](#)), the Local Radius Index (LRI, [Zhai *et al.* \(2013\)](#)), and are still improved with time (e.g., [Liu *et al.* \(2014\)](#)). Current texture analysis / synthesis methods involve either statistics of several scales of the image (e.g., [Galerie *et al.* \(2018\)](#), or [Sifre & Mallat \(2013\)](#) using the scattering transform representation), or patch re-arrangement (e.g., convolutional neural-net approaches for synthesis: [Gatys *et al.* \(2015\)](#), [Jetchev *et al.* \(2016\)](#)), or both (see a review by [Raad *et al.* \(2017\)](#)).

Textural analysis was finally applied to seismic data in 2D and 3D with a focus on local statistical attributes ([West *et al.* \(2002\)](#), [Gao \(2003\)](#), [Gao \(2008\)](#), [Eichkitz *et al.* \(2015\)](#)), GLCM attributes enjoying large popularity. [Berthelot *et al.* \(2013\)](#) showed how textural attributes of different kinds (GLCM, frequency-based, and geometrical attributes) are valuable for salt detection in seismic data. [Long *et al.* \(2015a\)](#) showed that texture attributes, either based on scale decomposition (steerable pyramid, curvelet transform), or not (LBP, LRI), are able to characterize a migrated seismic volume with great accuracy. Sizes of local seismic patches used to compute textural attributes depend on the quality of the data and the aim of the study. For studies on reservoirs, [West *et al.* \(2002\)](#) propose a size of about 50m vertically and 325m laterally (i.e. 13 samples for 25m inter-trace distance). For the textural characterization of seismic data in time in general, [Gao \(2008\)](#) recommends that the vertical size of the patch contain at least one wavelength of the dominant frequency of the signal, with lateral sizes of 5 to 9 samples.

In his review of state-of-the-art seismic attributes, [Marfurt \(2015\)](#) expects statistical textural attributes to be developed more and more, together with other improvements in geomorphology thanks to geometrical segmentation methods.

We have seen that seismic data representation is achieved by seismic attributes. Some attributes are close to the trace waveform, and may be used by an interpreter for enhancing specific geological features. Others rely on textural characteristics of the image; they are rather designed to be a decomposition of the signal, thus conveying more information than the former.

Now, to be able to use a seismic attribute representation, we need to know how to estimate the difference between two seismic facies. This question is tackled in the next section.

2.2.2 Comparing seismic patches: similarity quantification

Representing a seismic image via attributes yields a vector of attributes, or 'attribute vector', for every considered patch in the image, close values of attributes representing similar facies. Such similarity has to be quantified by a metric, chosen together with the attributes. For instance, according to the two GLCM attributes of Figure 2.1, the dissimilarity of the seismic patches can be quantified by the Euclidean distance between points in the graph.

The choice of attributes and metric should ensure discriminative power, low computational requirements, and robustness (Liu *et al.* (2014)). In this respect, the attributes set should be as uncorrelated as possible (e.g., Barnes (2006)) to avoid any bias in the metric. The attributes set should also be small, to limit computation time and to avoid the so-called 'curse of dimensionality' causing unreliable distance assessment in too high-dimensional spaces (e.g. Mougeot (2015)).

To satisfy these needs, a dimension-reduction method can be used. It keeps the highest amount of non-correlated information, which may be done by finding the rank of the matrix of attributes. A feature extraction method (e.g., Principal Component Analysis) or feature selection method (e.g., Lu *et al.* (2007)) can be applied for this purpose. The resulting set of attributes is a new, lower-dimensional data representation.

In the context of textured images, Zhao *et al.* (2008) introduced the Structural Texture Similarity Metrics (STSIM), inspired from the Structural Similarity Metrics (SSIM), which were originally designed for image quality assessment (Wang *et al.* (2004)). An STSIM is defined by the association of 4 elements:

1. A subband decomposition / multiscale frequency decomposition, i.e. a decomposition of an image into several components of different scales and orientations. 'Scale' and 'orientation' are, respectively, the typical size and direction of heterogeneity in the image component;
2. A set of statistics that describe one image component at the scale and orientation studied (e.g. statistical moments, horizontal or vertical autocorrelation, or other);
3. Formulas for comparing statistics of 2 image components;
4. A pooling strategy to combine all the results from the formulas and finally compare the 2 images.

STSIMs have the advantage of using statistical attributes of an image instead of pixel-based attributes (Pappas *et al.* (2013), Zujovic *et al.* (2013)), which is relevant for texture comparison. In this framework, seismic textural attributes correspond to the statistics computed in step 2.

Long *et al.* (2015b) introduced SeiSIM, an STSIM specifically designed for seismic images. In SeiSIM, the subband decomposition is a steerable pyramid decomposition (Simoncelli & Freeman (23-26 Oct. 1995)). Statistical attributes are computed on the subbands of the image X , comprising horizontal and vertical correlations ρ_X^h and ρ_X^v :

$$\rho_X^h = \frac{E[[X(i, j) - \mu_x][X(i, j + 1) - \mu_x]^*]}{\sigma_x^2}$$

$$\rho_X^v = \frac{E[[X(i, j) - \mu_x][X(i + 1, j) - \mu_x]^*]}{\sigma_x^2}$$

where i and j are the indexes of a subband of X and (μ_x, σ_x^2) are the empirical mean and variance of X .

They additionally use a global attribute (computed on X rather than its subbands); it is computed from autocorrelations on the discontinuity map DM_X ¹ of the image X :

$$\rho_{DM_X}^h = \frac{E[[DM_X(a, b) - \mu_{DM_X}][DM_X(a, b + 1) - \mu_{DM_X}]^*]}{\sigma_{DM_X}^2}$$

$$\rho_{DM_X}^v = \frac{E[[DM_X(a, b) - \mu_{DM_X}][DM_X(a + 1, b) - \mu_{DM_X}]^*]}{\sigma_{DM_X}^2}$$

where a and b are the indexes of position in DM_X and $(\mu_{DM_X}, \sigma_{DM_X}^2)$ are the empirical mean and variance of DM_X .

The comparison of attributes from two images is done with a power-like distance, for instance to compare ρ_X^h and ρ_Y^h :

$$a_h(X, Y) = 1 - 0.5|\rho_X^h - \rho_Y^h|^q$$

with q equaling 1 in the article of Long *et al.* (2015b). $a_v(X, Y)$, $a_{DM}^h(X, Y)$ and $a_{DM}^v(X, Y)$ are similarly defined. Long *et al.* (2015b) also use luminance and contrast comparing terms $l(X, Y)$ and $c(X, Y)$ originating from the SSIM framework.

The pooling step is performed by multiplying all distance values, weighting them with appropriate powers:

$$Q_1(X, Y) = [l(X, Y)]^{\frac{1}{4}}[c(X, Y)]^{\frac{1}{4}}[a_h(X, Y)]^{\frac{1}{4}}[a_v(X, Y)]^{\frac{1}{4}}$$

$$Q_2(X, Y) = [a_{DM}^h(DM_X, DM_Y)]^{\frac{1}{2}}[a_{DM}^v(DM_X, DM_Y)]^{\frac{1}{2}}$$

$$SeiSIM(X, Y) = [Q_1(X, Y)]^{\frac{1}{2}}[Q_2(X, Y)]^{\frac{1}{2}}$$

¹The discontinuity map DM is derived from a semblance attribute map. High values of DM tend to relate to the occurrence of a fault. We refer to Long *et al.* (2015b) for the equation defining DM .

The framework of STSIMs (Zhao *et al.* (2008)), as applied above, is advantageously flexible, for instance to add or remove as many statistical descriptors as wanted, and to put different weights on them within the metric according to a certain objective (e.g. the powers q , $\frac{1}{4}$, $\frac{1}{2}$ in SeiSIM description).

The main contribution in SeiSIM is the discontinuity map, added to the textural correlation-based attributes. It could be replaced by any kind of seismic dissimilarity or inversed semblance attribute in general. SeiSIM has shown good results for seismic image retrieval with four difference textural facies in Long *et al.* (2015b), however it has not been tested on large datasets and for very diverse textures.

When a proper set of attributes and metric is chosen, object retrieval can be performed. It is tackled in the next section.

2.2.3 Highlighting regions of interest in a seismic image: segmentation

'Segmenting' an image means creating a partition of this image according to some defined rule. The output of a segmentation is a categorization of pixels into groups.

When one kind of object, or region of interest, is searched for in an image, two groups of pixels only are generally expected: 'object' pixels and 'background' pixels. For such a binary partition, segmentation algorithms often focus on geometrical properties of the image. They can also rely on more local, pixel-based approaches. In the following, both kinds of methods as applied for seismic images will be explained.

2.2.3.1 Segmenting an object with geometrical methods

Several families are found among geometrical segmentation tools (Bernard (2013), Kervrann (2010)): Deformable models, Graph-based methods, Region-growing methods, Mathematical morphology and Probabilistic methods.

Deformable models assume the contour of the targeted object is a flexible 2D line or 3D surface that deforms until reaching the optimal shape and position. Parametric models, where the curve/surface is explicitly parameterized, and non-parametric (or geometric) models, where the curve is implicitly defined, have been proposed. The former allow fast real-time implementations, the latter allow topological changes (the contour may split or merge (Xu *et al.* (2000))).

Active contours, or 'Snakes' (Kass *et al.* (1988)) are part of deformable models. They rely on the optimization of an energy comprising two main terms: an external energy constraining the contour to fit the data, and an internal energy which puts some prior constraint (regularization) on the contour (Rousselle (2003), Kervrann (2010)).

Also part of deformable models, level-set methods, introduced by Caselles *et al.* (1997),

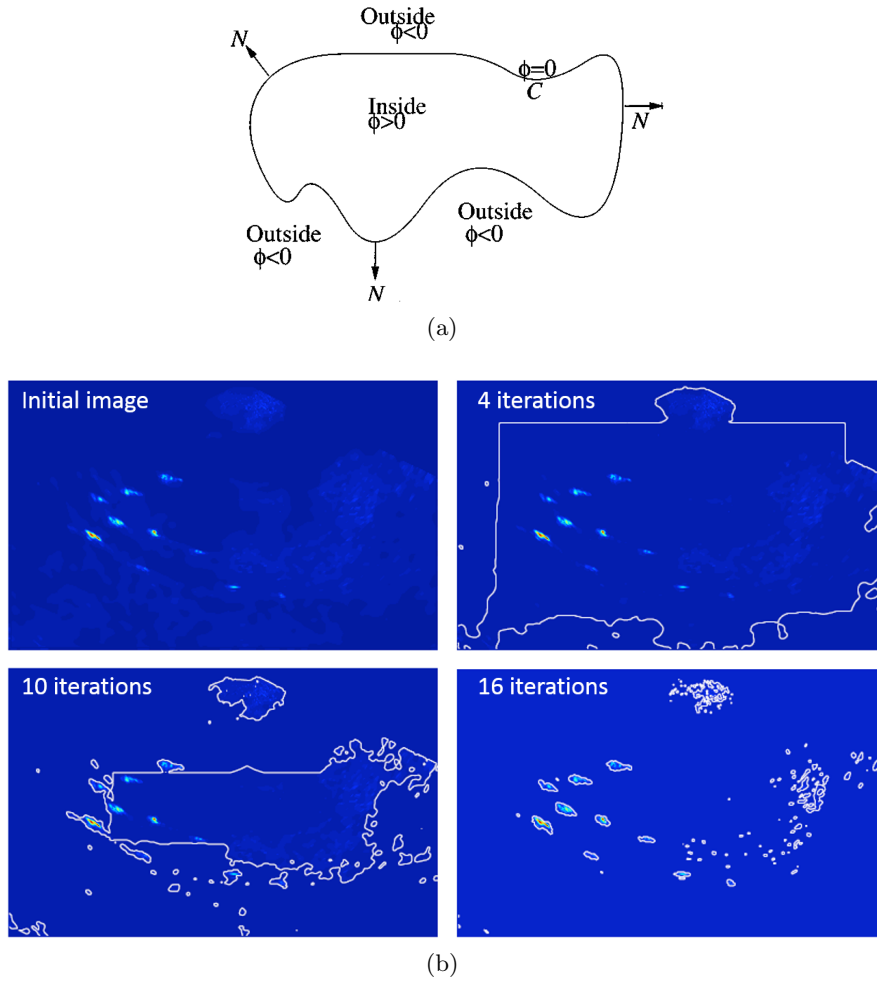


Figure 2.2: The Chan-Vese deformable model (Chan & Vese (2001)). (a) The level-set formulation of the delineation problem states that the contour line is the zero-level set of a function Φ . Φ is modified iteratively to fit a contour in the image while respecting a regularization constraint (e.g., on the total curvature or length of the contour). (b) Example of application: detection of freely swimming fish in a SONAR image; initial image, and zero-level-set contour after 4, 10 and 16 iterations. From Sharma & Anton (2009)

define the contour line or surface as the zero-level set of a function defined on the whole image.

Deformable models in general can be related to the Mumford-Shah functional (Mumford & Shah (1989)). This functional models the image as a piecewise-smooth function; its optimization may be simplified by rather considering piecewise-constant images, as proposed by Chan & Vese (2001); an example of application of their model on a SONAR image (Sharma & Anton (2009)) is shown on Figure 2.2.

Graph-based methods correspond to representing the image as a graph, where each pixel is a node, and pixels are connected by the graph edges. The weight (i.e. strength) of the edges joining pairs of pixels has to be representative of the inverse of the similarity that is

used (e.g. a grayscale similarity). A binary segmentation is called a 'cut'; it corresponds to partitioning the graph into two distinct sub-sets of nodes, by removing some edges. The weight of a cut is the sum of the weights of removed edges. In a 'min-cut' approach, the best segmentation is the cut with lowest weight.

Region growing methods start from a seed point: a pixel selected a priori as belonging to the targeted region. Neighboring points to that pixel are determined as belonging to the same region or not, based on some criteria on the points properties and/or on the internal statistics of the object; the region is updated iteratively with the validated points. It expands until a stopping criterium is reached.

Segmentation through mathematical morphology is mostly performed by the watershed algorithm (Beucher & Meyer (1993)); watershed segmentation focuses on the major contours in an image. A scalar-valued image (or its gradient) is represented as a topographic surface. 'Sources' are introduced in the topographic minima, and they gradually flood the surface. The last parts of the topographic surface that are kept out of the flooding are the edges of segmented regions. Edges are flooded at different levels of the water flooding. If all of these edges are kept, it yields an over-segmentation; an appropriate selection of markers for sources among all local minima helps avoid this problem. Alternatively, weights can be assigned to the edges, corresponding to the level at which they were flooded. Watershed segmentation results differ from region-growing segmentation in that the watershed runs on the whole image; the final edges around one object depend on both the presence of a marker inside and the outside markers.

Probabilistic methods for segmentation consider an image as a noisy realization of a model image whose pixels are all labeled, i.e. tied to one region. From a prior probability model on the field of labels to recover, a Bayesian formulation allows to get the posterior probability of this field of labels, given the observed image (Kervrann (2010)).

Some of these methods have already been used in seismic image segmentation (see Figure 2.3). For example, Gao (2003) proposes a region growing algorithm for salt body delineation inside a 3D seismic volume. In Purves *et al.* (2015), the authors combine two deformable models to efficiently find the contours of a geological object of interest, based on its unique character. Haukås *et al.* (2013) use a level-set method for salt body delineation, allowing for manual constraint inside an automated workflow (Figure 2.3a). For this, they define a specific attribute: the squared Frobenius norm of the local structure tensor, which allows to discriminate non-spatially-coherent reflections from stratified regions. Kadu *et al.* (2017) introduce salt body delineation inside a full-waveform inversion workflow, representing salt edges by the zero level-set of a function that evolves during the inversion. Shafiq *et al.* (2015) use one seismic attribute, the Gradient of Texture (GoT in

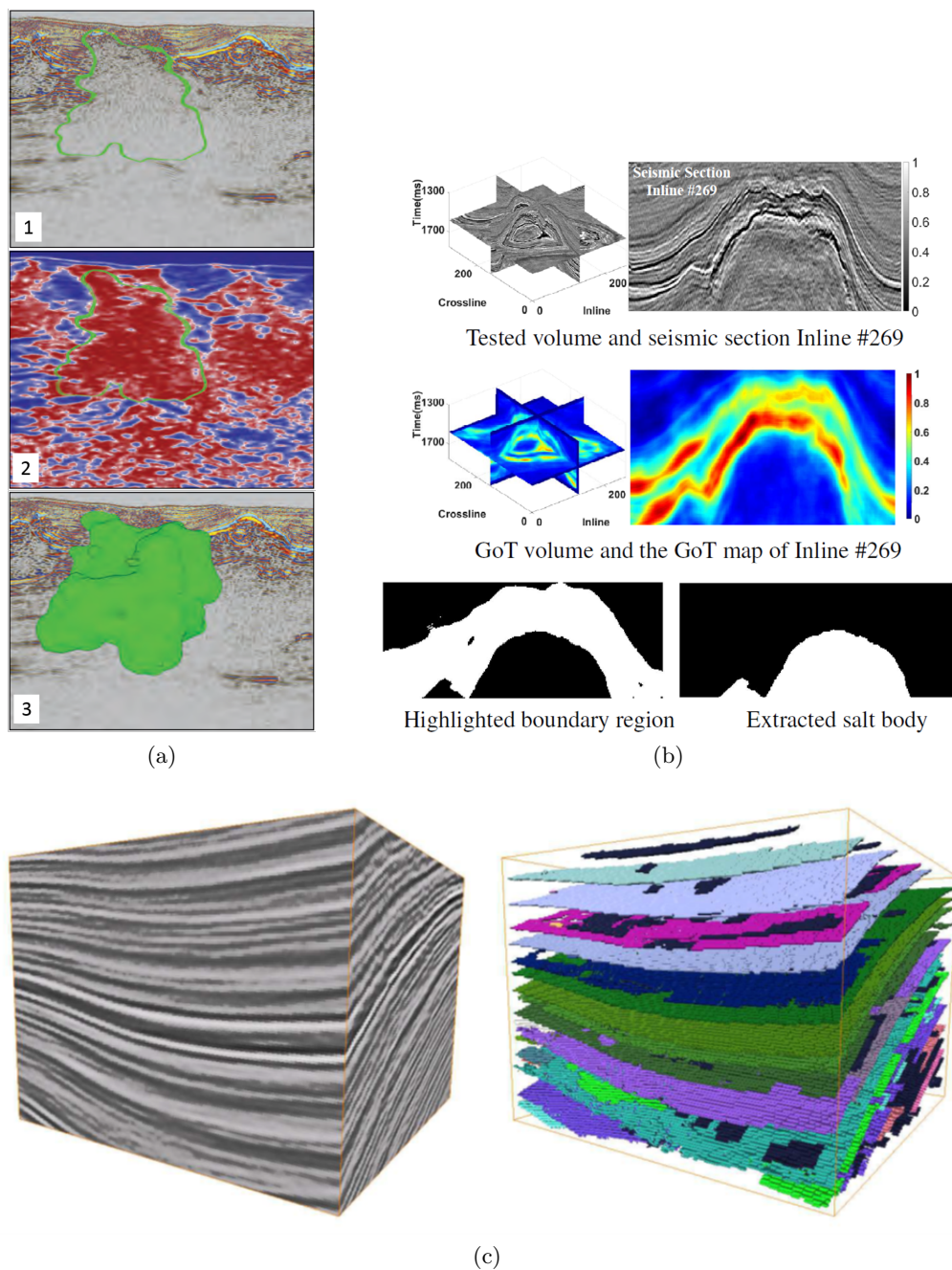


Figure 2.3: Examples of geometrical segmentation methods for seismic image partitioning: (a) salt body delineation via level-set and manual constraint based on a specifically-designed seismic attribute, from [Haukås et al. \(2013\)](#): 1- seismic section and intersection of extracted boundary in green; 2- attribute section and intersection of extracted boundary (red indicates lack of spatially coherent seismic reflections, blue indicates locally stratified region); 3- 3D view of extracted salt body. (b) Salt body delineation via region-growing and morphological post-processing, from [Shafiq et al. \(2015\)](#) (GoT: Gradient of Texture). (c) Morphological and topological segmentation (right) of a 3D seismic volume (left) according to its structural surfaces, from [Faucon \(2007\)](#).

Figure 2.3b), and then couple a region-growing result with morphological post-processing in this attribute space for retrieving consistent salt body contours.

We have seen in section 1.6.2 that the 'structure' of a seismic image is related to the scale of study. Morphological segmentation allows a hierarchical approach of the detected contours, giving more strength to more important ones. Thanks to this, Faucon (2007) develop morphological methods to segment a whole 3D seismic volume, not into 'object vs. background', but according to its structural surfaces (Figure 2.3c). To our knowledge, however, morphological segmentation has not yet been applied specifically for object retrieval purposes in seismic images.

The examples of Haukås *et al.* (2013) and Shafiq *et al.* (2015) show attributes designed specifically for one application: salt body retrieval. In fact, in applications of geometrical methods for object retrieval, much of the result relies on the accuracy of the data representation.

2.2.3.2 A local approach: classifying pixels

All segmentation methods reviewed in the previous section take advantage of the geometrical nature of images, i.e. the arrangement of pixels on a 2D or 3D grid, for partitioning them. In this section we focus on a slightly different approach: classifying pixels as individual vectors, e.g. of RGB values for segmenting a colored picture. In pixel classification, the pixels spatial arrangement is not taken into account, unless some constraint is put in the process.

However, if considering pixels individually, the dataset (set of pixels) is then comparable to any other dataset of independent points/individuals. This allows to use any existing classification algorithm, supervised or unsupervised. In this case, feature vectors attached to each seismic pixel are local descriptors of either the seismic waveform, or the neighborhood seismic amplitudes.

Automated classification algorithms (either neural networks or not) involve an iterative optimization, which should converge to the 'best' partition according to the criteria of the cost function. These criteria are different when the classification is supervised or unsupervised.

In a supervised classification, some reference dataset is given for the algorithm to be 'trained' on it. This reference dataset (also called 'training dataset') is usually part of the whole dataset to be processed; it includes an associated 'ground truth', i.e., labels of classes available for all its data points. The 'best' partition is a transformation of the training data into labels that match the labels of the training ground truth: the cost function to minimize is then based on the difference of true labels to computed labels.

On the other hand, in an unsupervised classification, no ground truth is available. The

'best' partition is defined according to the intuition that the data is naturally clustered into groups of similar points. A basic criterion for designing the cost function is to suppose the optimum is reached for lowest intra-class variance and highest inter-class variance.

Supervised classification for seismic image segmentation

In seismic facies analysis, supervised classification is useful for cases when a targeted facies is known and part of the seismic data has already been labeled by an interpreter. Carrillat *et al.* (2002) provide an example of such supervision: six seismic facies of interest are defined, and a few patches of the seismic dataset are labeled to one of these facies. The authors choose some seismic attributes for data representation. Then a neural net classifier is trained on the training patches in the attributes space; after the training, the resulting neural net is parameterized so that for all training patches, it produces labels that match the true labels. That way, when applying the neural net classifier to any part of the seismic dataset, one of the six labels of interest will be output, so that the whole seismic dataset can be labeled. Similarly, West *et al.* (2002) classify a seismic dataset with a neural net, starting from a set of training patches. Their case mainly differs from the previous by the use of a textural data representation. Figure 2.4 shows the typical resulting labeled data obtained from such classifications.

Supervised seismic facies classification is also extensively developed for salt body detection. In this application, not all seismic facies are targeted; the classifier rather produces a binary result of 'salt vs. background'. This is done by two approaches:

- Designing an adequate seismic data representation and learning the best binary partition according to training patches labeled as 'salt' or 'background' (or alternatively, labeled as 'salt boundary' or 'other'). This approach has been promoted by the efficiency of textural attributes for salt representation (e.g., Berthelot *et al.* (2013)); so that a lot of improvements are done more on the data representation itself than on the learning algorithm. The example of Carrillat *et al.* (2002) cited above is a case where 'engineering' the appropriate seismic attributes is crucial, more than the classifier quality.
- Designing an adequate learning algorithm that, from a simple initial data representation or the image itself, may automatically find the best data representation for the goal of discriminating salt from background. This is typically an area of application of deep neural networks (e.g., Gramstad & Nickel (2018)); the parameterization that is learnt in such cases actually corresponds to an automated data representation, the best representation for discriminating salt from the rest (deep neural networks will be presented in section 2.2.3.3). Orozco-del Castillo *et al.* (2017) propose a similar approach: they use a genetic algorithm to learn the optimal size of volume elements

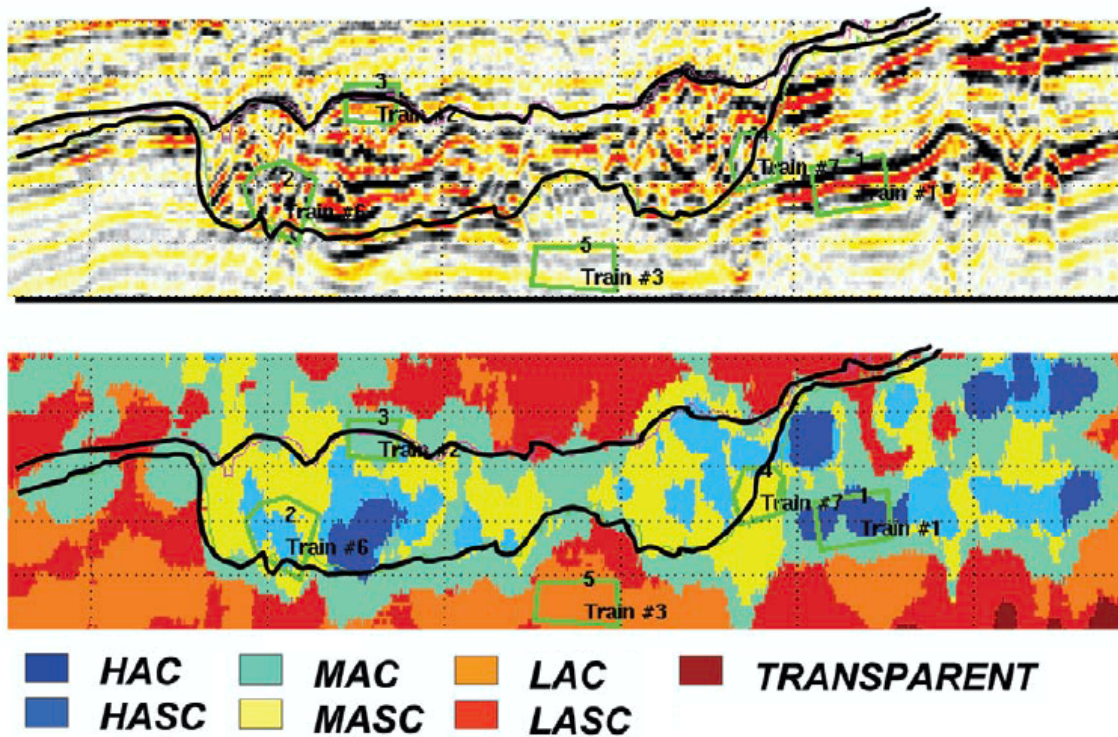


Figure 2.4: A typical seismic facies classification using the interpreter trained probabilistic neural net, where multiple seismic facies classes have been identified. The seismic classification scheme on the right consists of high amplitude (HA), moderate amplitude (MA), low amplitude (LA), continuous (C) and semi-continuous (SC) seismic facies. Training patches are contoured in green lines. From [West *et al.* \(2002\)](#).

for texture representation, according to the goal of distinguishing salt regions.

In the case of salt detection, only one training facies is defined, e.g. non-spatially-coherent reflections in the case of [Haukås *et al.* \(2013\)](#) (see Figure 2.3a). A supervised approach is thus interesting for object-based approaches where the targeted facies is homogeneous; then, the similarity of a data region to this facies can be quantified, interpreted and thresholded to produce a binary partition. However, it is not adapted for objects or regions that are internally heterogeneous.

In the case of several user-defined training facies, two drawbacks appear:

- The user-defined reference set of facies may not cover the whole variability of seismic facies actually present in the data. This may lead to some regions of the seismic data being classified into one facies class by default, but being in fact quite dissimilar to them.
- The user-defined reference set of facies may give an unbalanced representation of this data variability, as some chosen pairs of facies may be more similar than others; e.g., the user may define many distinct classes for facies that have actually very similar textures, while other different textures would be covered by too few distinct facies. This yields a bias in the output facies classes probabilities.

Unsupervised classification schemes can, to a certain extent, limit this drawback, as the produced clusters are data-driven only, i.e. with no (or very limited) input from the user.

Unsupervised classification for seismic image segmentation

Unsupervised learning methods for seismic facies analysis are mostly used in the exploratory stage of seismic interpretation. In unsupervised methods, no training dataset is used. The best partition of the data should give a representation of how seismic regions are grouped into similarity-based clusters. Methods such as the k-means clustering ([MacQueen \(1967\)](#)) and its derived/improved versions (e.g. [Veenman *et al.* \(2002\)](#), [Arthur & Vassilvitskii \(2006\)](#)) are now standards of unsupervised classifications.

In their work, [Marroquín *et al.* \(2009\)](#) note four kinds of unsupervised classification algorithms: partition models (type 1), probabilistic models (type 2), hierarchical models (type 3), soft competitive models (type 4). Types 1, 2 and 3 produce clusters, but do not output any information on the similarity *between* clusters. This is also highlighted by [Coléou *et al.* \(2003\)](#), when comparing, as [Marroquín *et al.* \(2009\)](#), several methods that are used in seismic facies analysis: k-means, Principal Component Analysis, Projection Pursuit, Neural networks - and, among them, the Self-Organizing Map (SOM) algorithm ([Kohonen \(1986\)](#)). The latter (SOM, of type 4 in the framework of [Marroquín *et al.* \(2009\)](#)), contrary to the others, yields information about the similarity between clusters;

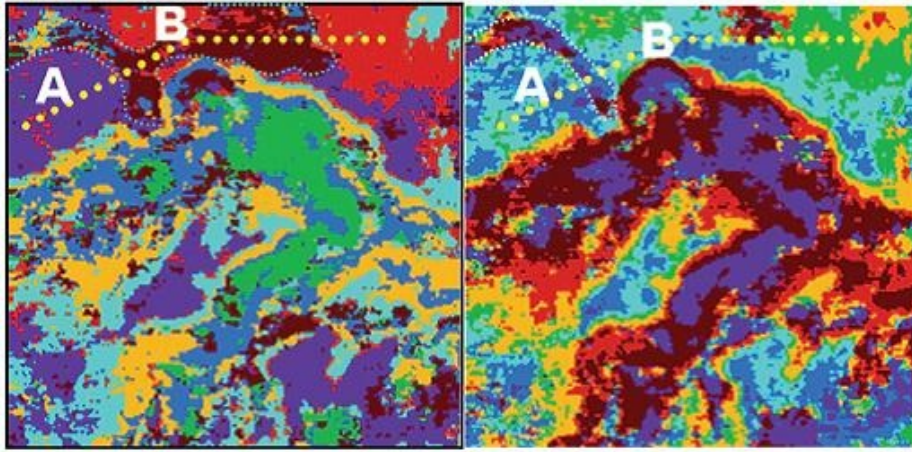


Figure 2.5: Comparison between a k-means clustering map (left) and a SOM clustering map (right) of a Frio Channel gas play (South Texas). One color corresponds to one cluster. From Coléou *et al.* (2003).

it is therefore more suited to further interpretations. According to Coléou *et al.* (2003), the main advantages of SOM lie in the continuous characteristics of the created clusters. This allows the algorithm to be almost independent of the number of clusters input initially by the user: above a certain number, additional clusters are created within the existing clusters map and only refine its precision rather than artificially adding variability in the results. Results of a SOM clustering are more visually sensible, as the similarity in colors corresponds to the similarity of clusters, as shown by Figure 2.5.

The Generative Topographic Mapping (GTM), an alternative to SOM, was provided by Svensen (1998) and Bishop *et al.* (1998b). It shares the same cluster ranking properties as the SOM; however, it is based on a probabilistic framework using an iterative Expectation-Maximization algorithm for optimizing a Gaussian Mixture Model as the final clustering. GTM builds a mapping from a regular grid of cluster nodes in a latent space, to a grid of cluster nodes in the data space that lies on a manifold (Figure 2.6a). Therefore, GTM learns both a manifold representation and serves as a clustering of the data. Contrary to SOM, GTM has mathematical advantages such as proven convergence and continuity of the mapping from the latent space to the data space. Figure 2.6b displays, for an application similar to that presented in section 2.3, the GTM-built magnification factors (Bishop *et al.* (1997), Svensen (1998)), MF, which give a measure of how stretched the manifold is in the data space. The higher the MF, the more stretched the manifold, and generally the less data points have been assigned to this cluster; regions with high MF values correspond to natural boundaries between groups of points in the data space. Above a certain number of clusters, the MF map becomes stable and is only refined, not modified in shape. Details on the mathematical formulation of GTM can be found in Appendix A. Roy (2013) has shown the applicability of GTM for seismic facies interpretation. Since then a few applications have been published; for example, Roy *et al.* (2014) show how clustering seismic inversion volumes allows to visualize the heterogeneity of a carbonate

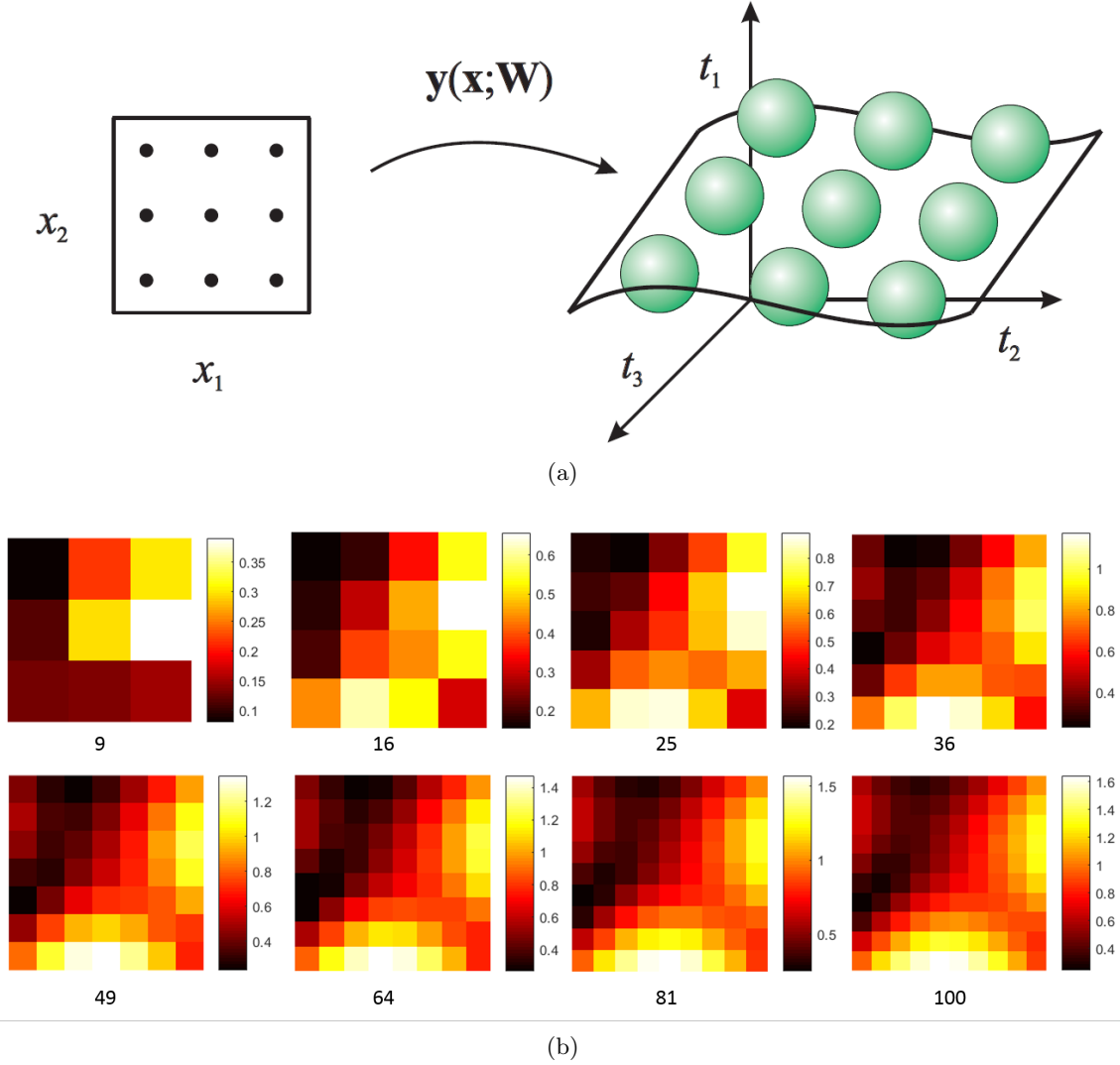


Figure 2.6: Generative Topographic Mapping: principle and characteristic of the Magnification Factors. (a) GTM principle; \mathbf{x} is the data representation in the latent space, \mathbf{W} is the parameter matrix built during the optimization, and y is the mapping function. From [Svensen \(1998\)](#): “Points on a regular grid in the low-dimensional latent space (left) are mapped, using a parameterized, non-linear mapping $y(\mathbf{x}; \mathbf{W})$, to corresponding centers of Gaussians (right). These centers will lie in the low-dimensional manifold, defined by the mapping $y(\mathbf{x}; \mathbf{W})$, embedded in the potentially high-dimensional data space”. (b) Magnification factors maps of applied GTM clustering for increasing number of clusters. From 36 - 49 clusters and above, the shape of the manifold is caught by the algorithm; more clusters refine it but do not modify it.

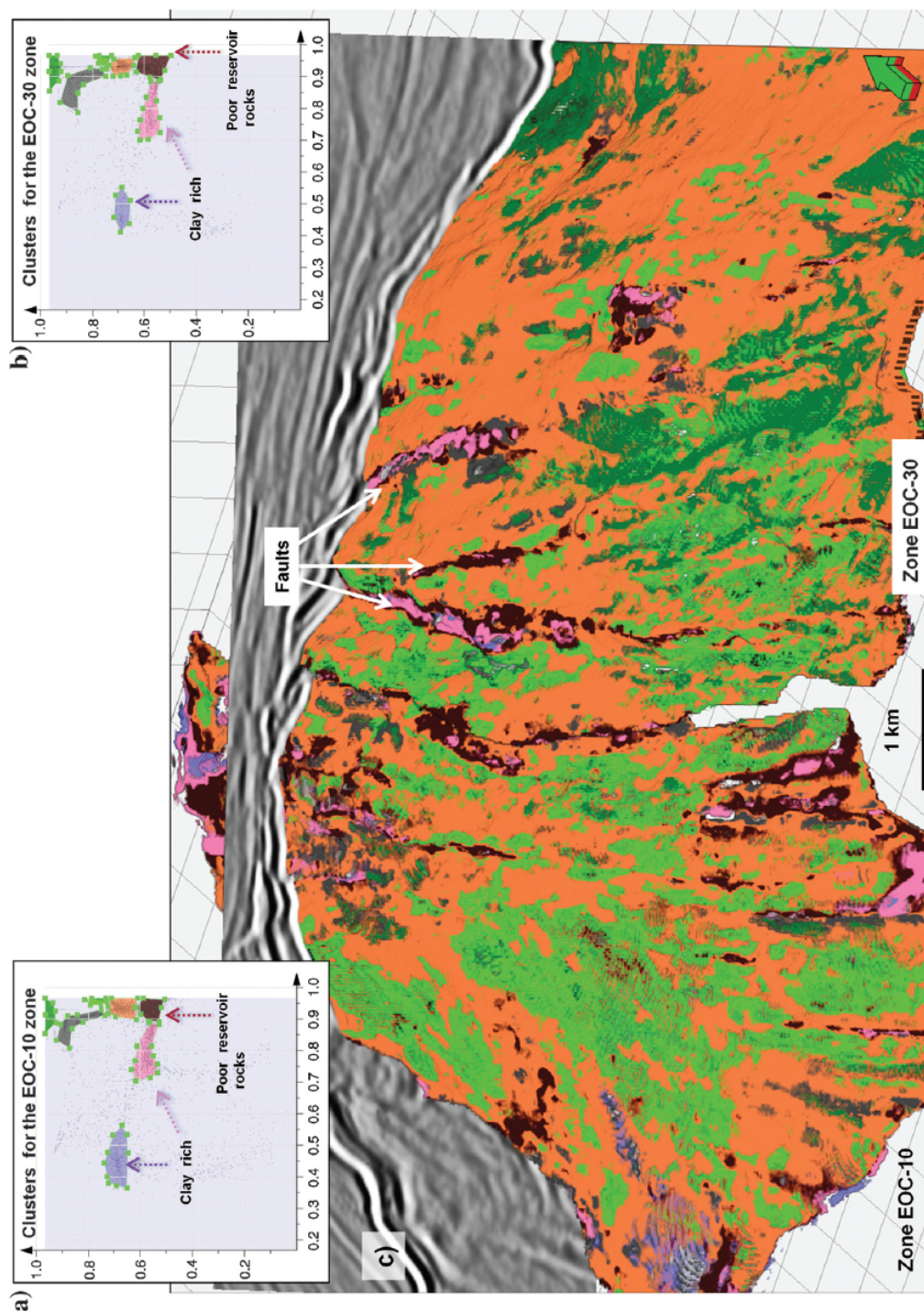


Figure 2.7: GTM and posterior clustering analysis for highly heterogeneous facies classification. (a), (b) Data distribution in the GTM 2D latent space for two different reservoir units. Seven different polygons with different colors around clusters signify rock types for the two reservoir units. (c) Generated seismic facies volume. From Roy *et al.* (2014).

conglomerate reservoir (see Figure 2.7).

For both SOM and GTM, further processing is often carried out on the results of the algorithm. Interpreting how clusters relate to geological facies is done by studying the 'U-matrix' (SOM case) or the GTM *mean* posterior probabilities of the data points projected onto the latent space (GTM case). In these two cases, data points are gathered into semantic groups, as proposed by de Matos *et al.* (2007) for SOM, and Roy *et al.* (2014) for GTM. This is exemplified in Figure 2.7a and 2.7b, where polygons were drawn manually to obtain a meaningful grouping. Note that gathering data points based on the projected GTM *mode* of posterior probabilities would also be relevant; these modes all lie on cluster centers (Bishop *et al.* (1998b)), which leads to gathering several clusters of interest rather than individual data points. In any case, some posterior work has to be done by an interpreter, as emphasized by Chopra & Marfurt (2014) and Qi *et al.* (2016). This leads us to the last sub-part of this section: in the end, performing a meaningful segmentation requires both data-driven input and input from an interpreter - which may be prior input, posterior input, or external knowledge that constrains parameters.

Seismic image segmentation: data-driven vs. model-driven information

For seismic interpretation, a few studies have been led to combine an unsupervised clustering with some external input. For instance, Zhao *et al.* (2016) modify the SOM cost function by adding a stratigraphic constraint, through the Variational Mode Decomposition of a seismic trace. The resulting clustering is constrained so that regions that belong to a same stratigraphic layer are assigned to similar clusters. In another approach, Hashemi *et al.* (2017) constrain the results of SOM a posteriori, by iteratively modifying the clustering according to some facies maps created from well logs. This way, similarity of well-log-extracted facies is added to the data-driven similarity facies.

On the other hand, other authors start from a supervised classification, and focus on limiting the afore-mentioned biases it can involve. For example, Ebuna *et al.* (2018) propose a statistical method to optimize the inputs of a neural network for multi-attribute analysis. Such a method should then enforce the neural net to be fed more from the data itself than in a standard supervised learning approach. Alaudah & AlRegib (2016) propose a 'weakly-supervised labeling of seismic volumes', where very few training patches are used: the training dataset is actually built from a mix of the patches of this manual input and other patches, recovered from the dataset thanks to an efficient similarity function.

These examples illustrate the need to use both data-driven and model-driven information to create a local seismic facies representation. Knowing this, uncertainties corresponding

to both domains have to be taken into account for analyzing results.

A number of methods have been presented for segmenting an image with geometrical methods, or via classifying pixels based on local descriptors. In a last section, we present a kind of local approach which is specifically designed to convey multi-scale information.

2.2.3.3 A specific kind of local approach: learning abstract high-level representations for segmentation

Classifications presented earlier could be called 'machine learning' algorithms, in the sense that the computer learns to partition the image given a certain data representation and a certain optimization scheme. 'Machine learning', however, commonly refers to neural network-based classifications.

An artificial neural network is a set of connected entities called 'neurons' as they were initially biologically-inspired, to mimic the signal transmission of a real neuron. In a standard neural net, each neuron computes a linear combination of its inputs plus a scalar value called 'bias'; its output is a nonlinear function of this intermediate result (see Figure 2.8a). The nonlinear function is called 'activation function', and transforms the combined input signals into an activated or non-activated answer (similarly to a real neuron being 'activated' when its input stimulation reaches a threshold). The sigmoid, hyperbolic-tangent functions, or Rectified Linear Units (ReLU, [Nair & Hinton \(2010\)](#)) are examples of activation functions. Once chosen the activation function, one neuron is parameterized by its weights and bias. Training the neural net consists in finding the 'best' parameterization of the weights and biases of all neurons of the net, according to an objective task, e.g. classification. As presented on Figure 2.8a, a neural net is typically organized with one input layer of neurons (the input multi-dimensional signal, typically the feature representation of a data sample), one or several hidden layers or neurons, and one output layer yielding the result. Designing a neural net implies choosing several hyper-parameters, e.g. the size and number of layers.

Deep neural networks are networks with a large number of hidden layers (e.g., [LeCun et al. \(1998\)](#), [Krizhevsky et al. \(2012\)](#), [LeCun et al. \(2015\)](#)). A deep neural network is typically trained not from an initial 'handcrafted' representation of the data (with pre-defined features), but from the data itself; it is supposed to learn the most-appropriate data representation for its task. Convolutional Neural Networks (CNNs) are the deep networks used for image data, often for classification purposes. They include (Figure 2.8b, from [Deshpande \(2016\)](#)) a series of linear and nonlinear operations on an input image: typically convolutions and pooling, which create features of different scales of the image.

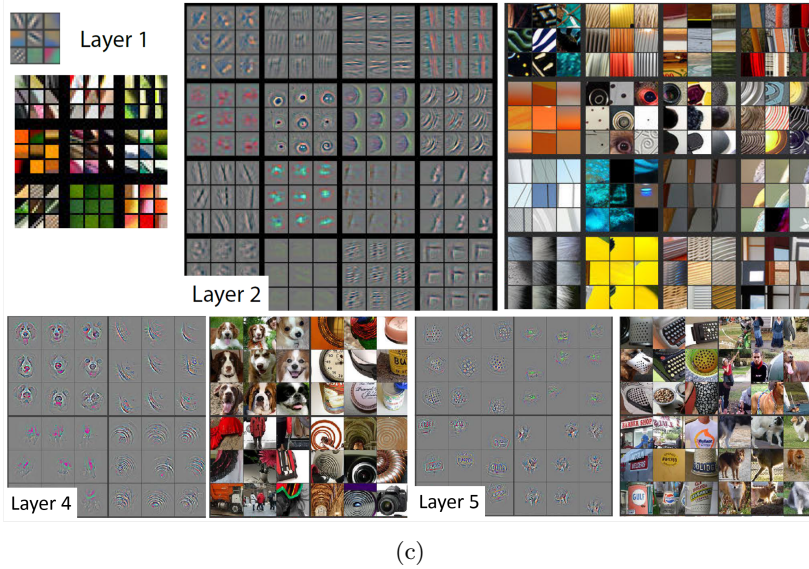
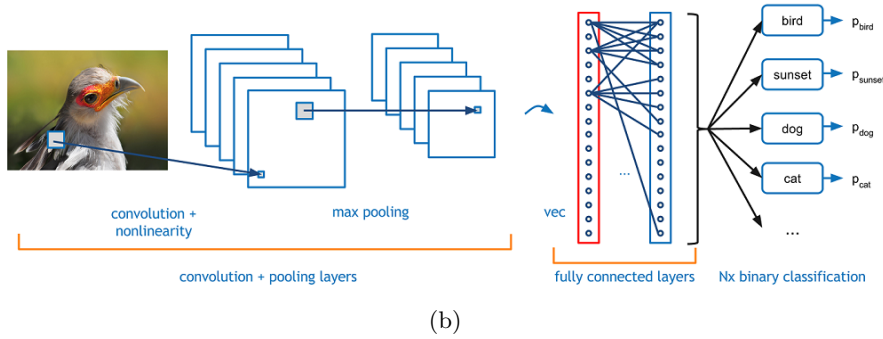
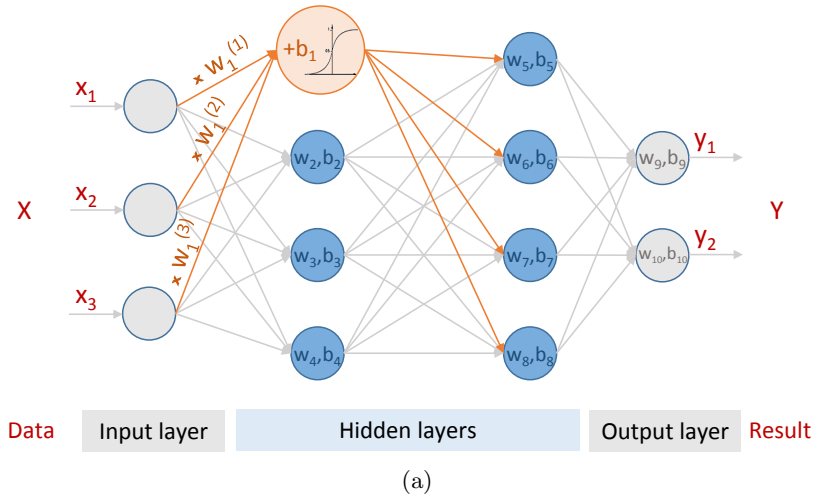


Figure 2.8: (a) A simple neural net structure. The parameters of the orange neuron are its input weights $w_1^{(j)}$ ($j = 1..3$) and its bias b_1 . Its output is a (nonlinear) activation function (e.g. sigmoid as represented) of the weighted sum of its inputs plus the bias. Deep learning is based on the use of a lot of hidden layers. (b) Convolutional Neural Nets structure: after a series of 2D operations (convolution, pooling), fully-connected layers allow to produce a classification result. From [Deshpande \(2016\)](#). (c) Extract of Figure 2 from [Zeiler & Fergus \(2014\)](#); for each layer, their visualization of features (gray pictures) of a deep CNN allows to understand a posteriori which parts of the input images (photos) were the most important in training the network for the given classification task.

The resulting representation is then described as 'hierarchical'; appropriate structures of CNNs allow to take full advantage of this multi-scale information (for instance, the U-Net by [Ronneberger *et al.* \(2015\)](#), or the Feature Pyramid Networks by [Lin *et al.* \(2017\)](#)). These layers dedicated to 2D data processing are followed by some 'fully-connected' layers, similar to the standard neuron layers of Figure 2.8a, and connected to the output layer. There, the 2D data is brought back to 1D.

Once a CNN is optimized, the information carried by the features is gradually of a higher level while gradually passing through the hidden layers; consequently, with deeper and deeper CNN architectures, a higher and higher level representation of the data is learnt by the network. Analyzing CNN responses, [Zeiler & Fergus \(2014\)](#) visualized the 2D features learnt by the network, thus highlighting the most important parts of the image that the CNN used to achieve a classification task (Figure 2.8c).

In this way, CNNs provide ways to bridge the gap between data, data-extracted low-level attributes and high-level interpretation, as the image representation is then learnt by a machine, not 'engineered' anymore. Furthermore, unsupervised clustering can also be addressed with CNNs, for instance through Auto-Encoders (e.g., [Kingma & Welling \(2014\)](#)) or Generative Adversarial Networks (GANs, [Goodfellow *et al.* \(2014\)](#)).

If applied to seismic data, the image to consider for classification would be a seismic patch. In a CNN, the several steps of convolution would retrieve patterns of several scales in the patch, which corresponds to our needs; it would then be usable in a supervised or unsupervised framework.

There are, however, some drawbacks to the deep learning approach. The design of a neural net, especially of a CNN, requires to choose hyper-parameters: the size and number of layers, but also the filters used for convolution layers, and how hidden layers are organized; this is usually done based on earlier experience and depending on the application. Despite deep neural net practical efficiency, their good results rely on empirical rather than mathematical proof. This is related to their 'black box' character (e.g., [Lipton \(2016\)](#)): because there is no mathematical model in a neural net, it is actually hard to know why certain network architecture is better than another - although there was initially a rationale motivating its design (e.g. the U-Net by [Ronneberger *et al.* \(2015\)](#), where the specific 'U-like' CNN structure aims at capture both context and precise localization).

In supervised analyses, deep networks are characterized by the need for high amounts of training data to learn from, which can be a strong limit for applications on specific kinds of images (e.g. seismic images) where training data is not freely available, or is subject to uncertainty.

Recently, though, [Veillard *et al.* \(2018\)](#) have shown the applicability of unsupervised learning with CNNs on seismic data. Their methodology relies on learning an unsupervised

representation of a seismic dataset (via the afore-mentioned GAN and Auto-Encoder), thus creating a high-level, low-dimensional representation of this dataset. This representation is then available to apply any supervised learning task, being application-independent. Such a local approach still requires to choose a size of seismic patch (e.g. 16 time samples x (16x16) traces in [Veillard *et al.* \(2018\)](#)) around each seismic sample to represent it; the multi-scale character is thus limited by the prior-defined size of the patch. This makes a CNN-based representation actually comparable to local textural representations presented in [2.2.1.2](#).

Textural attributes are therefore attractive for local seismic data representation when it comes to classifying seismic patches, as their multi-scale information somehow compares to the hierarchical representation induced by CNNs. [Bhalgat *et al.* \(2018\)](#), for instance, have implemented the scattering transform, initially introduced by [Mallat \(2012\)](#), for categorization of seismic patterns. The scattering transform itself offers a mathematical framework of interest for deep network understanding. In their application, [Bhalgat *et al.* \(2018\)](#) show that this transform allows to distinguish specific types of seismic patterns; their approach is supervised, with only four kinds of patterns, which are defined on 512x512 images. A smaller patch size, as suggested in section [2.2.1.2](#), may be preferable for more local studies at the sample level.

Contrary to a CNN, a textural representation of seismic data may help to understand all steps of an interpretation process, from the low-level data description to the higher-level object retrieval, in order to have a consistent support for geological interpretations.

2.2.4 Synthesis

Although efficient segmentation schemes are essential for seismic interpretation, we have seen a number of methods which heavily rely on a specific seismic data representation. For instance, a region-growing algorithm ([Gao \(2003\)](#)), or a similarity thresholding to segment different parts of the image ([Wang *et al.* \(2015\)](#)), may allow to distinguish objects that are rather homogeneous in terms of seismic properties, such as salt bodies or mineralized bodies. CNN developments also tend to show that the data representation may be even more important than the classifier or segmentation method itself. Our objects (MTDs) are precisely *not* homogeneous, which constrains the choice of the data representation. In the next section, we thus present an efficient scheme for coupling a heterogeneous representation carrying the seismic facies variations, with a homogeneous one, carrying a prior delineation information.

In section [1.4.2](#), we have presented two approaches for seismic facies definition. The

first one (from seismic stratigraphy) consists in associating facies names or labels, to descriptions of reflectors' organizations; such labels carry an interpretation in terms of depositional environments. The second one is limited to the description of the data only: they are representations of a lower level than the first type.

In a similar way, we have seen two different kinds of seismic attributes. The first kind results from some 'feature engineering', where an attribute is custom-built from a specific content of the data in order to represent certain rock property. For the second kind of attributes, signal decomposition is chosen, such as curvelets (Alaudah & AlRegib (2016)) or scattering networks (Bhargat *et al.* (2018)) for example. These attributes are independent of any prior knowledge on their relationships to rock properties; as signal decompositions, they are designed to convey more information than the former kind of attributes. They are textural attributes, as they bear information on several scales and orientations in a window of the seismic image. The first kind of attributes relates to the first approach of seismic facies definition, while the second kind of attributes relates to the second approach.

The contribution presented in the next section tends to bridge both ways, by using a sensible attribute decomposition as an initially low-level data representation, and a data-driven clustering algorithm, to then learn in this higher-level representation space the regions that allow to singularize a multi-facies geobody. This learning step is the way to go to a semantic data representation, i.e. one where the seismic data is annotated with objects. It requires an input labeled database (the training set) which is usually given by an interpreter after a time-consuming manual work. In our approach, the training set is of reasonable size - and in 2D, thus easier to annotate manually. More importantly, the input annotations are not a crisp delineation of objects but a fuzzy one, i.e. with probabilities; a confidence parameter is also given to account for potential uncertainties in this input annotation. The interpreter is therefore only weakly involved, and these input annotations may also be provided by external computations rather than given manually.

In concrete terms, we choose a local yet multi-scale approach. We use the GLCM attributes as an initial textural representation of the seismic data, calculated at the sample level on 2D sections. The patch size for GLCM computations is 11 samples vertically (40 ms TWT) and 11 samples laterally (250 m). The final attribute set is recovered after a dimension-reduction scheme. The metric comparing two pixels (or samples) is then an Euclidean distance between their respective attribute vectors, in a low-dimensional space which avoids any dimensionality bias in the similarity. Our approach fits in the framework of STSIMs; instead of relying on multiplicative pooling like SeiSIM (see section 2.2.2), our additive pooling should avoid abnormally high similarities when only one attribute has similar values in the compared patches. The GTM unsupervised clustering algorithm is then used for pixel classification, based on the MATLAB Netlab toolbox by Nabney & Bishop (2002). It is followed by a novel supervised learning of probabilities, which adds a

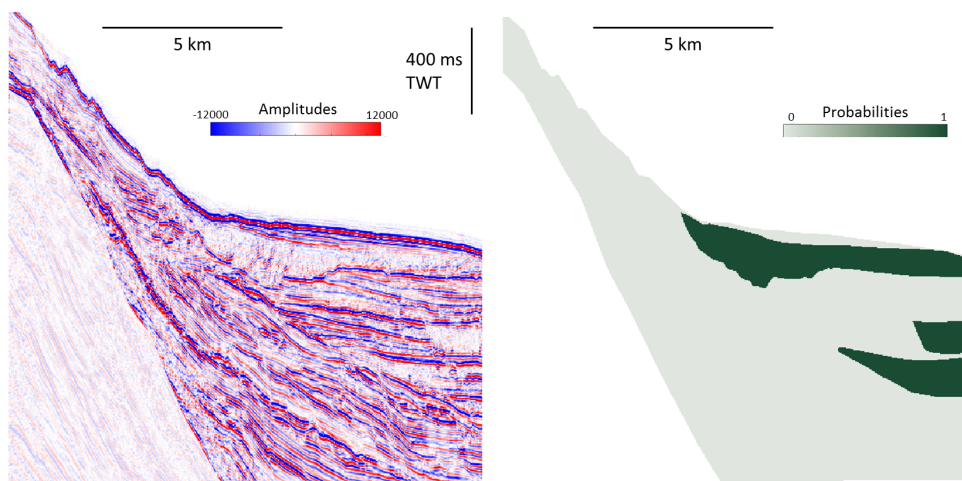
global constraint to the delination. The whole process runs on MATLAB code.

2.3 Recovering MTDs as heterogeneous geobodies from seismic data - ARTICLE

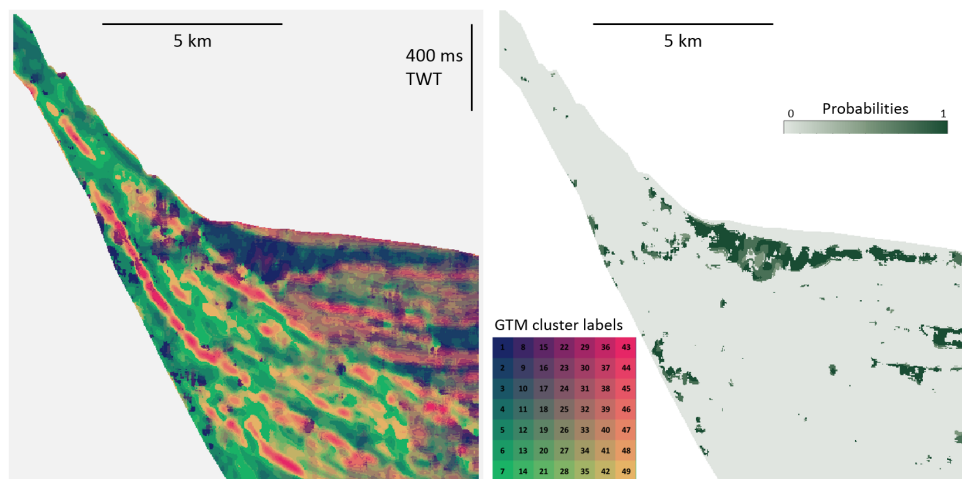
In this section, we present our main contribution on MTD identification in seismic data.

First, Figure 2.9 illustrates the main steps of image processing performed on a seismic section. On Figure 2.9a, one section is presented with available prior information in the form of probabilities of presence of an MTD (on this exemplar section, all prior positive probabilities are 1). On Figure 2.9b, the GTM-clustered section is shown, as well as posterior probabilities resulting from the supervised learning step of our method. On Figure 2.9c, the result of propagating the probability computation is presented.

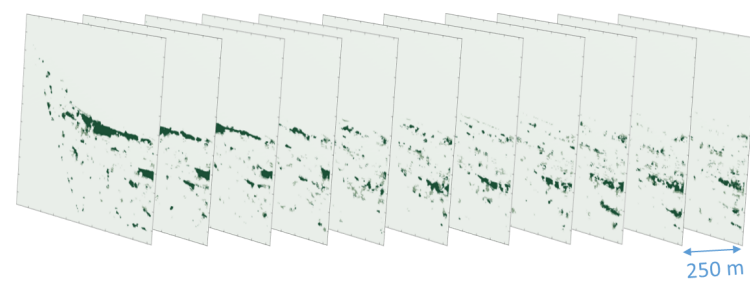
We then give the article that presents the methodology. It was submitted to the Mathematical Geosciences journal on October 1st, 2018. It is related to a patent application (Le Bouteiller & Charl  ty (2018)) made on May 18th, 2018.



(a)



(b)



(c)

Figure 2.9: Illustration of the method presented in this section. (a) One seismic section and the available prior probabilities on MTD occurrence. (b) The same section where every pixel is colored according to its GTM cluster label (a number between 1 and 49), and the posterior probabilities computed from our method. A 2D colormap is used for GTM labels to account for the 2D topographic “ranking” given by GTM. (c) Retrieval of probabilities for several sections.

Semi-supervised multi-facies object retrieval in seismic data

(version revised for second submission after peer review)

Pauline Le Bouteiller, Jean Charléty

February 27, 2019

Abstract

Characterizing buried sedimentary structures through the use of seismic data is part of many geoscientific projects. The evolution of seismic acquisition and processing capabilities have made it possible to acquire ever growing amounts of data, increasing the image resolution, so that sedimentary objects (geobodies) can be imaged with more precision within sedimentary layers. However, exploring and interpreting them in large datasets can be a tedious work. Recent practice have shown the potential of automated methods to assist interpreters in this task. In this article, a new semi-supervised methodology is presented for identification of heterogeneous geobodies within seismic data. The approach couples a nonlinear data-driven method and a novel supervised learning method. It requires a prior delineation of the geobodies on a few seismic images, coming with an a priori confidence on that delineation. The methodology relies on a learning of an appropriate data representation, and propagates the prior confidence to posterior probabilities attached to the final delineation. The proposed methodology was applied to three-dimensional real data, showing consistently effective retrieval of the targeted multi-facies geobodies, mass transport deposits in the present case.

Keywords

Seismic interpretation - Object recognition - Semi-supervised analysis - Multi-facies geobody

1 Introduction

Within three-dimensional seismic data interpretation, detecting geobodies such as salt bodies, channels or mass-transport deposits can prove critical in assessing the reservoir potential of a region or basin, or in improving the understanding of a geological structure. Characterization of their various features on seismic amplitude data is also needed, to properly describe the variability of such geobodies and provide clues for interpreting their diversity (e.g., Ogiesoba & Hammes 2012). In this respect, geobody detection and characterization is one task that remains challenging.

Seismic interpretation methods are characterized by a still relatively high expert guidance, due to complex aspects of the amplitude data themselves, particularly the inherent intricacy of all scales of geological structures that appear on the data. Depending on which scale is chosen (horizon delineation for stratigraphic interpretation / object delineation / intra-object variations), the outlined structure is not the same, mainly because what is looked for is defined by the interpretation objective. Once fixing the objective, dedicated, automated methods can be implemented to limit manual time-consuming tasks.

In seismic interpretation, a seismic facies is an identified local aspect of the seismic image, defined by the spatial organization of reflectors in a zone. ‘Seismic attributes’ have been well-known for a long time (Haralick *et al.*, 1973), especially for depicting seismic facies. They can be used similarly as data ‘features’ in machine learning vocabulary. In particular, a seismic image can be dealt with as a textured image, where each pixel (or three-dimensional “voxel”) is described by the amplitude values arrangement in its neighborhood. Textural features characterize the local distribution of intensities around each pixel. When computed on seismic amplitudes, they have been shown to describe well the variety of pattern sizes and orientations present in seismic datasets (e.g., Long *et al.* 2015). They provide a mostly data-driven representation, contrary to representations based on “engineered” attributes such as acoustic impedance, which, although giving more physical insights on rock properties, require to introduce more steps of model-driven computation. A textural representation of the seismic data at several scales is appropriate to depict seismic facies, given the structurally-mixed sizes of seismic patterns.

Automated approaches for local interpretation in seismic datasets mainly concern geobody delineation and facies classification. The former use object-based approaches in image processing, focusing either on the object contours (e.g., Wang *et al.* 2015, Shafiq *et al.* 2015, Wang *et al.* 2016) or on its internal homogeneous patterns or facies (e.g., Gao 2008), often with supervised learning. The latter commonly use data classification or image segmentation methods (e.g., Pitas & Kotropoulos 1992), and tend to look through the intrinsic variability of a whole dataset (e.g., de Matos *et al.* 2007, Zhao *et al.* 2016), often with unsupervised learning. In this respect, the Self-Organizing Map (SOM, Kohonen 1986), as well as its probabilistic alternative, the Generative Topographic Mapping (GTM, Bishop *et al.* 1998), have proven efficient clustering tools (e.g., Marroquín *et al.* 2009, Roy *et al.* 2014, Chopra & Marfurt 2014). Recent methods have mixed the use of unsupervised learning and external, or prior, information. For instance, Hashemi *et al.* (2017) constrain the resulting clustering by prior probabilities expanded from well log data, through an iterative grouping of clusters; Zhao *et al.* (2017) constrain the SOM via the variational mode decomposition of the seismic signal, thus introducing stratigraphic information in the result; Qi *et al.* (2016) combine a

GTM model to user-defined facies and preconditioning of attributes.

Such mixed approaches have not been proposed yet for object delineation purposes. However, they could help in the design of a heterogeneous geobody detection method that allow the characterization of intra-class facies variability. In particular, the internal distribution of the various seismic facies of geobodies, be them layered, chaotic, transparent, deformed, compressive or other, is for now rather quantified by a manual delineation of regions disclosing intuitively-appealing facies groups. An automated delineation of such geobodies that involve their different kinds of facies would be highly recommended for faster and more robust interpretations.

In this paper, a novel methodology is proposed, to detect multi-facies geobodies in three-dimensional seismic data while preserving their internal facies variability and keeping track of the input uncertainty. It is applied to the detection of multi-facies mass-transport deposits (MTDs), on a three-dimensional seismic cube for which full-stack and partial-stack analyses are conducted.

In Sect. 2, the methodology is introduced step by step. Sect. 3 presents results of a real case-study application. A discussion is led in Sect. 4 on the relevance, sensitivity and future outlooks of the method, before concluding with Sect. 5.

2 Methods

In this section, the steps of the new methodology are described, as summarized in Fig. 1 and illustrated in Fig. 2. It starts with a selection of subparts of the dataset to be analyzed; it eventually outputs a set of 3D-delineated objects together with probability values and cluster labels for each of their voxels. Phase 1 in Fig. 1 corresponds to parameterizations or “training” (sects. 2.1 to 2.3), performed on a training dataset. The training dataset is typically a small subpart of the whole dataset where some prior information for each data sample is available. This prior information has some uncertainty and is therefore not considered a “ground truth”. If such prior information is available on the whole dataset and if computing resources enable it, the training may be run directly on the whole dataset. If not (as in more common cases), Phase 1 is followed by a propagation phase (Sect. 2.4; Fig. 1, Phase 2), and then by a post-processing phase (Sect. 2.5; Fig. 1, Phase 3). In this paper, the training set consists of several parallel sections of the three-dimensional seismic volume and their associated prior probabilities.

2.1 Unsupervised clustering for bringing to light the facies variability in the training set (Fig. 1, Phase 1, A., B., C.)

A first main stage of Phase 1 aims at scanning the whole range of the natural variety of facies in the training dataset, by partitioning samples according to their facies in a data-driven manner. For this, the seismic data is represented as a set of feature images; its dimension is reduced and an unsupervised clustering is performed on the data.

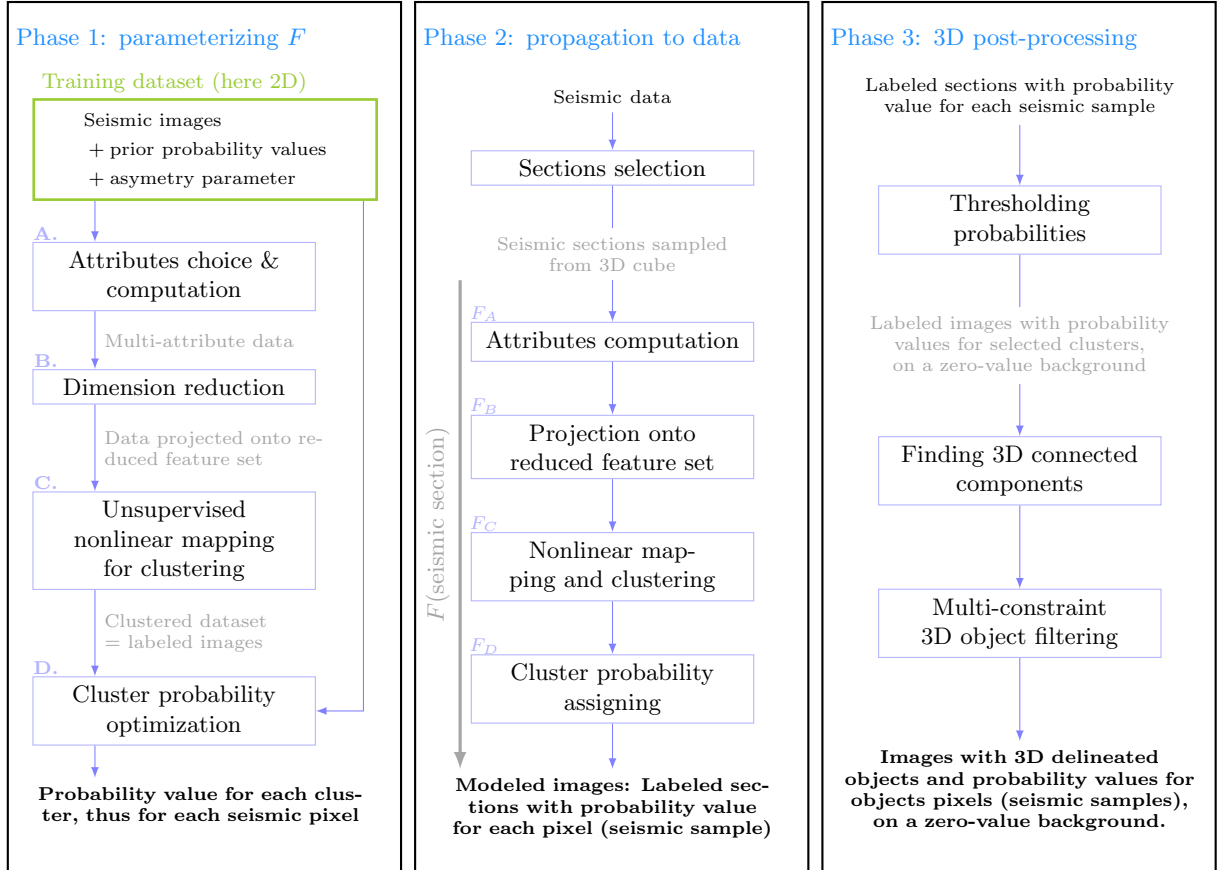


Figure 1: Global workflow for automated heterogeneous object detection in seismic data. Phase 1 corresponds to a training phase performed on a small sample of the whole dataset, where F is created via parameterizing each of its four components F_A , F_B , F_C and F_D in steps A., B., C. and D. respectively. In Phase 2, F is applied to other samples of the dataset. In Phase 3, some post-processing is applied so as to retrieve the 3D connected components with highest probability of corresponding to the targeted heterogeneous objects.

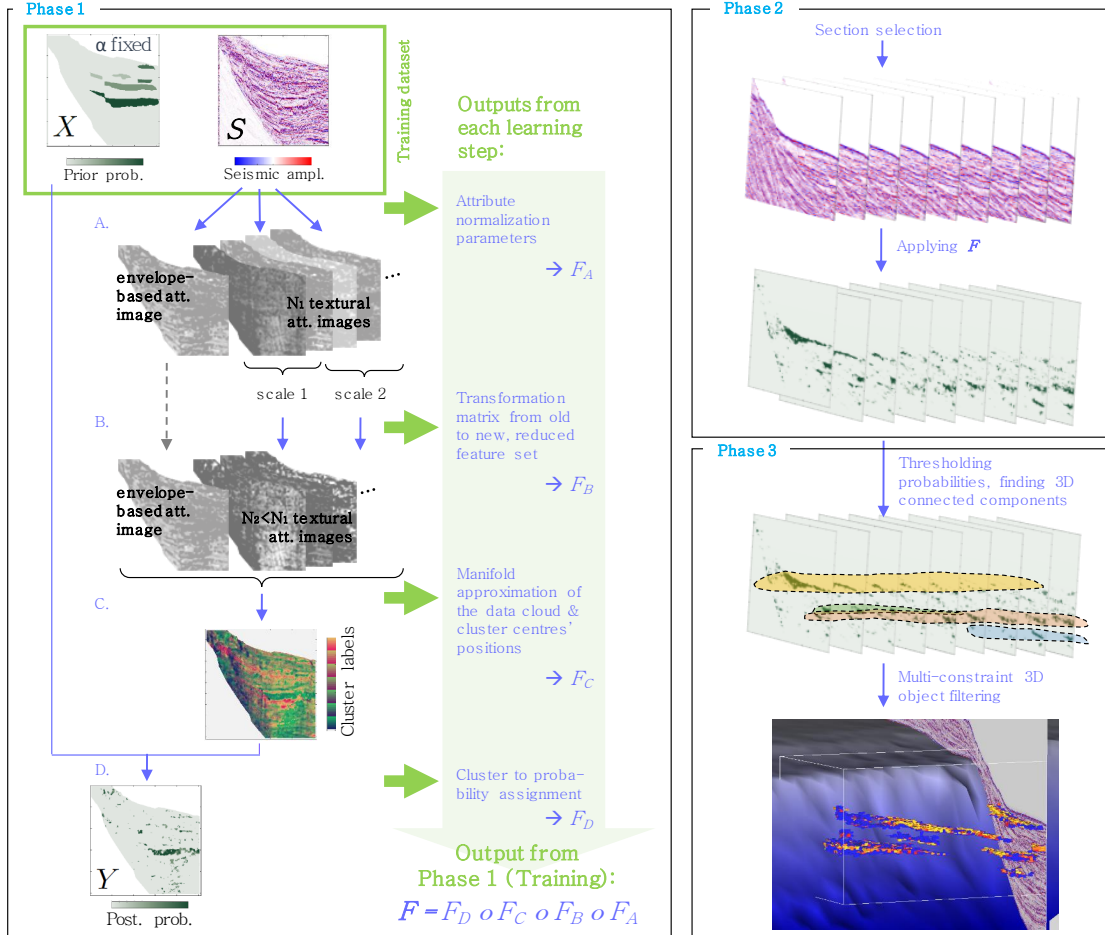


Figure 2: Example-based schematic workflow for automated heterogeneous object detection in seismic data, illustrating Fig. 1. Phases 1, 2, 3 and A., B., C., D. refer to Fig. 1. X and Y are the prior, resp. posterior probability images as defined in Sect. 2.2. In Phase 1, F is created as a composition of four components F_A , F_B , F_C and F_D , which are parameterized resp. through steps A., B., C. and D., so that $F(S) = Y$.

2.1.1 Data representation: attributes choice & computation

The whole seismic dataset consists of amplitude samples organized in a three-dimensional space ((time or depth) * distance * distance), thus also considered as pixels or voxels of a two- or three-dimensional image. One column of this volume is called a seismic “trace”.

Representing the training dataset consists in computing several textural features on all training samples, which extracts relevant information on their seismic facies. Here two-dimension textural features are used.

The statistical two-dimensional Gray-Level Co-occurrence Matrix (GLCM) features initially introduced by Haralick *et al.* (1973) were chosen, for several reasons: (i) they are 2nd-order statistical features, adapted to depict and distinguish textures in an image better than 1st-order features like mean or standard deviation; (ii) they can be reasonably rapidly computed thanks to a computational strategy by Clausi & Zhao (2003), and (iii) they are of common usage and have already proven efficient for seismic interpretation (e.g., West *et al.* 2002, Berthelot *et al.* 2013, Eichkitz *et al.* 2015). A GLCM is computed on a grayscale image which intensity values have been reduced to a discrete number of gray levels, usually 256, 64 or 8. One GLCM is the joint gray level distribution of pairs of pixels/voxels related by a vector with specific norm and direction, respectively accounting for typical scale and orientation of patterns. The “GLCM features” are statistics extracted from this matrix. Here the contrast, correlation, energy and homogeneity features are used (see Appendix 6.1).

A gliding window of 11x11 pixels is chosen for two-dimensional GLCM calculation, with 10-pixel overlap. Two gray levels only are used, i.e. a black-and-white binary image distinguishing positive and negative amplitude values. GLCM computing time essentially depends on the number of gray levels used (Clausi & Zhao, 2003). Using the binary image enables us to use the standard MATLAB built-in GLCM functions without any further computing strategy.

Several vectors are defined to account for spatial relationships in the image with two typical scales: distances of 1 and 2 pixels respectively; and 12 typical orientations: 4 for scale 1, 8 for scale 2 (for an illustration see fig A.1e). For each pixel, 4 GLCMs are computed, each corresponding to one vector, yielding 16 (4×4) features for scale 1 and 32 (8×4) features for scale 2.

To compensate for the loss of the amplitude information due to the data “binarization”, another feature is added, designed from the signal envelope of each seismic trace. The envelope of one trace is the modulus of its discrete-time analytic signal, itself computed from the Hilbert transform of the signal. The two-dimensional envelope sections are filtered via a two-dimension Gaussian kernel with standard deviation $\sigma = 3$ pixels, so that the neighborhood impacting one pixel is approximately the same as the GLCM analysis neighborhood. The feature is then divided by its 95% quantile value – not by its maximum, to avoid outlier effects – to bring it back to an interval close to [0 1].

At this point, a first data representation is completed, comprising: 16 scale-1 GLCM features, 32 scale-2 GLCM features and 1 envelope feature.

2.1.2 Information selection and dimension reduction

To limit the redundancy contained in this 49-dimensional dataset, two different methods of dimension reduction are tested.

First dimension reduction method: feature extraction

The first method is Principal Component Analysis (PCA), a common feature extraction method. PCA is performed separately for scale 1 and scale 2. Principal Components (PCs) to be kept are defined according to a desired variance threshold of 97%, for both scales. This leads to keep N_1 and N_2 PCs as new features for both scales respectively, for all datasets tested. Individual weights of $\frac{1}{N_1}$, resp. $\frac{1}{N_2}$, are applied to PCs of scale 1, resp. scale 2, so that the global weight of each scale is 1. The envelope feature is then added with weight 1 to the final feature set.

Second dimension reduction method: feature selection

The second method is a feature selection method modified from the one of Lu *et al.* (2007). Feature selection methods differ from feature extraction methods (such as PCA) in that the new features were originally in the feature set: they are not combinations of the old features. This enables to (i) analyze which of the original features carry the most information, and (ii) limit further computations to only those selected features.

Unlike most feature selection methods (de Silva & Leong, 2015), here the “best” feature set is not the one that best predicts a targeted classification. The feature selection method of this paper only aims at removing irrelevant, redundant features.

It uses the same principle as in Lu *et al.* (2007), starting by the initial results of PCA. By computing the PCs of the dataset, an orthonormal base of vectors is initially created, in which each feature can be represented. Consequently, each feature can be written as a linear combination of all PCs. PCs to be kept are defined as in the PCA; all feature components collinear to lower-variance PCs are put to zero.

An unsupervised clustering algorithm is then applied to the features (now considered as “points” within the base of the highest-variance PCs), to create clusters of most-correlated features; the number of clusters is pre-defined. Lastly, in each cluster, the feature closest to the cluster centroid (and therefore most-representative of the cluster) is selected. The final feature set is composed of all so selected features, one from each cluster.

The differences between this method and the one in Lu *et al.* (2007) are that: (i) the metric d to compare two features A and B in the PC base is $d(A, B) = 1 - \frac{|A \cdot B|}{\|A\| \|B\|}$. This cosine-similarity-based metric allows for two highly negatively-correlated features to be considered very “similar”, i.e. very redundant. (ii) Given the relatively small total number of features here, the unsupervised clustering algorithm chosen is a hierarchical clustering instead of the k-means algorithm. This leads to test three possible hierarchical representations using single, complete or average linkage (see e.g. Ward 1963), and select the most-representative based on its cophenetic correlation coefficient (Sokal & Rohlf, 1962). Feature sets are selected separately for scales 1 and 2.

Finally, individual weights are applied to selected features so that the global weight of each scale is 1. The envelope feature is then added with weight 1 to the final feature set.

2.1.3 Unsupervised clustering of data samples

The training data as represented in the space of the previously-defined feature set, is then clustered with an unsupervised method. Such a step aims at revealing the variety of facies in the seismic images, i.e. the various groups of points that may occur in the feature-represented dataset. The Generative Topographic Mapping (GTM, Bishop *et al.* 1998) is chosen. GTM represents the data points as mixtures of Gaussians on m reference vectors. The GTM model maps a low-dimensional latent space into a nonlinear manifold of same low dimension, but embedded within the data space, and which optimally fits the data cloud. The reference vectors lie on this manifold; they are thus organized on it according to their similarity (this organization is called “ranking”).

The mapping relies on a set of n_{rbf} radial basis functions. m and n_{rbf} are user-defined parameters.

Each data point can finally be attached to the mode of its probability distribution in the latent space, i.e. to the reference vector with highest probability in the mixture. This yields a clustering of all data points into m clusters, which are considered representative of the various facies of the dataset, even if the term ‘facies’ might refer to a group of clusters - with intra-group variability (e.g., Roy *et al.* 2014). The GTM cluster ranking advantageously preserves similarities between facies.

For one data point, the higher the probability value of the mode, the better the confidence in its cluster assignment by GTM. Here, the median of this value for all points (i.e. all seismic pixels) is used to assess the reliability of the clustering. If higher than 0.5, this median ensures that the assignment of half of the pixels to their cluster was determined with absolute majority among clusters. Note, however, that this indicator controls the performance of the clustering *regarding* the set of input features.

At this stage, the data-driven part of the training is complete: all training samples have a unique cluster label. It is followed by the introduction of external input in a supervised manner.

2.2 Supervised learning of multi-facies object detection on the training set (Fig. 1, Phase 1, D.)

In this section, a mapping is built, from the previously-determined data-driven clustering to probabilities of presence of an object of the targeted kind.

The ground-truth information available with the training dataset consists of images of the same size, where each pixel t has been assigned a prior probability value X_t on the presence of an object, by an interpreter or by any other relevant external computation (see e.g. Fig. 2). The prior values X_t could also result from the integration of other data such as well data, introducing strong-confidence prior information in a small region around the well. In this paper these probabilities have discrete values in $S = \{s_1, s_2, \dots, s_n\} = \{s_k, k \in 1 : n\}$ with $0 = s_1 < s_2 < \dots < s_n = 1$. The method could also be conducted with continuous values, e.g. if the prior probabilities were obtained through an external computation or from other data.

A confidence value $\alpha \in [0, 1]$ ($\alpha = 1$ for a high confidence) is given together with the prior input X ; α characterizes the confidence in X considered as possibly non-entirely-annotated data.

The present supervised step aims at building “modeled images” Y containing for each pixel t a posterior probability value Y_t on the presence of object, that take into account both the data-driven clustering and the prior probabilities X . In this view, a unique posterior probability value y_i will be assigned to every cluster C_i (Le Bouteiller & Charléty, 2018).

This probability y_i should then be representative of the values of X on all points of C_i . If X has the same value s_k for all points of C_i , then $y_i = s_k$. Otherwise, an optimum has to be found for y_i , to minimize the error between X and Y on the points of C_i .

The global error between X and Y is defined as follows:

$$E_{global} = \sum_t f(X_t, Y_t) \quad , \quad (1)$$

where

$$f(X_t, Y_t) = \begin{cases} X_t - Y_t, & X_t - Y_t \geq 0 \\ -\alpha(X_t - Y_t), & X_t - Y_t < 0 \end{cases} \quad ,$$

with $\alpha \in [0, 1]$ introduced with X . If $\alpha < 1$, the f function is asymmetric, which yields a smaller cost for lacks of annotation in the ground truth (false positives) than for parts of the ground truth that are too low in the model (false negatives). Thus, the confidence level α in the prior X determines the asymmetry of the f function.

This error can be minimized cluster by cluster. Writing N_i the number of points in C_i and $p_{k,i} = p(s_k|C_i)$ the proportion of points in C_i whose prior probability value is s_k , the error E_i associated to one cluster C_i is:

$$E_i = N_i \sum_{k \in 1:n} f(s_k, y_i) p_{k,i} \quad ,$$

$$\text{so: } \frac{E_i}{N_i} = \sum_{k \in 1:n, y_i \leq s_k} (s_k - y_i) p_{k,i} + \alpha \sum_{k \in 1:n, y_i > s_k} (y_i - s_k) p_{k,i} \quad .$$

By studying the variations of $\frac{E_i}{N_i}$ with respect to y_i (see Appendix 6.2), the optimal value for y_i , denoted y_i^{opt} , can be derived using the cumulative distribution function of X : $g_i(k) = \sum_{j \in 1:k} p_{j,i}$,

and proceeding as follows:

If $p_{1,i} > \frac{1}{\alpha+1}$, $y_i^{opt} = s_1 = 0$.

If $p_{1,i} \leq \frac{1}{\alpha+1}$, then an intermediate value q is determined:

$$q = \max \left\{ k \in 1 : n \text{ such that } \sum_{j \in 1:k} p_{j,i} \leq \frac{1}{\alpha+1} \right\} \quad .$$

Then:

- if $\sum_{j \in 1:q} p_j = \frac{1}{\alpha+1}$, $y_i^{opt} = s_q$.

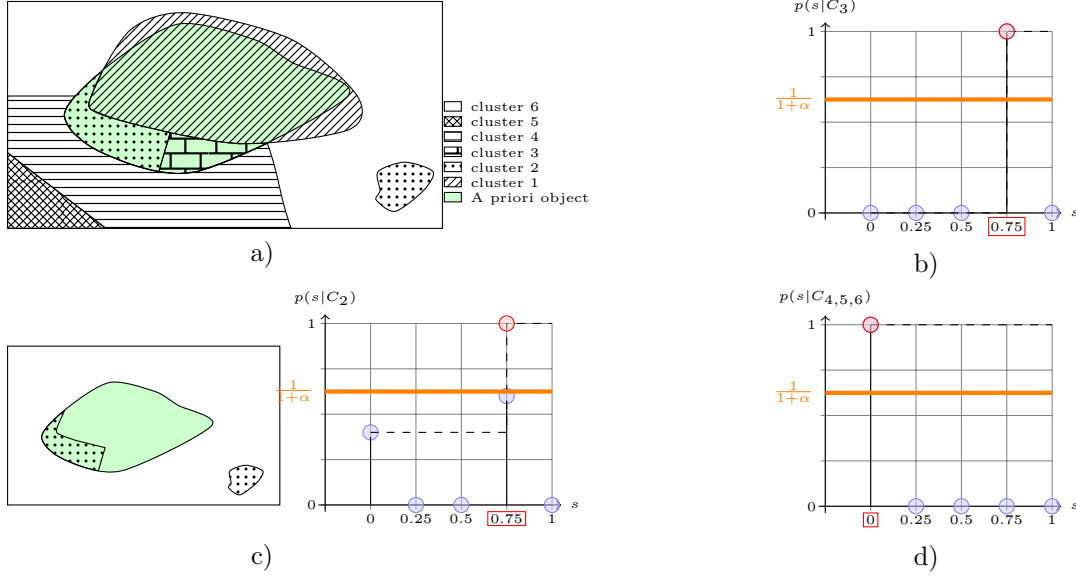


Figure 3: Posterior probability estimation with $\alpha = 0.6$. (a) Schematic image with prior annotation in green: one object with prior probability of 0.75. For (b), (c) and (d), the prior probability density is shown by full black lines and blue circles on top; the cumulative density is shown by dashed lines. (b) Estimation of cluster 3 (C_3) posterior probability: the red point is the first point of the cumulative density function that is superior to $\frac{1}{1+\alpha}$, which determines the posteriori probability as its abscissa: 0.75. (c) Similarly for cluster 2 (C_2). (d) Similarly for clusters 4, 5 and 6, which pixels only have zero-valued prior probabilities: the cumulative density function is superior to $\frac{1}{1+\alpha}$ from 0, which is set as their posterior probabilities. From Le Bouteiller & Charl  ty (2018).

- if $\sum_{j \in 1:q} p_j < \frac{1}{\alpha + 1}$, then:
 - if $q_i = n$, $y_i^{opt} = s_n$;
 - if $q_i < n$, $y_i^{opt} = s_{q+1}$.

A schematic illustration of this step of the method is provided in Fig. 3. Note that, in a continuous case, y_i^{opt} would be the $\frac{1}{\alpha+1}$ quantile of the distribution of $p(s_k|C_i)$.

At this stage, the parameterization (on the training dataset) of an operator F for calculating probabilities on the presence of object on samples of a seismic image is complete. This operator consists in computing attributes, reducing the dimension to the subspace defined in Sect. 2.1.2, applying the GTM model defined in Sect. 2.1.3, and finally attaching to each pixel the posterior probability corresponding to its cluster (see Fig. 1, Phase 1). Applying F on one seismic image yields a probability image, hereafter “modeled image”.

2.3 Testing stage

In addition to a visual qualitative comparison of the modeled training images (posterior probabilities) and their corresponding ground-truth images (prior probabilities), several quantitative indicators are used to check the validity of this model or to compare models created with different parameterizations of F .

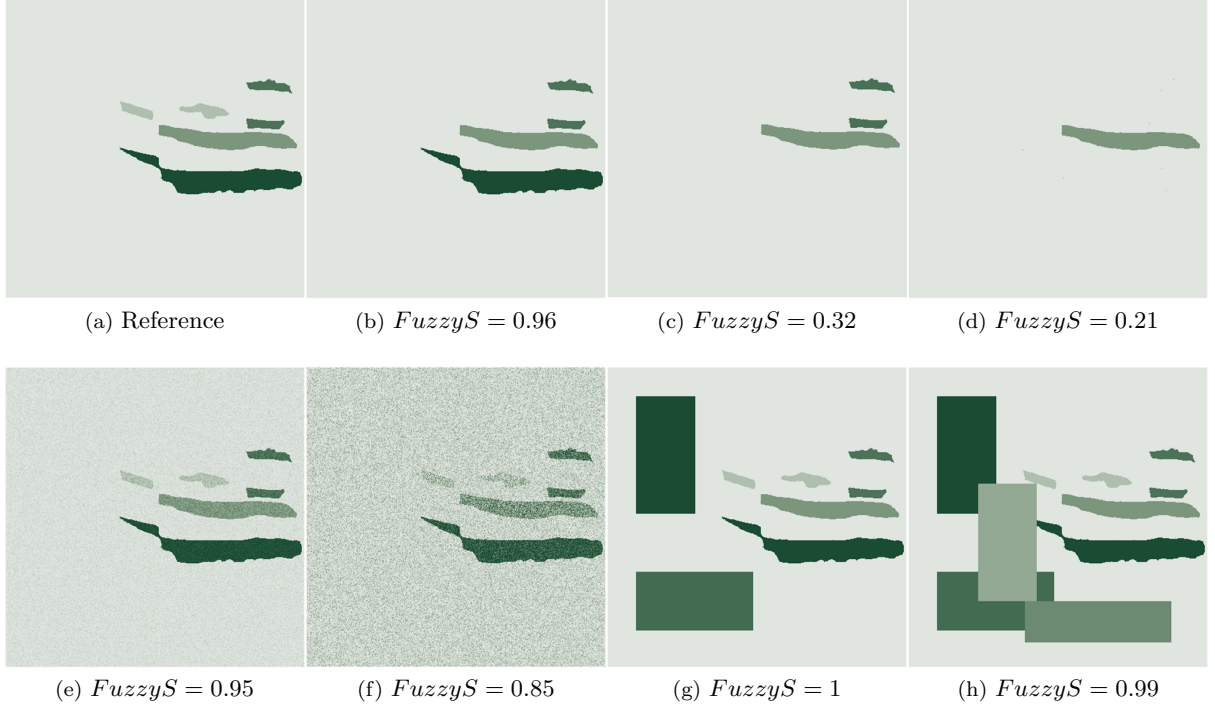


Figure 4: Fuzzy sensitivity ($FuzzyS$) for seven synthetic images ((b) to (h)) as compared to one ground-truth image from the training set (a). FS is lowest when an expected object is totally or partly missing (c,d); it is also low when some noisy pixels inside the detected objects do not have the appropriate value (e,f). It is highest when other objects are detected but not (g) or very little (h) affecting the detection of expected objects.

Sensitivity is an overlap-based metric for comparing two segmentations. For binary segmentations, it represents the proportion of positive pixels of the ground-truth image (GT) that are also positive in the modeled image (“true positives”, TP):

$$Sensitivity = \frac{card(TP)}{card(GT > 0)} \quad .$$

Here, the two segmentations are not binary but probability-valued images. Therefore, a fuzzy formulation of the Sensitivity, $FuzzyS$, is used, as defined in Taha & Hanbury (2015), to compare several results. Fig. 4 shows the typical behavior of $FuzzyS$ values for synthetic images.

The parameterized operator F is then tested on a validation dataset. Two metrics are calculated for both training and validation sets, in order to quantify the suitability of the operator. This is done for different seismic datasets and for the two dimension reduction methods. The Variance Metric (VM) is the average of the per-cluster variance of the prior X , weighted by the number of pixels N_i in each cluster:

$$VM = \frac{\sum_i N_i var(X|C_i)}{\sum_i N_i} \quad .$$

In one cluster C_i , a low variance implies that the step in the cumulative distribution of $p(s_k|C_i)$ is sharper (see Fig. 3), i.e. the computed y_i^{opt} is more representative of the pixels. The Error Metric (EM) is the value of the minimized E_{global} as defined in (1).

For this article, EM is computed for the several tested cases of different α confidence values; VM does not depend on α , as α only affected the cluster probability assignment.

Note that although tests are performed for several α confidence values, α is normally given as an input attached to the ground truth. Here, this comparison enables us to support arguments on the trends of the method in different settings.

2.4 Propagation (Fig. 1, Phase 2)

After parameterization and testing, in Phase 2 the whole seismic cube is used, to “propagate” the trained operator F in the third spatial direction of the cube. A series of sections parallel to the training sections and sampled regularly (1 section over S sections) throughout the cube. The sampling rate $\frac{1}{S}$ is determined according to the dimensions of the targeted multi-facies objects. It limits the precision of the intra-object variations recovered in this third spatial direction. If computing capacities allow, one can choose $S = 1$ (i.e., use all seismic sections).

F is then applied on all the sampled sections.

Concatenating these resulting probability sections then yields the processed version of a three-dimensional “degraded” seismic cube (not actually degraded if $S = 1$).

2.5 3D object processing (Fig. 1, Phase 3)

In Phase 3, considering the three dimensions allows for more constraint on the final detection. In the three-dimensional degraded processed cube, all connected components (CC) of voxel probabilities superior to 0.5 are retrieved. Among these CC, two filters are applied: one thresholding the volume of the CC (in terms of number of voxels) to a minimum value, and one thresholding the orientation of the major axis of the CC (calculated as the major axis of its equivalent ellipsoid). In concrete terms, all voxels of the cube are here tagged with a binary label 1 (“object”) vs. 0 (“non-object”); the applied filters allow to tag voxels of artifacts and non-relevant CC within the degraded cube as “non-objects”, through using very simple external information.

The so processed degraded cube is then upsampled to the original seismic cube format by replicating each section S times.

Finally, a morphological closure (e.g., Soille 2010) is applied on the remaining objects within the cube of binary tags using a spherical structuring element; voxels added in the closure process are kept only if their corresponding probability value is strictly positive.

3 Application on a real case study

This semi-supervised methodology was applied on a real three-dimensional seismic dataset. This Section presents the results of this application.

3.1 Data and training set

A seismic volume in time domain was chosen for the application, containing 512 crosslines, 710 inlines and 512 samples vertically. The inter-trace distance is 25 m in both horizontal directions, and the vertical sampling rate is 4 ms, so that the dimensions of one voxel are 4ms x 25m x 25m, and those of a pixel in a vertical section are 4ms x 25m. Three partially-stacked datasets (near-offset, mid-offset and far-offset datasets) and the full-stack dataset were considered. In a partial stack, each trace is the combination of the seismic signals obtained for a given range of angles of incidence of the input seismic wave (small, medium or large). The full stack combines all of them. All datasets have an average power signal-to-noise ratio between 10 and 11dB, a good-quality value for seismic data.

The targeted objects are mass transport deposits (MTDs), sedimentary bodies resulting from mass wasting along a continental slope (e.g., Shipp *et al.* 2011). They are typically characterized by several facies, including compressive-ridged, transparent, deformed and/or chaotic facies, which typically involve patterns of different sizes, orientations and gray-level intensity (e.g., Alves *et al.* 2014). A set of faults affects the Southern-most region of the cube, where even manual delineation of objects is very uncertain.

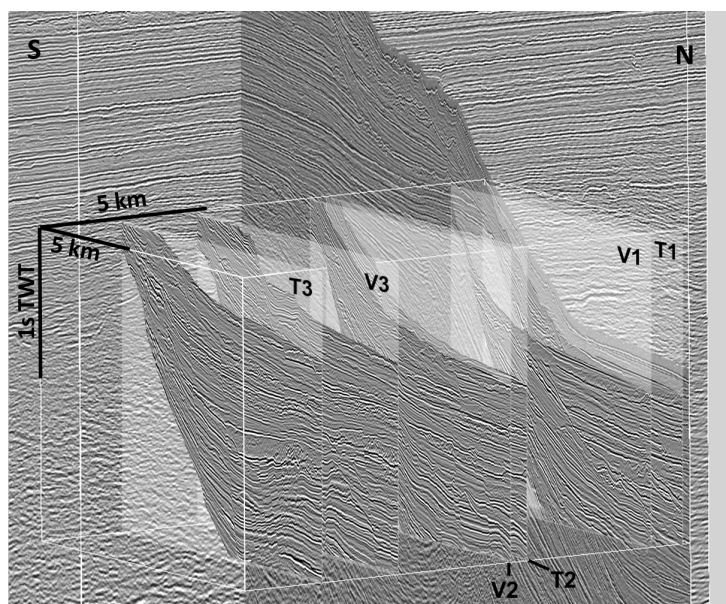
Six seismic sections oriented along the regional principal slope direction were chosen and interpreted manually, yielding one prior probability image for each. These prior probabilities take values in $S = \{s_1 = 0, s_2 = 0.25, s_3 = 0.5, s_4 = 0.75, s_5 = 1\}$. The α value associated with this prior interpretation is 0.8. The six sections were split into three training images (training set) and three validation images (validation set), as shown on Fig. 5.

3.2 Dimension reduction

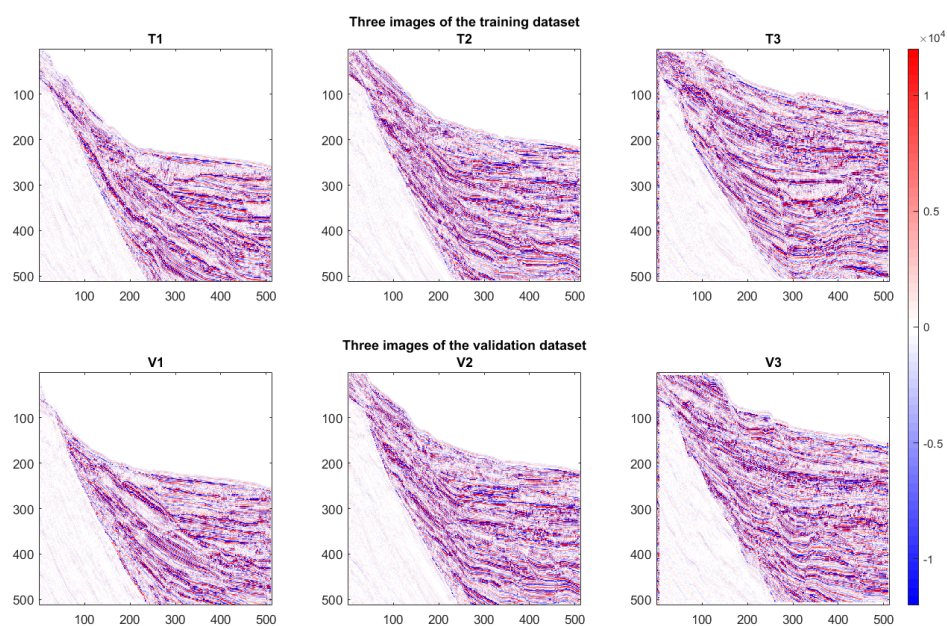
The Principal Component Analysis (PCA) and the Feature Selection (FS) were performed on the training images of the three pre-stack datasets and the full-stack dataset with the initial 16, resp. 32 GLCM attributes, for scale 1, resp. scale 2, separately. In all cases, PCA selected 3 and 6 PCs for both scales respectively.

Concerning FS, as stated in Lu *et al.* (2007), the number of feature clusters (hence, of selected features) should be equal to, or higher than, the number of PCs kept in PCA. Given the 4 main orientations represented by the GLCM attributes in scale 1, 4 clusters were asked in scale 1. The FS selected one feature per orientation, for all datasets except the far-offset dataset. Scale-2 GLCM attributes have 8 possible orientations; 6 clusters only were asked to stay close to the number of PCs. For the full-stack, near-offset and mid-offset datasets, the FS selected one feature per orientation except for 2 of them, keeping mainly oblique orientations rather than strictly horizontal and vertical. For the far-offset dataset, two features of same orientations were selected by FS, so that 3 orientations were actually not represented in the selected feature set.

Fig. A.1 (Appendix 6.3) illustrates the groups of features determined during the FS process.



(a)



(b)

Figure 5: Data used for this study. (a) Global view of the cube with position of the training and validation images; (b) training and validation datasets. Transparent areas correspond to data outside the considered seismic unit (former stratigraphic unit below, sea above). Axes are in pixel numbers.

Median prob	Full-stack	Near-offset	Mid-offset	Far-offset
PCA	0.689	0.762	0.767	0.759
FS	0.875	0.876	0.881	0.889

Table 1: Median values of the GTM mode probabilities of all pixels of the training images, for each of the three pre-stack datasets and the fullstack dataset, for each case of dimension reduction: PCA or FS.

3.3 GTM clustering

The GTM clustering with a two-dimensional latent space, for $n_{rbf} = 4$ radial basis functions and $m = 49$ clusters, was applied on the training images of all four datasets, for each case of dimension reduction: PCA or FS. Table 1 shows the median value of the clustering probabilities of all pixels, which are higher than 0.5 in all cases. This validates the GTM clustering process. Also, note that the FS-based method leads to generally higher maximum probability of the GTM outputs.

3.4 Cluster probability assignment

3.4.1 Global results concerning α : confidence in the prior probabilities

The cluster probability assignment was applied on the results of the GTM clustering for each data stack, each case of dimension reduction (PCA or FS). Confidence values of $\alpha = 0.2, 0.3, 0.4, 0.5, 0.6, 0.7, 0.8, 0.9$ and 1.0 were tested, although the α value actually associated to the ground-truth data is known to be around 0.8 (see 3.1). For increasing α values, probabilities assigned to clusters were lower and lower. The increasing trend of the curves in Fig. 6 according to α illustrates the α weighting in part of the error E_{global} as defined in (1). In both cases (PCA or FS) the maximum error is reached first for the far-offset dataset, corresponding to $y_i^{opt} = 0$ for all clusters C_i (i.e., the modeled images are zero-valued in all pixels). In the FS case this situation is reached even for mid to low confidence in the ground truth.

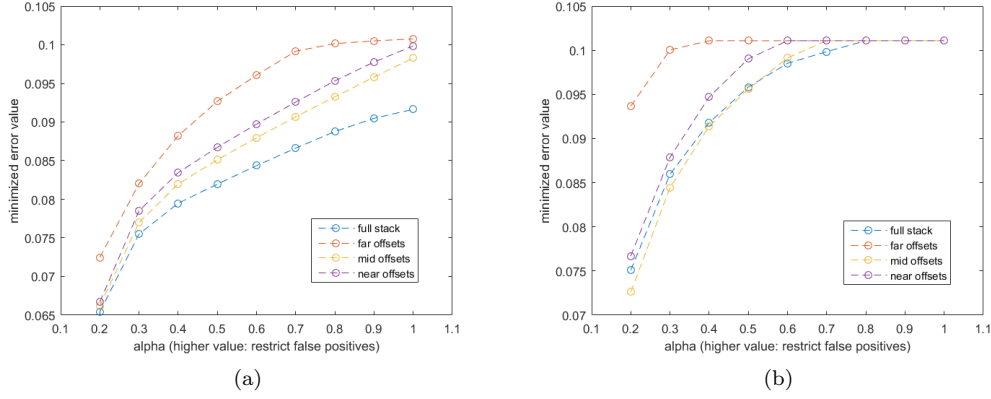
3.4.2 Training data: distance between modeled and ground-truth images

The fuzzy Sensitivity $FuzzyS$ was calculated to compare the modeled images to their corresponding training images of the different datasets, for different α confidence values and for the two dimension reduction methods. Results for $\alpha = 0.2, \alpha = 0.5, \alpha = 0.8$ and $\alpha = 1.0$ are shown in Table 2.

The highest $FuzzyS$ is reached with the PCA dimension reduction in all cases. It is attained on the full-stack dataset for $\alpha = 0.5$ (medium a-priori uncertainty) and on the mid-offset dataset for $\alpha = 0.2, 0.8$ and 1.0 (very high, respectively low a-priori uncertainty). For all α values, the lowest $FuzzyS$ are almost always reached for the far-offset dataset.

3.4.3 Results on the validation set

Results of the application of the method on the validation dataset were analyzed with the Error Metric EM and the Variance Metric VM (Fig. 6c and 6d, Table A.1 in Appendix 6.4). For the purpose of comparison, EM was normalized by the number of pixels in each of the training / validation sets.



α	D.R. method	EM change ($VI - TI$)/ TI
0.2	PCA	0.11
	FS	0.13
0.5	PCA	0.12
	FS	0.06
0.8	PCA	0.06
	FS	0.00
1.0	PCA	0.04
	FS	0.00

(c)

D.R. method	Full-stack		Near-offset		Mid-offset		Far-offset	
	TI	VI	TI	VI	TI	VI	TI	VI
PCA	0.064	0.063	0.067	0.064	0.066	0.063	0.071	0.065
FS	0.071	0.067	0.073	0.066	0.071	0.068	0.079	0.070

(d)

Figure 6: EM and VM results. (a), (b) Minimized error E_{global} (corresponding to EM , see Sect. 2.3) for several α values, for (a) PCA and (b) FS dimension-reduction (D.R.) case; (c) EM relative change from computation on training images (TI) to computations on validation images (VI), averaged over the four datasets (full-stack and far-, mid-, near-offsets); EM values have been normalized by the size of the TI or VI datasets for these results; (d) Variance Metric VM compared between TI and VI , for the four datasets. VM does not depend on α .

α	D.R. method	Full-stack	Near-offset	Mid-offset	Far-offset
0.2	PCA	0.62	0.64	0.64	0.52
	FS	0.57	0.52	0.59	0.40
0.5	PCA	0.31	0.30	0.30	0.25
	FS	0.23	0.21	0.24	0.00
0.8	PCA	0.27	0.27	0.28	0.04
	FS	0.00	0.00	0.00	0.00
1.0	PCA	0.18	0.20	0.27	0.01
	FS	0.00	0.00	0.00	0.00

Table 2: Fuzzy Sensitivity $FuzzyS$ for modeled images built with different data, methods and parameters. For one α value, the highest of $FuzzyS$ is in bold characters. D.R.: dimension reduction.

The change in the EM from training to validation set is always lower than 13%. It is lower for higher α values, implying a better predictability for higher-confidence prior inputs. VM values are all lower for the validation set than for the training set, showing a generally lower variance of intra-cluster prior probabilities in the validation set. This indicates that the parameterization was not over-fitted to the training set.

A visual comparison allowed to check the ground truth and the model for all training and validation images. Fig. 7 illustrates this for the full-stack dataset with $\alpha = 0.8$. With such value for α , the probabilities assigned to all clusters in the FS case were zero (see also Sect. 3.4.1).

3.5 Propagation and three-dimensional object processing results

For the rest of this study, the α value was fixed to 0.8 as given in input and the PCA-based dimension-reduction method was chosen. 72 sections (inlines) were selected out of the 710 sections of the cube, i.e. 1 section every 250 m. This sampling rate is typical of a manual interpretation of sections of a seismic cube. It is sufficiently high compared to the lateral dimensions of the targeted mass-transport deposits, which are a few kms to tens of kms. The operator F was then applied to these 72 sections.

The volume and the orientation of connected components of this processed “degraded” cube were analyzed so as to filter out most non-relevant objects (as presented in Sect. 2.5).

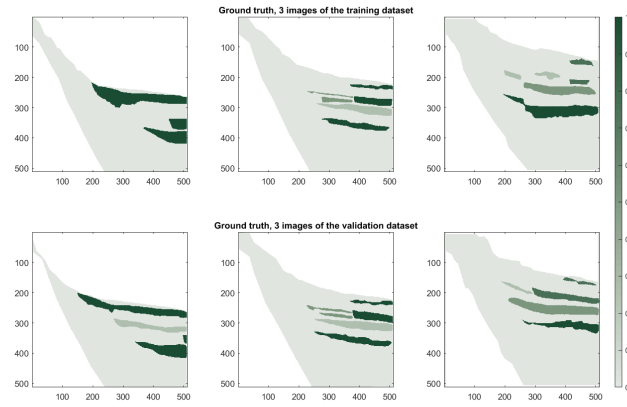
The morphological closure was applied with spherical structuring element on the remaining objects. After testing, a radius of 20 voxels for the spherical structuring element was chosen, to allow to fill the holes within connected components, while avoiding to artificially merge adjacent objects. Only voxels with strictly positive probability value were kept.

For the full-stack dataset, the volume filter allowed to select the 22 largest objects among the connected components (minimum volume: 1030 voxels, i.e. $25750 m^2.s$); the orientation filter left only 15 objects in this selection, among which 2 non-relevant objects remain (see Fig. 8). The largest, expected MTDs were correctly recovered (MTDs A, B, C and E, F, G, H), while the small thickness of MTD D prevented it from being tracked, by even the small-scale GLCM attributes, further than its thickest, most-Southern region, where it appears in 3 distinct parts covering the proximal to distal regions of the cube. On Fig. 8, MTD A, the largest of all, is formed by a dark blue object and a small yellow object due to a fault crossing the MTD separating the two regions. MTD C extends almost through the whole cube, consisting of two blue objects and a small red one. MTDs B, E, F, G, H were retrieved as only one object. Non-relevant objects occur (#1) at the extreme South-East of the cube (pale green object), i.e. in its much disturbed and faulted region, and (#2) in the Western part of the cube (light green object), uphill of MTD H.

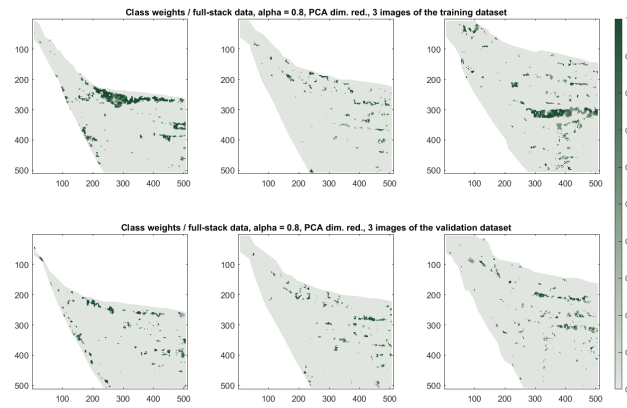
Results for the partial-stack datasets are illustrated on Fig. 9 and detailed as follows:

For the near-offset dataset, all MTDs were recovered, even MTD H. On top of the volume filter (minimum volume: 1900 voxels, i.e. $47500 m^2.s$), the orientation filter allowed to delete all non-relevant objects. The ten remaining objects were either MTDs or significant parts of MTDs.

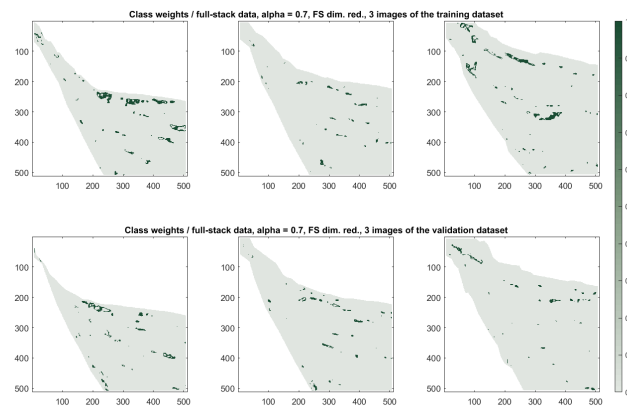
For the mid-offset dataset, all MTDs were recovered, except MTD H. On top of the volume filter (minimum volume: 1200 voxels, i.e. $30000 m^2.s$), the orientation filter allowed to remove the major part of non-relevant objects. Four non-relevant objects remained (#1, #2, #3 and #4 in Fig. 9), in addition to the eleven relevant ones.



(a) Ground truth

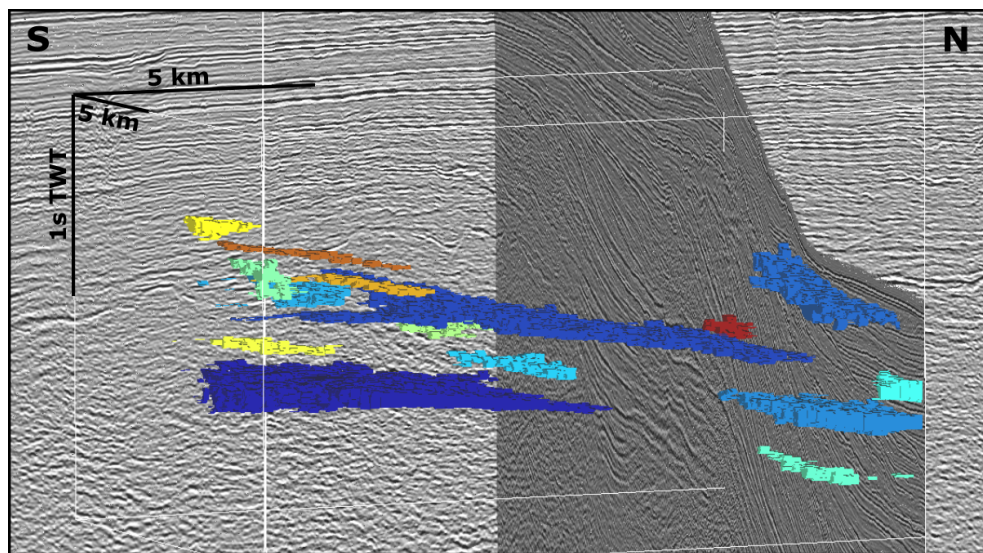


(b) PCA

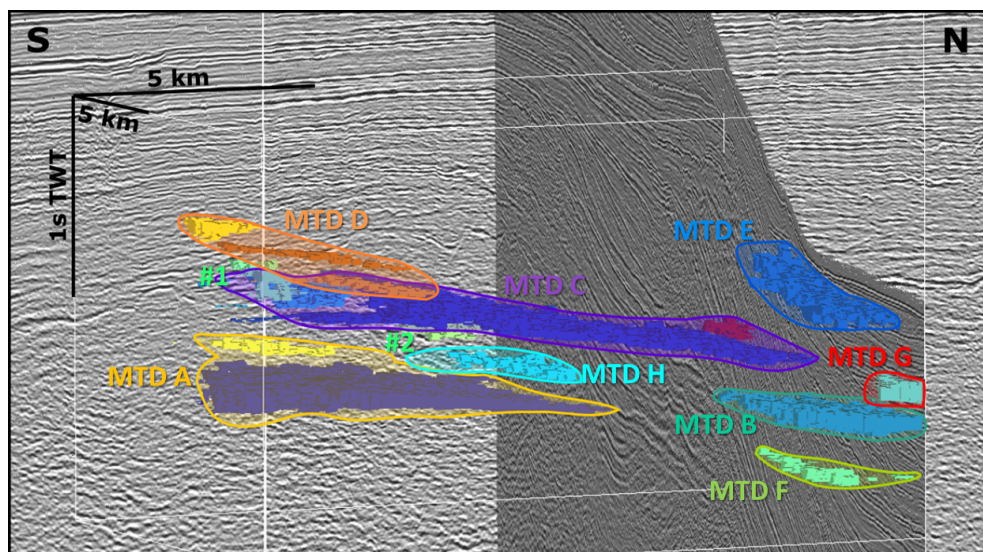


(c) FS

Figure 7: Results of the training and validation phase on the full-stack dataset, for the two dimension reduction methods. (a) Ground truth, with associated confidence value $\alpha = 0.8$; (b) PCA case ; (c) FS case if the confidence value were $\alpha = 0.7$, as for the actual $\alpha = 0.8$ all weights are zero. Transparent areas correspond to data outside the considered seismic unit (former stratigraphic unit below, sea above). Axes are in pixel numbers.

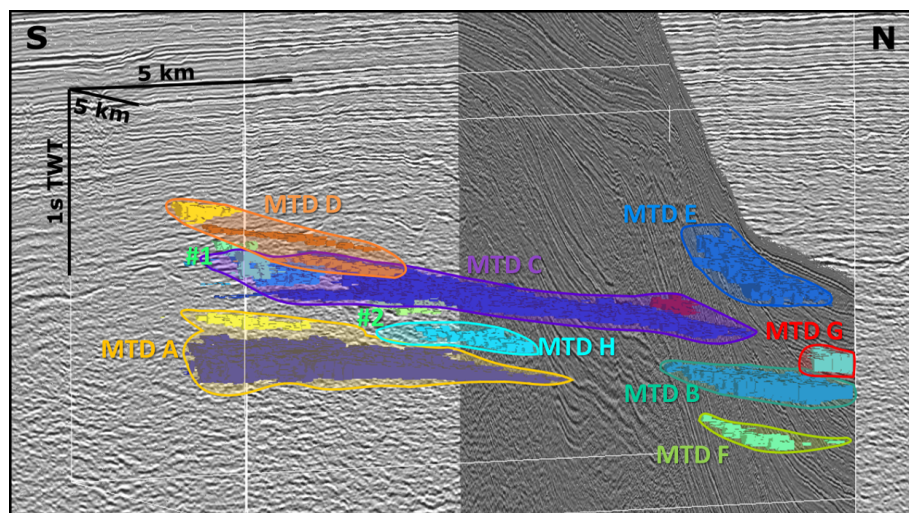


(a)

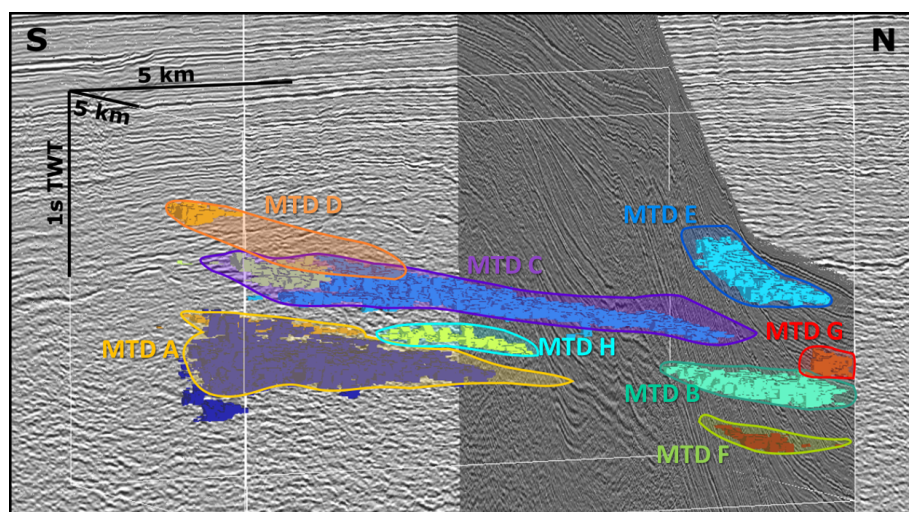


(b)

Figure 8: Results of the application of the method of this study on the full-stack dataset, without (a) and with (b) MTD names.

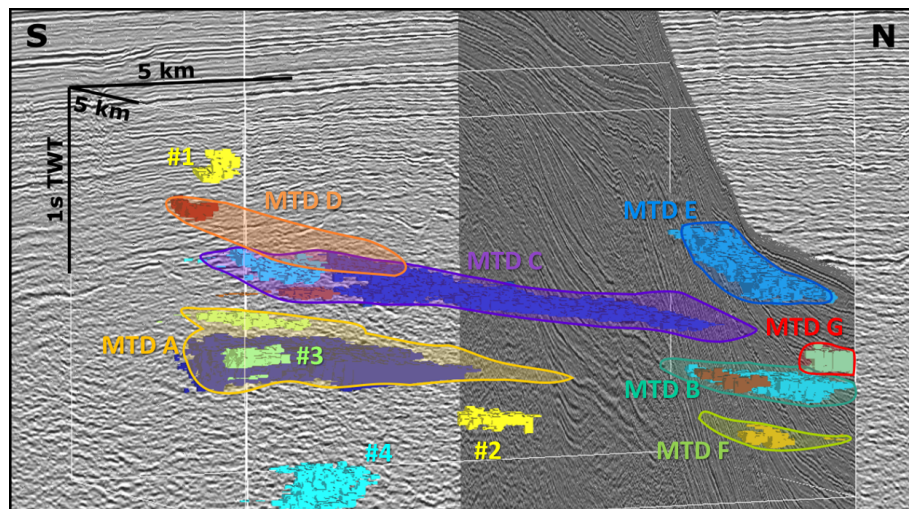


(a)

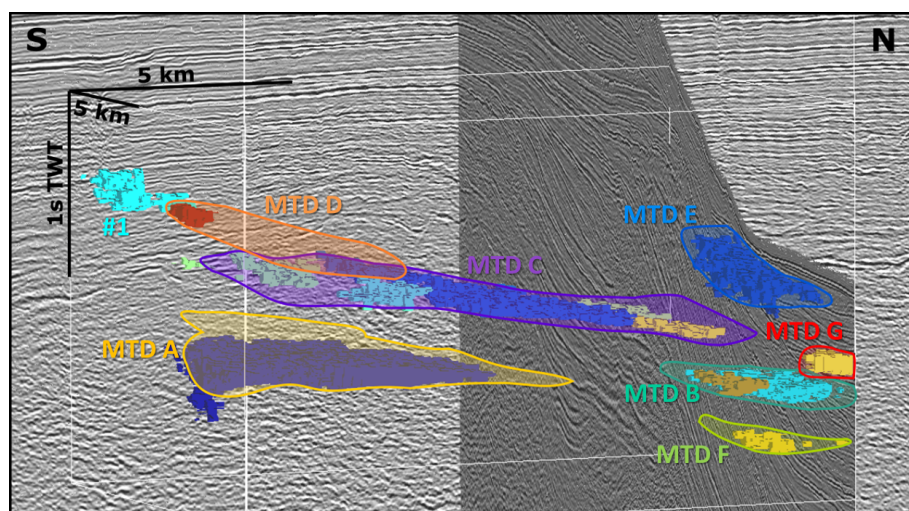


(b)

Figure 9: Results of the application of the method of this study on the (a) full-stack, (b) near-offset, (c) mid-offset and (d) far-offset datasets. Figure continued below.



(c) (cont.)



(d) (cont.)

Figure 9 (cont.)

For the far-offset dataset, all MTDs were recovered, except MTD H. On top of the volume filter (minimum volume: 1050 voxels, i.e. $26250 \text{ m}^2.s$), the orientation filter allowed to remove almost all non-relevant objects. One non-relevant object remained (#1 in Fig. 9), in addition to the twelve relevant ones.

4 Discussion

4.1 Sensitivity analysis to the dimension reduction method, to the a priori confidence and to partial- or full-stack seismic data

4.1.1 GTM output clustering probabilities

The GTM mode probabilities being generally higher in the FS dimension reduction than in the PCA (see Sect. 3.3 and Table 1) shows that the selected features transform the input data cloud into an artificially more “clustered” data cloud, thus having a more discriminative power than the PCA dimension reduction. This is due to the abandonment of some part of information in the FS process, which is more critical than in the PCA process, where the extraction of combinations of features keeps more information - at the expense of more computations. In itself, this discriminative power seems advantageous; however, it appears that final results of the cluster probability assignment are not satisfactory for this FS-based case (see Sect. 4.1.2). This thus suggests that the feature selection over-reduced the global information contained in the dataset, loosing the precision of discrimination between MTD-like facies and others.

4.1.2 Interpretation of the cluster probability assignment

Results of the cluster probability assignment (Sect. 3.4) show a decreasing trend of posterior probabilities assigned to clusters (ending with zero-probability for every cluster) with increasing α values, i.e. with increasing confidence in the prior input. This reveals that generally clusters are not composed of pixels bearing one unique value s_k of prior probability, although the VM low values ensure a low per-cluster dispersion of these prior probabilities (Fig. 6d). When increasing α , the optimization performed by the method of this paper method is more restrictive on “false positives”, so that the calculated y_i^{opt} of one cluster C_i having pixels t both such that $X_t > s_1$ and such that $X_t = s_1$ will be decreased *more* because of the pixels such that $X_t = s_1$. When increasing α , at some extreme point, the optimization error will be minimized when $y_i^{opt} = 0$ for all clusters C_i . This point is reached for lower values of α in the FS dimension reduction case than for PCA (Fig. 6). This severely weakens the usability of the method built with FS.

4.1.3 Differences between the full-stack, far-offset, mid-offset and near-offset datasets

MTD H is only retrieved in the cases of the near-offset dataset and the full-stack dataset. The mid-offset dataset seems best in terms of quality after the cluster probability assignment, when the confidence value α is high. The full-stack dataset seems best or quite good for this when α is low. The far-offset dataset is the worst in terms of quality at the validation stage, and the final detected objects are mostly in parts. This may be related to the initial data representation step: the far-offset FS-selected features being redundant in terms of orientations (see Sect. 3.2) suggests

a lack of representativity of the initial GLCM features for this far-offset dataset. This could be explained by the relatively “shallow” depth of study here, which makes the near- and mid-offset datasets more appropriate (in seismic acquisition, far offsets are typically more appropriate for deeper explorations).

Still, in the far-offset results, only one artifact-object remains, versus four for the mid-offset and two for the full-offset. Overall, objects are detected and their positions are consistent in all cases, which demonstrates the robustness of the method.

4.2 Outlooks for improving the methodology

The methodology proposed in this paper is the succession of steps described in Sect. 2. However, each step may be adapted according to specific preferences; the details used in each step of this paper are one way among others to reach the objective.

In particular, the selection of features for the initial data representation may be different. Here, GLCM textural features have been computed on a binary seismic image; besides, only a two-dimensional texture representation by GLCM was used. Using a three-dimensional textural representation on vertical “thick slices” of the cube (a few adjacent sections) with more gray levels would improve the precision of the facies representations, especially for distinguishing patterns that may be the same on a two-dimension section but with different orientations in a three-dimensional aspect; it would also allow to acquire prior probabilities on sections non-parallel to each other - a constraint that an interpreter may impose if providing manual prior input.

Both using three dimensions and considering more gray levels for GLCM computations are feasible (e.g., Eichkitz *et al.* 2015) but significantly increase the computation time, which can be limiting e.g. for using a precise-enough sampling rate in the propagation phase.

The clustering step could also be modified. In this article, the GTM is used with no external constraint, thus kept as unsupervised as possible. However, if intending to integrate geological knowledge from the start of the method, some spatial constraint could be added within the clustering itself (as proposed in SOM by Zhao *et al.* (2017)), to produce clusters that are both consistent with seismic textures and constrained by stratigraphy.

Future applications may involve other kinds of multi-facies geobodies or regions (e.g., channels or gas chimneys), or regions characterized in seismic data by a certain recognizable set of facies; applications may also use more detailed prior probabilities. The cluster probability assignment (see Sect. 2.2) is actually applicable for a continuous prior, so that external analyses based on another feature of the seismic image, or a feature coming from well-extrapolated properties, could be used as a prior input.

4.3 Benefits of a semi-supervised approach

The key principle of the proposed methodology lies in the combination of the first unsupervised, data-driven step and the second supervised, prior-input-driven step, in the training phase. By combining these two, one ensures (i) not to miss any unseen facies, as can be the case with directly supervised facies classification methods; and (ii) to introduce prior input with some uncertainty information, thus addressing major issues (mentioned e.g. by Nivlet (2007)) on the uncertainty

related to seismic facies classification. The combination of these two steps may be seen as a way to combine two image segmentations: one issued from data-driven classification, the other from object-focused interpretation.

Using the unsupervised clustering on only part of the dataset allows to reduce the associated computation time. For this, the training dataset should be representative of the whole dataset. Balancing computing time and prior information availability determines the choice of the training dataset accordingly.

The GTM unsupervised algorithm also gives an invaluable output: the cluster organization or “ranking”. This information on how similar clusters are to each other comes along with the clustering itself. It may enable one to analyze the internal facies distribution of specific objects, finding that it is characterized by, e.g., three facies of very distinct kind; or, on the contrary, by a set of clusters that are neighbors in the “ranking” (i.e. very similar in terms of seismic facies), suggesting a lower internal variability of the objects.

The three-dimensional object-processing step is, here, left to the user’s responsibility. Here simple filters were applied; they could easily be implemented as an interactive numeric tool in a seismic visualization software. For instance, by moving a cursor corresponding to the size (or orientation) threshold, the user could change the filter result, hence update the visualization of retrieved geobodies. It is expected that, with such an interaction, smaller objects may appear and suggest other interpretations on the very definition of the objects looked for.

5 Conclusion

Automated delineation of heterogeneous geobodies in two-dimensional or three-dimensional seismic data is a challenging task to address. A novel semi-supervised methodology has been proposed for this aim in this article. The heterogeneous seismic signatures of the targeted geobodies can be represented by several textures and not a unique, stable one from an object to the other. To learn the appropriate way of distinguishing the objects from the remaining part of the seismic image, a data-driven analysis is led first, followed by a supervised learning approach, on a training set. The training set includes delineations of the geobodies for a few seismic sections, together with prior uncertainty in the presence of the object. The resulting object delineation thus includes some posterior uncertainty. This approach was tested on partial-stack and full-stack seismic datasets to retrieve multi-facies mass-transport deposits. The difficulty of MTD retrieval lies in their heterogeneous seismic signature. The proposed workflow is shown effective with good and robust results.

Acknowledgements

The authors are grateful to the CGG Houston office for data provision and permission to publish, and to Karine Labat for proof-reading the article.

6 Appendix

6.1 Definition of the GLCM features and the envelope-based feature used for initial data representation (Sect. 2.1.1)

The two-dimensional GLCM contrast, correlation, energy and homogeneity features are defined as follows.

$$\begin{aligned} contrast &= \frac{\sum_{i,j} (i-j)^2 M_{ij}}{(n-1)^2} \\ correlation &= \frac{1}{2} \left(\sum_{i,j} \frac{(i-\mu_i)(j-\mu_j)M_{ij}}{\sigma_i\sigma_j} + 1 \right) \\ energy &= \sum_{i,j} M_{ij}^2 \\ homogeneity &= \sum_{i,j} \frac{M_{ij}}{1+|i-j|} \end{aligned}$$

where M_{ij} is the (i, j) component of the GLCM matrix M computed for a specific vector; sums are done over all pairs of pixels in the image; and n is the number of gray levels used (n^2 is the number of elements in M).

The envelope-based feature f_{env} is computed from the envelope-seismic image S_{env} where every trace has been replaced by its envelope. Denoting $G_{2D}^{\sigma=3}$ the two-dimension Gaussian filtering with standard deviation $\sigma = 3$ pixels, and q_{95} the 0.95 quantile of a set of values, the computation of the envelope-based feature can be resumed to:

$$\begin{aligned} f_{temp} &= G_{2D}^{\sigma=3}(S_{env}) \\ f_{env} &= \frac{f_{temp}}{q_{95}(f_{temp})} \end{aligned}$$

All features are in a range close to $[0 \ 1]$.

6.2 Proof for posterior probability assignment

This section gives a proof for the method presented in Sect. 2.2. Let us recall that here the goal is to minimize the error E_i associated to each cluster C_i , thus obtaining y_i^{opt} , the optimized posterior probability associated to C_i . With N_i the number of points in C_i and $p_{k,i} = p(s_k|C_i)$ the proportion of points in C_i whose prior probability value is s_k :

$$\begin{aligned} E_i &= N_i \sum_{k \in 1:n} f(s_k, y_i) p_{k,i} \quad , \\ \text{so: } \frac{E_i}{N_i} &= \sum_{k \in 1:n, y_i \leq s_k} (s_k - y_i) p_{k,i} + \alpha \sum_{k \in 1:n, y_i > s_k} (y_i - s_k) p_{k,i} \quad . \end{aligned}$$

Let us assume i is fixed, write E in the following for $\frac{E_i}{N_i}$, and omit the i index in the rest of this section. One may now study the variations of E with respect to y in order to find y^{opt} which minimizes E .

6.2.1 Variations of E outside $[0, 1]$

If $y < s_1 = 0$, then: $E(y) = \sum_{k \in 1:n} (s_k - y) p_k$ and every term of this sum decreases when y increases up to s_1 , i.e.: E is a strictly decreasing function of y for $y < s_1$.

If $y > s_n = 1$, then: $E(y) = \alpha \sum_{k \in 1:n} (y - s_k) p_k$ and every term of this sum decreases when y decreases down to s_n , i.e.: E is a strictly increasing function of y for $y > s_n$.

Consequently (as expected), $y^{opt} \in [s_1, s_n] = [0, 1]$.

6.2.2 Variations of E inside $[0, 1]$

Let be $k \in 1 : n - 1$. Let be $y, d > 0$, such that : $s_k \leq y < y + d \leq s_{k+1}$.

$$\begin{aligned}
 \text{Then : } E(y + d) &= \alpha \sum_{j \in 1:k} (y + d - s_j) p_j + \sum_{j \in k+1:n} (s_j - y - d) p_j \\
 &= E(y) + \alpha \sum_{j \in 1:k} d p_j + \sum_{j \in k+1:n} (-d) p_j \\
 &= E(y) + d \left(\alpha \sum_{j \in 1:k} p_j - \sum_{j \in k+1:n} p_j \right) \\
 &= E(y) + d \left(\alpha \sum_{j \in 1:k} p_j - \sum_{j \in k+1:n} p_j - \sum_{j \in 1:k} p_j + \sum_{j \in 1:k} p_j \right)
 \end{aligned}$$

As $\sum_{j \in 1:n} p_j = 1$ (sum of proportions), one can then write ($d > 0$):

$$\frac{E(y + d) - E(y)}{d} = (\alpha + 1) \sum_{j \in 1:k} p_j - 1 \quad .$$

Thus, the variation of E does not depend on y on $[s_k, s_{k+1}]$: E is monotonous on this interval. More precisely:

$$\begin{aligned}
E \text{ is strictly decreasing on } [s_k, s_{k+1}] & \quad \text{if and only if } \sum_{j \in 1:k} p_j < \frac{1}{\alpha + 1} \quad ; \\
E \text{ is strictly increasing on } [s_k, s_{k+1}] & \quad \text{if and only if } \sum_{j \in 1:k} p_j > \frac{1}{\alpha + 1} \quad ; \\
E \text{ is constant on } [s_k, s_{k+1}] & \quad \text{if and only if } \sum_{j \in 1:k} p_j = \frac{1}{\alpha + 1} \quad .
\end{aligned}$$

Different cases according to the distribution of p

If $p_1 > \frac{1}{\alpha+1}$, then E is strictly increasing on $[s_1, s_2]$, so also on $[s_1, s_n]$. E being strictly decreasing for $y < s_1$ (see above), E reaches its minimum on $y^{opt} = s_1$ (i.e. 0).

If $p_1 \leq \frac{1}{\alpha+1}$, then one can define:

$$q = \max \left\{ k \in 1 : n \text{ such that } \sum_{j \in 1:k} p_j \leq \frac{1}{\alpha + 1} \right\} .$$

There are now two cases:

- **Case 1:** $\sum_{j \in 1:q} p_j = \frac{1}{\alpha + 1}$

Here, the sub-case $q = n$ corresponds to the case when $\alpha = 0$. The optimal value will then be $y^{opt} = 1$; note that this value will be for any clustered considered: taking $\alpha = 0$ is not interesting.

In the sub-case $q < n$: E is constant on $[s_q, s_{q+1}]$ and y^{opt} can take any value in $[s_q, s_{q+1}]$. Here it is taken as $y^{opt} = s_q$ (for consistency with the sub-case $q = n$).

- **Case 2:** $\sum_{j \in 1:q} p_j < \frac{1}{\alpha + 1}$

Here, the sub-case $q = n$ corresponds to a function E strictly decreasing on $[s_1, s_n]$; E being strictly increasing for $y > s_n$ (see above), E is minimum for $y^{opt} = s_n = 1$.

In the sub-case $q < n$: E is strictly decreasing on $[s_q, s_{q+1}]$ and strictly increasing on $[s_{q+1}, s_{q+2}]$ (from q 's definition), so E is minimum for $y^{opt} = s_{q+1}$.

6.3 Results of the dimension reduction

Fig. A.1 shows the results of the FS dimension reduction and its relationship with the Principal Components space, as explained in Sect. 3.2.

The alignment of features of a same cluster along a line crossing the origin of the graph confirms that the clusters were formed according to the positive and negative correlations of features. It also ensures that at least one feature was selected among each group of correlated features.

For scale 1, there were 4 possible orientations; one feature per orientation was selected for all datasets except the far-offset dataset.

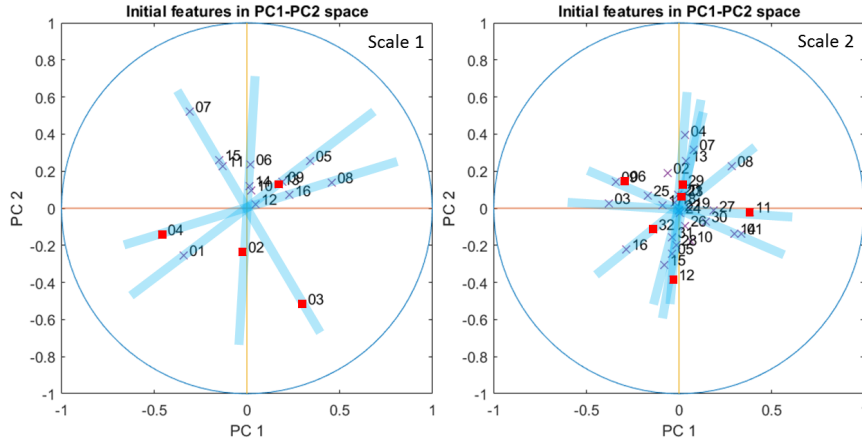
For scale 2, there were 8 possible orientations. For the full-stack and near-offset datasets, one feature per typical orientation was selected, except for orientations $[0, 2]$ and $[2, 0]$; similarly for the mid-offset dataset, orientations $[0, 2]$ and $[2, 1]$ were not selected. For the far-offset dataset, two features of same orientation were selected, so that three orientations were not represented in the selected feature set: $[2, 0]$, $[2, 2]$ and $[1, -2]$.

6.4 Detailed results on EM

Results presented in Table A.1 are a detailed support for Fig. 6c.

α	D.R. method	Full-stack		Near-offset		Mid-offset		Far-offset		Mean $(VI - TI)/TI$
		TI	VI	TI	VI	TI	VI	TI	VI	
0.2	PCA	0.647	0.725	0.660	0.746	0.655	0.731	0.717	0.774	0.112
	FS	0.743	0.823	0.759	0.836	0.718	0.878	0.927	0.991	0.125
0.5	PCA	0.811	0.937	0.858	0.939	0.842	0.944	0.917	1.018	0.120
	FS	0.948	1.033	0.980	0.975	0.946	1.108	1.0	1.0	0.064
0.8	PCA	0.878	0.983	0.943	0.996	0.923	1.003	0.991	0.985	0.064
	FS	1.000	1.000	1.000	1.000	1.000	1.000	1.000	1.000	0.000
1.0	PCA	0.907	1.006	0.988	1.024	0.972	0.992	0.997	0.992	0.041
	FS	1.000	1.000	1.000	1.000	1.000	1.000	1.000	1.000	0.000

Table A.1: Error Metric EM compared between training images (TI) and validation images (VI), for several datasets, dimension-reduction (D.R.) methods and α values. Values have been normalized by the total mass of probability distribution on the “ground truth” images, so that VI and TI values are comparable.



(a)

Selected features	Scale 1	Scale 2
Full-stack dataset	2,4,3,13	6,23,29,32,11,12
Near-offset dataset	4,2,3,1	6,23,29,8,11,12
Mid-offset dataset	2,16,3,1	2,23,5,8,11,12
Far-offset dataset	15,4,12,13	30,5,4,9,23,7

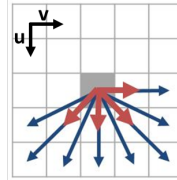
(b)

Scale 1 vectors $[u, v]$	$[0, 1]$	$[1, 0]$	$[1, 1]$	$[1, -1]$
Contrast	1	2	3	4
Correlation	5	6	7	8
Energy	9	10	11	12
Homogeneity	13	14	15	16

(c)

Scale 2 vectors $[u, v]$	$[0, 2]$	$[2, 0]$	$[2, 2]$	$[2, -2]$	$[1, 2]$	$[2, 1]$	$[2, -1]$	$[1, -2]$
Contrast	1	2	3	4	5	6	7	8
Correlation	9	10	11	12	13	14	15	16
Energy	17	18	19	20	21	22	23	24
Homogeneity	25	26	27	28	29	30	31	32

(d)



(e)

Figure A.1: GLCM Feature Selection. (a) Case of the full-stack training dataset: GLCM features (blue X; (c) and (d) give the legend of the numbered labels) in the first PCs space. Blue thick lines show the groups of features created by the Feature Selection method of this study, with representative feature of each group in red; (b) Representative features selected in each scale for each dataset; (c) Legend for feature numbers of scale 1; (d) Legend for feature numbers of scale 2; (e) Legend for orientation of GLCM vectors.

References

- Alves, Tiago M., Kurtev, Kuncho, Moore, Gregory F., & Strasser, Michael. 2014. Assessing the internal character, reservoir potential, and seal competence of mass-transport deposits using seismic texture: A geophysical and petrophysical approach. *AAPG Bulletin*, **98**(4), 793–824.
- Berthelot, Angélique, Solberg, Anne H.S., & Gelius, Leiv-J. 2013. Texture attributes for detection of salt. *Journal of Applied Geophysics*, **88**, 52–69.
- Bishop, Christopher M., Svensén, Markus, & Williams, Christopher K. I. 1998. GTM: The Generative Topographic Mapping. *Neural Computation*, **10**(1), 215–234.
- Chopra, Satinder, & Marfurt, Kurt J. 2014. Seismic facies analysis using generative topographic mapping. *Pages 1390–1394 of: Birkelo, Brad (ed), SEG Technical Program Expanded Abstracts 2014*.
- Clausi, David A., & Zhao, Yongping. 2003. Grey level co-occurrence integrated algorithm (GL-CIA): A superior computational method to rapidly determine co-occurrence probability texture features. *Computers & Geosciences*, **29**(7), 837–850.
- de Matos, Marcilio Castro, Osorio, Paulo Léo, & Johann, Paulo Roberto. 2007. Unsupervised seismic facies analysis using wavelet transform and self-organizing maps. *GEOPHYSICS*, **72**(1), P9–P21.
- de Silva, Anthony Mihirana, & Leong, Philip H. W. 2015. Feature Selection. *Pages 13–24 of: de Silva, Anthony Mihirana, & Leong, Philip H. W. (eds), Grammar-Based Feature Generation for Time-Series Prediction*. SpringerBriefs in Applied Sciences and Technology. Singapore: Springer Singapore.
- Eichkitz, Christoph Georg, Davies, John, Amtmann, Johannes, Schreilechner, Marcellus Gregor, & de Groot, Paul. 2015. Grey level co-occurrence matrix and its application to seismic data. *First Break*, **33**, 71–77.
- Gao, Dengliang. 2008. Application of seismic texture model regression to seismic facies characterization and interpretation. *The Leading Edge*, **27**(3), 394–397.
- Haralick, Robert M., Shanmugam, K., & Dinstein, Its'Hak. 1973. Textural Features for Image Classification. *IEEE Transactions on Systems, Man, and Cybernetics*, **3**(6), 610–621.
- Hashemi, H., de Beukelaar, P., Beiranvand, B., & Seiedali, M. 2017. Clustering Seismic Datasets for Optimized Facies Analysis Using a SSCSOM Technique. *In: 79th EAGE Conference and Exhibition 2017*. Proceedings. EAGE Publications BVNetherlands.
- Kohonen, Teuvo. 1986. *Learning Vector Quantization for Pattern Recognition: Technical Report TKK-F- A601*. Helsinki University of Technology.
- Le Bouteiller, Pauline, & Charléty, Jean. 2018. *Procédé pour la détection d'objets géologiques dans une image sismique (Patent pending)*.
- Long, Zhiling, Alaudah, Yazeed, Qureshi, Muhammad Ali, Farraj, Motaz Al, Wang, Zhen, Amin, Asjad, Deriche, Mohamed, & AlRegib, Ghassan. 2015. Characterization of migrated seismic volumes using texture attributes: a comparative study. *Pages 1744–1748 of: Schneider, Robert Vincent (ed), SEG Technical Program Expanded Abstracts 2015*.
- Lu, Yijuan, Cohen, Ira, Zhou, Xiang Sean, & Tian, Qi. 2007. Feature selection using principal feature analysis. *Page 301 of: Lienhart, Rainer, Prasad, Anand R., Hanjalic, Alan, Choi, Sunghyun, Bailey, Brian, & Sebe, Nicu (eds), the 15th international conference*.
- Marroquín, Iván Dimitri, Brault, Jean-Jules, & Hart, Bruce S. 2009. A visual data-mining methodology for seismic facies analysis: Part 1 — Testing and comparison with other unsupervised clustering methods. *GEOPHYSICS*, **74**(1), P1–P11.

- Nivlet, P. 2007. Uncertainties in Seismic Facies Analysis for Reservoir Characterisation or Monitoring: Causes and Consequences. *Oil & Gas Science and Technology - Revue de l'IFP*, **62**(2), 225–235.
- Ogiesoba, Osareni, & Hammes, Ursula. 2012. Seismic interpretation of mass-transport deposits within the upper Oligocene Frio Formation, south Texas Gulf Coast. *AAPG Bulletin*, **96**(5), 845–868.
- Pitas, I., & Kotropoulos, C. 1992. A texture-based approach to the segmentation of seismic images. *Pattern Recognition*, **25**(9), 929–945.
- Qi, Jie, Lin, Tengfei, Zhao, Tao, Li, Fangyu, & Marfurt, Kurt. 2016. Semisupervised multiattribute seismic facies analysis. *Interpretation*, **4**(1), SB91–SB106.
- Roy, Atish, Romero-Peláez, Araceli S., Kwiatkowski, Tim J., & Marfurt, Kurt J. 2014. Generative topographic mapping for seismic facies estimation of a carbonate wash, Veracruz Basin, southern Mexico. *Interpretation*, **2**(1), SA31–SA47.
- Shafiq, Muhammad A., Wang, Zhen, Amin, Asjad, Hegazy, Tamir, Deriche, Mohamed, & AlRegib, Ghassan. 2015. Detection of Salt-dome Boundary Surfaces in Migrated Seismic Volumes Using Gradient of Textures. *Pages 1811–1815 of: Schneider, Robert Vincent (ed), SEG Technical Program Expanded Abstracts 2015*.
- Shipp, R. Craig, Weimer, Paul, & Posamentier, Henry W. (eds). 2011. *Mass-Transport Deposits in Deepwater Settings*. SEPM (Society for Sedimentary Geology).
- Soille, Pierre. 2010. *Morphological image analysis: Principles and applications*. 2. ed., corr. 2. print edn. Berlin and Heidelberg: Springer.
- Sokal, Robert R., & Rohlf, F. James. 1962. The Comparison of Dendrograms by Objective Methods. *Taxon*, **11**(2), 33.
- Taha, Abdel Aziz, & Hanbury, Allan. 2015. Metrics for evaluating 3D medical image segmentation: analysis, selection, and tool. *BMC medical imaging*, **15**, 29.
- Wang, Shangxu, Yuan, Sanyi, Yan, Binpeng, He, Yanxiao, & Sun, Wenju. 2016. Directional complex-valued coherence attributes for discontinuous edge detection. *Journal of Applied Geophysics*.
- Wang, Zhen, Hegazy, Tamir, Long, Zhiling, & AlRegib, Ghassan. 2015. Noise-robust detection and tracking of salt domes in postmigrated volumes using texture, tensors, and subspace learning. *GEOPHYSICS*, **80**(6), WD101–WD116.
- Ward, Joe H. 1963. Hierarchical Grouping to Optimize an Objective Function. *Journal of the American Statistical Association*, **58**(301), 236–244.
- West, Brian P., May, Steve R., Eastwood, John E., & Rossen, Christine. 2002. Interactive seismic facies classification using textural attributes and neural networks. *The Leading Edge*, **21**(10), 1042–1049.
- Zhao, Tao, Zhang, Jing, Li, Fangyu, & Marfurt, Kurt J. 2016. Characterizing a turbidite system in Canterbury Basin, New Zealand, using seismic attributes and distance-preserving self-organizing maps. *Interpretation*, **4**(1), SB79–SB89.
- Zhao, Tao, Li, Fangyu, & Marfurt, Kurt J. 2017. Constraining self-organizing map facies analysis with stratigraphy: An approach to increase the credibility in automatic seismic facies classification. *Interpretation*, **5**(2), T163–T171.

2.4 Discussion

As stated in the article, the developed method allows to recover several multi-facies objects from seismic data, by mixing data-driven and prior information. Figure 2.10 provides a global view of the workflow used for this identification. The workflow starts from the acquisition of training and validation datasets. The training consists in two main steps: unsupervised representation of the training dataset and supervised learning of posterior probabilities. This training phase corresponds to Phase 1 in Fig. 1 of the article presented before. It is followed by propagation, i.e. apply the trained representation and probability assignment to other parts of the dataset. Finally, 3D post-processing is added to select and retrieve the most appropriate objects corresponding to MTDs. The inputs that are

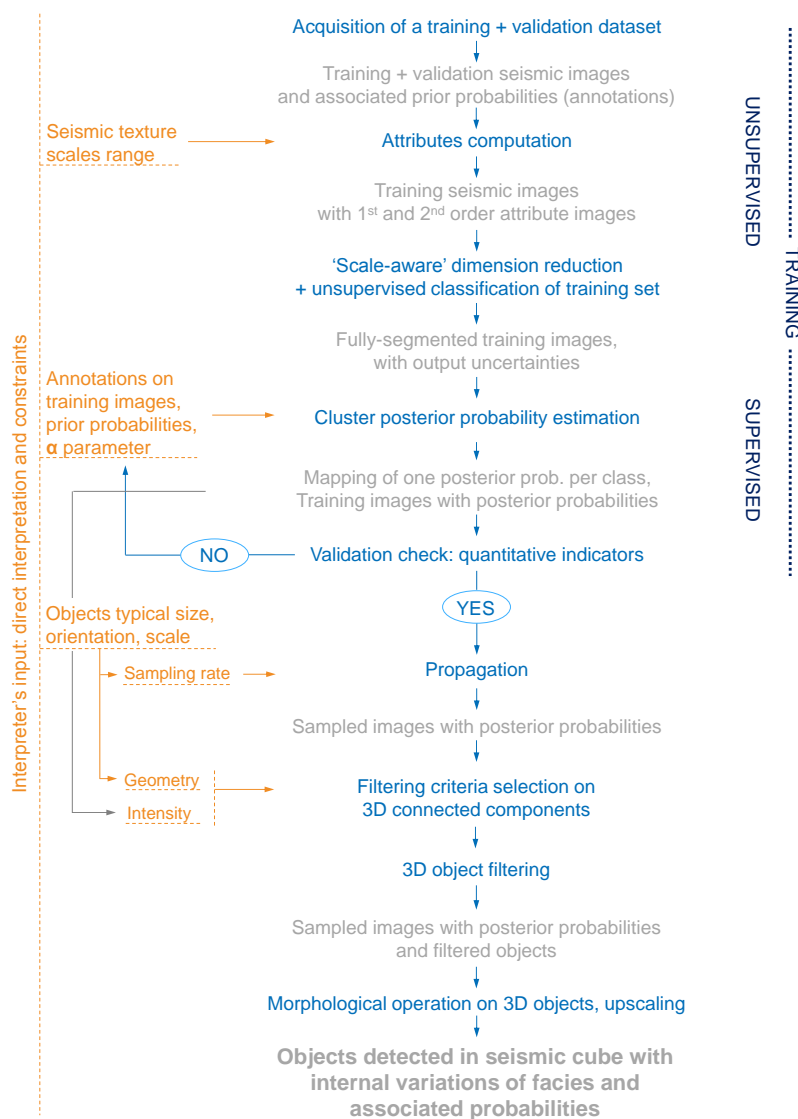


Figure 2.10: Proposed workflow for MTD identification in seismic data.

given by the interpreter at the several steps of the methodology are displayed on the left column of Figure 2.10.

In this section, further analyses are provided, in order to put in perspective this contribution regarding the first objective of the PhD. The first section concerns the way we have handled seismic data. The second section enhances the different ways that MTDs are depicted as well as their common points, in the four different seismic stacks. Then, we examine the variability of the objects we detect. And finally, we compare our approach to existing approaches. Note that a side discussion on the choice of the metrics we used in the article for the validation step is given in Appendix B.

2.4.1 Handling seismic data: balancing computer power constraints and orientation representativity

The methodology we have developed dealt with 2D sections extracted from a 3D seismic block, and then used the third dimension during the propagation and post-processing stage. Using 2D sections first essentially limits the quality of the textural facies that are recovered by the attributes and the clustering. As physical sediment structures are 3D, computing 3D-textural attributes would be more relevant. Two main reasons led us to use 2D sections only:

- (i) Getting access to some prior delineations from a seismic interpreter was eased by the fact that seismic manual interpretation is done on 2D views or random lines.
- (ii) Computing 3D-textural attributes requires an extended computation time (for GLCM attributes, the computation time then grows as n^3 instead of n^2 - Clausi & Zhao (2003)).

The choice of using 2D sections was thus helpful for building and testing the methodology. In future developments and applications, 3D data would yield attributes more representative of sediment structures.

One option that would allow point (i) (but not point (ii)) would be to consider 'slices' of the seismic cube instead of 2D sections, i.e. a series of e.g. 10 adjacent sections, that would have to be interpreted a priori by the interpreter. In this case he/she could use the central section of the series as a usual 2D view for interpretation. However, this option still requires 3D computations, which can be long especially during the propagation stage. For our methodology to be applied as in our case study (i.e. with 2D sections), it is needed to consider parallel sections, that have to be oriented so that an interpreter may provide the prior delineations: in our case, dip-aligned sections allow to spot several mass-transport-related facies such as compression ridges, deformations of strata etc.

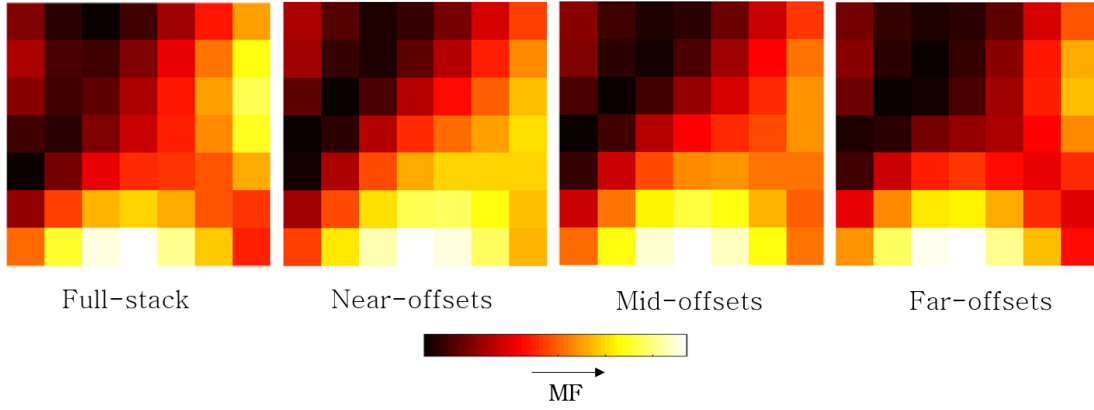


Figure 2.11: Qualitative comparison of the Magnification Factor (MF) maps resulting from GTM mappings on our four seismic datasets: full-stack, near-, mid- and far-offsets.

2.4.2 MTD depiction in the four studied datasets

We have applied our methodology to four different seismic stacks of a same cube. Their content differs due to different seismic processing applied after acquisition; we take advantage of them to analyze the response of the methodology for slightly different input data, where the difference is due to seismic processing. For each cube, the workflow went from a seismic section, through an unsupervised representation, to learnt probabilities on MTD occurrence in the seismic image.

Four different GTM-based manifolds have been created and, together with the supervised step, the four manifolds allow to distinguish MTDs in their respective datasets. Their respective Magnification Factor (MF) maps are presented on Figure 2.11 for qualitative comparison. They show similar trends of the shape of the generated manifold in the four cases. Lighter regions correspond to high values of MF, i.e. regions where the manifold is relatively more stretched (details on MF are given in Appendix A.4). Thus, we can derive that, although optimized to fit four different data clouds, the variations between clusters within each of the four manifolds are similar.

By studying the posterior probabilities associated to clusters, we can observe which regions of the manifold have been assigned positive probabilities; Figure 2.12 displays these probabilities, projected on the grid of 49 clusters, for the four datasets used, and for two cases: $\alpha = 0.3$ and $\alpha = 0.8$. As defined in the article, $\alpha = 0.3$ corresponds to a low confidence in the prior input of the training dataset; the emergence of high probabilities away from the initially delineated MTDs is not much limited. By contrast, $\alpha = 0.8$ corresponds to a high confidence in this prior input, more restrictive on the emergence of unexpected high probabilities.

We observe that, from the first case (Figure 2.12a) to the second case (Figure 2.12b), fewer clusters are highlighted with positive probabilities. This illustrates the point given before.

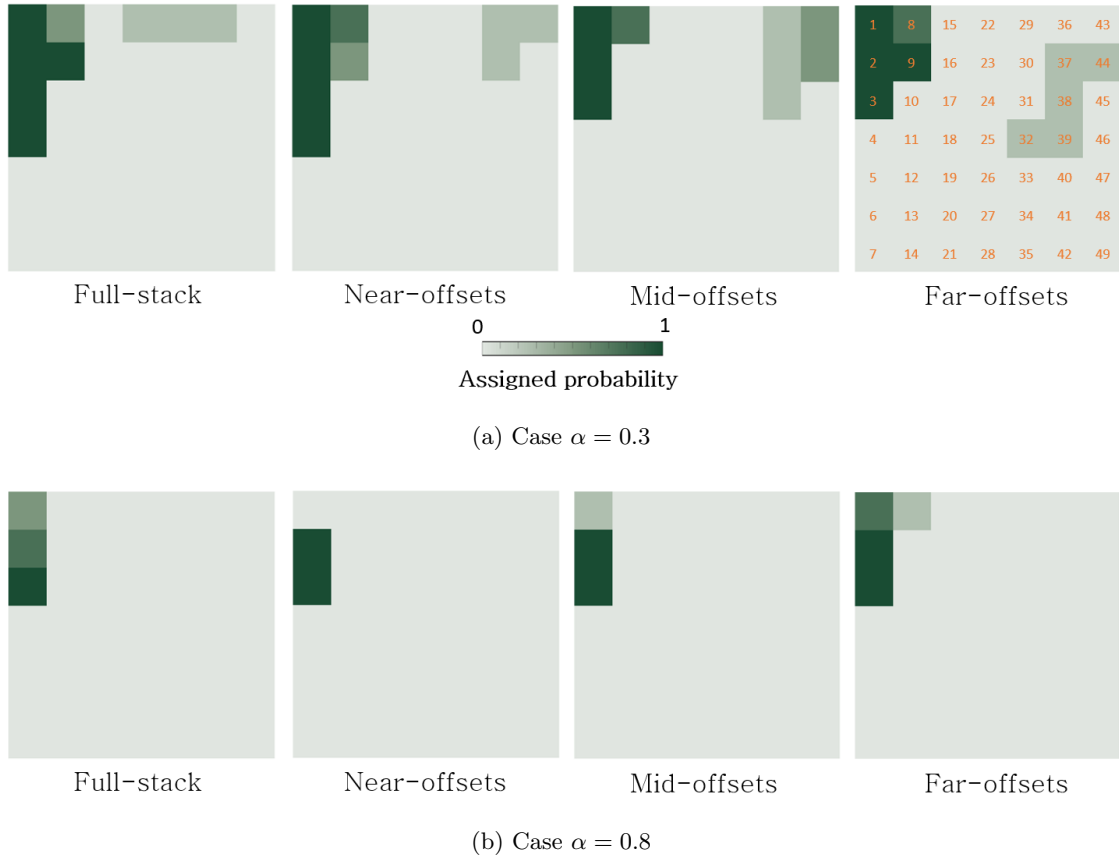


Figure 2.12: Computed probabilities on MTD representativeness for the 49 clusters of the GTM-built manifold in each case of the four seismic datasets: full-stack, near-, mid- and far-offsets. Cases where $\alpha = 0.3$ or 0.8 correspond to low or high confidence in the prior annotations, respectively. False positives are less permitted for $\alpha = 0.8$ than for $\alpha = 0.3$. GTM cluster labels (numbers from 1 to 49) are displayed only once for simplicity.

One may also note that the clusters with positive probabilities are in the same regions of the manifold for the four datasets: highest probabilities in the top-left region (clusters $\sim 1, 2, 3, 8, 9$), lower in the top-right region for $\alpha = 0.3$ (clusters $\sim 36, 37, 38, 43, 44$). Together with the similar trend of their MF maps, this shows that the manifolds created for each of the four datasets have similar “rankings”, or topographic orderings. This element is worth noting, as it suggests that the unsupervised representation scheme we have built (textural representation and unsupervised clustering), and applied to all four datasets, is relatively robust to their dissimilarities in the data space.

In Figure 2.13, one section extracted from the cube is shown for the four datasets, together with the probabilities associated to each pixel. Case $\alpha = 0.8$ is presented. From Figures 2.12b and 2.13, we observe several things:

- In the near-offset dataset, posterior probabilities are binary, i.e. clusters are assigned either 1 or 0;

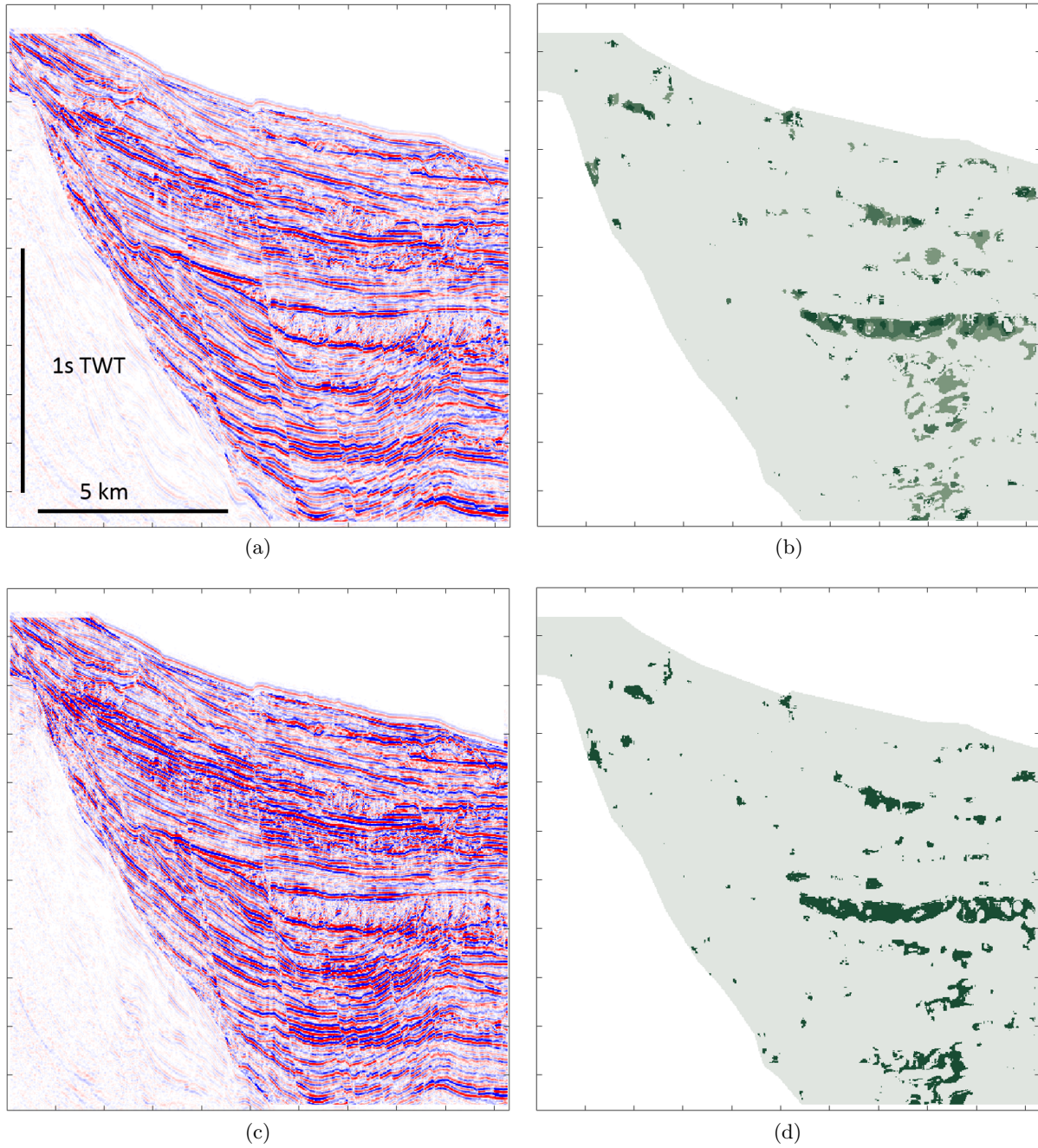


Figure 2.13: Posterior probabilities on one inline of the seismic cube used in our study, for the four datasets. Left: seismic section; Right: posterior probabilities on all pixels of the section. (a), (b) Full-stack section. (c), (d) Near-offset section. (e), (f) Mid-offset section. (g), (h) Far-offset section. Figure continued below.

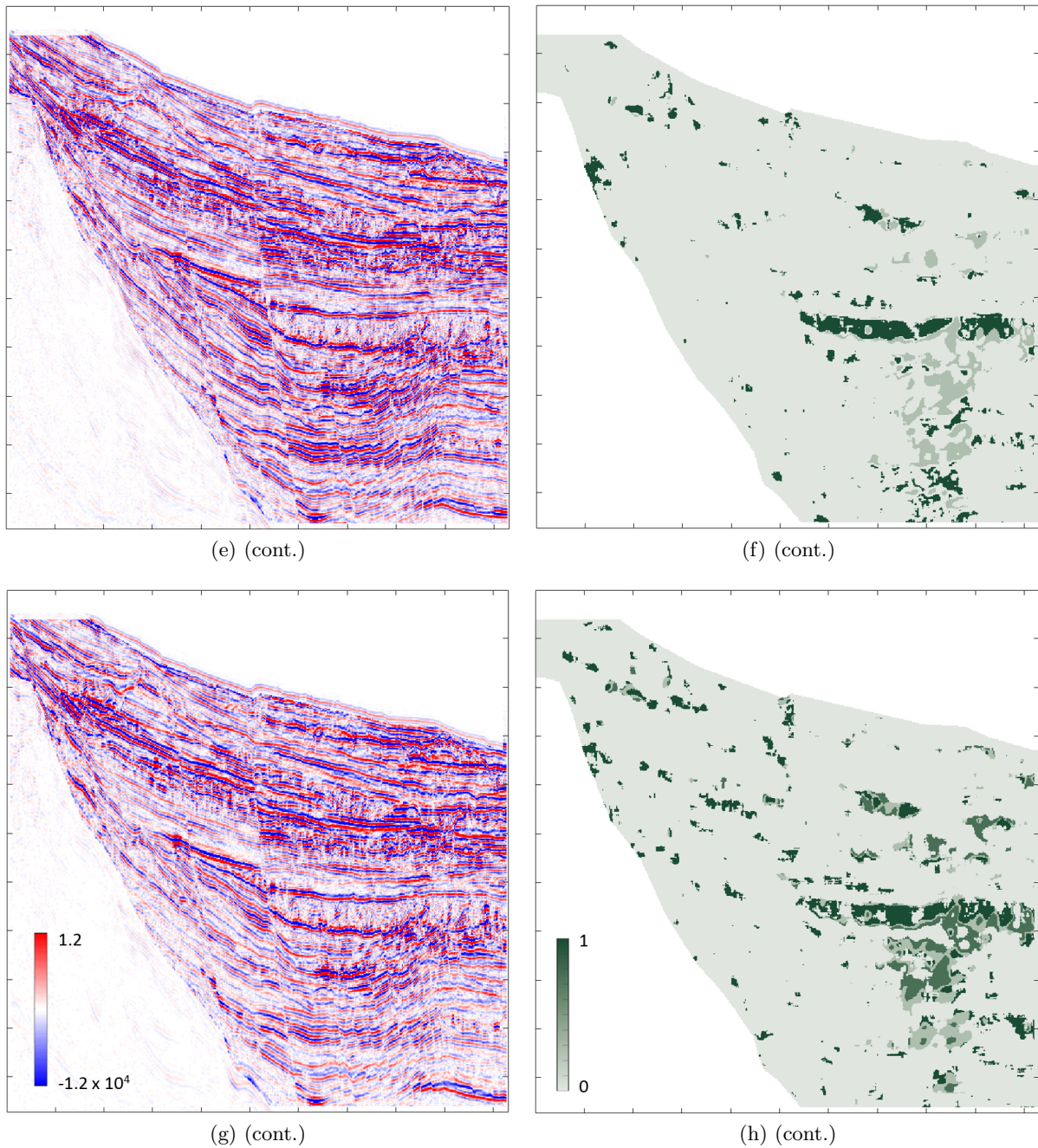


Figure 2.14: Posterior probabilities on one inline of the seismic cube used in our study, for the four datasets.

- In the mid-offset dataset, posterior probabilities are either 0, or 0.25, or 1. On this section, regions with probability 0.25 correspond to high-amplitude, semi-discontinuous regions with reflectors oriented contrary to the dip; they are present in the bottom of the large MTD and below it;
- In the far-offset dataset, the region below the MTD is covered with posterior probabilities below 1, but higher than in the mid-offset dataset;
- In the far-offset dataset, many outlier patches appear upslope with posterior probability 1, i.e. similar to regions that are otherwise quite characteristic of MTDs;
- In the full-stack dataset, comparatively less pixels are weighted 1; the MTD is highlighted by a mix of 1, 0.75 and 0.25 probabilities; it is also underlined by a thin, elongated region of low probabilities as in the mid- and far-offset datasets; correlating these low-probabilities with the seismic section on all the regions where they appear, we remark that for all three datasets, these clusters of low probabilities (cluster 1 for the full-stack and the mid-offset datasets, clusters 1 and 2 for the far-offset dataset) correspond to a visually middle-amplitude, chaotic facies type at the transition between high-amplitude reflectors (under the MTD) and low-amplitude or ridged regions of the MTD;
- Low-amplitude regions inside MTDs are almost always covered by clusters weighted 1 a posteriori, for the four datasets. This shows that the most MTD-characteristical clusters at least in part correspond to low-amplitude regions, be them also chaotic, ridged or other.

On the whole, the full-stack dataset shows less confidence in the outputs, but the main MTD of the figure is still recovered. We note that at least the low-amplitude internal regions of MTDs are recovered by the highest probabilities in all datasets; other kinds of facies that differ depending on the dataset are also depicted in the results, with varying levels of probability.

A comparison between cluster regions and corresponding regions in the seismic image was done (in the case $\alpha = 0.8$). Clusters were displayed either altogether on the section (as in Figure 2.9b), or one by one, to check the association between a seismic facies and a cluster. This association step will be described further in section 3.2. Together with our observations, it has shown that, for all four datasets, only a few facies are truly needed to build a representation that is sufficient to discriminate between MTD and the background seismic image. These 'minimal' facies are the low-amplitude or transparent facies, the ridged facies, and the chaotic facies. Among the positively-weighted clusters of the full-stack case (see Figure 2.12b), these correspond respectively to clusters 2 and 3, cluster 2 and cluster 1; note, however, that these facies groups actually include more than only

these clusters (see section 3.2).

Although only a few facies are needed for MTD identification, more facies may be associated to their occurrence in seismic images, such as those depicted by clusters with positive probabilities in the case $\alpha = 0.3$ - see Figure 2.12. For the full-stack dataset for instance, clusters 1, 2 and 3, already positively weighted for $\alpha = 0.8$, have higher probabilities when $\alpha = 0.3$; clusters 4, 8 and 9 are close to them on tight regions of the manifold (Figure 2.11), so similar in terms of seismic facies. Clusters 22, 29 and 36 are also added with low probability; we have associated them to high-amplitude facies seen within MTDs or at their contours in very small regions. These lower-probability clusters, added for decreasing α , are interpreted with less confidence.

These clusters are found in MTDs but also a lot in other regions of the seismic images, which leads to their being assigned a low (or zero) posterior probability for high values of α . In the identification workflow, a threshold is applied on these probabilities (for example, 0.5 in the article). As a result, the 3D detected objects do not contain these clusters.

Our method is therefore more appropriate for *detection* than accurate *delineation* of MTDs. Another discussion on this is provided in section 2.4.4.1. The morphological closure performed after the object detection can add pixels of low probability to the objects if they are in its immediate surroundings; this step of the methodology is therefore interesting, for example to include the bottom high-amplitude regions that are missing in the lower-right part of the MTD on Figure 2.13.

An alternative approach to our cluster probability assignment method that may allow more accurate *delineation* of MTDs could be to introduce higher-level prior information: a typical pattern of clusters (including e.g. high-amplitude bottom reflectors) that would be searched for in the image. Thus, to produce this 'prior' information, the clustering would already have to be understood and interpreted by the user. This approach, which was not tested during the PhD, would differ drastically from ours where the prior information is independent from the processing workflow.

2.4.3 How much variation is there among the detected MTDs?

Considering our objective, one remaining question is: what is the variability in the MTDs we retrieve? In this section, we give elements concerning the internal aspects and morphological properties of the MTDs recovered in the article of section 2.3.

Let us first note that two filters were applied in the final phase of the object retrieval methodology. These two filters (i) select the largest connected components of all, and (ii) select only those with 'consistent' orientation. Ideally, this phase should be interactive

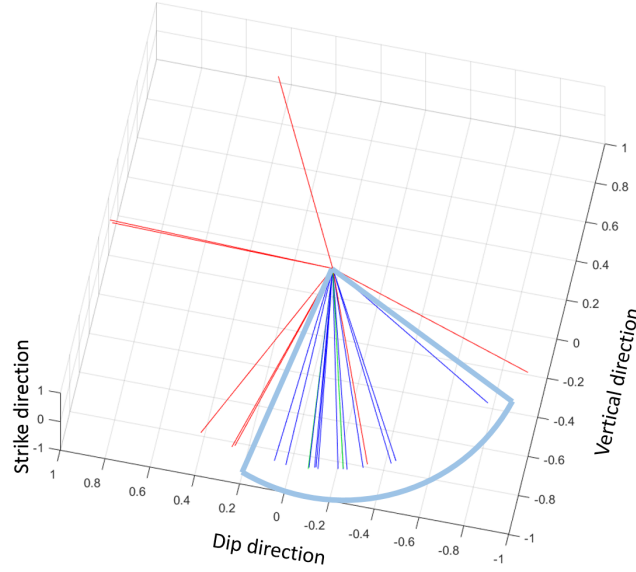


Figure 2.14: Illustration of the orientation filtering results for the 23 largest objects of the processed full-stack dataset. Vectors are normed and represent the orientation of the objects. Blue vectors correspond to MTDs, red vectors correspond to non-MTD objects, and green vectors correspond to unsure or unexpected objects. The light blue contour is a sketch of the cone used for filtering out most non-MTD objects. Note that the 3D view does not render the whole direction of vectors or cone.

inside a seismic interpretation software.

The volume filter only selected connected components with the highest number of pixels, selecting the volume threshold iteratively. Now, for the orientation filter, an illustration is provided in Figure 2.14: for every object, the three major axes $A1$, $A2$ and $A3$ of the equivalent ellipsoid were computed; $A1$, the longer of the three, is the one defining the object 3D orientation. We plotted the $A1$ of all objects on a 3D plot, coloring the ones corresponding to MTDs in blue and others in red or green (see Figure 2.14). The filter was applied as a 'cone' leaving out undesired object orientations. The red or green vectors remaining inside the cone are either artifacts or unexpected objects.

From the figure, we see that the orientation filter, although reducing the range of 3D orientations that MTDs can have, is loose enough to allow variability within the MTD group.

Figure 2.15 presents crossplots of some resulting morphological and internal characteristics of the volume-filtered objects: volume, 'aspect ratio', and 'DTU' for 'divergence to uniform'. Here we defined the 3D 'aspect ratio' as the ratio $\frac{\|A1\| \cdot \|A2\|}{\|A3\|}$. It is highest when $A3$ is much smaller than $A1$ and $A2$, meaning that the object is very thin, or flat. 'DTU' is a measure of how class labels are distributed inside an object. It was computed as the Kullback-Leibler divergence of the distribution of class labels inside the object to a supposed uniform distribution of the same class labels. A low value then corresponds to a quite uniform distribution of class labels, i.e., an object having approximately identical

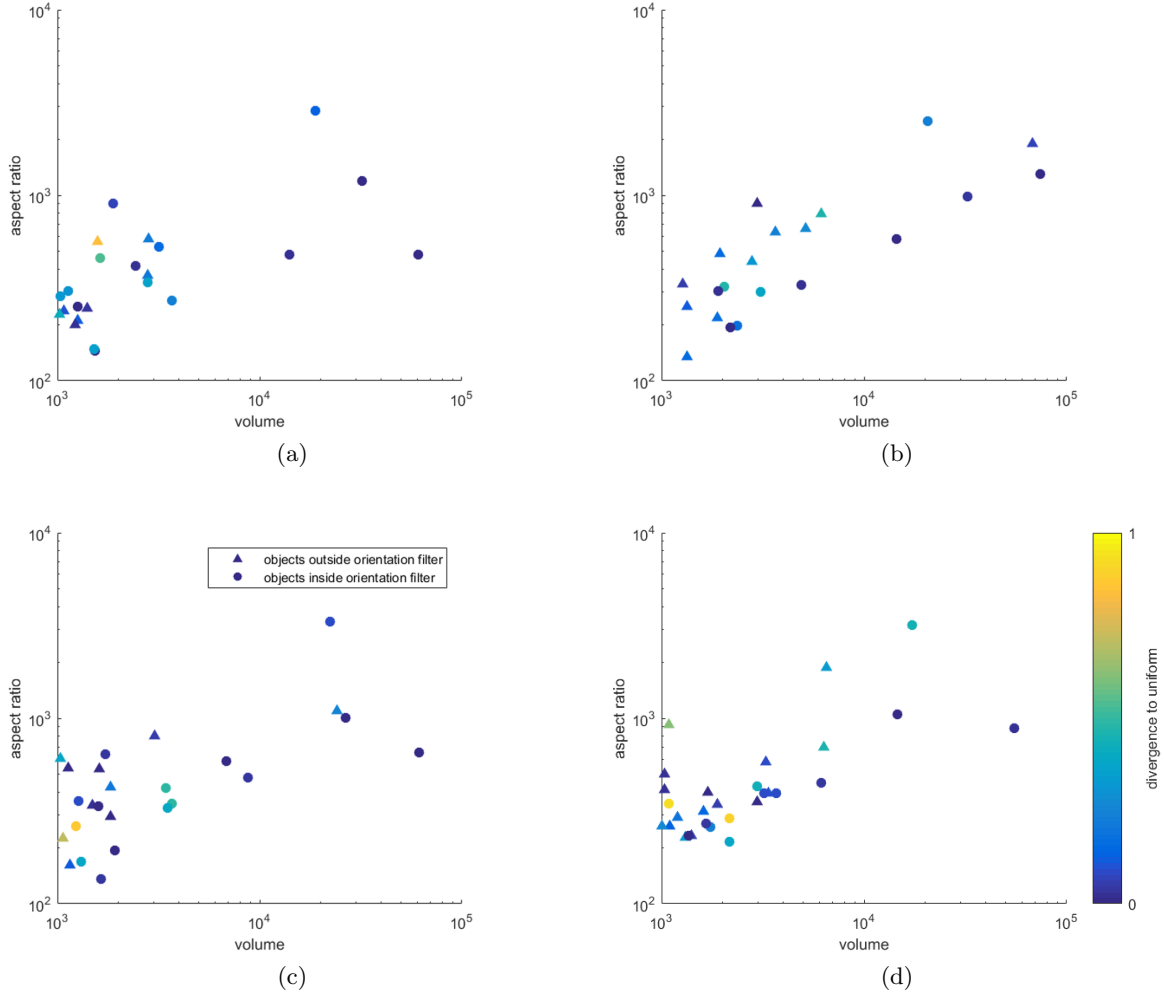


Figure 2.15: Crossplots comparing the volume, aspect ratio, and divergence to uniform (DTU in this report), of the largest connected components retrieved by our method. (a) full-stack dataset, (b) near-offset dataset, (c) mid-offset dataset, (d) far-offset dataset.

proportions of each of its facies.

From this figure, we note that:

- In all four datasets, objects preserved by the orientation filter (circles on the plots) are of various size and internal DTU.
- In all four datasets, the objects with highest volumes have rather low values of DTU. And they are almost all preserved by the orientation filter.
- In all four datasets, there is a globally increasing trend of aspect ratio with volume: the largest objects are not the 'thinnest' in terms of aspect ratio. In other words, largest objects (so, largest deposits) are large because they are thick.

- In all datasets but the full-stack dataset, for a given volume, objects that are rejected because of orientation (represented with triangles on the plots) are often also the least uniform in facies distribution, i.e. the ones with highest values of DTU. In a sense then, both orientation and internal characters converge to show that true MTDs are characterized by a plurality of facies.

Apart from these observations, neither morphological nor internal characters seem specific to our true MTDs. Far from characterizing the full variability of the MTDs we retrieve, this simple analysis at least ensures that the retrieval method does not constrain them to specific morphological or internal property values.

2.4.4 Highlights of the mixed approach for our objective

The objective of this part of the PhD was to locate MTDs in seismic data, in position and extension, while preserving the variety of their characters. The previous article presented a mixed data-driven and model-driven method, where the MTD identification is extracted from the seismic data, thanks to a guiding by little prior information carrying uncertainty. This method advantageously produces 3D geobodies and textural facies within them, thus meeting the objective.

Now, to what extent is the method 'better' (considering our objective) than existing methods?

2.4.4.1 Comparison with a model-driven approach

Let us compare our method to a 'model-driven-only' interpretation method, which could then be either an entirely manual interpretation, a geometrical segmentation, or a supervised seismic facies classification (see section 2.2.3).

Comparison with a manual delineation

The developed method is less precise in its delineation than a manual binary interpretation (see Figure 2.16); in general, borders with strong amplitudes are not reached, as textural facies which are assigned positive posterior probabilities are rather characteristic of the interior of MTDs. Facies associated to strong-amplitude reflectors which are at MTD borders are also often present in the rest of the seismic images. Consequently, their prior CDF (cumulative distribution function) is already above the $\frac{1}{\alpha+1}$ threshold from the $s_1 = 0$ level (see Fig. 2 in the article). Therefore, the posterior probability value of such facies will stick to zero. This induces that the volumes of the MTDs identified by our method are under-estimated compared to a manual delineation.

However, as an automated method, its advantage is to be less time-consuming. Moreover, thanks to the consideration of an input confidence on the prior probabilities (by choosing

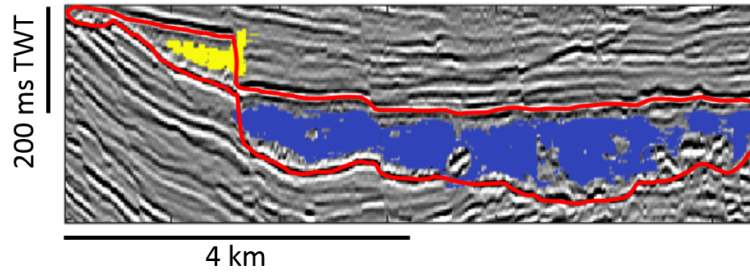


Figure 2.16: One seismic section after the 3D processing, with pixels of two objects (one yellow, one blue) on top of the seismic. Note that the two objects correspond to only one MTD. The red contour is a manual delineation of the targeted MTD.

an appropriate α), this automation may reveal unexpected geobodies that are similar to MTDs and, in some cases, that are actually MTDs. This is actually the case of MTDs F and H (see Fig. 7 and 8 in the article); these objects were not initially expected as they were not seen as well as the others on a lot of seismic sections; they were yet depicted as MTDs by posterior analysis. The method therefore enables to build, from a little prior input and from a dataset, objects based on the data content that an interpreter might have missed. Again, thanks to the formulation of prior probabilities, this method proposes a way to tackle the variability of manual interpretations by different experts, or, the uncertainty associated to the output of any first rough automated estimation. Finally, the outputs of the method include some internal description of the object on top of the delineations themselves, thus giving insight into the intra-class variability of the objects.

Comparison with a geometrical segmentation

A geometrical segmentation method was tested during this PhD for MTD delineation, following interesting examples on seabed segmentation or fish detection on acoustic data from [Lianantonakis & Petillot \(2007\)](#) and [Sharma & Anton \(2009\)](#). Our trials were not led further, as parameter tuning in 2D, and even more in 3D, was too critical to be efficient. The tested method was the Chan-Vese active contour algorithm as described in [Chan & Vese \(2001\)](#) for scalar-valued images and in [Chan *et al.* \(2000\)](#) for vector-valued images. The scalar-valued version was tested on the posterior-probability images, referred to as 'modeled images' in the previously presented article. The principal advantage of such a method would be the retrieval of smoother contours than only the borders of positively-weighted facies in the posterior probabilities. Smoother contours would be appreciable for more realistic MTD shapes, although some morphological features do imply that the contour be non-smooth in some region of the MTD (e.g., 'tongues' at the toe of the MTD, ramps on the basal surface, etc.). Parameterizing the weight given to the curve-smoothing constrain with respect to the weight of the data-fit term (see [Chan & Vese \(2001\)](#)) proved very touchy and not feasible without introducing too much a priori interpretation; in this

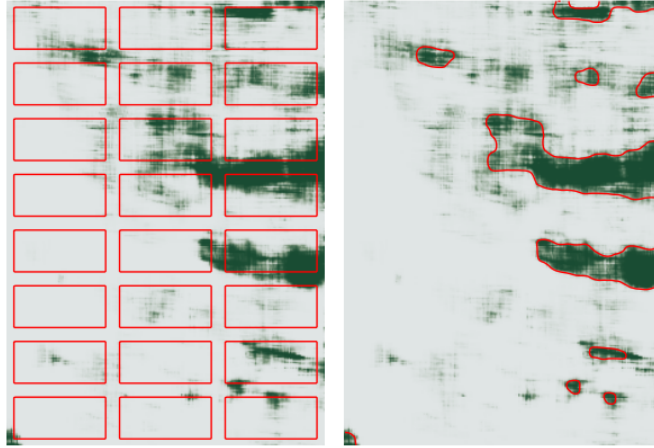


Figure 2.17: An example of application of the Chan-Vese algorithm (Chan & Vese (2001)) on one 2D attribute image of the seismic volume: initial (left) and final (right) state of the contour (red line). Parameters to be tuned include the initial position of the contour (here chosen as split into multiple contours for accelerating the convergence, as proposed by Lianantonakis & Petillot (2007)) and the weight for constraining the curve smoothness. Here very small objects are kept, which is the signature of a low smoothness constraint.

case, a direct manual delineation seemed more appropriate. The vector-valued version was applied in preliminary tests, not on the same seismic data; there, the considered vector for one pixel was the set of textural attributes. However, tuning the weights given to each data-fit term (one term per vector component, see Chan *et al.* (2000)) proved yet another factor of non-objectivity and non-repeatability. See Figure 2.17 for an example.

Using the simple segmentation of connected components in our 3D 'modeled' volume freed us from the choice of too fine parameters, which were replaced by only the threshold of posterior probability to take into account for the connected component detection. It was also considerably quicker, as the connected component retrieval is basic pixel-to-pixel comparison, already implemented in MATLAB, while the active contour model is based on an iterative deformation of the contour.

Given these arguments, the geometrical segmentation method was left apart.

Comparison with a supervised seismic facies classification

As compared to a seismic facies classification, our method produces objects, which a facies classification alone does not. The comparison rather holds between our GTM facies classification and a supervised one. Tests of supervised labeling were initially done. In particular, the algorithm by Bergmann *et al.* (2017) for data labeling by iterative multiplicative filtering was applied on a test image (see Figure 2.18a). For this supervised partitioning, we first manually picked 20 classes on the reference image (class centers 1-8 picked inside MTDs, 9-20 picked outside). A second test was run with picking 25 classes (class centers 1-8 picked inside MTDs, 9-25 picked outside). Results are shown on Fig-

ure 2.18b and 2.18c, for two different sizes of neighborhood for the filters (3x3-pixel or 5x5-pixel uniformly weighted windows). It appears that, with more input class centers, a better discrimination of MTDs against the 'background' was achieved. This simple example illustrates the potentially non-representative class center set when picked manually, i.e. when performing supervised facies classification. A manual choice of class centers was therefore abandoned.

2.4.4.2 Comparison with data-driven or mixed approaches

A purely data-driven method would not be able to delineate objects in a volume, unless using a machine-learning method with (convolutional) neural networks. In our case, the too low amount of training data prevents from such an approach.

Our methodology should therefore be compared to mixed approaches, like the already-mentioned work by Hashemi *et al.* (2017). The global approach is the same: generate a data-driven clustering of the seismic, and then 'tie' it to some external, global input data. A difference in our case is that our prior information is of a 'binary' kind, i.e. an image with binary values or continuous probabilities in $[0, 1]$, while Hashemi *et al.* (2017) define regional facies. In our method, no iterations are used to constrain the clustering a posteriori. Our idea is that the clustering is already done with a high number of clusters (ideally, very high), so that the clusters probability assignment phase creates groups of more or less 'probable' clusters in terms of object representativity (see part 2.2 in the article).

In a recently published patent, Osypov *et al.* (2018) propose a method for 'seismic facies identification using machine learning'. This method is not far from the one developed in our article. One option of their workflow is to start from a supervised, or unsupervised, clustering of seismic data (e.g. thanks to an attribute representation); it is then followed by matching some geological facies, available from 'an appropriate computational stratigraphic model', to the clusters. This is done with a machine-learning tool (claim 9 of Osypov *et al.* (2018)'s patent). Although the authors do not mention the case of object delineation, it is clear that their 'facies-matching' step corresponds to our 'cluster probability assignment' step. A point remains unclear, however: whether the 'facies-matching' is done in the seismic data space (i.e. using a synthetic seismic block formed from the computational stratigraphic model), or directly from the stratigraphic model itself.

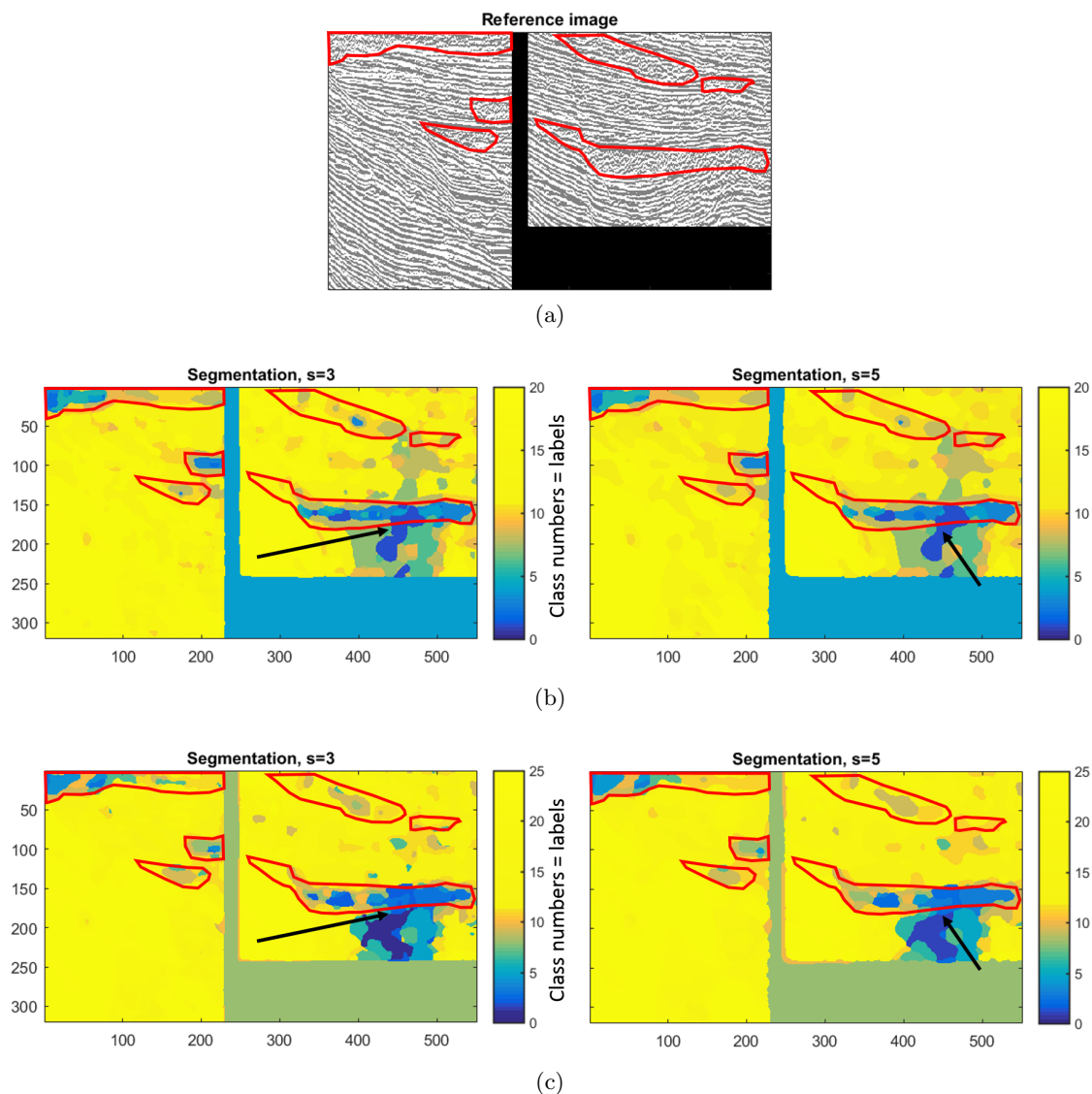


Figure 2.18: An example of application of the (supervised) iterative multiplicative filtering for data labeling by Bergmann *et al.* (2017) on a test image (a), represented by 7 textural attribute images. 20, resp. 25, class centers were picked manually on the reference image in cases (b), resp. (c). Black arrows show the area of improvement (better discrepancy) from (b) to (c). Both cases were tested for two different sizes of uniformly-weighted filters: 3x3 window (left) and 5x5 window (right). Red lines are rough contours of expected objects.

2.5 Conclusion

In this chapter we have focused on the development of a methodology for MTD identification in a 3D seismic dataset. To extract appropriate information efficiently from a seismic dataset, we have had to deal with the integration of data-driven and knowledge-driven information, the diversity of seismic characters of MTDs, the uncertainty associated to any 'ground truth' in seismic interpretation, and computing time.

Identifying MTDs in a seismic dataset can be done by extracting textural information from the dataset. The method we have presented is quick to compute on a training set. It conveys both the uncertainty in the prior input and the structure of the data cloud in the textural attributes space. It yields objects in the 3D volume, which correspond to expected MTDs, for most of them. We are therefore able to locate MTDs in seismic data, in position and extension, while preserving the variety of their characters. In this respect, we have reached our first objective.

The consistency of the method that was presented in this chapter enables us to validate and emphasize two points:

- At least in such relatively shallow depths as in our case, the textural information extracted with no a priori from the seismic data allowed for a 3D delineation globally consistent with the prior interpretation. This shows that an unsupervised data representation as we have done contains some ready-to-use high-level information, i.e. only a small step is needed to select from it the right information answering a specific application.
- Certain texture types, although present elsewhere in the seismic data, are characteristic of certain regions of MTDs. These objects can then surely be described as aggregates of some textural facies. In the full-stack dataset, the minimal facies needed to detect an MTD according to the prior information given in the training dataset are the transparent, ridged and chaotic facies. This point in particular accounts for the internal variability of MTDs, as the spatial distributions of these texture types is not the same from one MTD to the other.

Finally, distinguishing data-driven from knowledge-driven computations enables to provide an unsupervised data representation independently of the MTD identification objective, available for potentially other purposes. It also permits to weight the prior input according to its acknowledged level of uncertainty. The next chapter will also deal with such questions of how to use both data-extracted and knowledge-based information, although this information may be qualitative and concerns an interpretation objective.

Chapter 3

Interpretation of MTD properties: properties of mass transport events

3.1 Introduction

In this chapter, we focus on the second purpose of this PhD project: discriminating potential physical processes acting over geological times, responsible for location, geometry and internal heterogeneities of MTDs.

3.1.1 Assessing the responsibility of physical processes for MTD characters

In order to recover the history of one MTD from its seismic signatures, interpreters rely on models, concepts, heuristic rules, and also example cases, that their geological background gives them. All these elements, when explicitly mentioned in published articles, are a source of invaluable knowledge for other interpretations.

[Terzaghi \(1950\)](#) wrote about mass transports: 'A phenomenon involving such a multitude of combinations between materials and disturbing agents opens unlimited vistas for the classification enthusiast. The result of the classification depends quite obviously on the classifier's opinion regarding the relative importance of the many different aspects of the classified phenomenon.' [Varnes \(1958\)](#) commented on this citation that 'each classification (...) is best adapted to a particular mode of investigation, and each has its inherent advantages and disadvantages'. Indeed, several authors have provided classifications of mass transports and/or MTDs. [Varnes \(1958\)](#)'s criteria are the type of material involved and the type of movement. [Mulder & Alexander \(2001\)](#) classify sedimentary density flows, based on physical flow properties and grain-support mechanisms (which can be matrix support, particle interactions, fluid turbulence). [Moscardelli & Wood \(2008\)](#) classify mass transport complexes (large MTDs, or series of MTDs) in offshore Trinidad according to geomorphological factors, as well as causal mechanisms and source area characters. [Posamentier & Martinsen \(2011\)](#) classify mass transports according to the involved deformational pro-

cesses within the transported mass. In these classifications, classes relate to interpreted types of mass transport, as defined by expert authors - and thus, different classifications occur for different applications or viewpoints.

Submarine landslides are also studied with forward approaches. These produce models that prove certain causal relations between one physical parameter and a resulting characteristic of the MTD. For example, by analog modeling, [Sawyer *et al.* \(2012\)](#) show the dependency between the source area morphology and the initial flow factor F_f of a submarine flow (see [1.3.2](#)): for a high F_f , the source area is smooth and flat; for a medium F_f , it is irregular with steps produced by retrogressive failure; for a low F_f , only the surface of the region close to the slope failure is modified.

A physical model, however, is essentially a simplification of a natural event, that investigates one or a few processes at a time. In the case of submarine landslides, this point is worthy to note, as slope stability models, which describe the pre-triggering and triggering phase of a mass transport, are rarely joined to flow models involved during the transport (to our knowledge): the transition from a material holding within a morphology defined by the pre-failure bathymetry, to a set of grains or particles acquiring velocity and finally flowing, is not well known.

Inferring past processes from seismic data is a question of causation: what phenomenon triggered the mass transport? What processes did the mass transport, and then its deposit, undergo during their history until now? What current properties of the MTD are we actually imaging in seismic data? Overall, what phenomenon, processes and properties caused the MTD to give the seismic response we see? For each explanation to find, multiple causes may be invoked and causal chains (such as factor f1 causing f2, itself causing f3, itself causing f4, etc.) may be involved.

As shown in [section 1.3](#), a mass transport trigger occurs when the Flow factor F_f gets higher than 1, which can happen both because of long-term mechanical evolution or because of a punctual triggering event (e.g. tectonic-related uplift in a margin, as opposed to the sudden release of gas from gas hydrates and weakening of a sediment layer); a procedure called 'back analysis' typically aims at assessing some properties of the material just before the slide, based on the slope state immediately after the slide and a given slope stability analysis method (e.g. Limit Analysis, see [section 1.3.2](#)). Back analysis, however, is useful only when a lot of information is available on the slope state after and before the slide, which is not the case with MTDs.

One transport process can also result from several causal factors; for instance, a high velocity in a mass flow can be caused by an initially high upslope position of the destabilized mass, and/or by a steep slope favoring acceleration.

One seismic character can be due to several processes or current characters of the MTD; for example, strong seismic amplitudes in the MTD may result from lithologic changes, or

from heterogeneous fluid distribution. Discriminating between one or the other requires comparing different kinds of information, potentially coming from different kinds of data (e.g. cores and fluid-flow simulations).

To eventually trace back the original processes involved in a mass transport requires to have a sufficient net of arguments, one refuting the other or, on the contrary, confirming the other.

The challenge here is thus not to discriminate one process responsible for the characteristics of an MTD; instead, we have to take into account the multiple MTD seismic signatures and these multiple possibilities of causation, and to come up with one or several hypotheses, keeping track of all the possibilities.

3.1.2 Dealing with multiple heterogeneous causal factors in geoscience

In geoscience, many subjects involve such diversity of potential causal factors. A well-known example is the multiple factors that control the global climate change. They include the carbon and water cycles, plate tectonics and ocean dynamics, solar activity, volcanism, orbital variations of the Earth, and human activity. All these factors can impact each other and result in intermediate phenomena which may be considered causes for temperature elevation. For instance, the IPCC¹ emission scenarios (e.g. Pachauri *et al.* (2014)) represent the impact of human activity (under specific assumptions on societal evolutions) on the emission of several greenhouse gases; these emission scenarios are then fed to climate models, together with physical parameters, to estimate the temperature elevation with time. This result cannot be attributed to only one of the multiple factors acting in climate models.

However, by comparing climate models of a past time period with observed data of this period, it is possible to quantitatively assess which set of factors are the most likely to be causal for the temperature elevation. For example, Williamson *et al.* (2013) apply a statistical analysis to a climate model and a set of observed data to find out that among a lot of parameters, those concerning cloud processes and ocean mixing are more likely to 'explain the data' than others. Such an analysis is made possible by the quantitative nature of all examined factors and the presence of a complete (although complex) numerical climate model.

Another approach tends to conciliate several kinds of quantitative and qualitative data and information about one domain of study into one standardized description. This is done by building an ontology of the domain. An ontology of a domain is 'an explicit formal specification of the terms in the domain and relations among them' (Gruber (1993)).

¹Intergovernmental Panel on Climate Change. Link to IPCC webpage: <http://www.ipcc.ch/index.htm>.

In geosciences, according to [Reitsma *et al.* \(2009\)](#), 'semantics, ontologies and eScience are key areas of research that aim to deal with the growing volume, number of sources and heterogeneity of geoscience data, information and knowledge'. By exhaustively recording information on a domain, an ontology can be used as a reference of knowledge for any analysis on that domain.

For example, the geologic time scale, which relates stratigraphy to time, is formalized into an ontology available on the Internet ([Linked Data API \(2017\)](#)) ; every age is listed there with relationships to epochs, periods etc., i.e. all the levels of the chronostratigraphic chart - in several languages. The webpage works like an interactive dictionary where one can make queries with key words and retrieve information about e.g. any geological period wanted - see for example [Figure 3.1](#). This ontology is a kind of dictionary or reference set of knowledge useful for standardized sharing of information. Other ontologies can be built and related to that one; for instance, [Wang *et al.* \(2018\)](#) develop an ontology concerning the 'local geologic time scale of North America, paleontology, and fundamental geology'. They also provide a methodology to use their ontology, based on a numerical interactive tool that allows queries and comparisons of fossil information and geological information ([Wang *et al.* \(2018\)](#)).

[Reitsma *et al.* \(2009\)](#) report that ontologies give descriptions rather than explanations. [Malik *et al.* \(2010\)](#) call for more knowledge-based systems describing the links between data and physical processes, in order to formalize the understanding that a community has of a natural phenomenon. Some ontologies may then represent the rules of inference and logic that relate physical processes to data, within a specific domain of data interpretation.

In particular, we here present two ontologies dedicated to geological interpretations. The first one was proposed by [Verney \(2009\)](#). It is an ontology for horizon and fault interpretation. It contains several pieces of knowledge-based information, as shown on [Figure 3.2](#): some processing methods (allowing to retrieve major horizons and faults from the seismic block) in the 'Data management' block; the selection of appropriate descriptors for the analyzed surfaces, in the 'Visual characterization' block; some heuristic rules for analyzing relative positions and crossings of surfaces, and a method to apply them with the surface descriptors, in the 'Geological correlation' block. In [Figure 3.2](#), we have added the corresponding steps of our methodology (presented in [section 3.3](#)) in orange, below the blocks of [Verney \(2009\)](#) (see below).

[Verney \(2009\)](#) applied this framework to build a scheme of horizon interpretation. In [Figure 3.3a](#), horizon parts are shown together with interpretation of their relative ages. In [Figure 3.3b](#), several quantitative and qualitative descriptors of these horizon parts are analyzed, and the heuristic rules contained in the ontology propose to merge some horizon



Figure 3.1: Example of use of the International Stratigraphic Chart to retrieve Geologic Timescale Elements: the query was the word 'Cretaceous' to be 'within the label' of the elements searched. Results include all elements of the ontology having the word Cretaceous in their label. From [Linked Data API \(2017\)](#): [link to the webpage](#), last accessed Sept. 10, 2018.

parts into one horizon.

A second ontology devoted to geological interpretation was proposed by Perrin *et al.* (2009). It also concerns structural representation of a geological region, although sticking to the abstract description of a 3D model rather than explicitly related to seismic data. The authors define four concepts to build the ontology: (i) a Geo-object is a constitutive element of the region studied (it can be e.g. a surface or a sedimentary formation); (ii) a Geo-property is a descriptor of a Geo-object; (iii) a Geo-event is any geological event that occurs during the evolution of the region of study; (iv) a Geo-assertion is a relationship relating two Geo-events (Perrin *et al.* (2009)). Here the Geo-event and the Geo-assertion correspond to the formalization of the understanding of geological processes demanded by Malik *et al.* (2010), as do the heuristic rules of the ontology by Verney (2009).

Considering our objective, we have seen that multiple MTD characters and multiple potential causal processes should be taken into account. Overall, an approach such as ontologies should allow us to introduce qualitative and quantitative information from the seismic data, as both formats are involved in existing interpretation models from the literature. Results of ontology-based interpretations can come from mixed data-based and knowledge-based information, both involving various characteristics (in our case, seismic signatures and processes characteristics, respectively). An ontology also allows to display an exhaustive list of elements related to an object, so that all of them may be considered objectively. Finally, thanks to its formalized framework, it should allow to disclose explicitly a whole interpretation procedure; it is also repeatable, if possible with automated methods.

For these reasons, the second objective of the PhD was tackled by developing a novel methodology based on the concept of ontologies, for interpreting the diverse characteristics of mass transport processes at the origin of the various seismic signatures of MTDs.

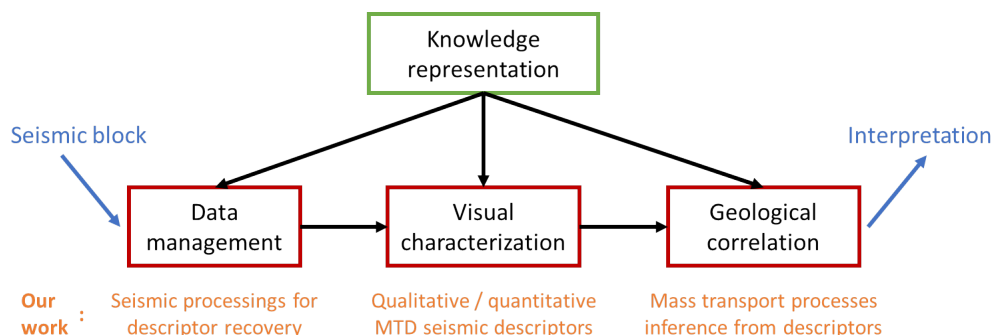


Figure 3.2: Proposed architecture for an ontology for interpretation of major surfaces in a seismic block, modified from Verney (2009). The orange text below red blocks are the corresponding steps of our methodology.

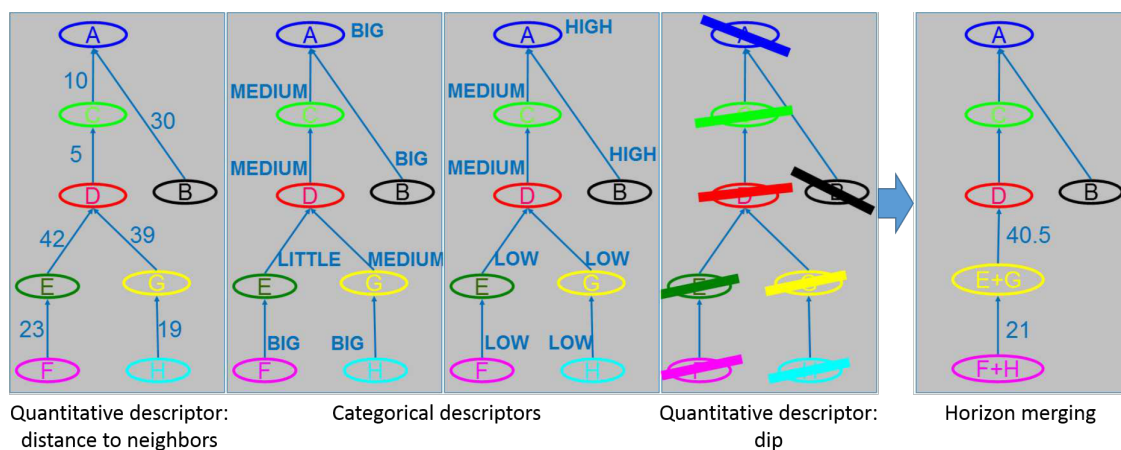
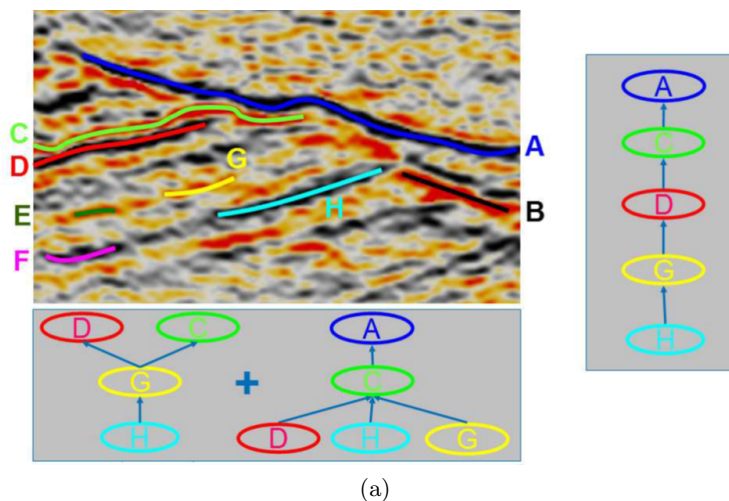


Figure 3.3: Example of horizon interpretation in the ontology proposed by Verney (2009). (a) Studied horizon parts shown on a seismic image; two different parts of the image give different information shown by the two graphs below the image, and resulting in interpretation of the horizons' relative ages (right). (b) Four descriptors depicted for all considered parts of horizons: two different quantitative descriptor (left and right), two different categorical descriptors (middle); the fifth rectangle on the right is the ontology proposal. The ontology proposes to merge part E with part G, and part F with part H, here based on the similarity of their descriptors.

We aim at integrating relationships between data-extracted descriptors and external explanatory processes. These descriptors and processes are the 'terms in the domain' in the definition by Gruber (1993).

The approach we propose in section 3.3 fits in the frame of the ontology by Perrin *et al.* (2009), even if it is more focused on one kind of Geo-object only: (i) we have considered MTDs as Geo-objects; (ii) we characterize them by their properties, and each property by descriptors, similar to Geo-properties; (iii) we list possible processes that can be related to Geo-events, although most of these processes are acting over time rather than punctually; (iv) we list potential impacts between events, like Geo-assertions - in our case we also have impacts from Geo-events on Geo-properties.

Our approach can also be related to the global framework proposed by Verney (2009); see Figure 3.2. The work we present in section 3.3 is not automated, however. Further work should be done if such purpose was chosen.

3.1.3 Organization of this chapter

The organization of this chapter is as follows: in section 3.2, we describe how we built facies groups on the full-stack seismic data thanks to the clustering presented in the previous chapter. These facies groups are used in the following. In section 3.3, we introduce the methodology that has been developed during this PhD, in the form of an article that was submitted to the Marine and Petroleum Geology Journal, reviewed and corrected accordingly. A discussion is led in section 3.4. Section 3.5 gives the conclusions and openings of this chapter.

3.2 Creation of seismic facies groups for MTD description

This section describes how we built the seismic facies that are used as input in the article of section 3.3. The methodology presented in that section relies on several MTD descriptors that characterize global properties of an MTD: its morphology, its basal and upper surfaces, its position, its headscarp, its internal facies organization and its global environment. Here, we explain how we defined the seismic facies groups. This subject was already approached in the previous chapter, to find the minimal facies needed for the detection of an MTD in our case study.

As detailed in section 2.2.3.2, when interpreting a GTM result out of a seismic dataset, clusters of interest are often gathered into groups, eventually called 'facies' in our study. We have shown in the previous chapter that for the purpose of *object detection*, we could use a simple mathematical method that selects and weights the right clusters; in this case, the semantic information retrieved is the probability that the seismic sample corresponds to part of an MTD. By contrast, the *association* between clusters and seismic

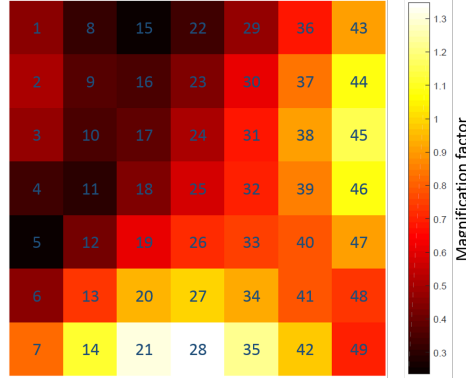


Figure 3.4: Magnification factors (MF) map of the GTM manifold for the full-stack dataset. Cluster labels (numbers from 1 to 49) are indicated. High values of MF indicate a stretched region of the manifold, corresponding to 'natural' boundaries between groups of points in the data space.

facies (with names such as 'chaotic', 'deformed', etc.) needs a manual labeling done by visually comparing a seismic image and its corresponding clustered image (i.e., each pixel colored according to its cluster number - see e.g. Figure 2.5). This is helped by visualizing the projected GTM posterior probabilities of the data points onto the latent space, as shown on Figure 2.7a and 2.7b, where grey dots correspond to the means of these posterior probabilities.

As mentioned in section 2.2.3.2 (p. 70 and following), the modes of these probabilities can also be used to create cluster groups. We used these modes, which all lie on cluster centers (Bishop *et al.* (1998b)). This way, we created the facies groups by merging GTM clusters, rather than merging individual points with polygons as is done on Figure 2.7. Figures 3.4 and 3.5 detail this step further.

Figure 3.4 shows the grid of cluster centers with cluster labels (numbers) in the 2D latent space, where color represents the magnification factor of the GTM-built manifold at each cluster center.

Figure 3.5 presents the interpretation of clusters in terms of seismic facies. On Figure 3.5a, an example of the method to assign clusters to facies groups is given, for the deformed facies. For one seismic section, clusters are interactively displayed and compared to the amplitude image; the final choice of clusters to define the facies group is also compared to the amplitude image, as also shown on Figure 5 of the article in section 3.3.

Figure 3.5b shows all the interpreted facies groups relevant for our application on the grid of 49 clusters produced by the GTM. Note that the strong-amplitude sub-horizontal facies group is opposite the other facies groups on the manifold; other facies groups, more representative of the internal MTD aspect, are closer to each other on the manifold. Also note that some of them overlap.

The seismic facies groups we have used for our study are the chaotic, transparent, deformed, strong-amplitude sub-horizontal and ridged facies. Their definitions and exam-

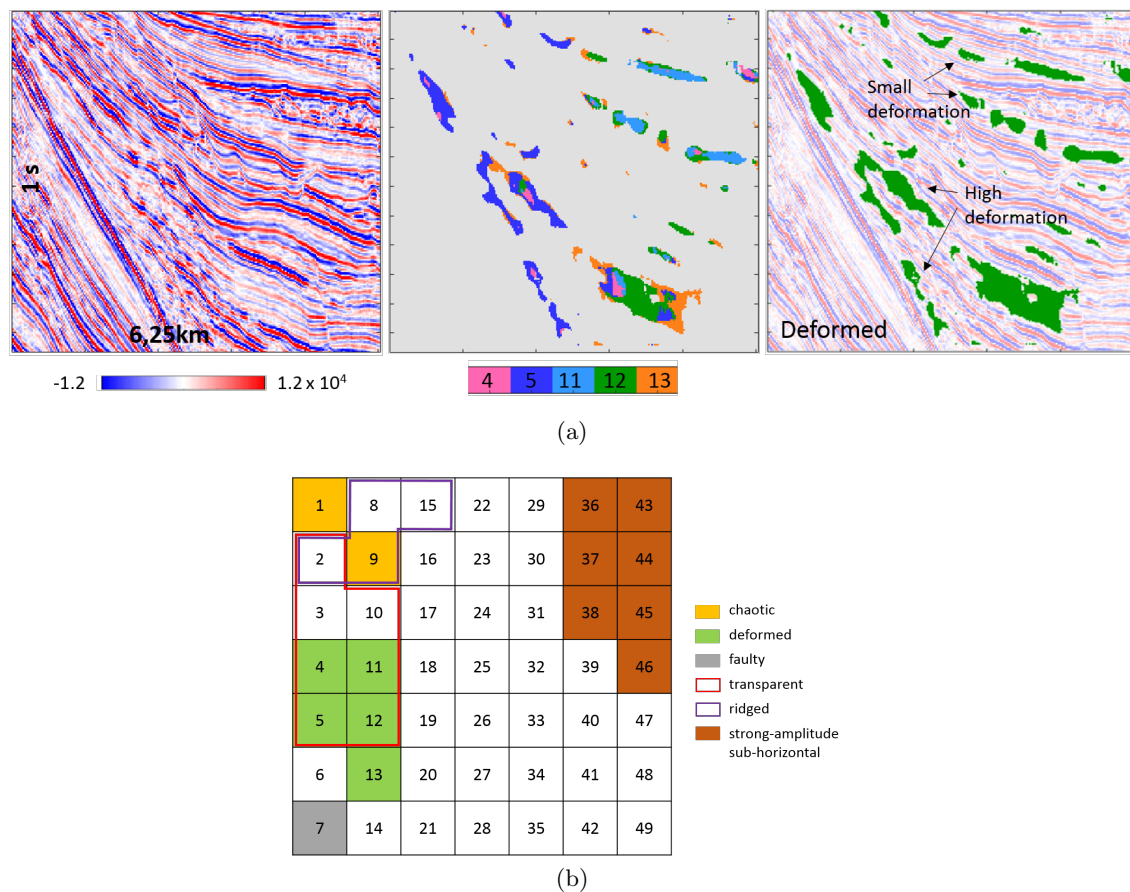


Figure 3.5: Interpreting facies groups from the GTM-defined clusters. (a) Example for the deformed facies: seismic amplitude image (left), selection of clusters (middle), all selected clusters grouped into one facies (right). (b) Interpreted facies groups used in our study, drawn on the 2D grid of 49 cluster centers. The deformed facies, for example, is defined by clusters 4, 5, 11, 12 and 13, as visualized on (a). Note that some facies groups overlap.

ples on the seismic data are shown, similarly as in Figure 3.5a, on Figure 5. of the article presented in section 3.3.

As mentioned in section 2.4.2 and shown in section 2.4.4.1 (comparison with a manual delineation), the MTD detection method of the previous chapter does not ensure a delineation that is precise enough for characterizing properties like object or surface morphologies; Figure 2.16 recalls that the MTD volumes are always underestimated, and that the strong-amplitude facies of the MTD basal regions are not selected by our method.

Consequently, for the development of this chapter, we introduced manually-delineated contours - although ultimately the automatically-retrieved contours should be used. We acquired them on 72 parallel inlines out of the 710 inlines of the cube with MATLAB and the GOCAD interpretation software.

The next section is devoted to the development of the methodology for proposing interpretations, in terms of causal processes, to MTD seismic signatures. We have taken advantage of the existing models and interpretation rules that have been acknowledged in the literature. We have also described various characters of MTDs with relevant object descriptors, extracted from a literature review. Seismic facies are used as an input in the application of this methodology; now not only the facies variability is taken into account, but also other aspects of MTDs: their morphology, the characteristics of their upper and basal surfaces, their position, their headscarp and their global environment.

3.3 Development of the methodology - ARTICLE

In the following article, we propose a methodology for interpreting MTD properties in terms of mass-transport processes, based on information retrieved from the literature. The article was submitted in February 2018 to the Journal of Marine and Petroleum Geology. It was given back for revision on June 25th. The version proposed here has been modified to take into account the three reviewers' comments and suggestions, and sent back to the journal on September 20th. The supplementary material associated to this article is given in Appendix C. Note that in this study, only MTDs A, B, C, D and E of the former chapter are used. MTDs F, G and H are not used, for several reasons: (i) at the time of the initial writing they were not already detected in the seismic data; (ii) they are small comparatively to the others; (iii) adding them would not change the content of the article.

A new conceptual methodology for interpretation of mass transport processes from seismic data

Corresponding author: Pauline Le Bouteiller^{a, b, 1}: pauline.le_bouteiller@upmc.fr

Sara Lafuerza^b: sara.lafuerza@upmc.fr

Jean Charléty^a: jean.charlety@ifpen.fr

Antonio Tadeu Reis^c: antonio.tadeu@pq.cnpq.br

Didier Granjeon^a: didier.granjeon@ifpen.fr

Florence Delprat-Jannaud^a: florence.delprat-jannaud@ifpen.fr

Christian Gorini^b: christian.gorini@upmc.fr

^a : IFP Energies nouvelles; 1 avenue du Bois-Préau, F-92852 Rueil-Malmaison, France.

^b : Sorbonne Université, CNRS-INSU, Institut des Sciences de la Terre Paris, IStEP UMR 719; 1 place Jussieu, F-75005 Paris, France

^c : School of Oceanography/FAOC, Universidade do Estado do Rio de Janeiro (UERJ); Rua São Francisco Xavier, 524, 4° andar, Bloco E; Maracáña, Rio de Janeiro, RJ, CEP 20550-900, Brazil.

Highlights

- MTD interpretation can be approached by a standardized graph-based methodology
- A proposed graph-based methodology clarifies and enhances MTD interpretations
- The proposed methodology integrates the variability of MTD physical processes
- The methodology is to be shared and improved by the interpretation community

Abstract

Identification and seismic mapping of mass-transport deposits (MTDs) are vital targets for marine geological studies both for a better understanding of mass wasting processes and geohazards and for economic prospects in sedimentary basins. Refinements on the interpretation of these geobodies have benefited in the last decades from increasingly good quality 3D seismic data. However, approaches to define characteristics, rheology and mechanics of such slope failure deposits still rely mainly on inferences of case-dependent interpretations of these stratigraphic elements; furthermore, features and seismic characteristics of MTDs may vary significantly from one case to another, implying the existence of many different environments and related physics. This makes the study of submarine mass movement a challenging task for a seismic interpreter. In this paper, we present a new conceptual analytical method based on an objective approach for interpreting the wide range of diverse objects related to mass wasting, in order to minimize seismic interpretation subjectivity. We propose an ontology-like methodology, based on a conceptual organization of a

¹ Permanent address : pauline.lebouteiller@mines-paris.org

diversity of interpretation elements arranged in a knowledge base. MTDs are considered as objects with representative properties, each one characterized by several descriptors, which are themselves impacted by multiple physical processes in a graph-based conception. We thus propose a method to infer the most probable interpretations for one mass-transport event from its deposit characteristics. We applied our graph-based methodology on two MTDs delineated in 3D seismic data in the Offshore Amazon Basin, Brazil. Based on the analysis of all MTD properties and their possible causes, several candidate interpretations were provided. These interpretations yielded by the graph are in line with the known geology and instability processes of the region, thereby validating the feasibility of the approach. The next development stage is a numerical definition of the knowledge base for further sharing and operability.

Keywords

Mass transport deposits

Mass transport processes

Submarine slope failures

Seismic interpretation

Knowledge-based interpretation

Ontology

1. Introduction

Mass transport deposits (MTDs) are geological bodies resulting from gravity-driven downslope mass movement. As such, they are an invaluable source of information on instability events themselves, and yield insights for current assessment of continental slope geohazards. Submarine slope failures have been shown to contribute significantly to sediment transport and sedimentary records in some basins (e.g. Lee *et al.*, 2007, Shipp *et al.*, 2011). Research on their genesis and evolution should improve stratigraphic analyses on basins infilling and geometries; it may also provide information on their economic petroleum potential and industrial hazard assessment (Alves, 2015).

The literature reports that MTD objects can provide direct information on former processes in a basin. Existing classifications of MTDs (e.g., Varnes, 1958; Mulder & Alexander, 2001b; Moscardelli & Wood, 2008; Posamentier & Martinsen, 2011; Talling *et al.*, 2012) illustrate this point properly, as they tend to relate typical aspects of objects with typical failure-related processes. Classifications are commonly based on a combination of internal and external features of the MTD, its depositional environment and the former event itself. Yet case-study interpretations are often site-specific and MTD objects do not always fit in widely validated classification schemes (Vanneste *et al.*, 2014). Similarly, large-scale statistics on MTDs (e.g. Owen *et al.*, 2007, Leynaud *et al.*, 2009, Urgeles & Camerlenghi, 2013), although demonstrating links between MTD characteristics and different environments, may not always be applicable in different geological settings. However, a lot of knowledge is unquestionably already available on how to interpret features of MTD objects. The question we tackle here is how to interpret MTD history from their seismic signatures, using available knowledge as objectively as possible.

1.1. MTD characterization

Given the great complexity and variety of MTDs, their characterization may stand as a quite challenging task. In any case, MTD characterization from seismic data starts by a description of the concerned geobody. In such a description, it is important: (1) to include all relevant descriptive features; and (2) to use the information contained in the seismic data as much as possible. A great variety of these features have been highlighted in the literature. They include: (i) geomorphologic features (e.g. Moscardelli & Wood, 2008), such as general shape and deposit geometry, spatial arrangement/continuity, recognizable ‘tongues’ showing deposit irregular extension, and a potentially visible headscarp, allowing to relate MTDs to their original stratigraphic position and loci if not already known (e.g. Vanneste *et al.*, 2014); (ii) kinematic indicators (Bull *et al.*, 2009), such as evidence for flow direction, deformation and/or erosional markers and signs of

compression/extension; (iii) stratigraphic elements, such as their position in the depositional succession for timing precision and any attempt to date the deposit. Internal features of MTDs are also valuable to infer event-related processes. Yet the internal architecture of MTDs, and their lateral facies variability, are not often taken into account (e.g. Ortiz-Karpf *et al.*, 2016). 3D seismic data may provide useful information in this respect (e.g. Frey-Martínez, 2010). Thanks to their higher resolution and two horizontal directions, 3D data enable refined and more reliable quantitative characterization of the properties of the object, although extra working time may be required for analysis with respect to studies from 2D data. Spatial distribution of several MTDs in a basin also proves useful to assess the frequency of slope failure (e.g. Urgeles & Camerlenghi, 2013), as well as the evolution of certain processes in space or over time (e.g., Wu *et al.*, 2011, Ortiz-Karpf *et al.*, 2016, Reis *et al.*, 2016) when ages are constrained.

In such a context, previous studies tend to highlight only certain kinds of MTD features depending on the study. But to obtain a complete, objective description of an MTD, all of its features need to be taken into account.

1.2. [Interpreting MTD processes](#)

From observed MTD seismic features, the processes related to physical failure suspected to play a role in the genesis of an MTD cannot always be quantitatively estimated. Thus, over-simplified interpretations based on descriptive approaches may come out (Vanneste *et al.*, 2014), whereas factual, verifiable relationships are required. In particular, an interpreter should be careful when inferring local or too precise conclusions on slope-failure-related processes from statistical or conceptual relationships only. For instance, Urlaub *et al.* (2013) emphasize that the claimed link between sea-level change and mass transport triggering (and therefore the presence of MTD in a sedimentary unit) cannot be statistically inferred from worldwide MTDs – which does not mean it does not exist. Focusing rather on intermediate impacts (e.g. the impact of sea level fall on fluid migrations within the slope basement), which in turn affect slope stability, may enable to fit distinct responses of various environments. Unlike over-simplified interpretations, too precise ones may result in interpretations that are ‘overfitted’ to the seismic data. A balance thus needs to be found in the way interpretation is performed.

A failure event can be described by its triggering phase (possibly involving pre-conditioning environmental factors), its transport phase and its deposition phase (to which post-deposition processes may be added). The final (present-day) configuration of an MTD typically results from a variety of mass transport-related processes. One event may be generated by several causal processes (Richardson *et al.*, 2011), encompassing both actual triggering factor and pre-conditioning factors.

Identifying one as the only triggering process is incorrect, as they may be mixed and interfere with each other both in temporal and spatial scales. The same is true for mass transport during the event: transport takes place at different scales (e.g. grain scale / flow scale); it implies several physical processes which are linked, even though modeling techniques tend to deal with one or other process at a time. Therefore, attempts to infer mass transport processes from MTDs should take into account the possibility of multiple influences, and also envisage the possibility of multiple interpretations before selecting the most probable one(s).

In all steps of an MTD characterization study (from initial description to inferring mass transport processes), to equivalently encompass various kinds of processes and MTD features would enhance the reliability of MTD interpretation. It would also enable objective comparisons. The principle of MTD classifications tends to oversimplify the description and characterization of MTD features and their generating mass transport processes. To date, the variety of physical processes involved in a mass transport, and the many seismic characteristics of their deposits, have not yet been integrated in non-oriented/agnostic seismic interpretation schemes. Such a scheme should take advantage of both existing knowledge (e.g. the literature) and seismic data specific to a case study, as two complementary sources of information.

1.3. Ontologies for inference problems in geological interpretations

Problems involving multiple data features of different kinds (e.g. quantitative and qualitative), multiple causal factors, and heterogeneous information sources, can be tackled by ontologies (e.g., Reitsma *et al.*, 2009). An ontology of a domain is an “explicit formal specification of the terms in the domain and relations among them” (Gruber, 1993). An ontology describes the domain exhaustively as a dictionary; it can be used as inference engine with an adequate methodology extracting information from it. In geoscience, it can e.g. link several kinds of data and models, as done by Wang *et al.* (2018) who proposed an ontology on the ‘local geologic time scale of North America, paleontology, and fundamental geology’, together with a methodology to retrieve information from it. It may also convey the heuristic rules of inference of a domain; for instance, Verney (2009) presented an ontology for structural interpretation of a seismic cube.

Ontologies have methodological advantages. They help formalize and separate data-based and knowledge-based elements. They are aimed at being shared and improved as much as wanted by anyone. They can be used in several ways. They yield repeatable results, and they can be automatized.

An ontology could therefore be a relevant approach to the problem of inferring potential causal processes explaining MTD seismic features.

1.4. Contributions and organization of this paper

In this paper, we build a knowledge base conceived as an ontology, which we consider an unbiased, standardized framework to convey the variety of features characterizing MTDs and their generating processes (section 2). We present a methodology for the interpretation of MTDs using this knowledge base. In this methodology, MTDs are considered as objects with representative properties, each one characterized by several features. These features are impacted by multiple physical processes, and these potential impacts are listed in the knowledge base. Our approach is an attempt to merge published results from a multi-disciplinary ‘review’, to enable a systematic comparison of several objects, while highlighting a variety of mass transport processes. We present an application of our methodology using 3D seismic data acquired offshore the Amazon River Mouth Basin (or Foz do Amazonas Basin, hereafter ‘Amazon basin’); the case study is presented in section 3, and the application of the methodology is detailed in section 4. The validity of our results is analyzed in section 5, and we discuss the global methodology in section 6. Our results enabled the validation of the methodology while showing its limitations and pointing out possible enhancements.

Throughout this article, the event(s) at the origin of one MTD will be called (a) mass-transport event(s).

2. Developing a new methodology for interpreting mass-transport processes from MTDs' seismic signatures

2.1. A new approach to an ontology

The methodology developed here relies on a global hypothesis: MTDs' observed characteristics are related to the processes that generated these objects, directly (one process acting on one observed characteristic) or indirectly (one process acting on another one, in turn affecting an observed characteristic).

We therefore have to consider an exhaustive description of MTD objects on the one hand, and an exhaustive description of the physical processes involved in the mass-transport event on the other hand. More precisely, the physical processes considered are the ones acting before, during or after the mass transport itself, and which may affect the mass-transport event; they may also be processes evolving at larger scale, related with the regional or global environment (hereafter 'environmental controls'). Finally, we need to represent the possible impacts of one phenomenon (process) on an observed characteristic of the MTD, or on another phenomenon.

Here, such an exhaustive representation of processes for geological object interpretation is approached by the use of an ontology. In our work, an 'MTD interpretation' ontology is a knowledge base containing information from this field of expertise, in the form of relationships, or laws, between key objects or concepts of that field. It is supposed to be exhaustive. The ontology is itself the set of objects (or concepts) and laws. The laws may be obvious, or heuristically admitted, e.g. 'arc-shaped pressure ridges on a MTD indicate a perpendicular flow direction' (e.g. Bull *et al.*, 2009). They may also be laws proven by numerical or experimental modeling, e.g. 'higher initial potential energy of unstable material yields higher runout distance for this material' (Mangeney-Castelnau *et al.*, 2005).

We build up our knowledge base as a graph (also called relation map in this paper). A graph is a diagram consisting of a set of nodes together with edges joining certain pairs of these nodes (Merris, 2001, Bondy & Murty, 2008). This representation shows how several objects / concepts, represented by nodes, are interconnected. It can also be represented in the form of an 'adjacency matrix', whose coefficients correspond to the connection between two nodes. In our case the nodes are physical processes of the mass-transport event, and are also their signatures named 'MTD descriptors'. The

word ‘descriptor’ is preferred to ‘feature’ as it conveys the notion of a description of an MTD property. Edges can be either lines (undirected relationship) or arrows (directed relationship), in which case they represent the impact of one node on another one (Figure 1 (a)).

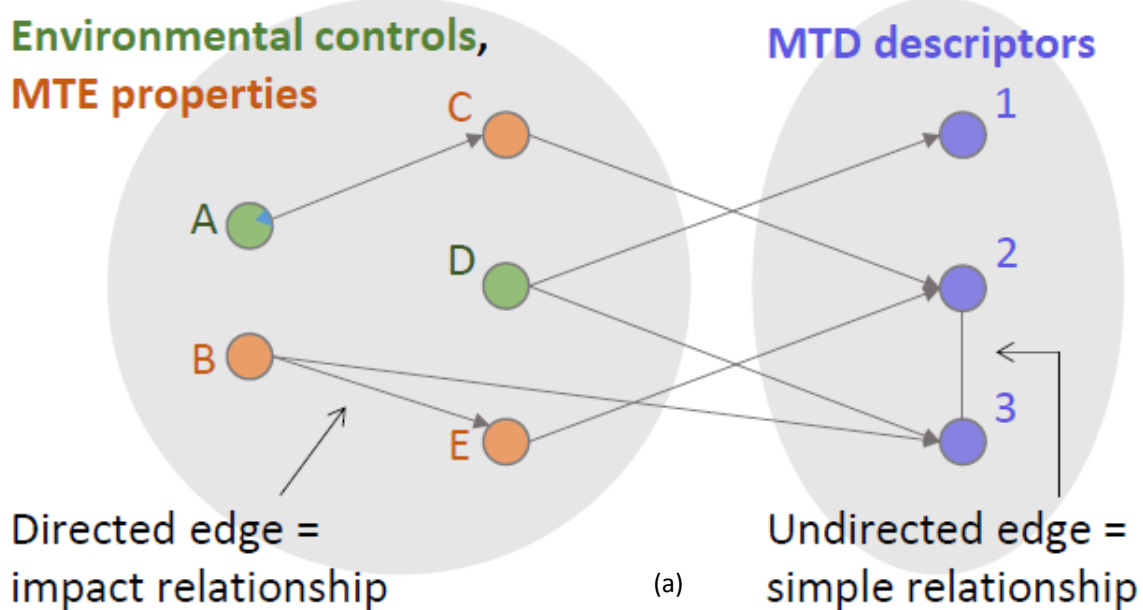
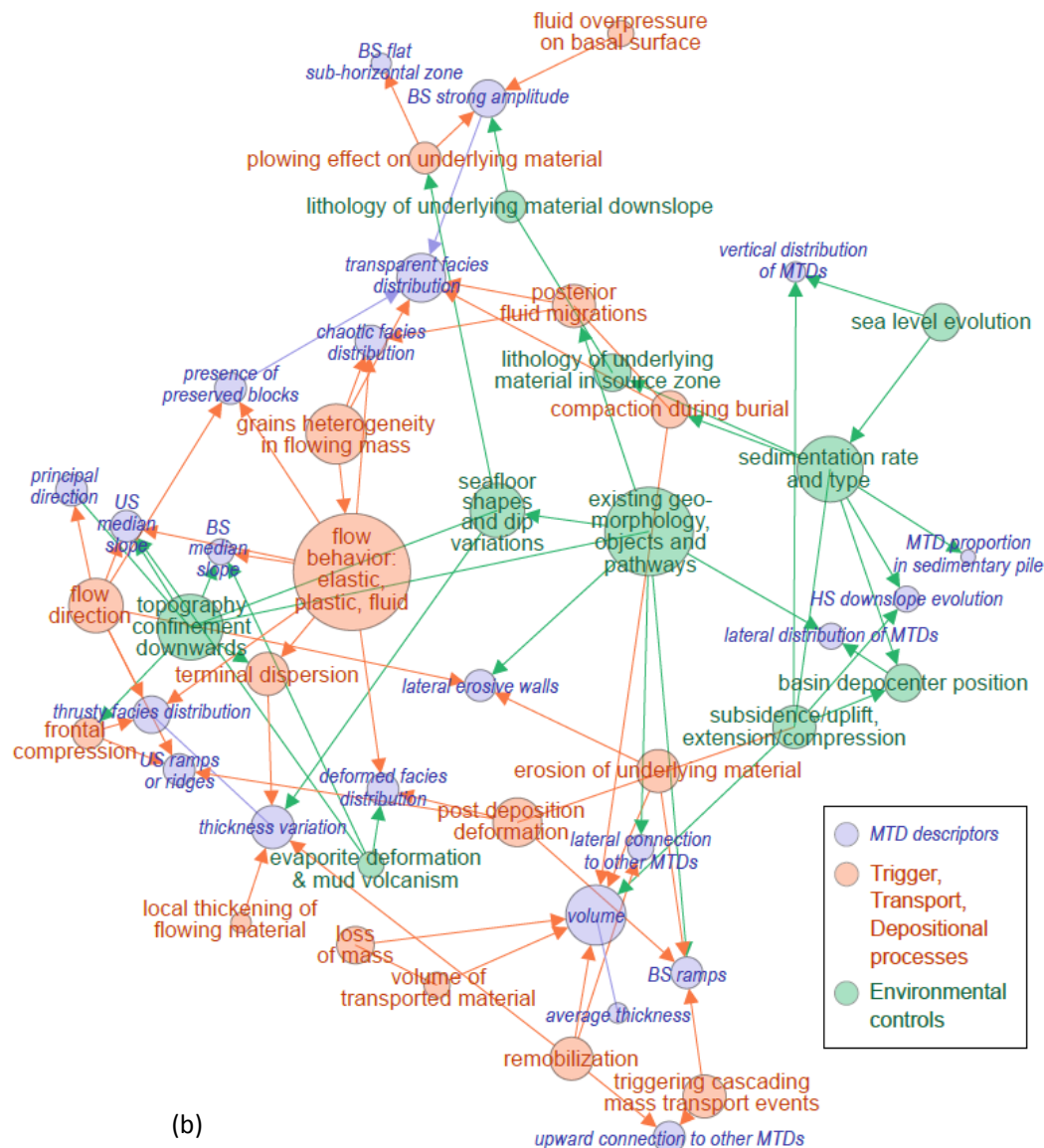


Figure 1. (a) Schematic representation of our graph (relation map). Dots are nodes, colored according to their category (environmental controls, mass transport event (MTE) properties or mass transport deposit (MTD) descriptors); lines/arrows are undirected/directed edges. Interpretation for MTD descriptor 2 yields nodes C and E as direct potential impacting processes, then nodes A and B; node 3 is only related to node 2. (b) Representation of a sub-part of the global knowledge base, with nodes mentioned in the proposed application (Section 4).



(Figure 1 - continued).

2.2. Building up the relation map: nodes and edges from a bibliographical study

From a bibliographical study, we created a list of the most-relevant MTD descriptors (Table 1) that may be signatures of the mass-transport event characteristics, and a list of the most relevant phenomena (processes) (Table 2) involved in a mass-transport event. These two lists contain all the nodes of the graph.

The bibliographical study considered only works based either on statistical approaches of several well-known MTD cases, or on conceptual, numerical or experimental modeling (e.g. Mourgues *et al.*, 2014). Case studies were also used when their results were considered generalizable to other cases

(e.g. Sutton & Mitchum, 2011). Each considered study focuses on one, or a series, of parameters controlling a mass-transport event and shows how (to a certain extent) these parameters impact some specific MTD descriptors (e.g. volume, shape of the basal surface, presence of preserved clasts inside the MTD, etc.). We kept these parameters and the MTD descriptors to be the nodes. Note that MTD descriptors and physical processes were filtered to keep only those that are relevant for interpreting seismic data. The bibliographical selection is hoped to be sufficient to meet the exhaustiveness criterion needed for the knowledge base – this point could weaken our definition, but the bibliography set can be augmented whenever needed.

MTD descriptors were gathered into 7 groups (hereafter ‘properties’) that characterize an MTD as a geological object: Global Environment, Morphology, Position, Basal Surface, Upper Surface, Internal Facies Distributions, and Headscarp. All descriptors (listed in groups in Table 1) are global; they are either qualitative or quantitative. In this article, every MTD descriptor will be written in *italic* characters.

Properties	Morphology	Basal Surface	Upper surface	Position	Head scarp	Internal Facies Distributions	Global Environ ment
Descriptors	thickness variation average thickness width variation horizontal aspect ratio volume surface area maximum horizontal length principal direction presence of ‘tongues’ at toe BS median slope BS flat sub-horizontal zone plunging pool indicator multiple terracing downslope BS ramps scours, grooves or striations lateral erosive walls BS strong amplitude	US median slope US ramps or ridges US with turbidites on top upward connection to other MTDs lateral connection to other MTDs near structural elements laterally runout distance	HS downslope evolution HS morphology presence of preserved blocks preserved blocks size chaotic facies distribution transparent facies distribution faulty facies distribution ridged facies distribution thrust fault angle increase to toe lithology distribution in MTD deformed facies distribution MTD proportion in sedimentary pile lateral distribution of MTDs vertical distribution of MTDs				

Table 1. MTD characteristic properties and their descriptors. BS: Basal Surface, US: Upper Surface, HS: Headscarp.

Similarly, we gathered processes into 2 main groups: external, large-scale environmental controls at the time of the mass-transport event (e.g. sea-level curve trend, type of depositional environment, presence or not of confined topography, etc.), and physical properties of the event itself. The latter were divided into 3 sub-groups, according to the 3 phases describing a mass transport: trigger-related, transport-related and deposition- (or post-deposition-) related properties. All the selected environmental controls and mass-transport event properties are listed in Table 2.

gravity, short term	Trigger phase	Mass-transport event properties
seismicity, short term		
fluid overpressure, short term		
offshore events and waves	Transport phase	
chemical effects		
flow velocity and energy		
flow behavior: elastic, plastic, fluid		
local fluidization		
local thickening of flowing material		
volume of transported material		
flow direction		
modifying basin morphology		
inducing seismicity		
triggering turbidity current		
triggering cascading mass transport events		
erosion of underlying material		
plunging pool effect		
plowing effect on underlying material		
detached MTD		
grains heterogeneity in flowing mass	(Post-) deposition phase	
fluid overpressure on basal surface		
fluid overpressure in moving mass		
initial potential energy of mass		
lithology in transported mass		
frontal compression		
loss of mass		
remobilization		
compaction during burial		
posterior fluid migrations		
post deposition regional deformation		
trigger turbidity current at stop		
post deposition of turbidites		
terminal dispersion		
seismicity or waves, long term	Environmental controls	
evaporite deformation & mud volcanism		
sea level evolution		
basin depocenter position		
subsidence/uplift, extension/compression		
existing geomorphology, objects and pathways		
sedimentation rate and type		
pore pressure increase by compression		
pore pressure increase by fluid migration		
permeability increase		
lithology of underlying material in source zone		
initial aspect ratio and top of mass slope angle		
topography confinement downwards		
seafloor effective friction angle		
seafloor shapes and dip variations		
source domain in basin		
lithology of underlying material downslope		

Table 2. Environmental controls and mass-transport event properties. 'Mass-transport event properties' comprise properties of the trigger phase, the transport phase and the deposition phase (possibly including post-deposition modifications). 'Environmental controls' are potential impacting large-scale processes.

Finally, relationships between nodes were drawn to construct the edges, similarly extracted from the bibliographical study. Here, most of them are directed (arrow), representing the potential impact of one node on another node. A directed edge may connect one process and one MTD descriptor, as a direct impact of the former on the latter; or it may connect two processes (two nodes from Table 2), thus allowing large-scale/conceptual/statistical controls to have an indirect impact on MTD descriptors through smaller-scale relationships. The list of edges is provided in supplementary material (Table_Supplementary 1).

2.3. [Graph content details and analysis](#)

Here we first give some precisions on a few nodes (Table 1 and Table 2) and the graph itself.

2.3.1. [MTD descriptors nodes](#)

In the Morphology property, descriptor *principal direction* corresponds to the principal orientation of the 3D geobody (in its current state, or inferred at the time of deposition if restoration has been performed). Descriptor *presence of 'tongues' at toe* is a binary indicator of whether some 'fingering' instability occurred at the front of the mass flow (typically triggered by grain size segregation), yielding a non-smooth toe region with 'tongues' (Pouliquen *et al.*, 1997, Woodhouse *et al.*, 2012).

In the Basal and Upper Surface properties, descriptor *median slope* includes the value of the slope median and its variability laterally over the MTD basal/upper surface, in order to capture typical relief while not taking into account fault- or ramp-induced extreme relief. *Ramps* are stair-like structures on basal or upper surfaces (e.g. Bull *et al.*, 2009). The *plunging pool indicator* is a reversed bell shape on a surface, associated to hydraulic jump at a slope change in turbiditic systems, or to a unique high-energy mass transport digging into the underlying sediment (Lee *et al.*, 2002, Bourget *et al.*, 2011).

The Headscarp property has two descriptors: *HS downslope evolution* indicates whether a series of headscarps are positioned gradually more basinwards with time (i.e. going up in the sedimentary deposits); *HS morphology* is a qualitative labelling of a headscarp between types 'onlap of upper surface on basal surface', 'cookie-bite', and 'unclear evacuation zone' (Richardson *et al.*, 2011, Dalla Valle *et al.*, 2013).

In the Internal Facies Distributions property, all facies distributions are typically described by their internal variations in the 3D space, comparing different regions within the geobody. The *ridged facies* is depicted by overlapping reflectors in the seismic data; whereas descriptor *thrust fault angle*

increase to toe is a binary indicator for cases with specific initial internal geometry or seafloor slope (Richardson *et al.*, 2011).

Note that all descriptors may not be available for all kinds of data/objects observed. In practice, two main limitations may prevent the availability of one or several descriptors: (i) if the MTDs and their corresponding headscarps are not entirely imaged within the seismic dataset used; (ii) if the data resolution is insufficient for Morphology, Facies and Environment precise descriptions, and if the surfaces needed were not picked with sufficient precision. First, to guarantee the detection of the top and bottom surfaces of an MTD, typically two reflectors, its thickness must be more than twice the seismic vertical resolution (ratio thickness/resolution > 2). For characterizing the MTD properties, more constraints apply. Facies descriptions within the MTD require a larger MTD thickness/resolution ratio: ~3 or higher, depending on the facies kind (~3 for imaging deformed reflectors, ~5 for spotting preserved clasts within a matrix). This is more often the case for MTDs that are not too deeply buried (Alves *et al.*, 2014). Concerning surfaces, slope variations that allow description of ramps, for example, will not be seen if occurring on smaller scales than the precision of the picked surface. Morphological descriptors, as well as specific descriptors of the headscarp, or of the toe, of an MTD, require that these parts of MTDs be covered by the dataset. An estimation of the needed data quality for acquiring each input descriptor is provided in supplementary material (Table_Supplementary 2).

2.3.2. Processes nodes

Processes nodes (Table 2) are not thoroughly detailed here. We here only mention that, in Environmental Controls, 'evaporite deformation' and 'mud volcanism' have been joined into one node to account for non-tectonic deformation in general, comprising mud volcanism, creep of evaporites, and even potentially diapiric movement of mud or salt (e.g. Moscardelli & Wood, 2008, Posamentier & Martinsen, 2011, Omosanya & Alves, 2013). Node 'subsidence/uplift, extension/compression' corresponds to large-scale tectonic or isostatic controls. Concerning node 'plowing effect on underlying material' (*sensu* Posamentier & Martinsen, 2011), it implies reworking the sediments of the underlying stratum with the basal material of the flowing mass, capable of inducing compaction and dense deposition in the basal part of the mass.

Finally, there are no nodes from mass-transport event classes according to existing classifications (see e.g. those mentioned in the Introduction), since mass-transport event classes may differ from one classification to another, and since they do not correspond to actual processes.

2.3.3. Graph analysis

Taking all nodes and edges together, the final graph built up in this work (relation map) counts 88 nodes (38 MTD descriptors and 50 processes) and 173 edges. A full graph visualization is provided in Figure_Supplementary 1 (supplementary material), with a mapping of nodes and edges, and a representation of the adjacency matrix; this visualization illustrates the variation of ‘degree’ (i.e. the number of edges connected to them) between nodes, by node size variation.

The ‘degree’ of the nodes is an analytical tool for graphs in general. Here (as also shown on Figure 1 (b)), it is not evenly distributed among nodes. Some processes (with high ‘degree’) are therefore more likely to impact final MTD descriptors than others. These are the flow behavior (rather viscous or fluid), geomorphological objects and pathways already present at the mass-transport event time, sedimentation rate and type at that time, the presence of topographic confinement downwards, and the heterogeneity of the flowing material.

From the adjacency matrix of the graph, we highlight that no edge exists between trigger-related processes and MTD descriptors (no connection appearing in the corresponding regions of the matrix). The impact of the former on the latter is indirect: trigger properties impact transport-related processes, which in turn impact MTD descriptors.

2.4. Methodology: how to use the graph (relation map)

As an ontology, our knowledge base can be used as an inference engine, i.e. to infer new results on potential causal processes from an applied case study.

The MTD interpretation methodology, relying on the graph, is divided into 3 steps:

- First, we characterize each MTD by a detailed description of its 7 properties: for each property, we give a value to its quantitative/qualitative descriptors. Qualitative values are given from data observation; quantitative values are obtained from a few computations on the data. Some edges guide the acquisition of descriptors, e.g. the description of ‘lateral erosive walls’ also includes whether they are seen on one edge only or more, as this element is impacted by an edge. After this step, the MTD is characterized by 38 descriptors (Table 1) if all are available on the data.
- Then, for each descriptor, we look for all edges (arrows) pointing at it; at the other end of these arrows, are given possible controls or event properties (among those listed in Table 2) that may have an impact on the considered descriptor. This corresponds to looking for the

possible *causes/explanations* for the descriptor's value. We note all the possible 'causes' that the graph suggests, no matter how relevant they are regarding other factors.

- Lastly, for each possible 'cause' listed in the previous step, we evaluate how uncertain it is: if the cause was found several times (i.e. if several descriptors pointed to it), then it is quite likely; if another cause was found that is contradictory to this one, then it is highly uncertain, as well as the other one. This implies that the *explanation* for some MTD descriptor might remain unsolved until cross-checking with one or several other descriptors. Thus, a result from the graph is obtained only when all available descriptors have been analyzed.

Final results of the relation map are not necessarily final interpretations, but rather hypotheses; the relevance of the methodology should be explicited by the consistency between these hypotheses and available knowledge on the zone.

3. Presentation of the Amazon case study

This Section presents the geological settings of the region selected for testing our methodology: the Amazon basin. It also presents the data and material we used as inputs for applying the methodology.

3.1. The Amazon basin and MTDs

The Amazon basin sedimentation has been highly impacted by gravitational processes, at large and small scales (e.g. Reis *et al.*, 2010, Reis *et al.*, 2016, Silva *et al.*, 2016). Its geological history is closely related to that of the South-American continent. Since the onset of the Amazon River as a transcontinental river, believed to have occurred during the Miocene together with the Andean uplift (11.8 – 6.8 Ma, Figueiredo *et al.*, 2009), the river sediment discharge has kept increasing, progressively building up siliciclastic series on top of an in-place Cenozoic carbonate platform and in the basin. A deep-sea fan has developed further from the continental shelf.

The current Amazon basin is marked by large-scale gravitational deformation and several huge MTDs, marks of intense destabilization on the margin. These large MTDs have been documented and approximately dated; they are positioned in two zones: NW and SE from the main canyon axis (e.g. Reis *et al.*, 2010, Reis *et al.*, 2016, Silva *et al.*, 2016, Figure 2).

Smaller-scale MTDs are also visible, on or near the fan; some of them are definitely linked to basin-scale compression-extension processes. Globally though, the origin of these MTDs could be related to channel-levee complex instabilities on the deep-sea fan (Damuth & Embley, 1981), instabilities from fold-and-thrust belts on the deep-sea fan (Reis *et al.*, 2010), sea-level drop inducing gas-hydrate destabilization (Maslin *et al.*, 2005), and/or sediment collapsing under their own weight (Reis *et al.*, 2016).

3.2. MTDs in the NW part of the basin

Our study focuses on a sub-basin: the NW region of the basin, where the Amapá Megaslide (AM) has been studied and mapped by Silva *et al.*, 2010, Silva *et al.*, 2016 and Reis *et al.*, 2016 (Figure 2). AM consists of several mass transport complexes (MTCs): (1) The Amapá Lower Complex, (AM1 in Reis *et al.*, 2016) is the oldest (late Miocene) and probably results from a collapse of the mixed carbonate-siliciclastic platform; (2) the Amapá Upper Complex (comprising AM2 to AM6 in Reis *et al.*, 2016) is more recent (Pleistocene) and probably results from destabilizations of siliciclastic sediments on the marine slope favored by a regional décollement level – they were indirectly triggered by overpressure on this level on the deep-sea fan. The 50°W and Western MTD (also called Western

Debris Flows) are superficial MTDs (Figure 2), uncertainly dated 15 to 75 ka (Damuth & Embley, 1981, Damuth *et al.*, 1988). Both of them are associated with the deep-sea fan development and instabilities in quickly accumulated sediments on the fan flanks (Maslin *et al.*, 2005, Damuth & Embley, 1981).

In this paper we analyzed five MTDs observed in the basin of this NW region (see next Section and Figure 3). Their lateral position covered by our seismic data (dark orange in Figure 2) is a few tens of km away from the sides of the Amapá Upper Complex and 50°W MTD.

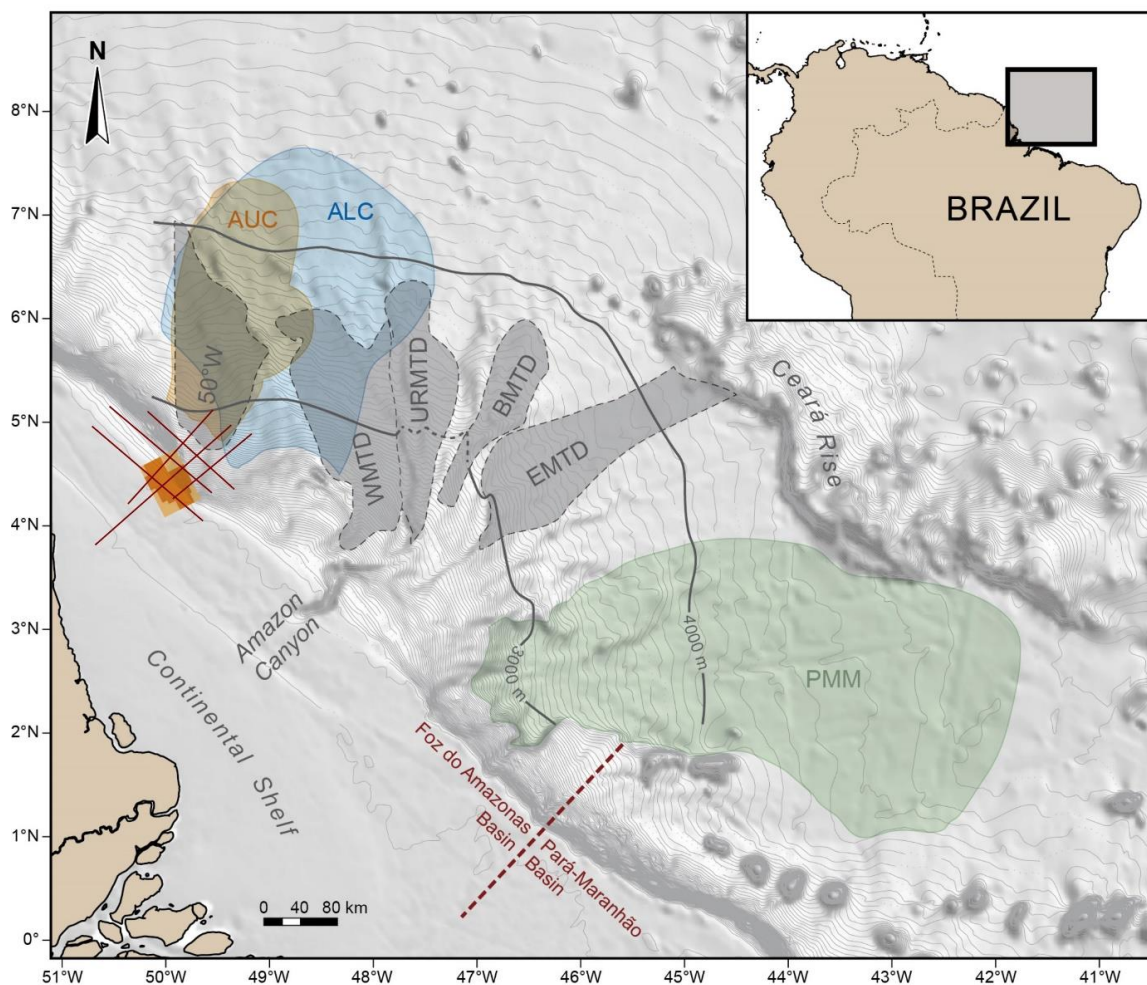


Figure 2. Bathymetric map of the Offshore Amazon basin with location of major previously-studied MTDs and seismic data used in this article. Modified from Reis *et al.*, 2016 and Silva *et al.*, 2016. The 50°W (Damuth & Embley, 1981), WMTD, EMTD (Western / Eastern MTDs, Damuth *et al.*, 1988) are superficial MTDs. URMTD and BMTD (Unit R / Buried MTDs, Damuth *et al.*, 1988) are buried. The Amapá and Pará-Maranhão Megaslides (ALC-AUC / PMM) were studied by Silva *et al.*, 2010 and Reis *et al.*, 2016. Amapá Lower Complex (ALC), the deepest mass transport complex of Amapá, is mapped in blue; Amapá Upper Complex (AUC), more recent, is mapped in orange, after Reis *et al.*, 2016. The 3D seismic cube is mapped with available seismic data in dark orange and 2D seismic profiles are mapped in dark red.

3.3. Data and materials – input descriptors for the methodology

Given the list of seismic MTD descriptors (Table 1), the mandatory data to test our relation map on MTDs in a seismic dataset consist of (i) basal and upper surfaces of each MTD delineated in the seismic data, (ii) position and headscarp descriptors of MTDs (contextual information), and (iii) seismic facies distributions for the seismic data and specifically for each MTD.

The seismic data used in this study is a post-stack time-migrated 3D cube granted by CGG Houston. The dominant frequency of the signal is 37 Hz, yielding a 10-20 m vertical resolution for velocity considered in [1500 to 3000 m/s]. The cube size is 60 x 43 km (2388 inlines, 1732 crosslines), with 25 m of intertrace; in this rectangle, data is available in parts only (see dark orange in Figure 2). The cube is on the current shelf break with dip-oriented inlines, at the junction of three major domains: shelf, basin and deep-sea fan in the southern part. Upslope scarps were hand-picked in this cube and interpolated as surfaces using the GOCAD interpretation software.

For the MTDs description, a smaller cube was selected, in the deep Amazon basin setting; it was restricted to a clastic sedimentary succession (2 sTWT thick) lying above the paleo-carbonate platform. The extent of our case study area was therefore 13 x 18 km, counting 512 crosslines and 710 inlines (see Figure 3). In this smaller cube, five observed MTDs were selected to be analyzed here. Their basal and upper surfaces were hand-picked on 72 inlines over the 710 of the 3D seismic cube, using MATLAB and the GOCAD interpretation software. Figure 3 shows the MTDs, and upslope scarps, within the 3D seismic frame. The MTD thicknesses are ~50 ms in average, 40 ms at minimum and ~95 ms at maximum. The thickness/resolution ratio is therefore of 3 to 7.1 (for velocity of 1500 to 3000 m/s), which ensures a proper acquisition of input descriptors (see section 2.3 and Table_Supplementary 2). Among the five selected MTDs, MTDs A and B, which we study further (see next Section), are the deepest. They appear to be at the base of a seismic unit overlying a slope sedimentary series (Figure 4).

Comparisons of our analytical results with those from published seismic data rely on a few 2D seismic lines with 10-20 m vertical resolution, and a few previously-dated horizon surfaces provided by published material (e.g. Gorini *et al.*, 2014, Reis *et al.*, 2016). The horizons and seismic lines correlating with our seismic block enabled to assess a stratigraphic constraint on the studied region; upslope scarps and downslope MTDs are all more recent than 2.4Ma.

We associated a seismic facies classification to the 3D input data. This classification, an input for this methodology, was done independently thanks to a method developed by the IFPEN research group. The quality of this classification is beyond the scope of this paper: a detailed discussion will be the purpose of a coming paper. This classification, resembling that of Roy *et al.* (2014), was applied as follows: (i) the data were clustered into most-similar regions, which led to associate seismic facies labels to clusters of similar seismic properties; (ii) such a procedure enabled us to label each sample of the seismic data with one or several names of seismic facies. We here use the chaotic, transparent, deformed, strong-amplitude sub-horizontal, and ridged facies. Note that other facies descriptions (e.g. Alves *et al.*, 2014), if associated with seismic facies labels ('chaotic', 'deformed' etc.), could be used equivalently. The associations of facies labels with their descriptions have to be reliable and avoid pitfalls related to acquisition/processing footprints in seismic facies analysis (Marfurt & Alves, 2015). Figure 5 gives explanations for the precise meaning we ascribe to each one of our facies, coupled with examples of seismic aspect of each MTD facies. Note that the seismic facies defined this way are not mutually exclusive, i.e. a region in seismic data may have a 'chaotic' facies and a 'transparent' facies at the same time². Such multi-facies samples simply carry several labels (e.g. chaotic and transparent) with no prevalence of one over the other.

Quantitative descriptors of the Internal Facies Distributions and of the Basal and Upper Surface properties were assessed within the MTDs and on their contours. Proportions of facies within MTDs were calculated, either summing globally, or along a vertical or lateral direction. This enabled us to get maps or lateral variation plots, respectively. Additional information include facies proportions integrated over the 3D cube, and basal and upper surface gradient magnitude and direction, initially calculated on the time data and then assessed in °, a more practical unit, for a wave velocity range of [1500 to 3000 m/s].

² This is to keep in mind for the analysis of results in terms of proportion of facies in MTDs: the addition of the proportion of several facies inside a 3D object is not relevant.

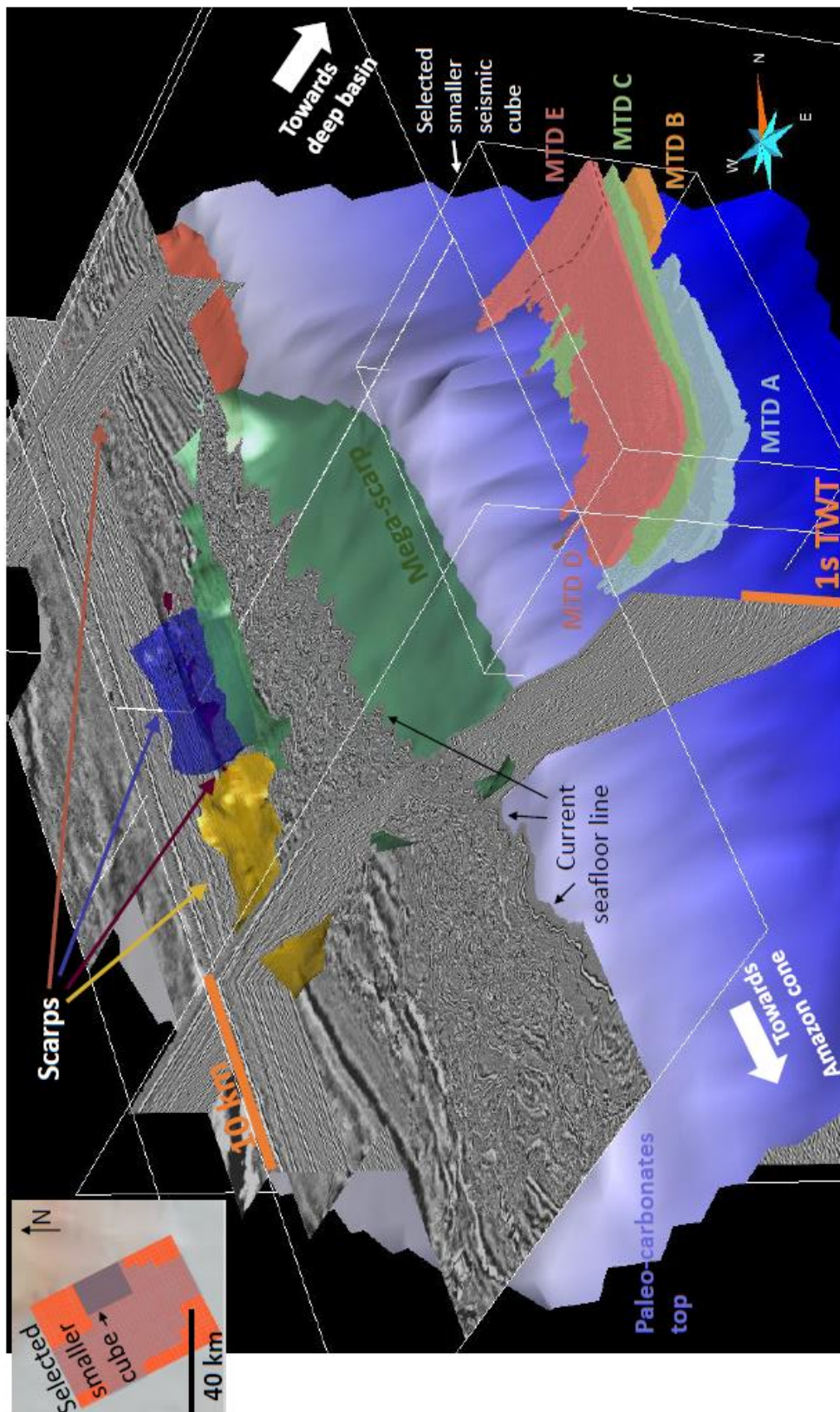


Figure 3. 3D view of the five MTDs highlighted in the studied data. MTDs D and E are separated by the brown dashed line. Colored surfaces are upslope scarps. Grey sections are seismic sections from the seismic cube. The largest blue surface is the carbonate platform-slope top (see also Gorini et al., 2014).

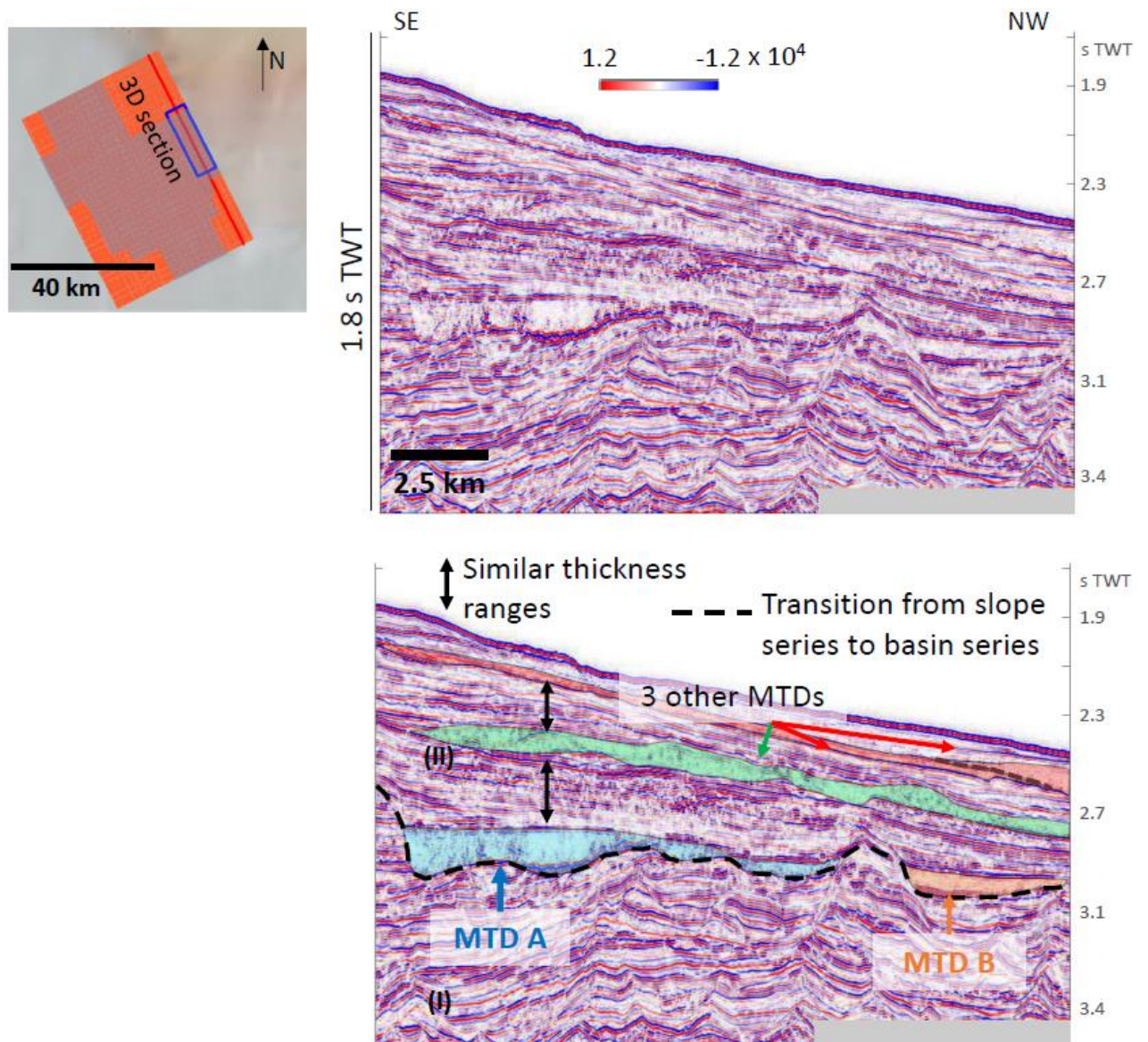


Figure 4. The 5 MTDs highlighted in one seismic section of the post-stack seismic cube (first/second view without, respectively with, interpretations on the seismic section). MTDs A and B seem to mark the beginning of seismic unit II above seismic unit I. The 3 stratigraphic periods for MTD deposition are separated by roughly similar thicknesses.

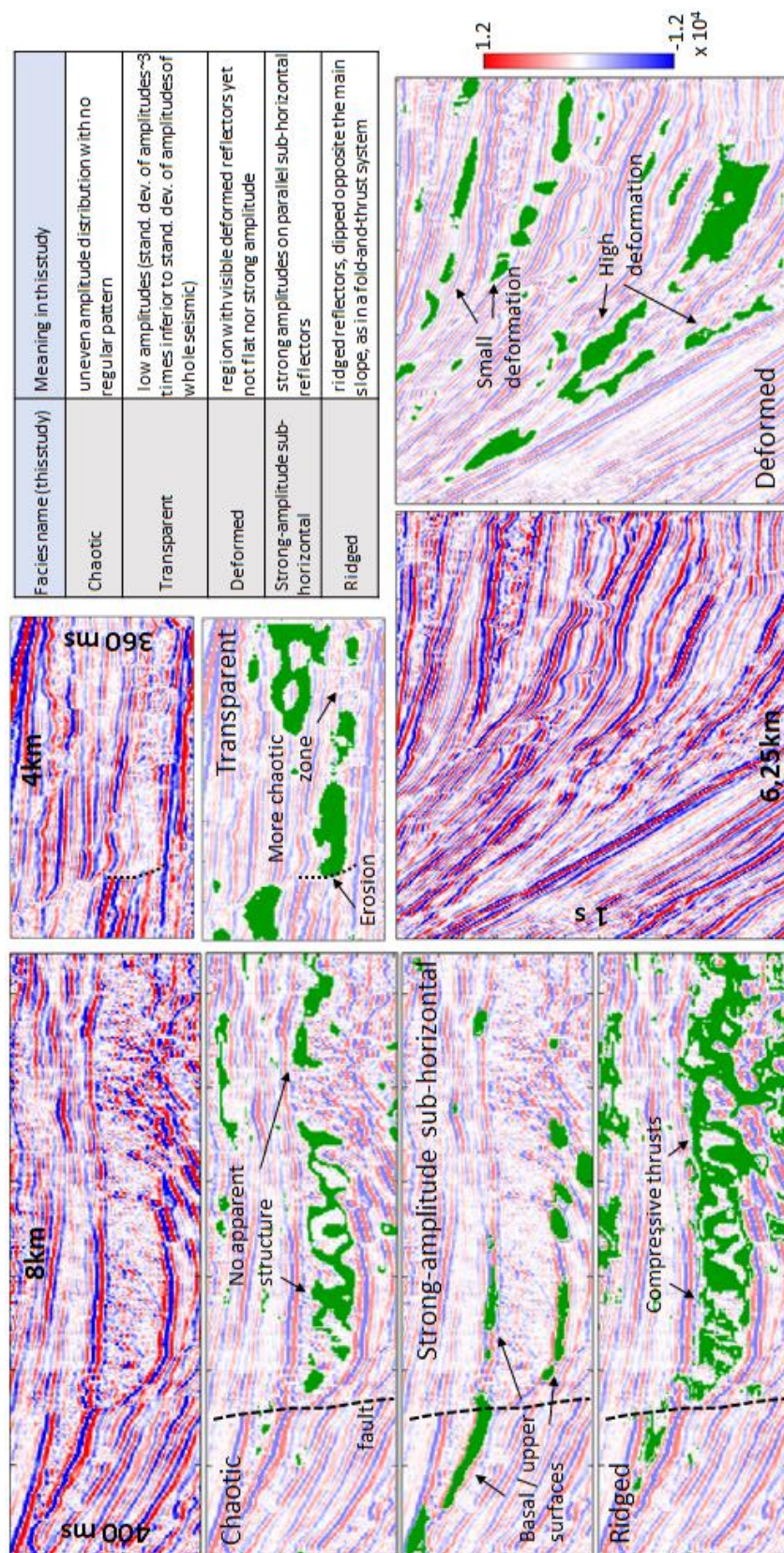


Figure 5. Five main seismic facies used in our study (shown in green patches on top of the seismic sections). Facies were interpreted based on an automatic method developed by the IFPEN research group, not detailed in this paper.

4. Application of the methodology to the case study

In this part, we present the use of the relation map to derive a set of possible interpretations from MTD descriptors. We study the two deepest MTDs: A and B (Figure 3, Figure 4), among the 5 MTDs available and within the cube.

For MTDs A and B, for each of the 7 properties (Table 1) defined in our methodology, we retrieve associated descriptors (among those available for these MTDs in our data) and detail the steps of the methodology. Note that the relation map yields several hypotheses that are not final interpretations; they are possibilities, listed and estimated with the unbiased approach of the ontology – contextual knowledge should then help select most-probable hypotheses. Figure 1 (b) illustrates this application with only the nodes mentioned in the text – the full graph is available in Figure_Supplementary 1 (supplementary material).

4.1. Global Environment

The Global Environment property has a few descriptors, which here concern the series of 5 MTDs (Figure 3). In our small seismic cube, the calculated global *proportion of MTD-delineated sediments* in the recent sedimentary series is 9%.

The *vertical distribution* of our 5 MTDs shows 3 main stages of deposition of sedimentary bodies (as two pairs of MTDs are in the same stratigraphic level). Firstly, this *vertical distribution* yields the relative age of all MTDs: MTDs A and B are the oldest. Secondly, the three main stages of sediment disruption are separated by a roughly similar thickness of sediments (Figure 4). According to the relation map, this vertical (almost) cyclical deposition could correspond to sea-level cycles (node ‘sea-level evolution’ impacting descriptor *vertical distribution*) – if MTD stages are interbedded with channel-levee systems (Sutton & Mitchum, 2011), which is not obvious from the data only. Alternatively, tectonic- or isostasy-related large-scale deformation could explain this vertical distribution (impact from node ‘subsidence/uplift, extension/compression’). Within the stages with two MTDs, nodes ‘existing geomorphology, objects and pathways’ and ‘basin depocenter position’ may impact the *lateral distribution* of MTDs, showing potential influences of the seafloor shape. The absence of MTD in the south-eastern part of the cube suggests that during all this period of clastic deposition, the sub-basin depocenter was never located in that part – but instead more basinwards, or more to the north-west; or, that the sub-basin south-eastern geomorphological conditions made it less exposed to mass-transport deposition.

4.2. Morphology

Descriptors depicting property Morphology are now highlighted, focusing on MTDs A and B specifically.

The *average thicknesses* of MTDs A and B, 97ms and 90ms respectively, are the largest of all 5 MTDs identified in the seismic cube. In the relation map, the *average thickness* node is related to the 'volume' node, which in turn is impacted by several nodes concerning transport- and deposition-related processes, such as: 'volume of transported material' (quantity of material), 'loss of mass', 'erosion of underlying material', 'compaction during burial', and 'remobilization'. Considering these MTDs are the oldest ones in the studied stratigraphic succession, they are the most likely ones to have been modified after deposition (by compaction); this suggests that they were maybe even thicker when deposited compared to the other MTDs. Moreover, 'loss of mass' during the event itself, or remobilization afterwards, would have decreased the final quantity of deposited material compared to the initially-deposited mass. As for process 'erosion of underlying material', it could decrease or increase the material quantity depending on the kind of erosion, which is not known for now. Therefore, the initial volume of sediment that was transported to generate MTDs A and B was probably equal to, or larger than, the current MTD volumes.

While MTD B is consistently thin on its upper sides and thickens downwards, MTD A has two distinct thicker zones. From the relation map, we know that node *thickness variation* is impacted by nodes 'remobilization', 'frontal compression', 'local thickening of flowing material', 'terminal dispersion', and 'seafloor shapes and dip variations'. According to the relation map then, MTD thicker zones may be related to (i) pre-existing depressions in the seafloor (see e.g. Sawyer *et al.*, 2012, Mulder & Alexander, 2001a and Table_Supplementary 1); or (ii) to a local thickening associated to ductile flow of the basal material (shown for sandy flows by Mourgues *et al.*, 2009); or (iii) to thrust-induced elevations of the upper surface. Further analyses on other properties should help limit possible interpretations. As for the 'terminal dispersion' and 'remobilization' nodes, they would cause thinning (rather than thickening), which we do not have here; thus for now we do not keep them as potential impacting processes.

Other descriptors of the Morphology property are not available due to the limited surface area covered by our data. Nevertheless, we note that the *principal direction* descriptor (i.e. principal orientation of the 3D geobody) is impacted by nodes 'flow direction' and 'topography confinement downwards'. For MTDs A and B, the *principal direction* is NNE, rather than ENE which is the basinward direction. One of the two mentioned processes could thus have influenced the deposit

principal direction to be eventually distinct from the main slope dip direction – but these interpretations are uncertain, due to the limited data available for *principal direction* assessment.

4.3. Position and Basal Surface (BS)

For both MTDs A and B, *lateral erosive walls* only occur along their southern limits, as highlighted on their basal-surface gradient map (Figure 6). The *lateral erosive walls* descriptor is impacted by nodes ‘erosion of underlying material’, ‘flow direction’ and ‘existing geomorphology, objects and pathways’ (Bull *et al.*, 2009, Moscardelli & Wood, 2008). These erosive walls are identified on the southern flank only; they are not aligned with the *principal direction* of the objects. These elements show a probable impact from node ‘existing geomorphology, objects and pathways’, which were therefore probably not symmetric with respect to the main flow direction at the time the event occurred; the ‘flow direction’ must have been modified from the ENE (main slope-dipping) direction to a NNE direction, thereby eroding the neighboring material.

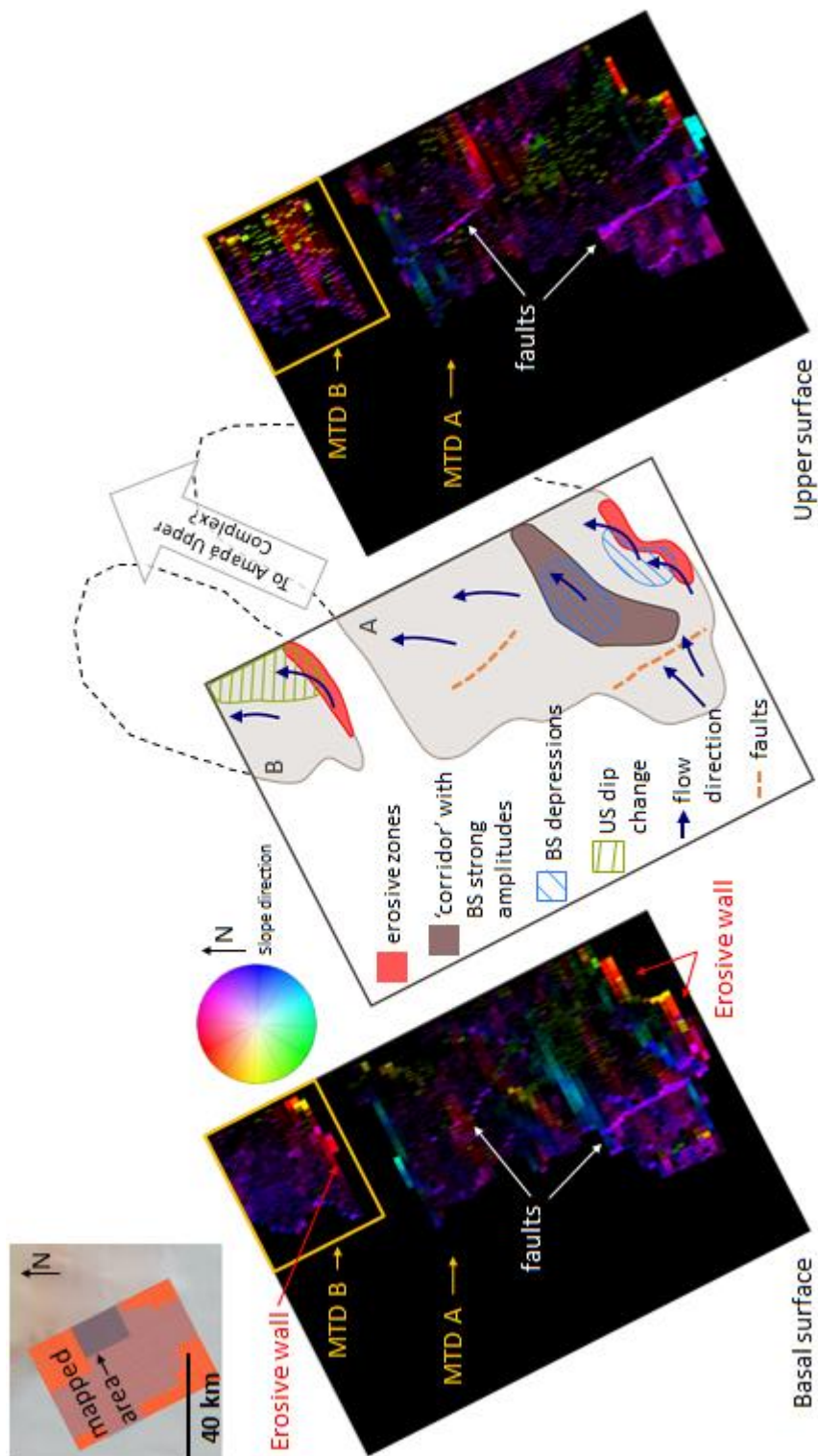


Figure 6. MTDs A and B slope maps of basal surfaces (BS) and upper surfaces (US). Dip direction shown by color hue, dip value by brightness. Both MTDs show a lateral erosive wall in their BS southern regions, and a change of BS and US dip orientation, indicating a change in orientation of the flow. Faults are visible on the BS and US of MTD A. Interpreted map shows a strong amplitude 'corridor' and two topographic depressions of the BS, retrieved from amplitude and topographic maps respectively. Amapá Upper Complex is described by Reis et al. 2016 (see Figure 2).

MTDs A and B are separated by ~500m laterally and underlined on the seismic sections by a common reflector (basal surface BS), thus implying events occurring in a same period of time. The *lateral connection to other MTDs* descriptor may be impacted by node ‘remobilization’ – suggesting on the one hand that MTD B was made from MTD A’s remobilized material –, and node ‘existing geomorphology, objects and pathways’ – suggesting on the other hand that MTDs A and B result from a single mass-transport event, whose deposit was separated by a topographic high downslope; note that these possible impacts are contradictory. Now, an *upward connection to other MTDs* is also observed, as the upper part of MTD B is located ~20msTWT above the lower part of MTD A. This *upward connection to other MTDs* node is impacted by nodes ‘triggering cascading mass transport events’ and ‘remobilization’ (which would be from MTD A to MTD B given their spatial relationship). Process ‘remobilization’ is enhanced as it appears for the second time. However, from what was proposed before (see Figure 6 and comments on the ‘lateral erosive walls’), the material of MTD B originates from the WSW and not from MTD A (SE). So, considering the remaining possible processes impacting the *lateral* and *upward connection to other MTDs*, MTDs A and B are probably either signatures of one single event (eventually separated because of pre-existing topography) or cascading events (having their sources close to each other, failure of MTD A triggering mass-transport event B).

While the basal surface of MTD B has no *BS ramps* and its *slope* is quite regular, from ~-1° to max. [-2.5° to (-5)°], *BS slope* of MTD A varies from [-5.5° to (-11.5)°] upslope, to +1° downslope, and is affected by *ramps* (Figure 7 – see similar examples in Richardson *et al.*, 2011). *BS ramps* are signatures either of node ‘triggering cascading mass transport events’, or of node ‘post-deposition regional deformation’, or of node ‘erosion of underlying material’, or yet of node ‘existing geomorphology, objects and pathways’ suggesting pre-existing ramps on the paleo-seafloor (e.g. Richardson *et al.*, 2011, Mienert, 2009, Frey-Martínez, 2010). Thus, these four processes are more likely to have occurred in MTD A than in MTD B. Further arguments from analyses on other descriptors/properties should allow to favor one among these four.

Basal surface (BS) of MTD A also comprises two deeper zones, or depressions; these account for the thickness variations mentioned previously. In these depressions, the BS has a *flat sub-horizontal* trend. This *BS flat sub-horizontal zone* descriptor may be the signature of a ‘plowing effect on underlying material’ (Posamentier & Martinsen, 2011, see also 2.3). This process seems here more likely in the two depressions of MTD A. To explain the local thickness variations analyzed in 4.2, it goes along with either (i) pre-existing depression in the seafloor or (ii) local thickening associated to basal ductile flow, rather than thrust-induced elevation of the upper surface (iii).

MTDs A and B are both characterized by the descriptor *BS strong amplitude*. Descriptor *BS strong amplitude* is impacted by nodes ‘lithology of underlying material downslope’, ‘fluid overpressure on basal surface’, and ‘plowing effect on underlying material’. In turn, node ‘lithology of underlying material downslope’ is related to node ‘lithology of underlying material in source zone’; this indicates that if the medium is homogeneous between source and deposition regions, then the impedance contrast seen at a *strong-amplitude* basal surface should be explained by a change in MTDs basal material rheology. In MTD A, one current topographic depression shows very high amplitudes, with a negative polarity (Figure 7); in MTD B, on the contrary, the polarity of the *BS strong-amplitude* region is positive. Based on the relation map then, two scenarios might explain these differences:

- MTDs A and B have similar acoustic impedances, but their respective underlying material has lower impedance in the south-east (under A) than in the north-west (under C). This could correlate with the occurrence of some degree of fluid overpressure along the BS of MTD A.
- The underlying material common to MTDs A and B has uniform acoustic properties, but the material of MTD B results in lower acoustic impedance than that in MTD A. As the material of MTD B does probably not originate from remobilized material of MTD A, the difference would then be due to different transport properties of the mass-transport event (either of the two ‘branches’ of a single event, or of the two cascading events). For instance, a plowing effect occurring in event A would lead to reorganization of its basal sediments, densifying the bottom of the MTD in one topographic depression (see ‘corridor’ on Figure 6).

The relation map here gives two main interpretation possibilities, which remain to be ranked according to further arguments from other properties or from posterior contextual information.

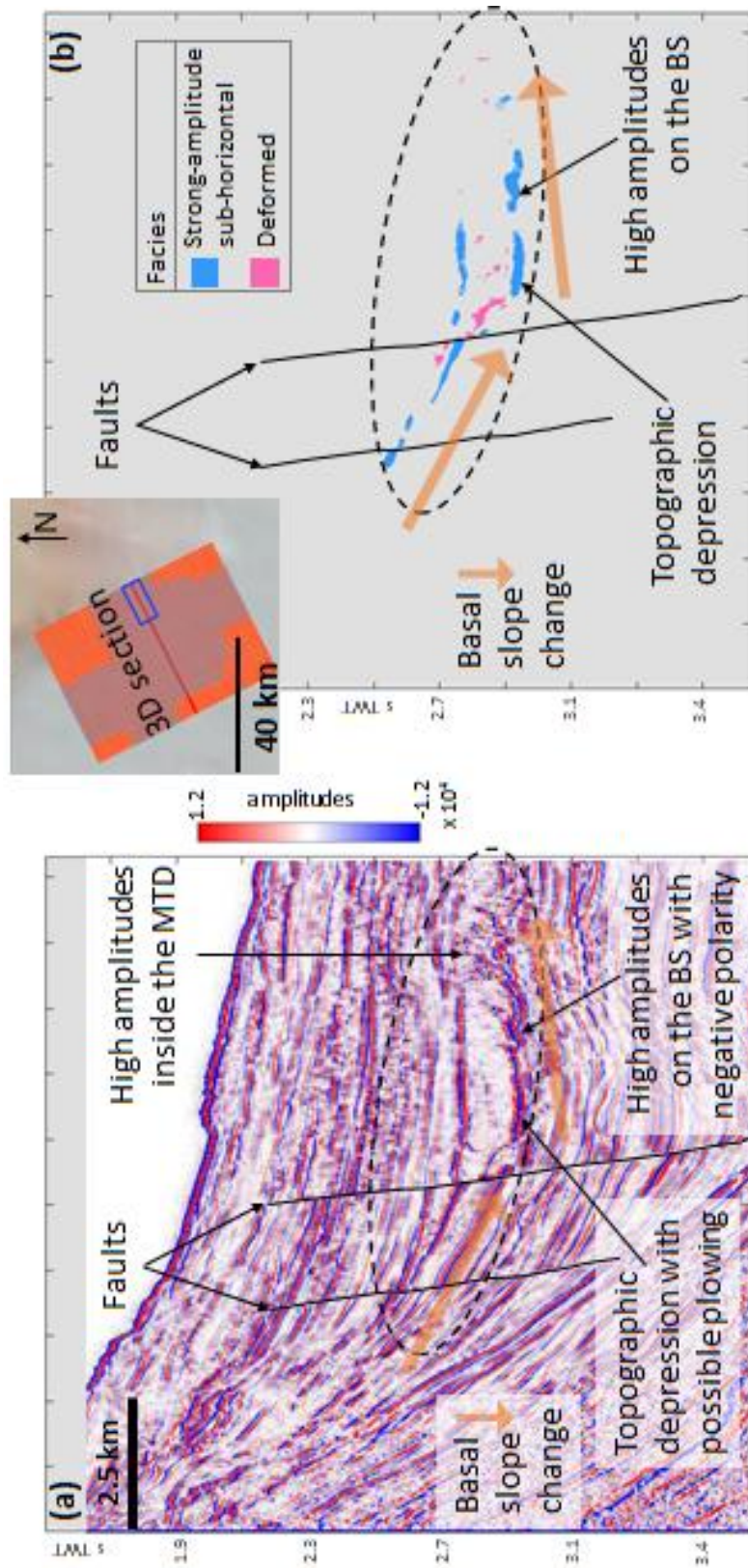


Figure 7. MTD A (circled in dashed line). Seismic section (a) and seismic facies (b). Faults and topographic depression are highlighted, with possible plowing (*sensu* Posamentier & Martinsen, 2011) on the high-amplitude negative-polarity basal surface (BS) of MTD A. Irregular high amplitudes are also visible inside. Deformed facies rather appears at the head part of MTD A (similar distribution for C).

4.4. Upper Surface (US)

On MTD A upper surface (US), similar *ramps* as on its BS are visible. According to the relation map, descriptor *US ramps or ridges* is impacted by nodes ‘post-deposition regional deformation’, ‘frontal compression’ and ‘flow direction’ – very different kinds of processes. Here, however, the most likely of them can be selected: the BS and US *ramps* coinciding on MTD A favor their common impacting node (‘post-deposition regional deformation’), indicating signatures of a faulting deformation of the MTD after deposition (Figure 6, Figure 7).

Upper surfaces (US) of MTDs A and B both have a *median slope* gradient of $[-1^{\circ}$ to (-2°)]; this value is much smaller than the *median slope* gradient of their basal surface $[-3.5^{\circ}$ to (-7°)]. Descriptor *US median slope* is impacted by nodes ‘flow behavior: elastic, plastic, fluid’, ‘flow direction’, ‘topography confinement downwards’, and ‘evaporite deformation and mud volcanism’. On the US of MTD B, a significant dip change is seen (Figure 6), which may be related to nodes ‘flow direction’ and ‘topography confinement downwards’; it correlates with the orientation change of the object (see 4.2). In this area, the *US slope* is an additional argument to the occurrence of a change in flow direction. On the other hand, the ‘flow behavior: elastic, plastic, fluid’ node may explain the smaller *median slope* gradient on US than on BS; this is to be compared to the $[-1.5^{\circ}$ to (-3.5°)] *median slope* gradient of two other MTDs of the same cube (MTDs C and D, Figure 3), and to the current seafloor *slope* of $[-1.5^{\circ}$ to (-3°)] in the downslope part. The low *US median slope* of MTDs A and B thus suggests the occurrence of a rather ‘fluid’ flow, compared to that of other MTDs of the cube with inferred more ‘viscous’ flow.

4.5. Internal Facies Distributions

MTDs A and B are globally 12% and 11% *chaotic* respectively, with internal variations: both are mostly *chaotic* in their southern part. *Ridged facies* are similarly distributed inside MTDs A and B, with global proportion of occurrence of 30% for both. Descriptor *chaotic facies distribution* is impacted by nodes ‘flow behavior: elastic, plastic, fluid’, ‘grains heterogeneity in flowing mass’, and ‘posterior fluid migrations’; *ridged facies distribution* is impacted by nodes ‘frontal compression’, ‘flow direction’ and ‘flow behavior: elastic, plastic, fluid’. These elements show that for both mass-transport events A and B, when arriving in the northern part, the material probably had a different flow behavior than that in the southern part (consistency of node ‘flow behavior’ for both descriptors). A change in compression constraints and flow direction between south and north is also in line with previously-mentioned orientation change of the objects. According to the other afore-

mentioned impacting nodes, additional possible interpretations are, for both MTDs A and B: increased homogeneity in material acoustic properties in the northern part, and post-deposition uneven fluid migrations occurring inside the southern part of the MTDs.

The *deformed facies* proportion of MTD A is quite low: 2% only, whereas for B it is 11%. For both of them, *deformed facies* are seen at the contact between the upslope part of the MTD and their underlying material (Figure 7 (b)); and noticeably MTD A is 10% *deformed* in its upper part while <5% everywhere else. The *deformed facies* descriptor is impacted by nodes ‘flow behavior: elastic, plastic, fluid’, ‘post-deposition regional deformation’, and ‘evaporite deformation & mud volcanism’. Thus, for both MTDs A and B (with more quantitative arguments for A), deformation occurred more on the bottom of the head part, either due to a particular flow behavior there, or to post-deposition regional deformation, or to local evaporite- or mud-related deformation in the zone.

MTDs A and B have different *transparent facies distributions*: MTD A is only 11% transparent on the whole, while MTD B is 28% transparent. However, MTD A is >20% transparent inside its 2 thicker regions; other interior parts of MTD A have unevenly-distributed high amplitudes, roughly aligned with the fractured BS patterns (Figure 7). Descriptor *transparent facies distribution* is impacted by several nodes: ‘grains heterogeneity in flowing mass’, ‘compaction during burial’, ‘posterior fluid migrations’, and ‘presence of preserved blocks’. The high-amplitude region inside A (low *transparent facies* proportion) may correspond either to preserved clasts (of size $\sim 1/3$ of the MTD thickness), or to over-pressured fluids heterogeneously trapped inside the MTD, migrating after its deposition or remaining from an undrained mass transport. Comparatively-lower amplitude (transparent) zones in MTDs A and B then correspond to regions with more internal homogeneity, possibly enhanced by compaction or homogenized fluid drainage during burial.

4.6. [Headscarp \(HS\)](#)

The multiple *headscarps* visible upslope are possibly related to downslope MTDs; however no direct relationship may be made between one single MTD (among the 5 seen in the cube, see Figure 3) and one upslope scarp – preventing us from analyzing descriptor *HS morphology*. Yet these *headscarps evolve downslope* (Figure 8); this description may suggest the impact of two controls: some large-scale ‘subsidence/uplift, extension/compression’, in the zone (inducing a progradation of sedimentary structures, as in e.g. Richardson *et al.*, 2011, Ortiz-Karpf *et al.*, 2016, Clark & Cartwright, 2009), and/or ‘sedimentation rate and type’ (in the sense of a sedimentation increase with time), according to the relation map. The period of time in which these scarps were created is from 2.4Ma to present (Gorini *et al.*, 2014, see Figure 8). Knowing the rate of tectonic or isostatic deformation since 2.4Ma would allow to constrain a potential impact on this evolution. Similarly, as node

‘sedimentation rate and type’ is itself impacted by the sea-level evolution, knowing this time more precisely could help confirm or infirm a eustacy-related headscarp series, and also above-mentioned MTD *vertical distribution*. The relation-map-based results do not favor any of these two interpretations.

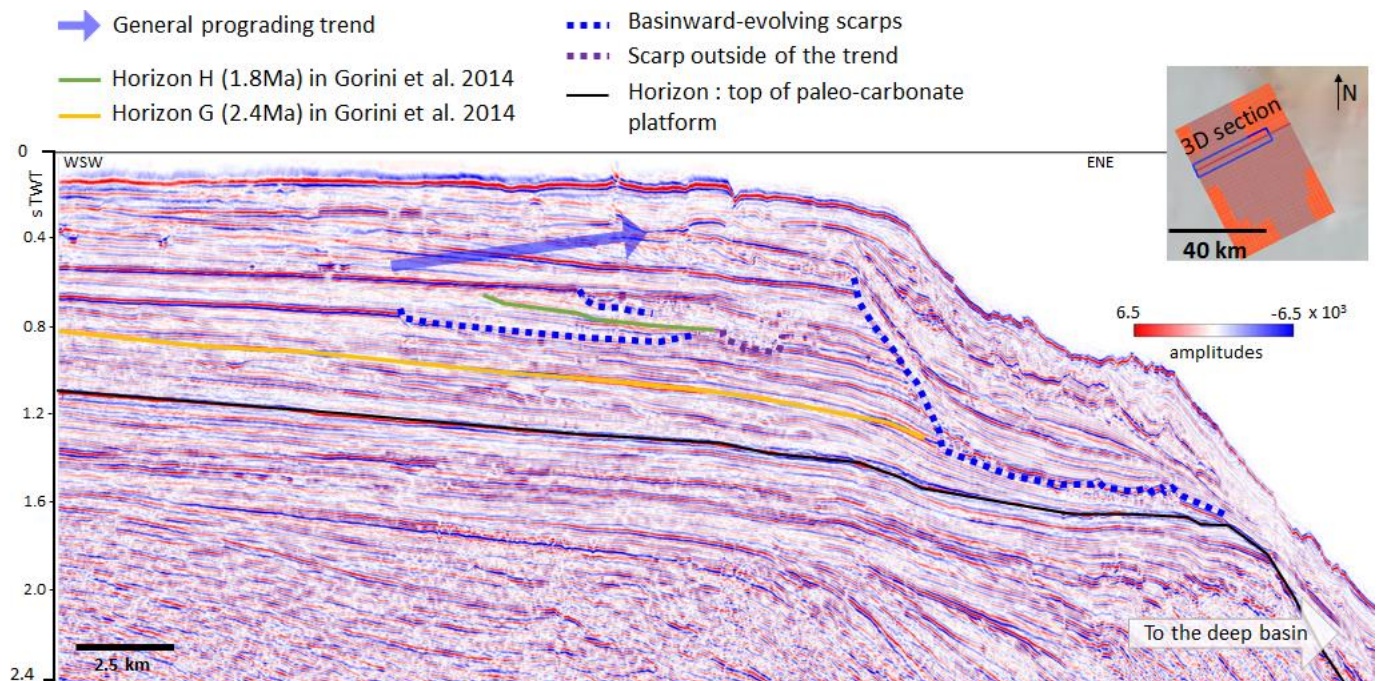


Figure 8. Upslope scarps showing fore-stepping evolution of the erosion on one dip seismic section from our seismic cube.

4.7. Summary of all results retrieved with the relation map analysis

The material of MTDs A and B probably originates from the WSW (rather than from the south), and both MTDs are probably signatures of one single event, or cascading events (one mass-transport event triggered by the change in slope stability induced by the other mass-transport event). MTD A is likely to have been subject to post-deposition regional deformation, in the form of extensional faults, more than MTD B.

On the whole, both MTDs may have resulted from more fluid-like material flows than the other MTDs of the same cube. A plowing effect may have occurred during mass-transport event A, more likely located in one of the two observed topographic basal depressions; furthermore, right above

the deepest part of these depressions, acoustic properties of MTD A are relatively homogeneous. In other parts of its southern region, preserved clasts or trapped/undrained fluids may be found. Deformation occurred more in the bottom head part of MTDs A and B, due to either a more viscous-like basal flow, or to post-deposition deformations.

For MTDs A and B, the flow direction during the event was modified in its distal part. The flow behavior of their material was probably different in the southern parts of both MTDs from in their respective northern part. In particular, compression and/or post-deposition uneven fluid migrations may have impacted the southern part of MTD A – compression is more obviously related with an orientation change, corresponding to a topographic impact. In their northern parts, a greater homogeneity in MTDs acoustic properties is found, suggesting more homogeneous distribution of material properties at the deposition time, and/or homogenization by posterior compaction effects or homogenized fluid drainage (during burial).

Two possible processes may explain the difference in polarity between the basal surfaces of MTDs A and B (in places where the basal surface has strong amplitude): either the occurrence of a lower impedance of the underlying material in the south (possibly including some fluid overpressure on the contact surface); or the two 'branches' of a unique event (or the two cascading events) having had different transport properties, e.g. plowing effect occurred in mass-transport event A and densified its bottom sediments during deposition.

Concerning more global aspects, the three main stages of "MTD layers" in the stratigraphy might be signatures of eustatic cycles – if other alternating systems like channel-levee systems are detected in the sedimentary pile, which is uncertain in our data. Some regional deformation due to tectonics or isostatic movements, inducing global progradation and/or sedimentation rate increase, may have occurred during the whole period when the 5 MTDs were deposited. And finally, the southern part of the cube was less exposed to mass-transport deposition during this period.

5. Assessing the validity of results

In this Section, we analyze the correlation between results based on our proposed relation-map and previous published studies on the Amazon basin.

5.1. How are our results consistent with previous knowledge on the Amazon basin?

Our seismic dataset is situated in a very proximal region of the Offshore Amazon basin (~120 to 1500 m deep), close to the upslope domain of the Amazon deep-sea fan. This region corresponds to the junction between the current shelf break, the Amazon deep-sea fan and the area affected by the Amapá Megaslides Complex (Figure 2). In the present study, we have analyzed cube-scale MTDs (a few tens of km). Previous studies on the northern part of the basin normally focused on much larger, basin-scale MTDs (a few hundreds of km), observed on 2D seismic data. In their studies, Gorini *et al.* (2014), Reis *et al.* (2016) and Silva *et al.* (2016) propose, for different MTDs of the Amapá Upper Complex, an age spanning from late Miocene to late Pleistocene. These basin-scale MTDs typically originated from marine slope instabilities. Maslin *et al.* (2005) focus on Quaternary MTDs of the 'Western Debris Flows' complex, considered as typical MTDs induced by the deep-sea fan development (Figure 2). These two kinds of MTDs characterize the entire basin sedimentation.

Thus, MTDs characterized in this paper are of much smaller scale than those previously studied across this basin. Nevertheless, our results still show the consistency between the results of the analysis based on the relation-map and the known context of the Amazon basin.

First, we know that MTDs in the northern Amazon basin region, resulting from mass-transport events dated from late Miocene to Present, are mostly debris flow signatures. General classifications define debris flows as being composed of a matrix containing internal blocks (Nelson *et al.*, 2011), resulting from 'spreading' (*sensu* Mourgues & Cobbold, 2006) or from 'mixed plastic-fluid' flow (*sensu* Posamentier & Martinsen, 2011), that still retains some competence and not being as energetic as a turbidity current (Lee *et al.*, 2007).

The MTDs we studied are at most a few Ma old, corresponding to the same period of deposition as the Amapá Upper Complex (Reis *et al.*, 2016) and the superficial MTDs described in the literature (e.g. Damuth & Embley, 1981, Damuth *et al.*, 1988, Maslin *et al.*, 2005). A few elements on MTDs A and B are in line with the interpretation of a debris flow type: (i) homogeneous acoustic properties (with low impedance contrast), alternated with heterogeneous regions where either clasts or fluids may be trapped. (ii) The overall low presence of deformed facies shows a very limited plastic deformation, which is characteristic of material flows compared to slides or creeps (Posamentier &

Martinsen, 2011), in which deformation plays an important role. (iii) Erosion signatures can be generated by debris flows, although slides may also erode their underlying material. Here, the erosion marker is located at a change in the direction of the material displacement, and some compression has left marks inside the MTDs; this tends to favor debris flow behavior rather than slide behavior.

Second, we know that the entire Amazon basin is subject to 'gravity-tectonic' deformation (Reis *et al.*, 2016), which produces extension in its proximal part and compression distally. The faults observed on MTD A could be a sign of the proximal extensional constraints – although possibly also linked to surficial compaction. Why they are not visible on MTD B is either linked to the (slightly) more distal position of MTD B (4-6 km more distal), or to the position of A closer (~10 km) to the edge of the deep-sea fan – generalized faulting in the southern part of the seismic cube seems to favor this argument. This leads us to the third point.

Third, results based on our relation map on MTDs A and B seem consistent with the presence of the deep-sea fan just south-east of the studied seismic cube (Figure 2). It has been shown that this deep-sea fan has created three major kinds of influences since its onset in the middle-late Miocene (Figueiredo *et al.*, 2009; 9.5 – 8.3 Ma according to Gorini *et al.*, 2014): acting as a secondary source of sediments for transport into the deep basin (e.g. Reis *et al.*, 2010, Maslin *et al.*, 2005, Araújo *et al.*, 2009), having a topographic control over the seafloor shape, and a structural control (Watts *et al.*, 2009) by flexuring the margin under its weight.

Here, MTDs A and B have been shown to originate from the paleo-shelf break; yet their direct environment may have been impacted by the presence of sediments coming from the fan direction, as suggested by the difference in BS polarity between MTDs A and B that were deposited either simultaneously or within a short period of time. Over such a short distance between the two MTDs, a local process (such as fluid presence, or locally different material properties) should explain this inversed polarity. Post-deposition compaction, and/or fluid migrations preventing efficient drainage from the BS of MTD A, could explain this difference, e.g. in the case of fluid present under MTD A (hypothesis that would be supported by the presence of fluids *inside* A too). Alternatively, near-fan sedimentation may be subject to different deposition conditions; these may include different sediment inputs, transported via contouritic currents around the fan or turbiditic currents coming from the fan which, mixed with recently deposited sediments downslope, would eventually yield lower-impedance sediments. This hypothesis could be supported by the BS polarities of other MTDs of the cube, which are always negative in the southern region (close to the fan) and positive in the north – if the influence of the fan has remained similar since MTDs A and B deposition.

The topographic control is highlighted in our results via the change in flow direction in MTDs A and B, which may be evidence for a topographic constraint. The deep-sea fan itself is an accumulation of material that creates a NW-dipping slope in the seafloor, already present at the deposition time of MTDs A and B. The debris flows probably changed their main direction from dip-oriented (originating from the WSW) to more northward-oriented, i.e. following the main slope direction in the more distal region of the cube, impacted by the fan sediments. Topographic control is also consistent with the fact that the southern part of this sub-basin, where the fan represents a topographic high, was less exposed to mass-transport deposition.

The structural control results from the weight of the Amazon deep-sea fan itself. The flexure caused by the fan load has greatly impacted the basin subsidence since the Late Miocene - Pliocene (Watts *et al.*, 2009). Here the distance between MTDs A and B is only ~10km. Nevertheless, we suggest that the presence of faults only in MTD A and not in MTD B may be related to the increased deformation near the upper domain of the fan compared to other places in equivalently proximal regions, which are all subject to basin-scale extensional constraints. This hypothesis is supported by the position of the seismic cube at the junction of 3 domains (shelf, fan and basin) and within a strongly flexured zone (Watts *et al.*, 2009, see Figure_Supplementary 2 in supplementary). Moreover, the processes that might have impacted the basinward-evolving headscarps upslope, may involve partly this fan control, and partly the larger-scale gravity-tectonic deformation of the entire basin.

Finally, the Amazon River sediment discharge has kept increasing since its onset as a transcontinental river (Gorini *et al.*, 2014). This element is recovered by the basinward evolution of upslope headscarps (see Section 4.6).

5.2. [How are our new results unexpected compared to previous literature on the Amazon region?](#)

According to our results, MTDs A and B were affected by deformation in the bottom of their head parts. Outside the MTDs, the deformed facies otherwise characterizes slope-deformed facies. Here, deformation within the heads of the MTDs is caused by either a specific flow behavior or by post-deposition deformation or evaporite/mud-related deformation in the zone, which highlights the deposition process: MTDs onlapping the continental slope and subject to internal, very small-scale post-depositional gravity-induced deformation – or to syn-depositional viscous ‘attachment’ (see Moscardelli & Wood, 2008 for ‘attached mass transport complexes’, whose upper part shows a deformed, slump character). In 2D-based studies, scale / resolution effects may prevent 2D data from revealing such detailed deformation variation. Note that the scale argument also tends to exclude

the impact of deformation by any tectonic- or non-tectonic process, which, given the small size of our MTDs, would probably rather affect the whole geobodies.

We have shown that our MTDs originate from upslope paleo-scarps. Former studies on the Amazon basin revealed MTDs whose headscarps are even more distally located than the area covered by our cube. These larger, more distal MTDs have been interpreted to originate from the submarine slope (Reis *et al.*, 2016). The relationship between these two sets of MTDs has not yet been established. However, the north-northeast (NNE) principal direction of MTDs A and B could suggest a link with the MTDs of the Amapá Upper Complex (Figure 6).

Our results suggest small-scale variations inside MTDs A and B. For example, MTD A includes regions, among which some have been homogenized since their deposit, and others have been subject to the presence of fluids, clasts, or apparent heterogeneity. Assessing the relevance of these internal variations is difficult when comparing to MTDs observed at basin-scale, for which no conclusion can be drawn at our finer scale. However, the frequent reworking of the recent sedimentary pile due to the fan influence or to high sedimentary influx (Reis *et al.*, 2010, Reis *et al.*, 2016) support these observations.

MTD A is not visible on any available 2D seismic line. MTD B can be found on one line, on which its extent is highly uncertain (Figure 9). Our results should thus be understood as concerning only parts (the head parts) of potentially larger MTDs (although probably not as large as the basin-scale ones).

Global analysis of the five MTDs in our cube suggested a signature of eustatic cycles in the vertical regularity of “MTD layering”, as long as this regularity is also visible in the interbedded sediments – which was not observed, making this statement very uncertain. These “MTD layers” do not have the same properties (number of objects, degree of internal heterogeneity, direct above- and below-environment), so that ‘cycles’ are difficult to depict. Moreover, the average thickness of MTDs decreases from deepest to shallowest, i.e. it decreases with time. This is not in line with the above-mentioned increase in sediment discharge from the Amazon River; this increase is also not recovered in the regular spacing between the three “MTD layers” pointed out on Figure 4. Thus, no conclusion can be drawn on this potential eustatic influence. The limited content of the relation map is not yet sufficient to explain this decreasing thickness trend.

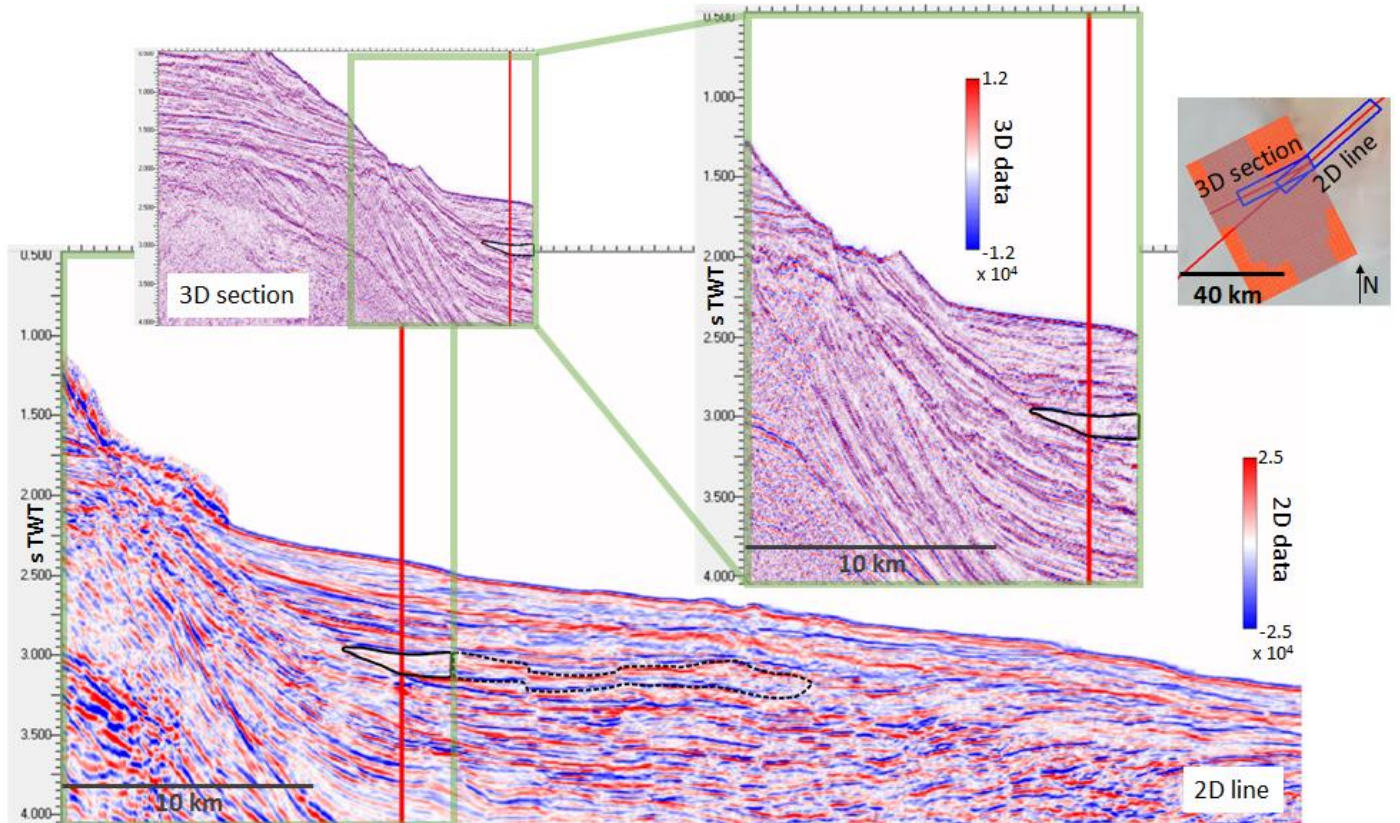


Figure 9. MTD B illustrated on a 2D seismic line. Black solid line: contour of MTD B drawn on a section extracted from the 3D cube (projected onto the 2D line). Dashed line: possible continuation of MTD B, interpreted from the 2D data.

Considering Sections 5.1 where our results agree with the general context of the region, and 5.2, where most of unexpected results refer to the scale or availability of data, we propose to validate our new methodology. Section 6 will discuss the main limits and potential outlooks that remain associated to it.

6. Discussion

6.1. Sensitivity analysis

In the graph analyses, some processes are inferred only once from a descriptor; if the descriptor is not available, the process will not be hypothesized at all. Conversely, other processes are suggested by several different descriptors, which decreases their uncertainty. Lastly, some processes are suggested by some descriptors but contradicted by others. In this case, the hypothesis is rejected and the process is not inferred. All these analyses may be different if insufficient data content / quality prevents from reliable property descriptions. Here, we assess the loss of results from our methodology for situations with data deficiency, leading to one or several descriptors missing.

- (i) Consider first the case where the thickness/resolution ratio is less than 3 (see Table_Supplementary 2). This could happen for occurrences of thin MTDs in a poorly-resolved seismic dataset. This typically limits the acquisition of Internal Facies Distribution descriptors to studies on rather shallow MTDs. If these descriptors were lacking in our application, this would result in less confidence in several processes: the heterogeneous fluid migrations, the south-north difference of flow behavior within the MTDs and their direction change. It would also suppress hypotheses on preserved clasts and the different compaction/drainage processes within the objects. Thus, this situation removes information on rather fine-scale transport properties and post-depositional processes, which may be crucial e.g. in exploration context.
- (ii) In another case, the picking grid of surfaces (basal and upper surfaces of the MTD, headscarp) may be too low for getting descriptors depicting the surfaces' morphologies: ramps or ridges, median slope values, presence of specific indicators like plunging pool / terracing and erosional descriptors on the basal surface. In our application, such a loss results in less confidence in the proposed direction change (absence of the asymmetric erosive walls and of the US dip change in MTD B), and in the relatively 'fluid' behavior of the MTDs; it also cancels the hypothesis on post-depositional regional deformation (faults). In our case, then, only few hypotheses would be less supported, and the post-depositional deformation would be guessed easily from global observation of the seismic data. In other cases however, the absence of 'basal ramps' and 'multi-terracing downslope' may prevent from retrieving the 'cascading events' hypothesis for example, which might lead to mis-interpretations.
- (iii) Another situation might be that the seismic amplitude range is not appropriate or reliable to distinguish between 'strong' and 'normal' reflectors (due to acquisition or processing

uncertainties), then part of the internal facies descriptors may be lacking ('transparent facies distribution', 'presence of preserved blocks') as well as the 'basal surface strong amplitude' descriptor. In our application, fluid migrations, different compaction/drainage, as well as differences in lithologies, would not be proposed at all. This supports the general need for good-quality amplitudes for assessing fluid presence.

- (iv) Finally, the data coverage may limit the acquisition of several descriptors, within the Morphology, Position and Global Environment properties in particular, and also including the Headscarp descriptors and toe-related descriptors if these regions are outside the dataset. From our application, a few hypotheses would then be missing: potential link between MTDs A and B, arguments on remobilization from A to B, and impact of large-scale deformations or sea-level cycles on the sedimentation in the zone. Such descriptors therefore yield crucial information on the basin- or regional-scale controls, as well as potential genetic relationships between MTDs, that may allow to classify them in series, or as regional events signatures (e.g. attached MTDs). Conversely, in our study, having access to the toe region of the MTDs would have given more indications on the paleo-seafloor topography and existing geomorphology at the time of the mass transport, as well as the flow behavior; it would also have given more reliable comparisons of volume and all morphological properties, yielding more constraints on the transport processes and more reliable comparisons between objects.

It is uncommon that all data deficiencies evoked above occur simultaneously. Generally, to be identified in seismic data, an MTD has a sufficient thickness to define its basal and upper surfaces. Large MTDs are often not completely imaged by 3D seismic data having rather good resolution, leading to either missing head or toe region; they may otherwise be studied with 2D seismic data having lower resolution but comprising the whole length of the object.

Missing parts of the object will globally hide information on regional processes, whereas an entirely-imaged MTD in a poorly-resolved dataset will hide the information on finer-scale transport style, posterior internal modifications and current state of the MTD. Too-loose picking of MTD-related surfaces lead to missing transport erosional properties and thus critical information on the flow direction and paleo-seafloor state, as well as posterior impacts of fluid migrations or large-scale deformations. However, depending on the application, interpreters use data that correspond to their needs. For reservoir-scale studies, high-resolution seismic data is preferred, while for assessing large-scale controls, datasets with larger coverage may be chosen at the expense of a lower resolution. Studies implying fluids will require precise surface definitions and high confidence in the seismic amplitudes distribution. Thus, despite the lower confidence with less available descriptors, the graph-based methodology can also be used in applications with limited amount of data.

6.2. What is the uncertainty related to our methodology?

The limited amount of data and limited information in the relation map show that the results produced by our methodology are subject to three main kinds of uncertainty.

The first kind of uncertainty is related to the input data. The seismic acquisition and processing stages, the interpretation of surfaces, the resolution and the coverage of the dataset are the key elements introducing uncertainty in the input (see previous Section). As in any seismic interpretation task, depth-converted data might also add some uncertainty, e.g. velocity pull-up/push-down effects affecting surface and global descriptors. Additionally, the facies classification (Internal Facies descriptors) itself involves some uncertainty, although the labels given to groups of ‘transparent facies’, ‘chaotic facies’, etc., are normally checked on several seismic sections; two different geological facies may have the same response in terms of seismic facies (e.g. Sun *et al.* (2017) show disrupted, low-amplitude patterns due to gas chimneys that might be considered ‘deformed’ or ‘chaotic’ facies). However, the descriptors used here are supported by seismic interpreters’ experience. Also note that initially flat morphologies and surfaces may be bent or steepened by large-scale deformation processes; this could be included in the graph (e.g. adding an edge between nodes ‘post-deposition regional deformation’ and ‘BS median slope’) if other parts of the graph are adapted consequently (e.g. analyzing facies distributions and surface properties along a dipping direction). For now such considerations are not included, which might limit the graph to cases with little, or known, such steepening.

A second kind of uncertainty is related to the relationships, or laws, comprised in the relation map. These laws come from the literature, but they also have limits; a possible, quantitative way to take these limits into account would be to weight every edge of the graph, thereby weighting the confidence of each possible interpreted physical process during the interpretation procedure.

The last kind of uncertainty is related to the construction of the relation map. The contents of the two lists in Table 1 and Table 2 were chosen based on a bibliographical study, which is the source of two main biases:

- The number of published studies, and the number of studies we considered, are limited, which necessarily limits the physical processes and MTD descriptors encountered in our study. However, we used a variety of sources, to ensure the studies came from several backgrounds (numerical, conceptual or analog modeling / seismic interpretation) and suffer as little as possible from this bias.

- Depending on what can be modelled and what cannot, the literature itself is biased. For example, among the links between Table 2 and Table 1, there is no direct link between trigger type and final MTD properties, because the physics that describe a trigger differ from the physics that describe a fall/flow, and no study has tackled this link to date.

The selection of most relevant elements to build our two lists was an iterative process. A few properties that are described in the literature were intentionally not included in this study; in particular, fine-scale properties of a wasted material, e.g. its grain size distribution or grains friction coefficients. Such properties may certainly impact the mass-transport event, and possibly the MTD itself (e.g. when a front of larger grains generates ‘tongues’ at the toe of the MTD, as suggested in Pouliquen *et al.*, 1997). Yet we considered them as ‘side’ effects compared to others, especially since for several of them the internal lithology of the MTD must be known, which is not the case in our seismic analysis. Too large-scale, or too rare, processes, such as the displacement of water that creates a propagating sea wave and may trigger other instabilities in another region of the basin, were also abandoned in our considerations. Finally, it should be recalled that all the elements listed in Table 2 depend on a timescale; they must always be considered as long- or short-term *relative* to some other phenomenon.

In order to quantitatively assess this last kind of uncertainty, ideally the relation map should be further developed, to include all the relationships left out of this work, until an entire formal ontology has been created with quantitative confidence weighting on edges according to how often they are cited and/or demonstrated in the literature. This is an ideal, probably very complex to reach.

This possibly high uncertainty (depending on the three factors mentioned above) is in line with the present approach of suggesting several scenarios, one of which will finally be chosen by the interpreter using other sources of information (geological context, other kinds of data such as log data, which noticeably increases confidence in facies interpretations). Our approach does not make it possible to select one scenario with certainty, but rather offers several possibilities. It is an attempt to reveal an on-going interpretation procedure when only a few input data and published results are used. The interpreter then uses the results of the relation map as he/she needs them, and consequently remains the only decision-maker.

6.3. Future outlook, other developments and uses of our methodology.

The graph constitutes a knowledge base from literature information only. The idea behind it is to convey the scientifically accepted information that already exists (within the existing nodes and edges), to be used jointly with specific information of a case study for applications. Improvements to

the results may come from both sides (graph content and data quality). Improvements to the methodology will come from the graph usage itself.

The first prospect is obviously its automation through a dedicated numerical representation: the Web Ontology Language (OWL)³, as promoted by Malik *et al.* (2010) and implemented for ontology edition by Musen (2015). A lot of details were provided here on the steps of interpretation, descriptor by descriptor, node by node; but in a numerical framework, these results could be obtained automatically, which would considerably accelerate the process. With this view, using quantitative weights on edges, as suggested above, would certainly benefit the procedure itself, and would output some uncertainty information. Automated acquisition of the MTD descriptors may be hard to implement, but this point can be solved separately and does not jeopardize the graph-based method itself.

Our work can be extrapolated further by using the relation map in a different way thanks to its automatized (i.e. rapid) version. An interesting application would be to test several hypotheses on unknown values of some MTD descriptors. The resulting hypothetical interpretations, if different, could be compared with outside knowledge about the MTD, thus enabling selection of the most-likely value of the descriptors of interest. Trials could then be run to see whether, based on a partial MTD characterization (i.e. having only part of MTD descriptors' values), using the relation map would make it possible to infer the values of the others. Another approach would be to input some "a-priori bias" on the edges' weights, according to some external information. The results of the modified-graph would then take this information (e.g. contextual knowledge) into account.

³ Developed by the W3 Consortium on Semantic Web: <https://www.w3.org/OWL/>, last accessed Sept. 2018

7. [Conclusion](#)

We propose the use of an ontology for MTD interpretation in seismic data based on the combination of literature sources. To this end, we built a knowledge base from existing literature as a graph (relation map). A graph-based methodology is provided to infer potential causal processes for the seismic signatures of MTDs. This novel method was applied on a case study with a 3D seismic dataset from the Amazon basin, which validated the methodology.

Our methodology yields objective proposals for interpretation based only on the ontology and the input data, with no other prior information. Some uncertainties linked to the relation map itself and to the input data remain. In a more complete interpretation process, additional information may make it possible to select the most-likely interpretation among those proposed by our method.

Improvements in the relation map will enable quantification of the probability of each interpretation proposed. Our work is a first step towards a more complete ontology, which we believe will help share new knowledge for various uses of MTD interpretation.

8. [Acknowledgements](#)

We thank the CGG Houston office for data provision and permission to publish. We also thank the Brazilian National Agency of Petroleum (ANP) for data made available to A. Tadeu dos Reis (UERJ-Brazil), who collaborates in the present research theme and on the study of the Offshore Amazon basin. We are very grateful to: Alberto Cruz from the ISTeP laboratory (Sorbonne Université) for fruitful discussions and improvements on some content of this article; Noalwenn Dubos-Sallée, from IFP Energies Nouvelles, for proof reading the article; and Alexandre Lethiers, from the ISTeP laboratory, for his support on map figures. Many thanks to Tiago M. Alves and two anonymous reviewers whose comments and suggestions significantly helped improve the content of this article.

9. [Supplementary material](#)

Here we give the full list of edges of the knowledge-based graph (relation map) (Table_Supplementary 1). The reference column gives non-exhaustive examples of previous studies whose results support the corresponding edges. Studies from Lafuerza *et al.* (2009), Lacoste *et al.* (2012), Frey-Martínez *et al.* (2011), Goujon *et al.* (2007), Chemenda *et al.* (2009), Elverhoi *et al.* (2010), Laberg *et al.* (2017), Li *et al.* (2017), Ogiesoba & Hammes (2012), and the Geological Survey of

Norway website (<https://www.ngu.no>, last accessed in January, 2018) were also used as contributions to our knowledge base, although they were not mentioned in the text of this article.

Table_Supplementary 1. Edges of the graph. Columns indicate the source node and target node, the directed/undirected character of the edge, and reference(s) that support its definition. A second tab in the table gives all references used in the first tab. A third tab gives all edges connected to MTD descriptors nodes.

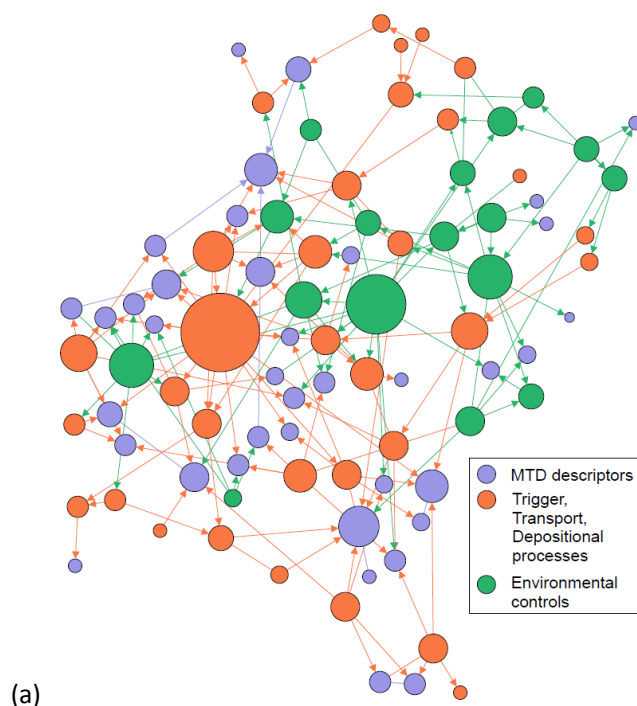
(Attached in a separate file.)

Table_Supplementary 2 provides details on the detection limits for MTD descriptors of Table 1.

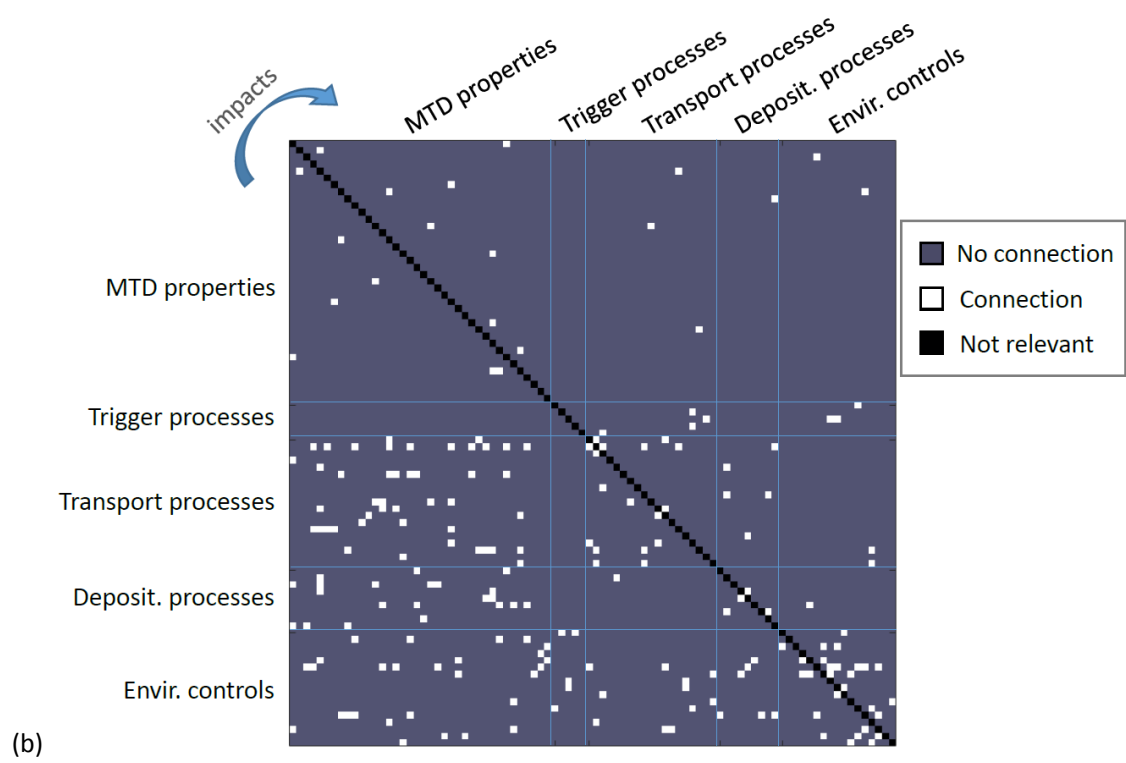
Table_Supplementary 2. Detection limit for descriptors of Table 1, in terms of dataset coverage, resolution, and other aspects.

(Attached in a separate file.)

We also give a figure illustrating the graph by one possible visualization (Figure_Supplementary 1 (a)) and the adjacency matrix of the graph (Figure_Supplementary 1 (b)). The visualization highlights the degree variation between nodes (by node size variation), indicating which nodes have the highest number of connecting nodes. The adjacency matrix shows directly the links between nodes, in a less graphical way; from this matrix, we show that no direct impact has yet been proven in the literature between trigger processes and MTD descriptors. These representations were obtained via the Gephi software (<https://gephi.org/>).

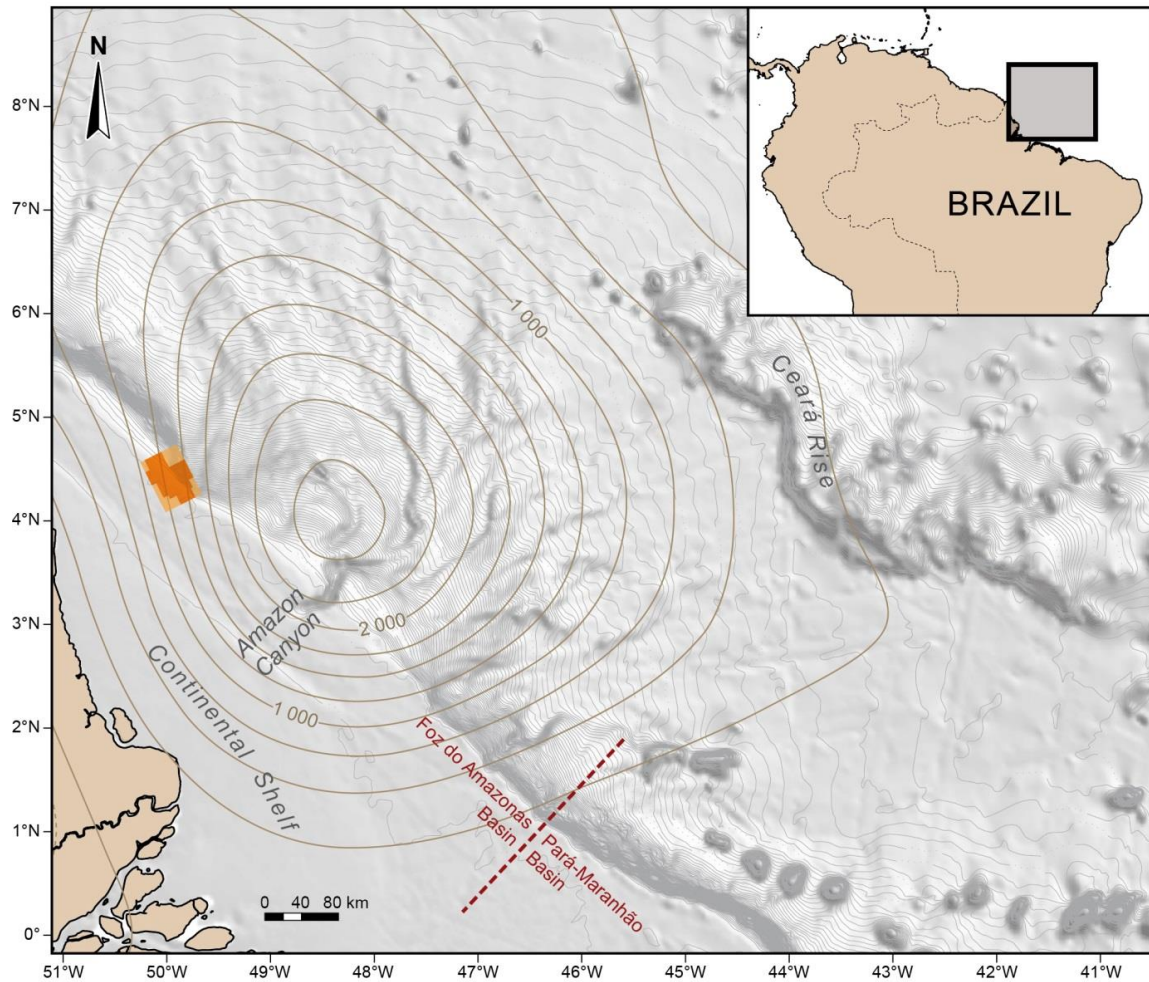


Figure_Supplementary 1. Knowledge-based graph representations: (a) one possible visualization, and (b) adjacency matrix. Figures obtained via the Gephi software (<https://gephi.org/>).



(Figure_Supplementary 1 - continued)

Finally, we recall a bathymetric map from Watts et al., 2009 (Figure_Supplementary 2), with results from their calculation of flexure due to the fan load. The position of the seismic cube used in this study has been added, to demonstrate its critical position and the potential variation of fan-induced flexure inside the cube.



Figure_Supplementary 2. Bathymetric map with flexure impact from the fan load; from Watts et al., 2009 and Rodger, 2009. Solid lines show the flexural depression (contour interval: 250 m). The inland flexural bulge is not visible on this map. The 3D seismic cube is mapped with available seismic data in dark orange.

References

- ALVES, T.M. (2015) Submarine slide blocks and associated soft-sediment deformation in deep-water basins: A review. *Marine and Petroleum Geology*, **67**, 262–285.
doi:10.1016/j.marpetgeo.2015.05.010
- ALVES, T.M., KURTEV, K., MOORE, G.F. & STRASSER, M. (2014) Assessing the internal character, reservoir potential, and seal competence of mass-transport deposits using seismic texture: A geophysical and petrophysical approach. *Bulletin*, **98** (4), 793–824. doi:10.1306/09121313117
- ARAÚJO, É.F.D.S., SILVA, C.G., REIS, A.T.D., PEROVANO, R., GORINI, C., VENDEVILLE, B.C. & ALBUQUERQUE, N.C.D. (2009) Movimentos de massa multiescala na bacia da foz do Amazonas - margem equatorial brasileira. *Rev. Bras. Geof.*, **27** (3), 485–508. doi:10.1590/S0102-261X2009000300013
- BONDY, J.A. & MURTY, U.S.R. (2008) *Graph theory*. Springer, New York.
- BOURGET, J., ZARAGOSI, S., ELLOUZ-ZIMERMANN, N., MOUCHOT, N., GARLAN, T., SCHNEIDER, J.-L., LANFUMEY, V. & LALLEMANT, S. (2011) Turbidite system architecture and sedimentary processes along topographically complex slopes: The Makran convergent margin. *Sedimentology*, **58** (2), 376–406. doi:10.1111/j.1365-3091.2010.01168.x
- BULL, S., CARTWRIGHT, J. & HUUSE, M. (2009) A review of kinematic indicators from mass-transport complexes using 3D seismic data. *Marine and Petroleum Geology*, **26** (7), 1132–1151. doi:10.1016/j.marpetgeo.2008.09.011
- CHEMENDA, A., BOIS, T., BOUISOUS, S. & TRIC, E. (2009) Numerical modelling of the gravity-induced destabilization of a slope: The example of the La Clapière landslide, southern France. *Geomorphology*, **109**, 86–93. doi:10.1016/j.geomorph.2009.02.025
- CLARK, I.R. & CARTWRIGHT, J.A. (2009) Interactions between submarine channel systems and deformation in deepwater fold belts: Examples from the Levant Basin, Eastern Mediterranean sea. *Marine and Petroleum Geology*, **26** (8), 1465–1482. doi:10.1016/j.marpetgeo.2009.05.004
- DALLA VALLE, G., GAMBERI, F., ROCCHINI, P., MINISINI, D., ERRERA, A., BAGLIONI, L. & TRINCARDI, F. (2013) 3D seismic geomorphology of mass transport complexes in a foredeep basin: Examples from the Pleistocene of the Central Adriatic Basin (Mediterranean Sea). *Sedimentary Geology*, **294**, 127–141. doi:10.1016/j.sedgeo.2013.05.012
- DAMUTH, J. & EMBLEY, R. (1981) Mass-transport processes on Amazon Cone: western equatorial Atlantic. *American Association of Petroleum Geologists Bulletin*, **65** (4), 629–643.
- DAMUTH, J., FLOOD, R.D., KOWSMANN, R.O., BELDERSON, R.H. & GORINI, M.A. (1988) Anatomy and growth pattern of Amazon deep-sea fan as revealed by long-range side-scan sonar (GLORIA) and high-resolution seismic studies. *AAPG Bulletin*, **72** (8), 885–911.
- ELVERHOI, A., BREIEN, H., BLASIO, F.V. de, HARBITZ, C.B. & PAGLIARDI, M. (2010) Submarine landslides and the importance of the initial sediment composition for run-out length and final deposit. *Ocean Dynamics*, **60** (4), 1027–1046.
- FIGUEIREDO, J., HOORN, C., VAN DER VEN, P. & SOARES, E. (2009) Late Miocene onset of the Amazon River and the Amazon deep-sea fan: Evidence from the Foz do Amazonas Basin. *Geology*, **37** (7), 619–622. doi:10.1130/G25567A.1
- FREY-MARTÍNEZ, J. (2010) 3D Seismic Interpretation of Mass Transport Deposits: Implications for Basin Analysis and Geohazard Evaluation. In: *Submarine Mass Movements and Their Consequences* (Ed. by D.C. Mosher, R.C. Shipp, L. Moscardelli, J.D. Chaytor, C.D.P. Baxter, H.J. Lee & R. Urgeles), pp. 553–568. Springer Netherlands, Dordrecht.
- FREY-MARTÍNEZ, J., BERTONI, C., GÉRARD, J. & MATÍAS, H. (2011) Processes of Submarine Slope Failure and Fluid Migration on the Ebro Continental Margin: Implications for Offshore Exploration and

- Development. In: *Mass-Transport Deposits in Deepwater Settings* (Ed. by R.C. Shipp, P. Weimer & H.W. Posamentier), pp. 181–198. SEPM (Society for Sedimentary Geology).
- GORINI, C., HAQ, B.U., DOS REIS, ANTONIO TADEU, SILVA, C.G., CRUZ, A., SOARES, E. & GRANGEON, D. (2014) Late Neogene sequence stratigraphic evolution of the Foz do Amazonas Basin, Brazil. *Terra Nova*, **26** (3), 179–185. doi:10.1111/ter.12083
- GOUJON, C., DALLOZ-DUBRUJEAUD, B. & THOMAS, N. (2007) Bidisperse Granular Flow on Inclined Rough Planes. In: *Traffic and Granular Flow'05* (Ed. by A. Schadschneider, T. Pöschel, R. Kühne, M. Schreckenberg & D.E. Wolf), pp. 147–156. Springer Berlin Heidelberg, Berlin, Heidelberg.
- GRUBER, T.R. (1993) A translation approach to portable ontology specifications. *Knowledge Acquisition*, **5** (2), 199–220. doi:10.1006/knac.1993.1008
- LABERG, J.S., STRASSER, M., ALVES, T.M., GAO, S., KAWAMURA, K., KOPF, A. & MOORE, G.F. (2017) Internal deformation of a muddy gravity flow and its interaction with the seafloor (site C0018 of IODP Expedition 333, Nankai Trough, SE Japan). *Landslides*, **14** (3), 849–860. doi:10.1007/s10346-016-0766-7
- LACOSTE, A., VENDEVILLE, B.C., MOURGUES, R., LONCKE, L. & LEBACQ, M. (2012) Gravitational instabilities triggered by fluid overpressure and downslope incision – Insights from analytical and analogue modelling. *Journal of Structural Geology*, **42**, 151–162. doi:10.1016/j.jsg.2012.05.011
- LAFUERZA, S., SULTAN, N., CANALS, M., FRIGOLA, J., BERNÉ, S., JOUET, G., GALAVAZI, M. & SIERRO, F.J. (2009) Overpressure within upper continental slope sediments from CPTU data, Gulf of Lion, NW Mediterranean Sea. *Int J Earth Sci (Geol Rundsch)*, **98** (4), 751–768. doi:10.1007/s00531-008-0376-2
- LEE, H.J., LOCAT, J., DESGAGNS, P., PARSONS, J.D., MCADOO, B.G., ORANGE, D.L., PUIG, P., WONG, F.L., DARTNELL, P. & BOULANGER, E. (2007) Submarine Mass Movements on Continental Margins. In: *Continental Margin Sedimentation* (Ed. by C.A. Nittrouer, J.A. Austin, M.E. Field, J.H. Kravitz, J.P.M. Syvitski & P.L. Wiberg), pp. 213–274. Blackwell Publishing Ltd, Oxford, UK.
- LEE, S.E., TALLING, P.J., ERNST, G.G. & HOGG, A.J. (2002) Occurrence and origin of submarine plunge pools at the base of the US continental slope. *Marine Geology*, **185** (3-4), 363–377. doi:10.1016/S0025-3227(01)00298-5
- LEYNAUD, D., MIENERT, J. & VANNESTE, M. (2009) Submarine mass movements on glaciated and non-glaciated European continental margins: A review of triggering mechanisms and preconditions to failure. *Marine and Petroleum Geology*, **26** (5), 618–632. doi:10.1016/j.marpetgeo.2008.02.008
- LI, W., ALVES, T.M., URLAUB, M., GEORGIPOULOU, A., KLAUCKE, I., WYNN, R.B., GROSS, F., MEYER, M., REPSCHLÄGER, J., BERNDT, C. & KRASTEL, S. (2017) Morphology, age and sediment dynamics of the upper headwall of the Sahara Slide Complex, Northwest Africa: Evidence for a large Late Holocene failure. *Marine Geology*, **393**, 109–123. doi:10.1016/j.margeo.2016.11.013
- MALIK, Z., REZGUI, A., MEDJAHED, B., OUZZANI, M. & KRISHNA SINHA, A. (2010) Semantic integration in Geosciences. *Int. J. Semantic Computing*, **04** (03), 301–330. doi:10.1142/S1793351X10001036
- MANGENEY-CASTELNAU, A., BOUCHUT, F., VILOTTE, J.P., LAJEUNESSE, E., AUBERTIN, A. & PIRULLI, M. (2005) On the use of Saint Venant equations to simulate the spreading of a granular mass. *J. Geophys. Res.*, **110** (B9). doi:10.1029/2004JB003161
- MARFURT, K.J. & ALVES, T.M. (2015) Pitfalls and limitations in seismic attribute interpretation of tectonic features. *Interpretation*, **3** (1), SB5–SB15. doi:10.1190/INT-2014-0122.1
- MASLIN, M., VILELA, C., MIKKELSEN, N. & GROOTES, P. (2005) Causes of catastrophic sediment failures of the Amazon Fan. *Quaternary Science Reviews*, **24** (20-21), 2180–2193. doi:10.1016/j.quascirev.2005.01.016

- MERRIS, R. (2001) *Graph theory*. Wiley, New York [u.a.].
- MIENERT, J. (2009) Methane Hydrate and Submarine Slides. In: *Encyclopedia of Ocean Sciences*, pp. 790–798. Elsevier.
- MOSCARDELLI, L. & WOOD, L. (2008) New classification system for mass transport complexes in offshore Trinidad. *Basin Research*, **20** (1), 73–98. doi:10.1111/j.1365-2117.2007.00340.x
- MOURGUES, R. & COBBOLD, P.R. (2006) Sandbox experiments on gravitational spreading and gliding in the presence of fluid overpressures. *Journal of Structural Geology*, **28** (5), 887–901. doi:10.1016/j.jsg.2005.12.013
- MOURGUES, R., LACOSTE, A. & GARIBALDI, C. (2014) The Coulomb critical taper theory applied to gravitational instabilities. *J. Geophys. Res. Solid Earth*, **119** (1), 754–765. doi:10.1002/2013JB010359
- MOURGUES, R., LECOMTE, E., VENDEVILLE, B. & RAILLARD, S. (2009) An experimental investigation of gravity-driven shale tectonics in progradational delta. *Tectonophysics*, **474** (3-4), 643–656. doi:10.1016/j.tecto.2009.05.003
- MULDER, T. & ALEXANDER, J. (2001a) Abrupt change in slope causes variation in the deposit thickness of concentrated particle-driven density currents. *Marine Geology*, **175** (1-4), 221–235. doi:10.1016/S0025-3227(01)00114-1
- MULDER, T. & ALEXANDER, J. (2001b) The physical character of subaqueous sedimentary density flows and their deposits. *Sedimentology*, **48** (2), 269–299. doi:10.1046/j.1365-3091.2001.00360.x
- MUSEN, M.A. (2015) The Protégé Project: A Look Back and a Look Forward. *AI matters*, **1** (4), 4–12. doi:10.1145/2757001.2757003
- NELSON, C.H., ESCUTIA, C., DAMUTH, J.E. & TWICHELL, D.C. (2011) Interplay of Mass-Transport and Turbidite-System Deposits in Different Active Tectonic and Passive Continental Margin Settings: External and Local Controlling Factors. In: *Mass-transport deposits in deepwater settings* (Ed. by R.C. Shipp, P. Weimer & H.W. Posamentier), pp. 39–66. SEPM (Society for Sedimentary Geology), Tulsa (Okla.).
- OGIESOBA, O. & HAMMES, U. (2012) Seismic interpretation of mass-transport deposits within the upper Oligocene Frio Formation, south Texas Gulf Coast. *Bulletin*, **96** (5), 845–868. doi:10.1306/09191110205
- OMOSANYA, K.O. & ALVES, T.M. (2013) Ramps and flats of mass-transport deposits (MTDs) as markers of seafloor strain on the flanks of rising diapirs (Espírito Santo Basin, SE Brazil). *Marine Geology*, **340**, 82–97. doi:10.1016/j.margeo.2013.04.013
- ORTIZ-KARPF, A., HODGSON, D.M., JACKSON, C.A.-L. & MCCAFFREY, W.D. (2016) Mass-transport complexes as markers of deep-water fold-and-thrust belt evolution: Insights from the southern Magdalena fan, offshore Colombia. *Basin Res*, **57** (4), 294. doi:10.1111/bre.12208
- OWEN, M., DAY, S. & MASLIN, M. (2007) Late Pleistocene submarine mass movements: Occurrence and causes. *Quaternary Science Reviews*, **26** (7-8), 958–978. doi:10.1016/j.quascirev.2006.12.011
- POSAMENTIER, H.W. & MARTINSEN, O.J. (2011) The Character and Genesis of Submarine Mass-Transport Deposits: Insights from Outcrop and 3D Seismic Data. In: *Mass-transport deposits in deepwater settings* (Ed. by R.C. Shipp, P. Weimer & H.W. Posamentier), pp. 7–38. SEPM (Society for Sedimentary Geology), Tulsa (Okla.).
- POULIQUEN, O., DELOUR, J. & SAVAGE, S.B. (1997) Fingering in granular flows. *Nature*, **386** (6627), 816–817. doi:10.1038/386816a0
- REIS, A.T., ARAUJO, E., SILVA, C.G., CRUZ, A.M., GORINI, C., DROZ, L., MIGEON, S., PEROVANO, R., KING, I. & BACHE, F. (2016) Effects of a regional décollement level for gravity tectonics on late Neogene-

- Quaternary large-scale slope instabilities in the Foz do Amazonas Basin, Brazil. *Marine and Petroleum Geology*, **75**, 29–52.
- REIS, A.T., PEROVANO, R., SILVA, C.G., VENDEVILLE, B.C., ARAUJO, E., GORINI, C. & OLIVEIRA, V. (2010) Two-scale gravitational collapse in the Amazon Fan: A coupled system of gravity tectonics and mass-transport processes. *Journal of the Geological Society*, **167** (3), 593–604. doi:10.1144/0016-76492009-035
- REITSMA, F., LAXTON, J., BALLARD, S., KUHN, W. & ABDELMOTY, A. (2009) Semantics, ontologies and eScience for the geosciences. *Computers & Geosciences*, **35** (4), 706–709. doi:10.1016/j.cageo.2008.03.014
- RICHARDSON, S.E.J., DAVIES, R.J., ALLEN, M.B. & GRANT, S.F. (2011) Structure and evolution of mass transport deposits in the South Caspian Basin, Azerbaijan. *Basin Research*, **23** (6), 702–719. doi:10.1111/j.1365-2117.2011.00508.x
- RODGER, M. (2009) *A marine geophysical study of the Amazon continental margin, North-Eastern Brazil*. University of Oxford, Oxford, UK.
- ROY, A., ROMERO-PELÁEZ, A.S., KWIATKOWSKI, T.J. & MARFURT, K.J. (2014) Generative topographic mapping for seismic facies estimation of a carbonate wash, Veracruz Basin, southern Mexico. *Interpretation*, **2** (1), SA31-SA47. doi:10.1190/INT-2013-0077.1
- SAWYER, D.E., FLEMINGS, P.B., BUTTLES, J. & MOHRIG, D. (2012) Mudflow transport behavior and deposit morphology: Role of shear stress to yield strength ratio in subaqueous experiments. *Marine Geology*, **307–310**, 28–39. doi:10.1016/j.margeo.2012.01.009
- SHIPP, R.C., WEIMER, P. & POSAMENTIER, H.W. (2011) Mass-Transport Deposits in Deepwater Settings: An Introduction. In: *Mass-transport deposits in deepwater settings* (Ed. by R.C. Shipp, P. Weimer & H.W. Posamentier), pp. 3–6. SEPM (Society for Sedimentary Geology), Tulsa (Okla.).
- SILVA, C.C., DOS REIS, A.T., PEROVANO, R.J., GORINI, M.A., DOS SANTOS, M.V.M., JECK, I.K., TAVARES, A.A.A. & GORINI, C. (2016) Multiple Megaslides Complexes and Their Significance for the Miocene Stratigraphic Evolution of the Offshore Amazon Basin. In: *Submarine Mass Movements and their Consequences* (Ed. by G. Lamarche, J. Mountjoy, S. Bull, T. Hubble, S. Krastel, E. Lane, A. Micallef, L. Moscardelli, C. Mueller, I. Pecher & S. Woelz), pp. 49–60. Springer International Publishing, Cham.
- SILVA, C.G., ARAÚJO, E., REIS, A.T., PEROVANO, R., GORINI, C., VENDEVILLE, B.C. & ALBUQUERQUE, N. (2010) Megaslides in the Foz do Amazonas Basin, Brazilian Equatorial Margin. In: *Submarine Mass Movements and Their Consequences* (Ed. by D.C. Mosher, R.C. Shipp, L. Moscardelli, J.D. Chaytor, C.D.P. Baxter, H.J. Lee & R. Urgeles), pp. 581–591. Springer Netherlands, Dordrecht.
- SUN, Q., ALVES, T., XIE, X., HE, J., LI, W. & NI, X. (2017) Free gas accumulations in basal shear zones of mass-transport deposits (Pearl River Mouth Basin, South China Sea): An important geohazard on continental slope basins. *Marine and Petroleum Geology*, **81**, 17–32. doi:10.1016/j.marpetgeo.2016.12.029
- SUTTON, J.P. & MITCHUM, R.M. (2011) Upper Quaternary Seafloor Mass-Transport Deposits at the Base of Slope, Offshore Niger Delta, Deepwater Nigeria. In: *Mass-Transport Deposits in Deepwater Settings* (Ed. by R.C. Shipp, P. Weimer & H.W. Posamentier), pp. 85–110. SEPM (Society for Sedimentary Geology).
- TALLING, P.J., MASSON, D.G., SUMNER, E.J. & MAGESINI, G. (2012) Subaqueous sediment density flows: Depositional processes and deposit types. *Sedimentology*, **59** (7), 1937–2003. doi:10.1111/j.1365-3091.2012.01353.x

- URGELES, R. & CAMERLENGHI, A. (2013) Submarine landslides of the Mediterranean Sea: Trigger mechanisms, dynamics, and frequency-magnitude distribution. *J. Geophys. Res. Earth Surf.*, **118** (4), 2600–2618. doi:10.1002/2013JF002720
- URLAUB, M., TALLING, P.J. & MASSON, D.G. (2013) Timing and frequency of large submarine landslides: Implications for understanding triggers and future geohazard. *Quaternary Science Reviews*, **72**, 63–82. doi:10.1016/j.quascirev.2013.04.020
- VANNESTE, M., SULTAN, N., GARZIGLIA, S., FORSBERG, C.F. & L'HEUREUX, J.-S. (2014) Seafloor instabilities and sediment deformation processes: The need for integrated, multi-disciplinary investigations. *Marine Geology*, **352**, 183–214. doi:10.1016/j.margeo.2014.01.005
- VARNES, D.J. (1958) Landslide Types and Processes. *Landslides and engineering practice*, **24**, 20–47.
- VERNEY, P. (2009) *Interprétation géologique de données sismiques par une méthode supervisée basée sur la vision cognitive*, Informatique. Ecole Nationale Supérieure des Mines de Paris, Paris.
- WANG, C., MA, X. & CHEN, J. (2018) Ontology-driven data integration and visualization for exploring regional geologic time and paleontological information. *Computers & Geosciences*, **115**, 12–19. doi:10.1016/j.cageo.2018.03.004
- WATTS, A.B., RODGER, M., PEIRCE, C., GREENROYD, C.J. & HOBBS, R.W. (2009) Seismic structure, gravity anomalies, and flexure of the Amazon continental margin, NE Brazil. *J. Geophys. Res.*, **114** (B7), 17. doi:10.1029/2008JB006259
- WOODHOUSE, M.J., THORNTON, A.R., JOHNSON, C.G., KOKELAAR, B.P. & GRAY, J. M. N. T. (2012) Segregation-induced fingering instabilities in granular free-surface flows. *J. Fluid Mech.*, **709**, 543–580. doi:10.1017/jfm.2012.348
- WU, S.-G., QIN, Z.-L., WANG, D.-W., PENG, X.-C., WANG, Z.-J. & YAO, G.-S. (2011) Analysis on Seismic Characteristics and Triggering Mechanisms of Mass Transport Deposits on the Northern Slope of the South China Sea. *Chinese J. Geophys.*, **54** (6), 1056–1068. doi:10.1002/cjg2.1684

List of Figures and Tables

Figure 1. (a) Schematic representation of our graph (relation map). Dots are nodes, colored according to their category (environmental controls, mass transport event (MTE) properties or mass transport deposit (MTD) descriptors); lines/arrows are undirected/directed edges. Interpretation for MTD descriptor 2 yields nodes C and E as direct potential impacting processes, then nodes A and B; node 3 is only related to node 2. (b) Representation of a sub-part of the global knowledge base, with nodes mentioned in the proposed application (Section 4).	8
Figure 2. Bathymetric map of the Offshore Amazon basin with location of major previously-studied MTDs and seismic data used in this article. Modified from Reis et al., 2016 and Silva et al., 2016. The 50°W (Damuth & Embley, 1981), WMTD, EMTD (Western / Eastern MTDs, Damuth et al., 1988) are superficial MTDs. URMTD and BMTD (Unit R / Buried MTDs, Damuth et al., 1988) are buried. The Amapá and Pará-Maranhão Megaslides (ALC-AUC / PMM) were studied by Silva et al., 2010 and Reis et al., 2016. Amapá Lower Complex (ALC), the deepest mass transport complex of Amapá, is mapped in blue; Amapá Upper Complex (AUC), more recent, is mapped in orange, after Reis et al., 2016. The 3D seismic cube is mapped with available seismic data in dark orange and 2D seismic profiles are mapped in dark red.	17
Figure 3. 3D view of the five MTDs highlighted in the studied data. MTDs D and E are separated by the brown dashed line. Colored surfaces are upslope scarps. Grey sections are seismic sections from the seismic cube. The largest blue surface is the carbonate platform-slope top (see also Gorini et al., 2014).....	20
Figure 4. The 5 MTDs highlighted in one seismic section of the post-stack seismic cube (first/second view without, respectively with, interpretations on the seismic section). MTDs A and B seem to mark the beginning of seismic unit II above seismic unit I. The 3 stratigraphic periods for MTD deposition are separated by roughly similar thicknesses.	21
Figure 5. Five main seismic facies used in our study (shown in green patches on top of the seismic sections). Facies were interpreted based on an automatic method developed by the IFPEN research group, not detailed in this paper.....	22
Figure 6. MTDs A and B slope maps of basal surfaces (BS) and upper surfaces (US). Dip direction shown by color hue, dip value by brightness. Both MTDs show a lateral erosive wall in their BS southern regions, and a change of BS and US dip orientation, indicating a change in orientation of the flow. Faults are visible on the BS and US of MTD A. Interpreted map shows a strong amplitude 'corridor' and two topographic depressions of the BS, retrieved from amplitude and topographic maps respectively. Amapá Upper Complex is described by Reis et al. 2016 (see Figure 2).	26
Figure 7. MTD A (circled in dashed line). Seismic section (a) and seismic facies (b). Faults and topographic depression are highlighted, with possible plowing (sensu Posamentier & Martinsen, 2011) on the high-amplitude negative-polarity basal surface (BS) of MTD A. Irregular high amplitudes are also visible inside. Deformed facies rather appears at the head part of MTD A (similar distribution for C).	29
Figure 8. Upslope scarps showing fore-stepping evolution of the erosion on one dip seismic section from our seismic cube.	32
Figure 9. MTD B illustrated on a 2D seismic line. Black solid line: contour of MTD B drawn on a section extracted from the 3D cube (projected onto the 2D line). Dashed line: possible continuation of MTD B, interpreted from the 2D data.....	38

Figure_Supplementary 1. Knowledge-based graph representations: (a) one possible visualization, and (b) adjacency matrix. Figures obtained via the Gephi software (https://gephi.org/).....	45
Figure_Supplementary 2. Bathymetric map with flexure impact from the fan load; from Watts et al., 2009 and Rodger, 2009. Solid lines show the flexural depression (contour interval: 250 m). The inland flexural bulge is not visible on this map. The 3D seismic cube is mapped with available seismic data in dark orange.	47
Table 1. MTD characteristic properties and their descriptors. BS: Basal Surface, US: Upper Surface, HS: Headscarp.	10
Table 2. Environmental controls and mass-transport event properties. ‘Mass-transport event properties’ comprise properties of the trigger phase, the transport phase and the deposition phase (possibly including post-deposition modifications). ‘Environmental controls’ are potential impacting large-scale processes.....	11
Table_Supplementary 1. Edges of the graph. Columns indicate the source node and target node, the directed/undirected character of the edge, and reference(s) that support its definition. A second tab in the table gives all references used in the first tab. A third tab gives all edges connected to MTD descriptors nodes.	45
Table_Supplementary 2. Detection limit for descriptors of Table 1, in terms of dataset coverage, resolution, and other aspects.....	45

Sizes (desired width) and colors of Figures and Tables

Figure 1. 2 columns if (a) and (b) are stacked horizontally, 1 column otherwise. Color needed.
Figure 2. 1.5 columns. Color needed.
Figure 3. 2 columns. Color needed.
Figure 4. 1.5 columns. Color needed.
Figure 5. 2 columns. Color needed.
Figure 6. 1.5 to 2 columns. Color needed.
Figure 7. 1 column (or 2 columns, (a) and (b) stacked horizontally). Color needed.
Figure 8. 2 columns. Color needed.
Figure 9. 2 columns. Color needed.
Table 1. 2 columns. No need for color.
Table 2. 2 columns. No need for color.

Table_Supplementary 1, Table_Supplementary 2, Figure_Supplementary 1 and Figure_Supplementary 2 are supplementary material.

3.4 Outlook on the knowledge base automation

In the previous section, we have presented a novel methodology to propose hypotheses on the causal factors at the origin of the seismic signatures of MTDs. It relies on a knowledge base built from the literature, thus corresponding to an ontology - although the knowledge base is not perfect nor exhaustive yet. The application we have made can constitute a proof of concept, showing that the knowledge base and the methodology to use it could be used for other applications.

In order for the knowledge base to be shared, usable and modifiable by others, it should be formalized with the standardized Semantic Web technologies, as referred to by the World Wide Web Consortium (W3C), “an international community that develops open standards to ensure the long-term growth of the Web” (W3C (2018)). For this, some specific tools are needed, as highlighted by Malik *et al.* (2010).

In particular, a specific formal language is to be used for expliciting the description of heuristics, logical rules, and relationships in general between data-extracted elements and external processes. The Ontology Web Language (OWL) is the standard language for such task. OWL is the format of ontology files that are shared accross the internet to share semantic representations of knowledge. An open-source ontology-edition software can be found on the [Protégé²](https://protege.stanford.edu/) webpage; the Protégé editor is developed and maintained by the Stanford Center for Biomedical Informatics Research (Musen (2015)).

Similarly to Wang *et al.* (2018) (mentioned in section 3.1.2), we then need to create a system that allow interactive queries and visualization in order to use the knowledge stored in the OWL-formatted ontology. Descriptor by descriptor, the user would ask for all the potential causal chains of processes leading to the descriptor, and visualize the rules that are associated to each edge of the graph involved in the chain, together with the associated literature source(s). In this way, the work presented in the article would be transcribed to the computer.

Several developments would then be required, e.g. in order to define how to enable tests of hypotheses via weighting differently several edges (of the graph). In a broader sense, the accurate representation of context-based information to be added a priori or a posteriori is another challenge, summarized by Reitsma *et al.* (2009) as abstract “incorporation of context into reasoning”.

²<https://protege.stanford.edu/>

3.5 Conclusion

In this chapter, we have focused on the second objective of the PhD: interpretation of MTDs in terms of processes that may explain their seismic signatures.

Several challenges were associated with this objective: diversity of mass transport processes, diversity of MTD characters; balancing the subjectivity of interpretation and the objectivity of existing geological knowledge; variability of interpretations, and possibly multiple causal processes for one MTD-related elements.

To address this question and these challenges, we have developed a novel methodology. It is based on a graph which contains information extracted from the literature. This information is represented by the nodes, which show the diversity of MTD characters on the one hand, and of mass transport processes on the other hand. The edges of the graph carry pieces of information which, as they are considered all together, becomes more and more free from the bias of observation or modeling. Introducing external knowledge on a specific study can be done, thereby adding subjectivity to interpretations, which is needed in particular to take other kinds of data into account.

The methodology has several limits, exposed in the previous section. It needs rather good-quality data as input, so that it may not be applicable everywhere; it is not complete, both because of potentially missed articles, and because of the biases present within the literature.

Nevertheless, we have shown an application on the seismic block of the Amazon basin which gives correct results. Next steps for improving this methodology is primarily by extending the graph content, formalizing it to a standard numerical representation, and automatizing the acquisition of results with an interactive approach.

Chapter 4

Implications of our methods for interpretation schemes and for sedimentary basin understanding

This chapter aims at showing how the two methodologies developed for Identification (chapter 2) and Interpretation (chapter 3) are valuable for interpretation schemes and sedimentary basin understanding. The two methodologies are examined together. We then evaluate the way seismic and external sources of information have been used and how our methodologies benefit from them. We finally give some insights on how this work can contribute to sedimentary basin understanding.

4.1 Relationship between the two objectives of identification and interpretation

The initial research problem leading to our objectives 1 and 2 is part of questions on the impacts of mass transport on the infilling of a sedimentary basin, and the factors that control mass transport processes. The two methodologies we have proposed are a step forward in the understanding of such impacts and factors, by using both data- and knowledge-based information. The identification methodology gives as output delineated objects with access to internal facies variations. The interpretation methodology takes as inputs several MTD descriptors, and yields hypothetical interpretations as outputs.

In this work, we have chosen to distinguish the two, as their contributions are different and they can be used independently anyway. Our applications have been done independently: for the input of the interpretation methodology, we have used manually-delineated MTDs within the cube, instead of the automatically retrieved ones. However, the respective contributions of both methodologies would be enhanced if the outputs of the identification could serve as input for the interpretation. Figure 4.1 summarizes the global workflow

joining the two methodologies in such case.

In this section, we reconsider all the inputs of the interpretation methodology. We evaluate the possibility to retrieve some of them from the identification outputs, and we examine how objective the methodology can be while using other qualitative and binary descriptors.

4.1.1 Objects and their contours

In section 2.4.4.1 (p. 124), we have compared the objects yielded by our identification methodology and those from a manual delineation. The volume of the retrieved objects with our method is underestimated compared to a manual delineation.

As shown in Figure 2.16 (p. 125), one manually-drawn object might be retrieved as two separate objects in our method. This first point can be related to (i) the quality of the seismic data to resolve thin regions of the object (which, if too thin, might create an artificial break), and (ii) the parameters used for the post-processing, precisely for the morphological closing of the 3D image. Regarding point (ii), Figure 4.2 shows the result of two different morphological closings on one section of the cube. A sphere was chosen as structural element for the closing as it is the least-informative 3D shape. The first result is the one as used in our article, section 2.3, i.e. where the structuring element is a sphere of radius 10 voxels (i.e. 225m laterally, 36ms vertically; it approximately corresponds to the size of the texture patches (11x11 voxels)). The second result was obtained with a sphere of radius 15 voxels (i.e. 350m laterally, 56ms vertically). We see that, due to this larger radius, the main body of the MTD has softer contours and even the two objects get joined. However, we keep only pixels with positive probabilities after this morphological operation, which separates the objects again. Although the result of the closing with larger structuring element (Figure 4.2b) seems more relevant (one object only, more relevant contours that follow the shape of the manual one), it does not take the posterior probabilities into account. In such a case, some pixels with seismic facies irrelevant of the MTD could be added, or hide specific traits of the contours (e.g. ramps) due to the closing operation. For consistency, we still keep only pixels with strictly positive probability. In this case, even with a closing with larger structuring element, our methodology is not able to recover the objects as one piece. This implies that, for them to be considered as inputs for the interpretation methodology, a manual step has to be included to join the regions that belong to a same MTD.

Figure 2.16 (p. 125) also shows that the contours of the objects retrieved by our methodology are not reliable for descriptor characterizations like basal surface ramps, plunging pool indicator etc., i.e. input descriptors for the interpretation. Thus, considering the

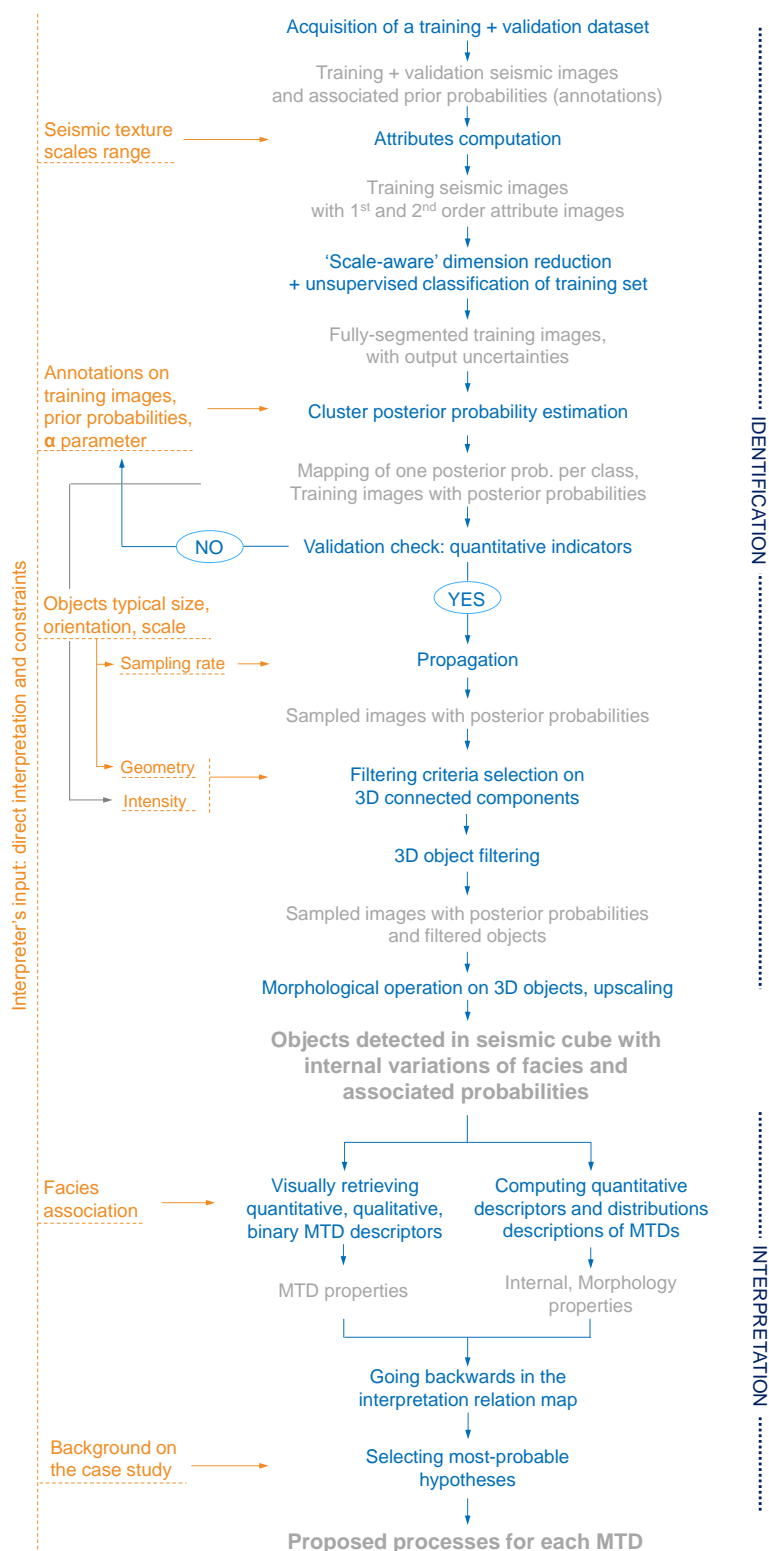
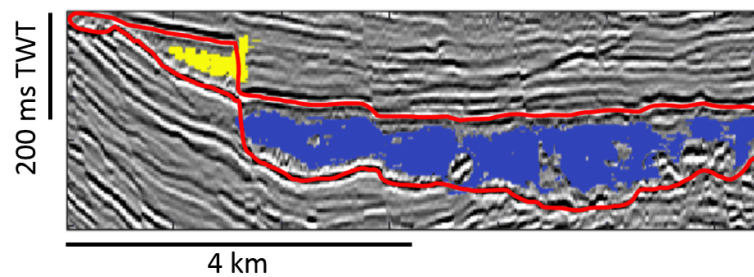
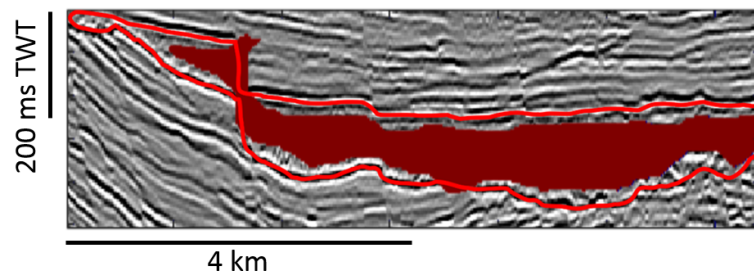


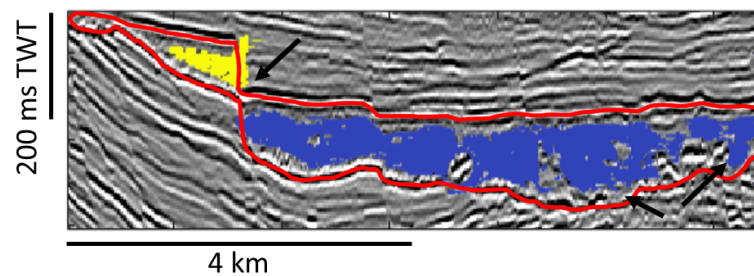
Figure 4.1: Proposed workflow joining our two contributions into a global methodology for mass transport process interpretation from seismic data.



(a)



(b)



(c)

Figure 4.2: Objects recovered as one or more pieces. (a) Result of the object post-processing on one seismic section as presented on Figure 2.16. (b) Result of the object post-processing, where the morphological closing uses a larger structuring element - including all pixels. (c) Result of the object post-processing, where the morphological closing uses a larger structuring element - selecting only pixels with positive probability. Black arrows indicate pixels added compared to (a).

state of the methodology to date, delineations obtained from our identification workflow cannot be used directly as inputs for the interpretation methodology.

A manual / semi-manual delineation of the objects' contours has to be used in complement to the automatic identification, to include all relevant features of the object contours. One could either use a horizon propagation (where surfaces follow a horizon) in dedicated softwares or a manual picking for erosional surfaces. In this case, the delineation must be picked with enough precision, as detailed in section 3.3. For example, missing upslope ramps that in reality affect the basal surface cancels the emergence of the hypothesis of a retrogressive series of mass transport events. A too loosely-picked basal surface could prevent from recognizing a relatively steep lateral erosive wall, thus an erosive transport and other potential causes to this erosive character. The replacing manual delineation should thus make it possible to further interpret the basal and upper surfaces with the interpretation methodology.

4.1.2 Objects and their internal facies

We have discussed in section 2.4 the improvements that 3D seismic facies consideration would allow. In the seismic cube and inside the identified MTDs, facies are one key result of our identification methodology. They are also used for input descriptors of the graph in the interpretation.

Facies maps and lateral proportion curves allow to characterize quantitatively the internal facies distributions (see Figure 4.3). One lateral proportion curve is the integration of a facies proportion map over one direction; for instance on Figure 4.3, the lateral proportion curve varying along direction 1 is the integration of the facies map over direction 2. Yet to relate these elements to orientation-related descriptors depends on the orientation of the cube. In our case study for example, the cube is dip-aligned, yet the MTD direction is not only aligned with this direction. Here 3D facies would be better adapted to show, e.g., ridged facies in directions other than dip, and, if any, preserved blocks aligned in the MTD principal direction.

The fact that MTDs may not be aligned with the inlines, or crosslines, of a seismic cube, makes it less relevant to use lateral proportion curves. Facies proportion maps are considered relevant because MTD morphologies are rather spread on the two horizontal directions compared to the vertical one. If the MTD is oblique to the inlines and crosslines, then one could pick a 'random line' crossing through the MTD, and integrate along this direction.

For now, facies descriptors within the MTD are studied with a lateral proportion curve only if analyzed together with the facies map. However, in the future, using curves rather than a map would allow to get simple quantifications of facies variations (e.g. on Figure

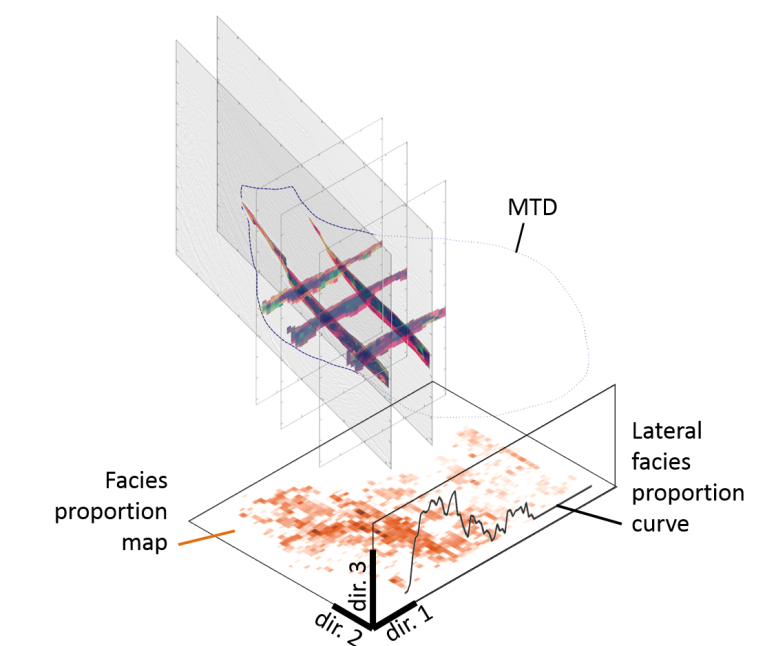


Figure 4.3: Integrating facies to create facies maps and lateral proportion curves. Five seismic sections are shown with the corresponding MTD sections, colored according to cluster numbers. The red-level facies map shows the vertical proportion of one facies (as defined in section 3.2 and Figure 3.5) in each column of the MTD (integration over direction dir. 3). The curve shows the lateral proportion of the facies, in each dip-oriented section of the MTD (integration over directions dir. 2 and dir. 3).

4.3, 'high facies proportions' vs. 'low facies proportion' on each end of the curve).

4.1.3 Qualitative and binary MTD descriptors

Among the inputs to the interpretation methodology, qualitative descriptors are categorical ones (e.g. the Headscarp morphology), that have to be assessed by the interpreter. These may be exposed to subjective observations. In this case the input carries some undesirable bias.

Concerning binary descriptors on the presence or absence of certain feature, a limit here is given again by the data resolution and coverage. The presence of ramps on the basal surface of an MTD, for instance, may not be seen if the picking grid for the contours was not precise enough.

While building the graph, we selected descriptor nodes to be 'elementary' descriptors of the MTD, i.e. that do not depend on other qualifiers, thus as unbiased as possible. The manual input is still needed, though. The objective of the interpretation methodology is not fundamentally to be fully automated (although in the long term it would be preferable) but primarily to provide a framework for comparable interpretations. An interpreter using the graph should therefore be aware of these limitations and, potentially, put less

weight a priori, either on the edges of the graph directed at these descriptors, or on the hypotheses arising from these descriptors.

4.2 How have we made the most of seismic data and prior information?

In section 1.6, we have mentioned several elements that challenged our objectives. We now recap how our approaches and contributions deal with these elements.

4.2.1 Mixing a-priori expertise and new objective methods

In both methodologies presented in this document, we have tried to differentiate the contributions of 'objective' origin - such as a dataset or a knowledge base -, from those of more subjective origin - such as interpretations from an expert. On the left-hand side of Figure 4.1 are displayed the stages of the global workflow where one or several user(s)/interpreter(s) are directly involved. They consist in:

1. Identifying the range of scales to use for characterization of patterns in the seismic data, in order to define the range of parameters for the textural attributes computation.
2. Potentially annotating the training images with prior probabilities; giving a value for the α confidence parameter according to the uncertainty on the annotation, coming either from the interpreter or from an external computation.
3. From an expectation on the objects typical size and morphology, giving (i) an adapted sampling rate for propagation, (ii) one or several geometric constraints for object filtering, (iii) one or several intensity constraints (i.e. based on the pixel values) for object filtering. This input may actually be not used, if all sections are used for propagation, and if an efficient computer interface enables to perform the filtering interactively.
4. Interpreting GTM clusters in terms of seismic facies, i.e. associating facies labels to textural descriptions (similarly to what is done in Figure 3.5, p. 140); retrieving MTD descriptors for the interpretation.
5. Weighting hypotheses according to the studied context, among the possibilities given by the graph methodology. This comes after, or prior to, the use of the graph, and could be done in a quantitative manner in the future.

Throughout this workflow, the user's input should be motivated by other data on the studied region. It could be well log measurements or cores allowing for precise facies definition guided by the seismic facies at the well positions. This strengthens the definition of seismic

facies for interpretation (item 4. of the list). It could also be results of previous studies on other parts of the basin, showing certain sizes/morphologies of MTDs and leading to expect the same kind of objects in the studied region (items 1., 2. and 3.), or certain kinds of processes (item 5.).

On the other hand, we emphasize three main contributions from a dataset and/or a knowledge base, i.e. not including any a priori interpretation and comparatively denoted 'objective':

- Data representation through texture as a non-selective set of seismic attributes, i.e. representation of the whole variability of multi-scale seismic textural facies;
- Unsupervised clustering for data-driven representation of similarities between pixels;
- Knowledge-based hypothesis proposal for interpreting mass transport processes.

Finally, the mix between both sources of information is mainly performed during the following stages:

- Cluster posterior probability assignment, where two image segmentations are combined: one containing the data-driven clustering, one containing the prior probability annotations (see e.g. Figure 2. of the article in section 2.3);
- Propagation, where the clustering and posterior probabilities are computed for pixels from other seismic sections;
- Assessing the final results of the knowledge-based interpretation.

Therefore, both sources of information are coupled in our methods. The whole workflow is not designed for automation only, but rather for interactive numerical work.

4.2.2 Adaptability of the method to any kind of seismic data

The applications presented in this document were done on a 3D seismic cube - although initially based on 2D extracted sections for the Identification. Both methodologies may nevertheless be applied as well on 2D seismic profiles alone.

Concerning the identification methodology: its main interests are to save time, to potentially cover the lacks of manual delineation, and to preserve a multiplicity of facies inside the objects. For a huge set of similarly acquired and processed 2D seismic profiles, the methodology will be useful, as the propagation stage will save time. For very few 2D profiles, however, confident manual delineation and facies classification might not be so long to acquire, in which case the methodology would not reduce the study time; nevertheless, distinguishing and quantifying the different facies, their similarity and their distribution

inside the MTDs still seems valuable with the unsupervised part of the methodology.

Concerning the interpretation methodology: as mentioned in the article (section 3.3), several limitations arise concerning the quality of the seismic data needed to have access to input property descriptors. Another point is that using 2D profiles rather than a 3D cube will give access to different MTD descriptors for the input. Typically, the whole length of a huge MTD can be covered by a 2D profile while it is less likely in a 3D cube. Conversely, the generally poorer seismic resolution of 2D data gives less precise facies and surface morphologies. The Global Environment property descriptors may also be lacking if using only one 2D profile.

Finally, on the whole, both methodologies produce their best results with high-quality data and high computer power - enabling a 3D textural attribute computation, a fine initial clustering (with more than 49 clusters), a propagation on many sections or the whole cube, an interactive seismic visualization interface, and a quick automation of the graph structure.

4.2.3 Point-by-point practical solutions

Here is a recap of the main challenging elements presented in section 1.6:

1. Mass transport processes and MTD characters are diverse;
2. The numerical definition of a structural model in a seismic image usually requires a manual input;
3. The numerical definition of objects within a seismic image is likely to depend on the scale of study;
4. The numerical definition of seismic facies is likely to depend on the scale of study;
5. Manually delineating an MTD in a seismic image starts by spotting only parts of it first;
6. Seismic facies are not sufficient to represent all the variability of geological facies;
7. Manual interpretations can differ from one interpretation to another: the 'ground truth' is never known in underground studies.

Items 1., 3., 4. and 5. have been handled by the choice of our local, yet multi-scale, approach: we work with several typical textural facies, instead of only one; and working with facies rather than geometrical constraints avoids having to use only one size or morphology of objects (the geometrical constraint is added only during the post-processing of the identification methodology). This release is limited of course, as seen in our results.

Patches are still to be defined anyway, thus their size still constrains the maximum and minimum sizes of discernible patterns.

Items 6. and 7. have been handled by the choice of our interpretation methodology, where (i) facies distribution descriptors are chosen among the most effective for interpretation according to the literature; and (ii) variable hypotheses are actually included in the graph. Item 7. has also been handled by the introduction of probabilities and a confidence parameter in-lieu of a 'ground truth' in the identification methodology.

Finally, item 2. is not improved by any feature of our contributions. Again, a manual input is needed for defining the structural horizons and faults that define a stratigraphic model from a seismic cube. Nevertheless, we will show in the next section how our contributions can be related to the stratigraphic understanding of a basin.

4.3 Implications for sedimentary basin understanding

Interpreting mass transport processes associated to MTDs is key to a better understanding of the sedimentary evolution of a passive margin. In this section, we propose ways in which the methodologies presented in this thesis could improve this understanding.

4.3.1 Facies-based approach

The facies classification and object presence probabilities that we have proposed could be used for inferring the evolution of depositional environment with time; from the analysis of the facies distributions in the seismic cube, one can find elements that distinguish several seismic units. For example in Figure 4.4, the deformed facies is shown on one section. This deformed facies appears to be related mostly to slopes and a little to some basal regions of MTDs. A delimiting horizon (Horizon H1) can be drawn to separate two seismic units, and the deformed facies spatial distribution appears to differ in both units, thus supporting the definition of H1.

The integration of facies as already presented in section 4.1.2 may further be done laterally in the geological time frame: following 'iso-age' surfaces determined by an assumption on the stratigraphy between two horizons. For this, we need a sufficient number of horizons. Figure 4.5 shows how, from the study of one seismic cube and its associated clustered cube, we could make a hypothesis on the positions of iso-age surfaces in the cube. Then, instead of integrating facies horizontally in the cube, one could integrate along these iso-age surfaces. In the figure, for a first approach we assume that these surfaces are parallel to the top horizon of the layer (here, the seismic unit). Figure 4.6 shows the 'sub-vertical' integration curves of several facies groups in this case, for the top-most seismic unit of Figure 4.4, i.e. the unit containing MTDs. It also shows a curve of 'MTD-like' facies, corresponding to the grouping of clusters having maximum posterior

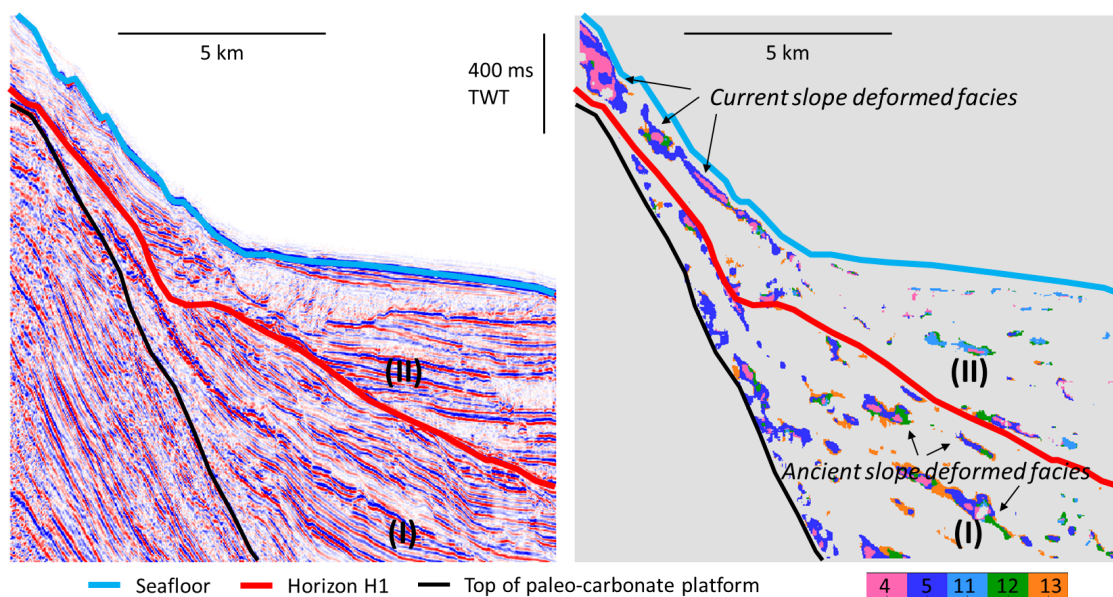


Figure 4.4: Clusters corresponding to the Deformed facies (numbers 4, 5, 11, 12, 13, see also Figure 3.5) on one seismic section. Horizon H1 is a hypothetical unconformity between seismic unit (I) (ancient slope) and unit (II) with MTDs.

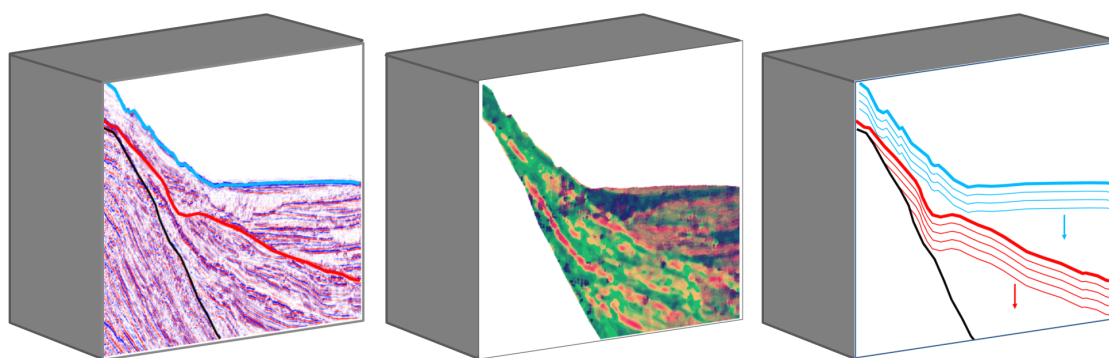


Figure 4.5: Determination of a stratigraphic pattern to use for calculating 'vertical' facies proportion curves along the geological time. From the study of a seismic cube (left) and its corresponding clustered cube (middle), we hypothesize the pattern to use (right). Here, for a first approach, iso-age surfaces are considered to be parallel to the top horizon of one layer.

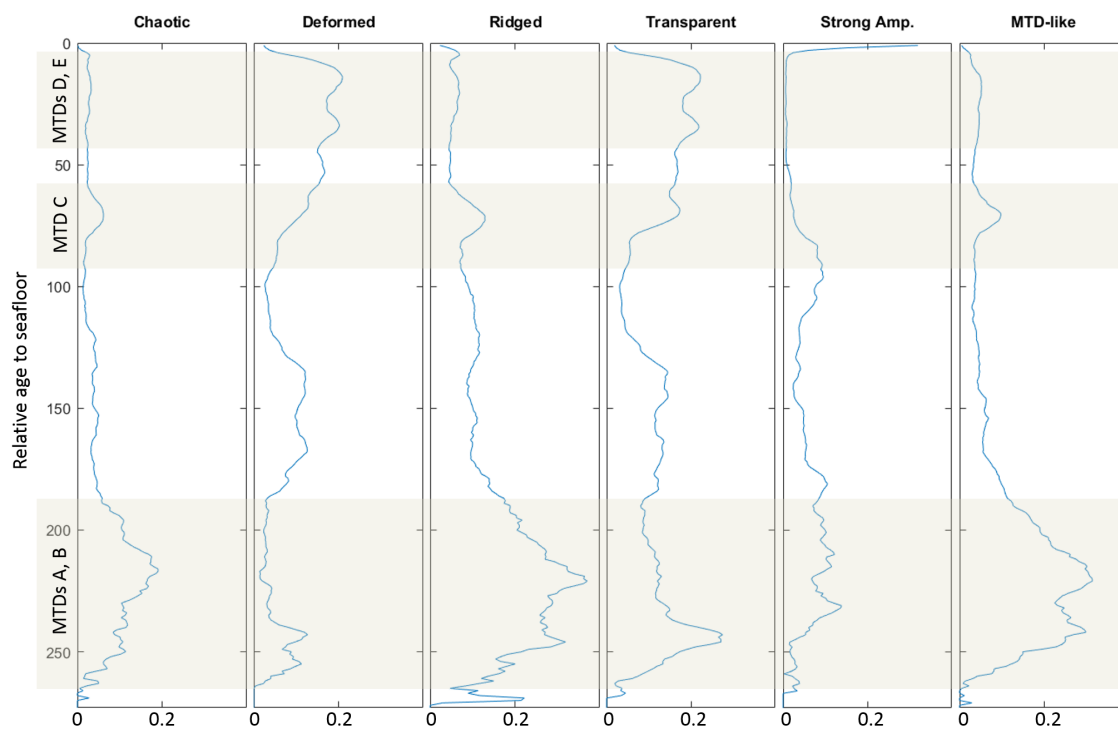


Figure 4.6: Facies proportion curves calculated along the geological time on the clustered full-stack seismic cube, in the top-most layer (between horizon H1 and the seafloor, see Figure 4.4), given the pattern shown on Figure 4.5. Approximate positions of MTDs in time are given. The 'MTD-like' facies kind is the grouping of clusters having maximum posterior probabilities in the cluster probability assignment presented in chapter 2.

probabilities in the cluster probability assignment of chapter 2. On these curves, the proportions of several facies, especially the chaotic, ridged and transparent facies, apparently correspond to the depths of MTDs A, B and C (for the position of MTDs in the cube, see Figure 3 in the article, section 3.3). MTDs D and E are less visible, probably due to their small thickness.

A potential development of using vertical proportion curves in the geological time frame is to infer the evolution of the deposition of certain facies kind with time, i.e. relating this facies to certain depositional environments. In particular, a cube of posterior probabilities such as given by our method (see e.g. Figure 6 of the article in section 2.3) could allow to assess the evolution of the proportion of 'MTD-like' sediments in successive sedimentary layers. This may provide interesting input constraints for sedimentary basin forward modelers.

4.3.2 Object-based approach

The MTD descriptors defined in the graph are global, i.e. one descriptor describes the whole MTD (for instance, facies-related descriptors characterize the entire facies distribution and not each pixel separately). This allows to compare two geobodies in a same seismic cube. It could also be used to compare one seismically-detected MTD and a second MTD, e.g. one lying on the seafloor, which is not visible in the seismic data; this would have to be done using only relevant descriptors - for example, comparable facies descriptors cannot be retrieved for the second MTD if it is not within the range covered by the seismic.

More importantly, for forward models that simulate the deposition of an MTD, the model could be compared to the real one through the use of such global descriptors.

4.4 Conclusion

In this chapter we have detailed the relationship between the two methodologies developed in chapters 2 and 3, to show the limits that remain; they mainly concern the need to improve the contours and volumes of the identified MTDs if they are to be used directly as an input for the interpretation methodology, and the quality of the seismic data used. We have also stated the key points that enable us to deal with the challenges associated to our objectives. Finally, we have proposed prospects for which our approaches could be advantageously exported in terms of understanding of sedimentary basins.

Chapter 5

Conclusion and perspectives

This PhD report has been devoted to understanding better mass transport deposits and their origin, through an approach of seismic data. Two main objectives were given: being able to locate MTDs in seismic data, in position and extension, while preserving the variety of their characters, and to characterize physical processes acting over geological times, responsible for location, geometry and internal heterogeneities of these MTDs. The Amazon Offshore River Mouth basin was chosen as a case study for our developments. In this concluding chapter, we synthesize the contributions of this PhD, discussing how our initial objectives have been reached. We also suggest some perspectives for future developments and research.

5.1 Main contributions of this PhD

5.1.1 Methodological contributions

The two objectives of this PhD were: (1-Identification) to locate MTDs in seismic data, in position and extension, while preserving the variety of their characters; and (2-Interpretation) to characterize physical processes acting over geological times, responsible for location, geometry and internal heterogeneities of these MTDs.

Identification

In chapter 2, we have proposed a novel methodology for MTD identification in seismic data. The methodology leverages existing approaches of unsupervised learning for clustering and supervised learning for integrating uncertain prior information to the whole dataset.

The coupling of such unsupervised and supervised learning methods is new; it may be seen either as a globally supervised approach, where the training is performed on top of an unsupervised clustering; or, as a globally unsupervised approach, where a post-processing

allows to characterize each cluster regarding certain supervised objective (here: selecting clusters that are most representative of MTD presence). Within the supervised stage, we have proposed a new method for incorporating uncertain prior object delineations into a learning scheme. This addresses the problem of uncertain prior information by giving access to posterior probabilities that depend on the prior ones. We have also demonstrated the need for an informative data representation, by comparing two dimension reduction methods, of which the feature-extraction method proved more adapted to convey the initially-extracted textural information.

Our application on the three partial-stack cubes and the full-stack cube of the Amazon case study was mostly successful: expected MTDs were retrieved, although some of them appear only in parts, and overall volumes are under-estimated; therefore the exact delineation is not achieved. The identification methodology preserves the internal textural facies variations of MTDs and gives an associated probability as a value of confidence for each positively-weighted facies, related to the prior training data. The confidence parameter associated to prior training data may allow additional interpretations: the possibility to consider the training dataset as non-entirely annotated allows the emergence of objects in unexpected areas.

The Amazon application has shown the robustness of the intermediate GTM-based unsupervised representation. It has additionally allowed to specify the minimal seismic facies labels that are needed to detect the MTDs in the studied full-stack cube: the transparent, ridged and chaotic facies. We have also shown that the object filtering used in the last step of the methodology is sufficiently neutral not to jeopardize the quality of results in terms of variety of MTD objects.

The most important limit to the methodology is related to the consideration of oriented seismic textures. The initial use of 2D rather than 3D information for data representation narrows the range of variable facies detected, as well as the applicability of the methodology in some cases.

However, despite its limits, this methodology has highlighted that an unsupervised seismic data representation contains ready-to-use high-level information usable for specific purposes requiring a learning step. It is therefore one way to answer the requirements of objective 1.

Interpretation

In chapter 3, we have proposed another methodology for guiding the interpretation of processes involved in a mass transport event, based on seismic characters of an MTD. This novel methodology proposes potential physical processes at the origin of these seismic characters. It relies on a literature review, which is organized in a structured way:

instances that characterize an MTD are separated from those characterizing a mass transport event; relationships between several instances are stored in a list. We have given a graph structure to this data, defining one node for each of the instances, and defining edges for the relationships, as impacts from one node onto the other. The choice of nodes and edges relies entirely on the literature review; it highlights the diversity of seismic signatures that may occur on MTDs as well as the diversity of natural processes involved in mass transports.

With this methodology, we promote an explicit interpretation procedure that is, ideally, free from any bias. This means that by gathering many different interpretation paths and considering them all in the application so that not one of them initially prevails over the other, we hope to approach a non-oriented interpretation method. It is a new way to use existing interpretation models, by combining all knowledge into one ontology, i.e. a 'dictionary' storing this knowledge efficiently; the graph itself goes together with a method to use it, i.e. to use the knowledge stored in the dictionary. Globally, our methodology allows to break the interpretation process into its objective and subjective components, by separating knowledge-based information (stored in the graph) and experience-based, or prior-based, information (added a posteriori to the results, or through edge weighting in an automated version of the graph).

The graph construction itself allowed to spot, from the literature, the expression of MTDs in seismic data; it is revealed by several features that we called 'properties', each one described by seismic 'descriptors' in our approach. These properties are: the morphology of the MTD, its basal and upper surfaces, its position in the basin, its headscarp, its internal facies distributions, and its global environment. The impacting processes were also listed.

We applied this methodology to the Amazon case study. Its results were globally consistent with existing knowledge on the basin. The applicability of this methodology is limited by the quality of the input set of descriptors, which are themselves dependent on the quality of the seismic data. This may limit or prevent applications in cases where datasets have poor resolutions or when the studied MTD is not covered entirely by the survey area. Nevertheless, the methodology enables comparisons between several MTDs; it keeps track of several hypotheses without selecting one based on any prior input other than the knowledge-base content. These elements, together with the organization of this information into the graph structure and the way to use this structure, contribute to answer the requirements of objective 2.

A global workflow

Finally, a workflow comprising both methodologies is envisaged. In this case, the delineated objects resulting from the Identification step would be used to define some input descriptors associated to MTD properties for the Interpretation step. Other descriptors

would have to be provided by the user, from external computations or data observations. In this respect, the contours of the delineated objects would have to be of sufficient quality to enable the retrieval of descriptors such as surface ramps or striations. Moreover, the categorical and binary descriptors that are also used in the Interpretation may be prone to subjective assessments, which is not desirable. Special care should be taken when getting the input MTD descriptions, as the output hypothetical interpretations of the methodology critically depend on them. Possible enhancements to both methodologies should be beneficial to their merging; for example, if contours are better retrieved in the first place, they will provide more reliable basal surface descriptors as inputs to the interpretation part.

5.1.2 The Amazon case study

We now recall the main points that have come out of our project concerning the Amazon case study.

We have found the approximate extent in the seismic cube of a series of eight MTDs. The Identification methodology actually allowed to spot two MTDs which were not initially expected, because not seen in the dataset.

Our work has brought several elements on the two deepest MTDs of the studied series (MTDs A and B in chapter 3):

- Their internal facies properties (alternating homogeneous and heterogeneous regions, low proportion of deformed facies) and their associated erosional markers suggest that they result from debris flows, similarly to other kinds of MTDs encountered in the Amazon basin, although at larger scale;
- Faults that impact MTD A may be related to the extension that characterizes the proximal part of the Amazon basin;
- Arguments on the polarities of MTDs' basal surfaces, on their principal direction, and on the difference between A and B suggest an influence of the Amazon fan acting as a secondary sediment source and topographic and structural controls, in this North-Western part of the basin at least;
- The downslope evolution of upslope scarps as seen in the seismic cube could be a signature of the global progradation occurring since the Miocene, with large increases of sedimentation discharges.

These results were obtained thanks to a careful acquisition of the MTD descriptors, as part of the validation of the knowledge-based methodology.

5.2 Perspectives

5.2.1 A more accurate and flexible Identification

In Identification, the key limit in the short term lies in computation power and efficiency. We have mentioned that 3D consideration is lacking for fully representing seismic facies in a cube, and that this could be addressed by using 'slices' of data rather than sections, with the advantage of flexible positioning of the slice within the cube. We have also mentioned that more gray levels could be used in the GLCM representation. Similarly, more clusters could be asked for during the GTM stage. All of these limits could be overcome with a dedicated implementation on powerful hardware. The attribute computation, which can be time-consuming, is independent for every sample; moreover, the propagation of the GTM representation to the whole dataset involves both attribute, projection and probability mapping computations, independently for every seismic section. Both of these operations can thus be parallel distributed. The presented work shows the concept and feasibility of the methodology; we expect more added value to come out with more efficient computing schemes.

To improve the accuracy of the data representation, one could consider adding an attribute related to the 'depth' of a seismic sample in the image, be it in time or depth. If in depth, this attribute could be related to the velocity at this depth according to the velocity model. Similarly to [Zhao *et al.* \(2016\)](#) who add a stratigraphic constraint to their SOM clustering, we would then add a depth constraint to the GTM - not within the cost function as [Zhao *et al.* \(2016\)](#) do, however.

Another way forward to improve the applicability of the Identification methodology would be to add interactivity, thanks to a user-friendly interface. This could help in prior and posterior processings involved in the methodology. For the prior processing, a dedicated module could allow to import and edit any kind of image chosen to serve as prior input. The interface could also allow the interpreter to directly draw the prior interpretation on the seismic image itself. This kind of interaction is partly available through manual picking or delineation of polygons within existing seismic interpretation softwares. However, facilitating the acquisition of prior probability images could be useful. An example of such integrated tool is the Ilastik software for medical image processing ([Sommer *et al.* \(2011\)](#)), see e.g. Figure 5.1).

As for the post-processing, we here refer to the several filters on 3D objects that can be applied after the propagation phase. An interactive interface, where objects can be visualized and 'filtered', directly showing which objects are affected by the filters, would be helpful for interpretation, in particular to study objects that appear but were not expected. Furthermore, with such an interactive tool, the morphological closing could be monitored and potentially manual tools could be provided to modify and improve the

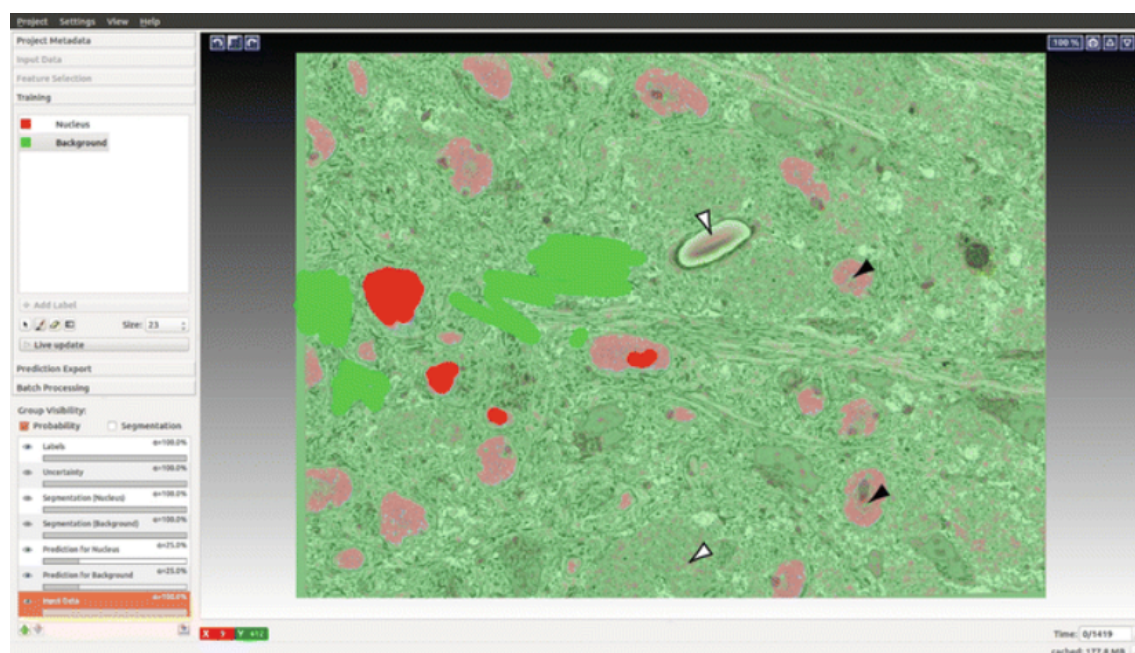


Figure 5.1: An application of the Ilastik software to the extraction of neuronal cell bodies and nuclei from electron microscopy image stacks. Red and green strokes, as well as arrows, are inputs by the user in the interface. From [Holcomb *et al.* \(2016\)](#).

resulting contours.

Additionally, as mentioned in chapter 2, another approach could be used for identification of heterogeneous geobodies or groups of facies: guiding the detection by a defined group of facies rather than by prior probabilities. In this approach, the user would need some expertise on the numerical facies created by the unsupervised representation; an interactive tool could help visualize facies one by one on the seismic data, thus easing the creation of this pre-defined group of facies.

Finally, machine- or deep-learning methods are precisely well-known for their accuracy and flexibility. The method promoted by [Ebuna *et al.* \(2018\)](#) is “objective” and it “minimizes potential interpreter bias”, while at the same time encouraging the use of ‘traditional’ seismic attributes that convey a physical meaning. In their ‘Karst Multi-attribute Workflow’, the input features to a classifying neural net (between karst and non-karst areas in a seismic dataset) result from a statistical analysis selecting the ‘best’ attributes among a large list of varied ‘traditional’ attributes. This method is an example where the seismic data representation is initially of a higher level than, for instance, textural attributes; in the following, the statistical analysis schemes they mention avoids making a potentially biased choice among these ‘traditional’ attributes. The choice is rather done statistically. This combination allows a careful creation of the seismic data representation, which in many cases is as important as the quality of the classifier itself.

Another path that seems interesting is suggested by the work of [Zeiler & Fergus \(2014\)](#),

in which the authors display the features learnt by the CNN, after the learning. This approach could be investigated for cases, like learning the position of salt bodies in seismic data, where it is not understood yet why such good results are obtained. Studying the features that an 'agnostic' and successful machine has learnt could lead e.g. to recognize in these features one or several of our 'traditional' attributes; conversely, it could lead to a complementary understanding of our perception and interpretation of seismic data.

5.2.2 Transferring Identification methods

The image processing methods proposed for Identification could be applied for several different cases. First, other seismic data in time or depth and other heterogeneous objects or regions could be targeted (e.g., for reservoir studies).

Still with seismic data, [Lewis & Vigh \(2017\)](#) have proposed an application which combines the creation of a probability image indicating salt position in a dataset, and a full-waveform inversion. The salt-probability image is retrieved by a deep learning approach and transformed into a prior velocity model by replacing in a basic velocity model the velocities of high-probability regions by salt velocities; then, this prior model is used in the inversion, and updated only at a few iterations. Several methods which 'deep-learn' a probability image like the one of [Lewis & Vigh \(2017\)](#) have been proposed recently (e.g., [Veillard *et al.* \(2018\)](#), [Gramstad & Nickel \(2018\)](#)). Our methodology could also be tested for salt-body application, yet it does not compare to those already existing in terms of computational efficiency. However, as applied for MTDs, it could for example provide prior estimates of the uncertainties for velocities in an inversion process, as these uncertainties should be high in MTDs with strong internal property variations.

The method could also be applied for maps, for instance bathymetric maps or horizon slices extracted from a seismic cube. Superficial MTDs could be studied considering these images. Additionally, at smaller scales, studies have been proposed to map seafloor marine habitats as classified regions. For instance, [Blondel & Sichi \(2009\)](#) propose textural analysis of multi-beam sonar imagery with GLCM-based attributes and using the K-means clustering. [De Clippele *et al.* \(2017\)](#) map live biogenic reef in cold-water habitats through classification of local topographic features within a GIS environment. [Ismail *et al.* \(2015\)](#) classify submarine canyons areas on sonar data. Our methodology could be adapted to depict heterogeneous marine habitat types.

Finally, object retrieval is a challenge in a lot of domains, among which satellite imaging and medical imaging. A few examples were given in chapter 1. Our methodology would be worth testing in such applications, especially when a representation with intra-object/intra-group variations is needed. Probably though, natural images (like photos) are not an applicable domain for this methodology, as learning a local representation (al-

though multi-scale) may not be efficient enough to address the problems posed by these images.

5.2.3 An automated, comprehensive knowledge-based system

A formalization into a numerical standard framework is an immediate improvement that would enhance the Interpretation methodology. As detailed in section 3.4, the ontology editor *Protégé*¹ (Musen (2015)) is adapted for that.

Deepening the literature review and keeping it up to date is definitely important for the knowledge base to be as comprehensive as possible. However, in order to have a wide range of references (as people from different communities do not use the same sources), the involvement of several researchers, ideally from different backgrounds (e.g., data interpreters and modelers) is recommended. Furthermore, a system able to perform the inference of hypotheses given certain observations, called a 'reasoner' or 'inference engine', has to be run on the defined ontology. The W3C (2018) gives some example of such systems on their website. Then, various uses could be proposed, for example putting different weights on edges of the graph for testing different hypotheses.

Note that by definition, ontologies are used in many different domains. The main work that needs to be done is for the expert of a domain to formalize his/her knowledge into the ontology elements. In our case, the literature had the role of the 'expert' as our main source of information.

5.2.4 Suggestions for advances on the Amazon case study

Our applications on the Amazon case study has raised several questions that would be interesting to tackle in the future. A first question concerns the Amapá Upper Complex (AUC) described by Reis *et al.* (2016) (see Figure 1.12). The direction of our MTDs A and B seems to be aligned with that of the AUC (Fig. 6 in the article of section 3.3). Now we have seen that the continuation of the MTDs further in the basin with the 2D data available for this project is hardly obtainable (Fig. 9 in the article). The question remains: are MTDs A and B, or the upper C, D etc., related to the AUC? They may not be directly connected, however their occurrence in a specific seismic unit of the dataset indicates that a lot of instability has taken place since the first MTDs of the series (MTDs A and B).

This leads us to the second question, mentioned in section 4.3.1, Figure 4.4. From our observations of the seismic dataset and some cluster-colored sections (as on Figure 4.4 (right) or Figure 4.5 (middle)), it seems that two seismic units appear in the downslope region of the cube, above the top of the paleo-carbonate platform. These units could correspond to a former slope sedimentary series (I) underlying a more recent basin series (II) which

¹<https://protege.stanford.edu/>

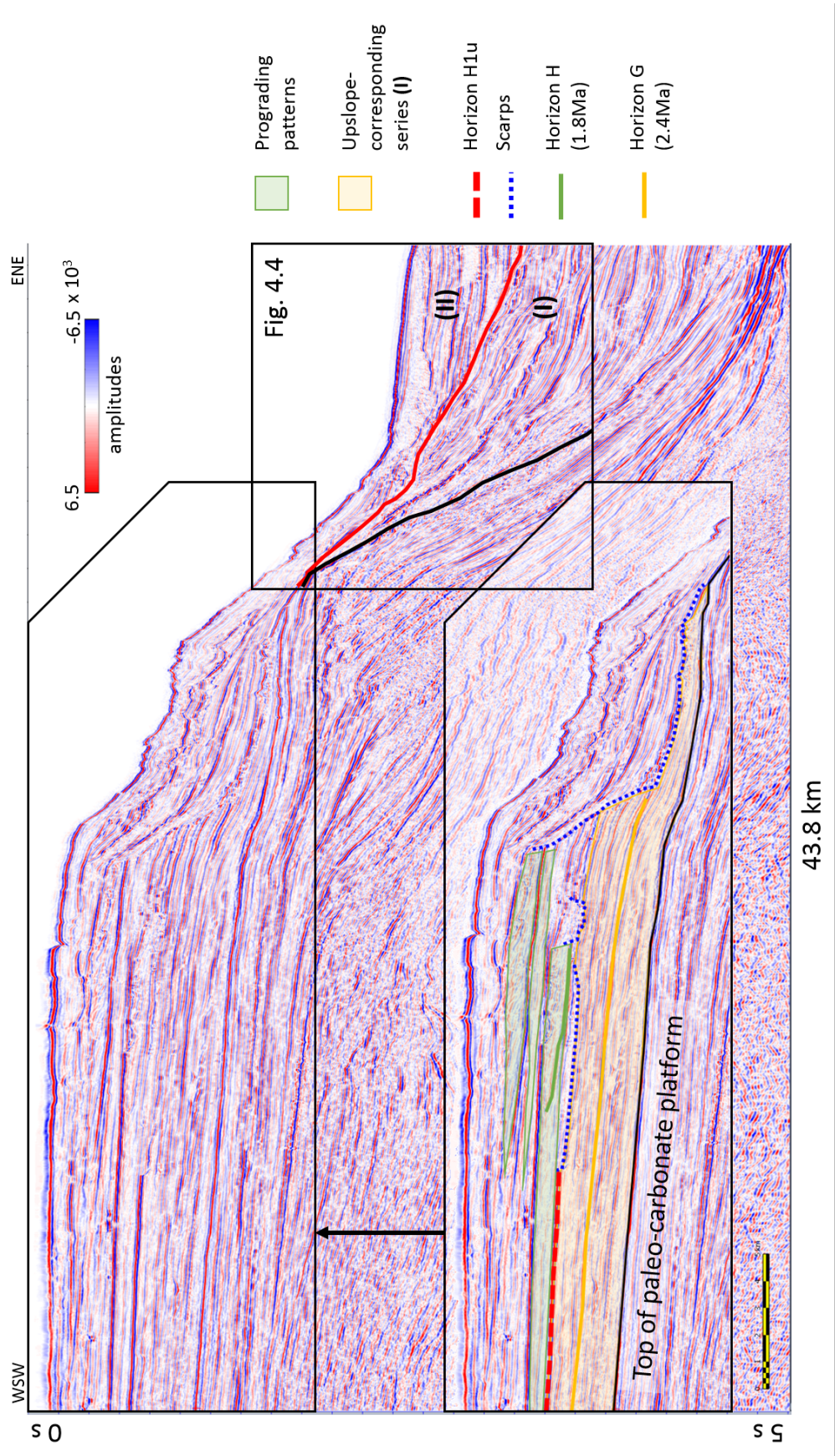


Figure 5.2: One inline of the seismic dataset with suggested relationship between the downslope region (displayed on Figure 4.4) and the upslope region. H1 downslope hypothetical unconformity illustrated as a red solid line similarly to Figure 4.4; H1u (upslope) hypothetical corresponding unconformity illustrated as a red dashed line.

includes MTDs. Meanwhile, the observation of the upslope part of the cube (also above the carbonate top) has led to describe progradation patterns and erosional scarps, that are probably linked to the downslope MTDs. The upslope series (see Figure 5.2) displays a former series of undisturbed reflectors that are topped by a high-amplitude, very regular reflector, cut by the first scarp. This reflector is termed 'H1u' in Figure 5.2. Above this series, at least one other reflector with similar properties, and other scarps, are found, together with prograding patterns in the seismic section. We thus suggest investigating whether H1 and H1u correspond to one stratigraphic event, and why such unconformity occurs on H1.

A last question to address concerns the shape of current and recent canyons on the seafloor of this North-Western Amazon basin. [Lisboa *et al.* \(2017\)](#) and [Gauthier & Gorini \(2018\)](#) have studied the spatial variations of these canyons on our seismic cube and on one North-West of ours. Within the canyons of our cube, [Gauthier & Gorini \(2018\)](#) have highlighted that South-Eastern canyons have an infilling character while North-Western canyons are more erosive. This South-East to North-West evolution is of same 'small' scale as the differences observed between MTDs A and B in our study. This evolution could be analyzed further in comparison with the Northern canyons studied by [Lisboa *et al.* \(2017\)](#). Depending on how the trend is confirmed, one could assess to what extent the Amazon cone may impact the canyons infilling processes in this part of the Amazon basin.

5.3 Conclusion

The two methodologies that have been presented in this report offer ways to take advantage of seismic information on mass transport deposits, by combining existing knowledge on their interpretation with low-level data-extracted features. They are appropriate to deal with the variability and uncertainty that underlie the objectives of identifying and interpreting the seismic signatures of MTDs. The applications we have done demonstrate that results obtained from the methodologies are consistent. In this concluding chapter, further developments have been suggested for each methodology and for a workflow which, in the future, could comprise them both. Perspectives also appear on possible extensions to other data or application domains. As more and more data and image data are produced or acquired in natural science, ever more methods will be needed to effectively process these data, get relevant information out of them, and finally understand the natural processes they display.

Appendix A

Generative Topographic Mapping for clustering a dataset

Explanations are given here on the GTM algorithm and how we applied it to our data. For more details, see Bishop *et al.* (1998a), Svensen (1998), Bishop *et al.* (1998b) and Bishop *et al.* (1997). Roy *et al.* (2014) also provide a clear summary on this subject.

A.1 GTM: the model

In the GTM probabilistic model, latent variables in a L -dimensional space are used to represent the ones of the data space of dimension $D > L$.

A prior probability $p(\mathbf{x})$ is given on these latent variables as a sum of Dirac delta functions centered on the K nodes \mathbf{x}_i of a regular grid:

$$p(\mathbf{x}) = \frac{1}{K} \sum_{i=1}^K \delta(\mathbf{x} - \mathbf{x}_i)$$

The mapping, a function y with a parameter matrix \mathbf{W} , will be defined to map all points from the latent space to a point in the data space. As the latent space is of dimension L , these mapped points will lie on an L -dimensional manifold embedded in the data space. Figure A.1 (same as Figure 2.6a of this report) illustrates the mapping function y in the case where $D = 3$ and $L = 2$.

However, in the data space, real points may not lie precisely on the constructed manifold. To allow for some noise with respect to the manifold model, the GTM models data points as being samples of a mixture of Gaussians centered on the reference vectors $y(\mathbf{x}_i; \mathbf{W})$,

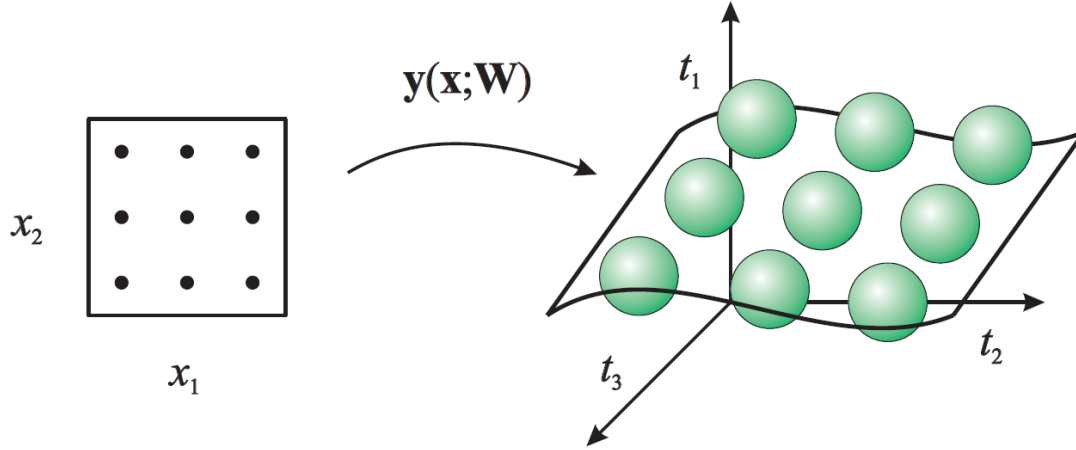


Figure A.1: GTM principle. From [Svensen \(1998\)](#): “Points on a regular grid in the low-dimensional latent space (left) are mapped, using a parameterized, non-linear mapping $y(\mathbf{x}; \mathbf{W})$, to corresponding centers of Gaussians (right). These centers will lie in the low-dimensional manifold, defined by the mapping $y(\mathbf{x}; \mathbf{W})$, embedded in the potentially high-dimensional data space”.

with common variance β^{-1} (see the green spheres on [Figure A.1](#)):

$$\begin{aligned} p(\mathbf{t}|\mathbf{x}, \mathbf{W}, \beta) &= \mathcal{N}\left(y(\mathbf{x}; \mathbf{W}), \beta\right) \\ &= \left(\frac{\beta}{2\pi}\right)^{\frac{D}{2}} \exp\left(-\frac{\beta}{2}\|\mathbf{t} - y(\mathbf{x}; \mathbf{W})\|^2\right) \end{aligned} \quad (\text{A.1})$$

The probability distribution model of the data points is then calculated by integrating $p(\mathbf{t}|\mathbf{x}, \mathbf{W}, \beta)$ with respect to the prior probability $p(\mathbf{x})$:

$$\begin{aligned} p(\mathbf{t}|\mathbf{W}, \beta) &= \int p(\mathbf{t}|\mathbf{x}, \mathbf{W}, \beta)p(\mathbf{x})d\mathbf{x} \\ &= \frac{1}{K} \sum_{i=1}^K p(\mathbf{t}|\mathbf{x}_i, \mathbf{W}, \beta) \quad , \end{aligned}$$

given the definition of $p(\mathbf{x})$.

For N data points, the log-likelihood function for this model is:

$$\begin{aligned} l &= \ln\left(\prod_{n=1}^N p(\mathbf{t}_n|\mathbf{W}, \beta)\right) \\ &= \sum_{n=1}^N \ln\left(\frac{1}{K} \sum_{i=1}^K p(\mathbf{t}_n|\mathbf{x}_i, \mathbf{W}, \beta)\right) \end{aligned}$$

Maximizing l determines the parameters \mathbf{W} and β . Note that, at this stage, the model holds without having defined the form of the function $y(\mathbf{x}; \mathbf{W})$.

The authors (Bishop *et al.* (1998a), Svensen (1998)) choose a generalized linear regression form:

$$y(\mathbf{x}; \mathbf{W}) = \mathbf{W}\phi(\mathbf{x}) \quad (\text{A.2})$$

ϕ is a set of J nonlinear basis functions ϕ_j in the latent space. As suggested by Bishop *et al.* (1998a), in section 2.3 we used Gaussian radial functions. Their centers are also arranged on a regular grid in the latent space. The number of nonlinear basis functions and their width (variance, for Gaussian functions) control the final smoothness of the manifold. A larger number of basis functions, and small variances, allow more degrees of freedom for the manifold but increase the risk of overfitting.

With these elements, the optimization scheme chosen by the authors for maximizing l is the Expectation-Maximization algorithm (Dempster *et al.* (1977)). By optimizing the parameters \mathbf{W} and β , the algorithm optimizes the fit between the manifold and the data cloud. Each iteration of the Expectation-Maximization algorithm consists in two steps: E and M.

In the E-step, posterior probabilities¹, $p(\mathbf{x}_i|\mathbf{t}_n, \mathbf{W}, \beta)$, or “responsibilities” R_{in} , are calculated, using the current parameters \mathbf{W}_{old} and β_{old} :

$$\begin{aligned} R_{in}(\mathbf{W}_{old}, \beta_{old}) &= p(\mathbf{x}_i|\mathbf{t}_n, \mathbf{W}_{old}, \beta_{old}) \\ &= \frac{p(\mathbf{t}_n|\mathbf{x}_i, \mathbf{W}_{old}, \beta_{old})p(\mathbf{x}_i)}{\sum_{i'} p(\mathbf{t}_n|\mathbf{x}_{i'}, \mathbf{W}_{old}, \beta_{old})p(\mathbf{x}_{i'})} \\ &= \frac{p(\mathbf{t}_n|\mathbf{x}_i, \mathbf{W}_{old}, \beta_{old})}{\sum_{i'} p(\mathbf{t}_n|\mathbf{x}_{i'}, \mathbf{W}_{old}, \beta_{old})} \quad \text{since for all } i, p(\mathbf{x}_i) = 1/K \end{aligned} \quad (\text{A.3})$$

In the M-step, using

- the Gaussian expression of $p(\mathbf{t}|\mathbf{x}, \mathbf{W}, \beta)$ given in A.1,
- the generalized linear form of y , in A.2, and
- the relationship of the distribution with the calculated responsibilities in A.3

will enable to derivate l with respect to parameters \mathbf{W} and β ; setting the derivatives to zero gives the equations to retrieve the updated values of \mathbf{W} and β . First, the derivation with respect to \mathbf{W} yields the following linear equation in matrix form:

$$\Phi^T \mathbf{G}_{old} \Phi \mathbf{W}_{new}^T = \Phi^T \mathbf{R}_{old} \mathbf{T}$$

¹Note that the term “posterior” probabilities is here used in the Bayesian context of the GTM; it is not the same use as in the supervised framework of section 2.3.

where Φ is a $K \times J$ matrix with elements $\Phi_{ij} = \phi_j(\mathbf{x}_i)$, \mathbf{G} is a $K \times K$ diagonal matrix with elements $G_{ii} = \sum_{n=1}^N R_{in}$, \mathbf{R} is a $K \times N$ matrix with elements R_{in} , and \mathbf{T} is a $N \times D$ matrix with one data point \mathbf{t}_n on each row.

This allows to recover \mathbf{W}_{new} . Then, l is derivated with respect to β using the updated \mathbf{W}_{new} . The following equation yields the updated β_{new} :

$$\frac{1}{\beta_{new}} = \frac{1}{ND} \sum_{n=1}^N \sum_{i=1}^K R_{in} (\mathbf{W}_{old}, \beta_{old}) \|\mathbf{W}_{new} \phi(\mathbf{x}_i) - \mathbf{t}_n\|^2$$

The optimization can be monitored by the evolution of l or β with iterations, and stopped when their values stabilize.

A.2 Using the GTM latent representation for clustering

After the optimization, the final “responsibilities” R_{in} of each \mathbf{x}_i for each data point \mathbf{t}_n are available. The posterior probability distribution for one data point \mathbf{t}_n is again a sum of Dirac delta functions centered on the \mathbf{x}_i of the latent grid, weighted by R_{in} . It is possible to use either the mean or the mode of this distribution for each data point \mathbf{t}_n (Bishop *et al.* (1998a)). The mean is

$$\text{mean} \left(p(\mathbf{x} | \mathbf{t}_n, \mathbf{W}_{opt}, \beta_{opt}) \right) = \sum_{i=1}^K R_{in} \mathbf{x}_i$$

It necessarily lies inside the latent grid. The mode is the point in the latent space with maximum probability; it is therefore one of the nodes \mathbf{x}_i :

$$\text{mode} \left(p(\mathbf{x} | \mathbf{t}_n, \mathbf{W}_{opt}, \beta_{opt}) \right) = \text{argmax}_{\{i\}} R_{in}$$

In the case of a multi-modal distribution, the mean and the mode may differ significantly.

For clustering, Roy *et al.* (2014) and we use $L = 2$. Roy *et al.* (2014) use the mean and plot a fraction of all their data points onto a 2D map representing the 2D latent grid. They analyze the groups of points that appear and draw clusters by combined analysis with the seismic data (see Figure 2.7). We use the mode of the distribution; the clusters are then composed of groups of points associated to the same \mathbf{x}_i . Further processing is done afterwards, either in an automated manner (section 2.3) or with an analysis similar to that of Roy *et al.* (2014) but based on points already clustered according to the modes of their posterior distribution.

Bishop *et al.* (1998a) highlight that the mapped points $y(\mathbf{x}_i; \mathbf{W})$ of the latent points \mathbf{x}_i have a topographic ordering, meaning that two points that are close in the latent space will be mapped to similar points in the data space. This topographic property is what

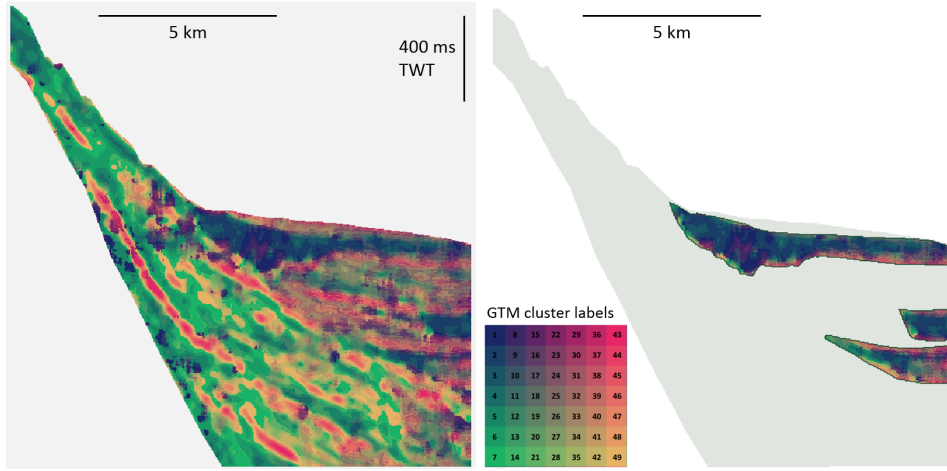


Figure A.2: One section of the training dataset, where every pixel is colored according to its cluster label (a number from 1 to 49). On the right, the same section is shown, with a mask corresponding to the ground-truth associated to this image (see also Figure 2.9a, p. 81).

allows to interpret the similarity between points or clusters.

A.3 Choice of parameters

In the application of GTM presented in section 2.3, we use the 2D version of GTM ($L = 2$). We use a latent grid of size 7×7 , i.e. with $K = 49$ nodes. Given our clustering scheme, this yields 49 clusters - to be characterized afterwards by a probability value of representing the occurrence of an MTD (as proposed in section 2.3), and/or to be grouped into seismic facies groups (as proposed in section 3.2).

This number 49 was chosen after qualitatively analyzing results of GTMs run for 9, 16, 25, 36, 49, 64, 81, 100, 121 and 144 nodes. The resulting clustered sections of the training dataset were each time studied, as shown on Figure A.2: with $K < 36$, GTM labels on the sections, and also within MTDs, are not varied enough to represent facies variations. For $K > 36$, variations of clusters begin to appear (on Figure A.2, $K = 49$). The trend of MF maps as K increases was also considered - see for instance Figure 2.6b (p. 72). $K = 36$ or $K = 49$ was considered sufficient to retrieve the stable state of the MF maps, thus a stable manifold representation. We chose $K = 49$.

We use $J = 4$ radial basis functions (denoted n_{rbf} in the article of section 2.3). We performed analyses on K in both cases $J = 4$ and $J = 9$. The stability of the MF map was reached for $K = 81$ to $K = 100$ for the latter case, with more uncertainty on the visual analysis of the MF maps than when $J = 4$ (case shown on Figure 2.6b). Thus, considering that we used a relatively small training dataset (on which the GTM was applied), we chose

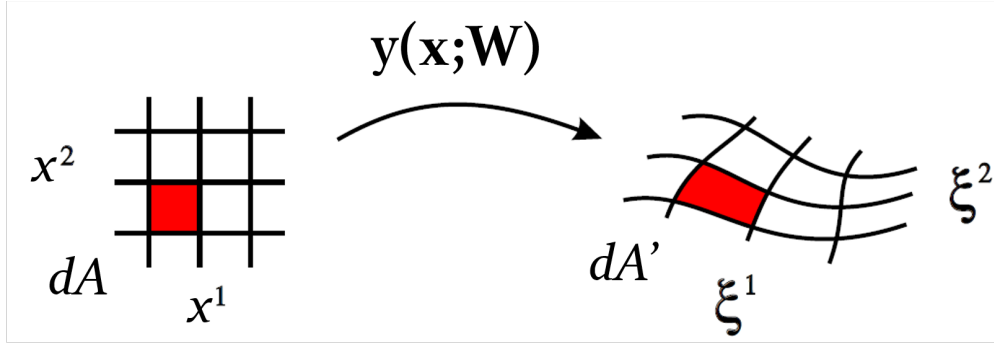


Figure A.3: Mapping of the Cartesian coordinate system x^i of the L -dimensional latent space onto the curvilinear coordinate system ξ^i in the L -dimensional manifold embedded in the data space. For $L = 2$, dA is an infinitesimal area in the latent space, and dA' is the corresponding region on the manifold. From Bishop *et al.* (1997).

to use only $J = 4$ basis functions, in order to avoid overfitting the training set.

Finally, as proposed by Bishop *et al.* (1998a) and Roy *et al.* (2014), the weight matrix \mathbf{W} is initialized so as to approximate the PCA of the dataset; β^{-1} is initialized as the $(L + 1)$ th, i.e. third, eigen value of this PCA (representing the remaining variance away from the plane induced by the 2 first eigen vectors).

A.4 Magnification factors

In section 2.2.3.2 (p. 70), we have mentioned the Magnification Factors (MF) of the GTM. These MF are of particular interest for our application. The definition of continuous MF is made possible by the fact that the manifold is completely defined by the mapping $y(\mathbf{x}; \mathbf{W})$ on all points of the latent space.

For the case $L = 2$, the local MF of a small area in latent space quantifies how 'stretched' the corresponding region of the 2D manifold is. With the notations of Figure A.3, the local MF of dA is $\frac{dA'}{dA}$. Bishop *et al.* (1997) provide all details on how to calculate this value given the mapping y .

In the MF maps we present in Figure 2.6b (p. 72) and then in Figure 3.4 (p. 139), each cell of the 49x49 grid is colored according to the MF of the node area in the latent space. It allows to see on Figure 3.5, for instance, that apart from the ridged facies, every seismic facies corresponds to a region of the manifold which is not much stretched, i.e. where the intra-cluster distances between points are relatively small. Cluster 15 (Figure 3.5), belonging to the ridged facies, has a higher MF value, indicating more dispersion of points along the manifold within this cluster.

Appendix B

Segmentation quality assessment

In the validation step of the methodology presented in section 2.3, we use three values: the Fuzzy Sensitivity *FuzzyS*, the Error Metric *EM* and the Variance Metric *VM*, in order to check the quality of our results. This Appendix gives further details on the choice of *FuzzyS* and *EM*.

One peculiarity of the methodology is the asymmetry of the error function f , designed to put less constraint on false positives than on false negatives: comparing the original image X and the modeled image Y on one pixel t ,

$$f(X_t, Y_t) = \begin{cases} X_t - Y_t, & X_t - Y_t \geq 0 \\ -\alpha(X_t - Y_t), & X_t - Y_t < 0 \end{cases}$$

This asymmetry is governed by the value of $\alpha \in [0, 1]$. If $\alpha < 1$, then f is asymmetric (see Figure B.1); in this case, comparing the prior-probability images with the posterior-probability images cannot be done as in the general case of segmentation quality assessment.

Most metrics for comparing two segmented images (i.e. assessing their similarity) are

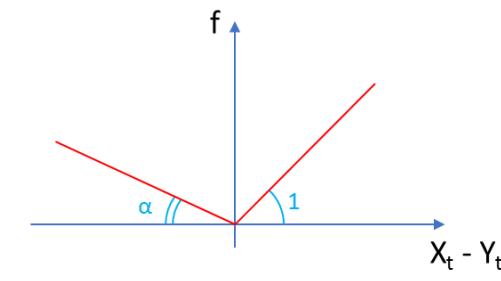


Figure B.1: Asymmetric error function for one pixel t : the error is smaller for false positives (i.e. where $X_t < Y_t$) than for false negatives (i.e. where $X_t > Y_t$). X : original prior image; Y : modeled image; $\alpha \in [0, 1]$.

built so that the metric value is zero for two exactly equal images. Here, if $\alpha < 1$, some false positives may have appeared during the process, and they are not to be removed. Consequently, the metric we choose should either not consider false positives, or consider only a case where $\alpha = 1$.

Moreover, the error is not quadratic, which prevents from using the commonly-used mean square error (MSE) or peak signal-to-noise ratio (PSNR).

A metric that does not constrain false positives

In a review of 20 metrics for segmentation evaluation, [Taha & Hanbury \(2015\)](#) recall the definition of overlap-based metrics, from the four values reflecting the overlap between two segmentations: false positives (FP), true positives (TP), false negatives (FN) and true negatives (TN). The most-common overlap-based metrics are the Sensitivity, the Specificity, the Jaccard index and the Dice index. Among them, the Sensitivity is the only metric which does not involve false positives:

$$\text{Sensitivity} = \frac{TP}{TP + FN}$$

This means that the Sensitivity metric can be equal to 1 if the segmented objects are larger than the expected ones, which precisely can happen when $\alpha < 1$. In the article, we used the fuzzy version of Sensitivity, *FuzzyS*; it has high values for a 'good' segmentation, i.e. when expected objects are retrieved, no matter how many other objects are 'created'. To compute it, we used the definition of [Taha & Hanbury \(2015\)](#) of FP, TP, FN and TN generalized to the fuzzy case, as the two compared images are probability images; *FuzzyS* is then defined as the Sensitivity but using the modified TP and FN. The fuzzy formulation notably allows for a continuous version of the probability images to be compared.

The Error Metric *EM* is the value of the error between two probability images, for a given α . This error is not quadratic. Therefore, metrics like the mean square error (MSE) or peak signal-to-noise ratio (PSNR) are irrelevant for this study. For a case where $\alpha = 1$, *EM* is simply the sum of pixel-wise absolute difference of the two images. When $\alpha < 1$, some of these absolute differences between pixels are lower weighted, often resulting in a lower global *EM* for lower α . As *EM* is not normalized by any α -dependent coefficient, two values of *EM* for different α are therefore not comparable.

A metric for only the symmetric case $\alpha = 1$

Other metrics were studied for the test case where $\alpha = 1$, i.e. the symmetric case. We tested several metrics of the different kinds presented by [Taha & Hanbury \(2015\)](#). The

Mutual Information between two images is a similarity metric based on the entropy of the probability distribution of each image and their joint entropy; it is especially useful for cases where outliers exist and sensitivity is important (Taha & Hanbury (2015)). The HaarPSI similarity index (Reisenhofer *et al.* (2018)) is a measure of local similarities between two images designed for image quality assessment. Taha & Hanbury (2015) also highlight volumetric distances for comparing the volumes of the segmented objects (irrelevant of their position). In our case, a comparison of the total mass of the probability

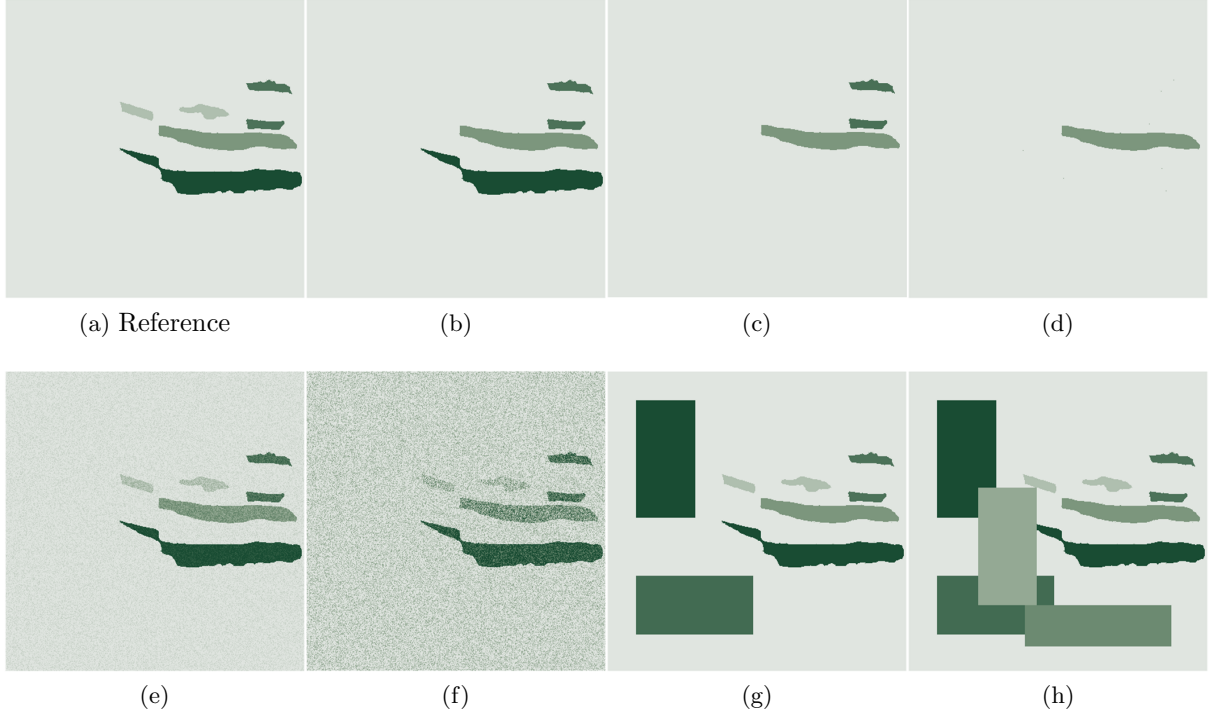


Figure B.2: One reference image (a) and seven synthetic images ((b) to (h)), used for testing several metrics.

Table B.1: Several metric results for the seven synthetic images of Figure B.2: metric values between one image ((b) to (h) of Figure B.2) and the Reference image (Figure B.2a). $1 - FuzzyS$: Fuzzy Sensitivity (1 - index value). EM : Error Metric (for $\alpha = 1$, here divided by the number of pixels, 512×512). $1 - FuzzyMI$: Fuzzy Mutual Information (1 - index value). $1 - HaarPSI$: Haar wavelet-based perceptual similarity index (1 - index value). MM : Mass Metric.

Metric	(b)	(c)	(d)	(e)	(f)	(g)	(h)
$1 - FuzzyS$	0.04	0.68	0.79	0.05	0.15	0.00	0.01
EM	0.002	0.04	0.04	0.04	0.12	0.14	0.18
$1 - FuzzyMI$	0.81	0.95	0.97	0.87	0.93	0.91	0.92
$1 - HaarPSI$	0.26	0.76	0.82	0.85	0.96	0.66	0.71
MM	0.04	0.68	0.79	0.67	2.06	2.62	3.39

images is valuable, in order to evaluate globally how much of the positive probabilities were actually recovered. Denoting N_k the number of points (pixels) in the dataset having

probability value s_k , the total mass is defined as the sum of probability values of all points:

$$Mass = \sum_k N_k s_k$$

The Mass Metric MM was thus defined as:

$$MM = \frac{|Mass_{posterior} - Mass_{prior}|}{Mass_{prior}}$$

Table B.1 shows the values of a few metrics for the images of Figure B.2. The $1 - HaarPSI$ metric is the most impacted by noise on the image. The $1 - FuzzyMI$ metric has highest values for missing objects (Fig. B.2c,d), yet all its values are on a small range. The EM metric (here the pixel-wise absolute difference of two images) has highest values for a much noisy image (Fig. B.2f) or unexpected objects (Fig. B.2g,h). For a less noisy image (Fig. B.2e), EM has a similar value as for missing objects (Fig. B.2c,d). The MM shows higher values for unexpected objects and a much noisy image (Fig. B.2g,h,f respectively) than for a little noisy image and missing objects. Computing the MM in our case study showed that, similarly to results given by $FuzzyS$ (see Table 2 in the article, last line), the mid-offset dataset gave the best results. Values of MM for the PCA dimension-reduction method are presented in Table B.2.

Another kind of metric involves comparing the two distributions of probabilities, for example the Bhattacharyya distance, the Hellinger distance or the Earth Mover's Distance (EMD - introduced by Peleg *et al.* (1989)). These are not consistent with the two probability distributions not having the same overall mass (as shown by Table B.2).

The HaarPSI-based metric (Reisenhofer *et al.* (2018)) shows a larger value in the case of noisy images than in other cases, while our perception and objective asks for the contrary. The Fuzzy-MI-based metric shows values that match perception but with a low range: we should get a lower distance between the reference image (a) and image (b) of Figure B.2 (see Table B.1). Finally, the MM metric shows good results on our data, which are redundant with those of the $FuzzyS$ -based metric. Considering these elements, we use only the EM as it is directly available from the optimization computations.

Table B.2: Mass Metric (MM) results for the PCA dimension reduction method, for Training Images (TI) and Validation Images (VI), with $\alpha = 1$.

MM	Full-stack	Near-offset	Mid-offset	Far-offset
TI	0.74	0.64	0.53	0.98
VI	0.86	0.78	0.70	0.98

Appendix C

Supplementary material for section 3.3

In this appendix, we give the supplementary tables associated to the article presented in section 3.3.

Table Supplementary 1 is attached separately, as it is too large to be put inside this PhD report.

Table Supplementary 2 provides some conditions on the availability of each MTD descriptor as defined in our article. We here deleted the 'Comments' column for it to fit in a page. Figure C.1 gives the main content of the table, and Figure C.2 gives the notations used within it.

Descriptors	Properties	<p><i>orange: condition on the resolution ; blue: condition on the dataset coverage .</i> <i>Descriptor available if...</i></p>
thickness variation average thickness width variation horizontal aspect ratio volume surface area maximum horizontal length principal direction presence of 'tongues' at toe BS median slope BS flat sub-horizontal zone plunging pool indicator multiple terracing downslope BS ramps scours, grooves or striations lateral erosive walls BS strong amplitude US median slope US ramps or ridges US with turbidites on top upward connection to other MTDs lateral connection to other MTDs near structural elements laterally runoff distance HS downslope evolution HS morphology presence of preserved blocks preserved blocks size chaotic facies distribution transparent facies distribution faulty facies distribution ridged facies distribution thrust fault angle increase to toe lithology distribution in MTD deformed facies distribution MTD proportion in sedimentary pile lateral distribution of MTDs vertical distribution of MTDs	Morphology	<p>H > 2 res H > 2 res W(avg) > 20 bins; whole MTD in dataset whole MTD in dataset whole MTD in dataset whole MTD in dataset whole MTD in dataset (almost) whole MTD in dataset "tongues" are > 5 x 5 bins; toe of MTD in dataset BIN (dip direction) < 20 bin slope variation occurs on scale > BIN slope variation occurs on scale > BIN slope variation occurs on scale > BIN slope variation occurs on scale > BIN slope variation occurs on scale > BIN slope variation occurs on scale > BIN envelope / RMS / max magnitude / other shows high amplitudes BIN (dip direction) < 20 bin slope variation occurs on scale > BIN minimum quality of previous interpretation Hs > 2 H Ws * Ls > 2 W * L minimum quality of previous interpretation headscarp of MTD in dataset and known min. quality of previous interpretation; several headscarps of MTDs in dataset slope variation occurs on scale > BIN; headscarp of MTD in dataset 2H/(ct) > 5 Ns (equivalently :) H > 5 res H > 5 res H > 3 res H > 3 res H > 10 res H > 5 res H > 5 res; toe of MTD in dataset minimum quality of previous interpretation with other data H > 5 res H > 2 res Ws * Ls > 2 W * L Hs > 2 H</p>
	Basal surface	
	Upper surface	
	Position	
	Headscarp	
	Internal facies distributions	
	Global Environment	

Figure C.1: Table Supplementary 2 of the article of section 3.3.

Notations (with units)	
c (m/s)	acoustic velocity
f (Hz)	dominant frequency
t (sTWT)	sampling rate
res (m)	resolution = $c / 4f$
bin (m)	lateral space between 2 traces
BIN (m)	lateral space between 2 picked surface points
H (m)	thickness of MTD
W (m)	width of MTD
L (m)	length of MTD
Hs (m)	total depth of seismic dataset
Ws (m)	total width of seismic dataset
Ls (m)	total length of seismic dataset
Ns (unitless)	min. number of samples to resolve 2 reflectors vertically
NB: $Ns = res / (t * c / 2)$, hence $Ns = 1/(2ft)$	

Figure C.2: Notations for Table Supplementary 2 of the article of section 3.3.

Appendix D

List of oral and written communications

This Appendix provides the list of communications that were done as a first author during the three years of PhD.

Integrating information from seismic data into sedimentary-processes modeling.

Pauline Le Bouteiller. April 13-14, 2016. Poster.

Journées des Doctorants de l'Ecole Doctorale Géosciences, Ressources Naturelles et Environnement. Sorbonne-Université, Paris, France.

Object retrieval in seismic data.

Pauline Le Bouteiller, Jean Charléty, Florence Delprat-Jannaud, Christian Gorini. October 30 - November 4, 2016. Poster.

SMAI-SIGMA Conference (Signal, Image, Géométrie, Modélisation, Approximation) 2016. Marseille, France.

Image processing for Mass Transport Deposits identification in seismic data.

Pauline Le Bouteiller. April 19-20, 2016. Oral presentation.

Journées des Doctorants de l'Ecole Doctorale Géosciences, Ressources Naturelles et Environnement. Sorbonne-Université, Paris, France.

Image processing for Mass Transport Deposit retrieval in seismic data.

Pauline Le Bouteiller, Florence Delprat-Jannaud, Jean Charléty, Christian Gorini, Didier Granjeon. September 10-14, 2017. Poster.

SIAM Conference on Mathematical and Computational Issues in the Geosciences 2017. Erlangen, Germany.

A new conceptual methodology for interpretation of mass transport processes from seismic data.

Pauline Le Bouteiller, Sara Lafuerza, Jean Charléty, Antonio Tadeu Reis, Didier Granjeon, Florence Delprat-Jannaud, Christian Gorini. Peer-reviewed article submitted February 28; revisions received June 25; revised submission sent September 19, 2018.

Journal of Marine and Petroleum Geology.

Understanding mass transport processes in sedimentary basins from their signatures on seismic data: a knowledge-based approach.

Pauline Le Bouteiller. April 4-5, 2018. Oral presentation.

Journées des Doctorants de l'Ecole Doctorale Géosciences, Ressources Naturelles et Environnement. Sorbonne-Université, Paris, France.

Procédé pour la détection d'objets géologiques dans une image.

Pauline Le Bouteiller, Jean Charléty. May 18, 2018. Patent application.

Referenced as [Le Bouteiller & Charléty \(2018\)](#) in this report.

Heterogeneous geobody retrieval in seismic images.

Pauline Le Bouteiller, Jean Charléty, Florence Delprat-Jannaud, Christian Gorini, Didier Granjeon. June 4-8, 2018. Poster.

SIAM Conference on Imaging Science 2018. Bologna, Italy.

Mixing unsupervised and knowledge-based analysis for heterogeneous object delineation in seismic data.

Pauline Le Bouteiller, Jean Charléty, Florence Delprat-Jannaud, Didier Granjeon, Christian Gorini. June 10-16, 2018. Oral presentation.

EAGE Annual Conference and Exhibition 2018. Copenhagen, Denmark.

Extended abstract referenced as [Le Bouteiller et al. \(2018\)](#) in this report.

Semi-supervised multi-facies object retrieval in seismic data.

Pauline Le Bouteiller, Jean Charléty. Peer-reviewed article submitted October 1, 2018.

Mathematical Geosciences.

List of Figures

1.1	Main features of a passive continental margin. Tilted fault blocks, dikes, salt (or evaporites), reef and lagoon deposits, are signatures of the passive margin formation and past evolution. Shallow marine sediments, slump blocks, turbidites and deep marine sediments are continuing deposited sediments in the basin. Modified from Christiansen & Hamblin (2015).	12
1.2	Various geohazards related to mass transport along a continental slope and their potential impacts on coastal to marine infrastructures. Among them: slope failures, impact of debris flows on infrastructure, dissociation of hydrates, shallow-gas pockets, overpressure, fluid escape features (gas chimneys, mud volcanoes), diapirism, seismicity, and highly destructive tsunamis. From Vanneste <i>et al.</i> (2014).	13
1.3	Schematic description of the three domains in an MTD. This scheme does not cover all kinds of MTDs.	16
1.4	Mass transport examples. (a) Subaerial mass-transport in the Austrian Alps; extensional and compressional features are seen, as well as lateral shear. These features are also seen in submarine mass transports. From Posamentier & Martinsen (2011). (b) Map (A), seismic profile (B) and interpreted seismic profile (C): MTD in brown (interpreted preserved blocks inside), headscarp in red. On this profile the MTD toe is its right-most part. From Moore & Sawyer (2016).	17
1.5	Mudflow features characteristic of Flow factor. A, C, E: lateral view of source area. B, D, F: top view of the basin area. From Sawyer <i>et al.</i> (2012).	19
1.6	Schematic cross-sections illustrating gravity-driven deformational processes, including those that form mass-transport deposits. Modified from Posamentier & Martinsen (2011).	23
1.7	Solutions of the model of Mourgues <i>et al.</i> (2014) for sand-like material. α is the slope angle of the free surface; λ_b^* is the overpressure ratio of the basal detachment surface, with value zero if no overpressure and 1 if overpressure equals hydrostatic pressure. The dashed line represents the solution for a compressive state of stress. The black bold line represents the solution for a gravity-driven extensional state of stress (the one studied in this PhD project): this line is the limit where the Flow factor (inverse of the Factor of Safety FS here) is $F_f = 1$. The grey area shows domains of slope instability triggered by gravity only. From Mourgues <i>et al.</i> (2014).	26

- 1.8 Sketches of subaqueous (a) clay-rich and (b) sand-rich debris flows, as observed in experiments. From Elverhoi *et al.* (2010). In their article, clay portion ranges from 5 to 25%, but the authors precise that these critical values may change depending on the kind of clay and the scale of the experiment / field data. 26
- 1.9 Marine seismic acquisition: example for 2D data. (a) The acquisition ship drags a system of sources (air guns) and receivers (hydrophones on the streamer). Modified from the Schlumberger Oilfield Glossary. (b) Display of seismic data (not depth-converted), positive amplitudes shaded for enhanced inter-trace continuity. Each trace results from the operation of stacking signals from all receivers. TWT: two-way traveltime. Modified from the US EPA web archive. 30
- 1.10 Sequence stratigraphy and stratal geometries. (a) Systems tract shapes and boundaries associated with eustatic cycles. Modified from Bacchi-ana (2008)). (b) Several reference geometries used for seismic stratigraphy. From Berton & Vesely (2016) and Mitchum Jr *et al.* (1977). 33
- 1.11 Seismic stratigraphic features on an example 2D seismic section, as interpreted by Berton & Vesely (2016): '(A) Seismic facies A, interpreted as shelf-margin deltas/shoreface deposits; (B) seismic facies B, interpreted as slope clinoforms with tangential (oblique) geometry; (C) seismic facies C, interpreted as slope clinoforms with sigmoidal geometry; (D) seismic facies D, interpreted as turbidites; (E) seismic facies E, interpreted as mass-transport deposits; (F) seismic facies F, interpreted as continental to shelfal deposits'. On the top image, the red and orange lines are horizons. From Berton & Vesely (2016). 34
- 1.12 Bathymetric map of the Amazon basin with location of major previously-studied MTDs and seismic data. Modified from Reis *et al.* (2016) and Silva *et al.* (2016). The 50°W (Damuth & Embley (1981)), WMTD, EMTD (Western / Eastern MTDs, Damuth *et al.* (1988)) are superficial MTDs. URMTD and BMTD (Unit R / Buried MTDs, Damuth *et al.* (1988)) are buried. The Amapá and Pará-Maranhão Megaslides (ALC-AUC / PMM) were studied by Silva *et al.* (2010) and Reis *et al.* (2016). Amapá Lower Complex (ALC), the deepest mass transport complex of Amapá, is mapped in blue; Amapá Upper Complex (AUC), more recent, is mapped in orange, after Reis *et al.* (2016). The 3D seismic cube is mapped with available seismic data in dark orange and 2D seismic profiles are mapped in dark red. 37
- 1.13 Interpretation of a 2D seismic profile accross the Amazon basin: horizons corresponding to the main evolution stages of the basin. From Cruz (2018). The top sin-rift dates back to the late Cretaceous (100 - 66 Ma); above it is the Limoeiro Formation (deep marine mudstones and siltstones). The base of the carbonate platform dates back approximately to the early Eocene (60 to 56 Ma). The 7-8 Ma horizon corresponds to the end of the top of the carbonate platform, and base of siliciclastic sedimentation. The dark lines connecting the slope and basin regions within the Limoeiro Formation are examples of an extensional-compressional tectonic system. 39

1.14	Synthetic schema of the main types of transport mechanisms in the Amazon River Mouth basin, according to the literature (Damuth & Embley (1981), Silva <i>et al.</i> (1998), Cobbold <i>et al.</i> (2004), Maslin <i>et al.</i> (2005), Figueiredo <i>et al.</i> (2007), Silva <i>et al.</i> (2010), Reis <i>et al.</i> (2016)).	42
1.15	Seismic section extracted from the 3D cube. Most recent, upslope sedimentary series are shown, together with several horizons. Progradation is the deposition of sediments gradually further in the basinward direction; aggradation is the deposition of sediments that gradually builds upwards. No MTD is visible on this section.	44
1.16	2D seismic profile compared with a 3D section extracted from the 3D cube. Most recent, downslope sedimentary series are shown, together with horizon G (2.4 Ma) from Gorini <i>et al.</i> (2014) (yellow line). The top-left image displays the context of the 3D section extract shown on the right; this green-contoured extract corresponds spatially to the green-contoured region of the 2D section.	44
1.17	Seismic recognition criteria for MTDs; modified from Posamentier & Martinsen (2011).	46
1.18	MTD seismic expression diversity in the literature: (a), (b), (c) (from the VSA (Virtual Seismic Atlas) website). MTD and extension processes diversity in the Amazon region: (d), (e), (f), (g), (h), (i), (j). Figure continued below.	48
1.19	Texture - geometry decomposition ($f = u + v$) applied to a natural image (left) and to a seismic image (middle), with expected main geological region borders (right). The algorithm clearly yields a distinction between the geometry and texture parts of both natural and seismic images. However, the geometry component of the seismic image does not reveal the expected geological structure. Images obtained by applying algorithm and code from Le Guen (2014).	51
2.1	Example of GLCM attributes computed on several patches of a seismic image. Axes of the scatter plot correspond to GLCM contrast (abscissa) for a reference vector drawn in light blue, and GLCM energy (ordinate) for a reference vector drawn in orange.	59
2.2	The Chan-Vese deformable model (Chan & Vese (2001)). (a) The level-set formulation of the delineation problem states that the contour line is the zero-level set of a function Φ . Φ is modified iteratively to fit a contour in the image while respecting a regularization constraint (e.g., on the total curvature or length of the contour). (b) Example of application: detection of freely swimming fish in a SONAR image; initial image, and zero-level-set contour after 4, 10 and 16 iterations. From Sharma & Anton (2009)	64

- 2.3 Examples of geometrical segmentation methods for seismic image partitioning: (a) salt body delineation via level-set and manual constraint based on a specifically-designed seismic attribute, from Haukås *et al.* (2013): 1- seismic section and intersection of extracted boundary in green; 2- attribute section and intersection of extracted boundary (red indicates lack of spatially coherent seismic reflections, blue indicates locally stratified region); 3- 3D view of extracted salt body. (b) Salt body delineation via region-growing and morphological post-processing, from Shafiq *et al.* (2015) (GoT: Gradient of Texture). (c) Morphological and topological segmentation (right) of a 3D seismic volume (left) according to its structural surfaces, from Faucon (2007). 66
- 2.4 A typical seismic facies classification using the interpreter trained probabilistic neural net, where multiple seismic facies classes have been identified. The seismic classification scheme on the right consists of high amplitude (HA), moderate amplitude (MA), low amplitude (LA), continuous (C) and semi-continuous (SC) seismic facies. Training patches are contoured in green lines. From West *et al.* (2002). 69
- 2.5 Comparison between a k-means clustering map (left) and a SOM clustering map (right) of a Frio Channel gas play (South Texas). One color corresponds to one cluster. From Coléou *et al.* (2003). 71
- 2.6 Generative Topographic Mapping: principle and characteristic of the Magnification Factors. (a) GTM principle; \mathbf{x} is the data representation in the latent space, \mathbf{W} is the parameter matrix built during the optimization, and y is the mapping function. From Svensen (1998): “Points on a regular grid in the low-dimensional latent space (left) are mapped, using a parameterized, non-linear mapping $y(\mathbf{x}; \mathbf{W})$, to corresponding centers of Gaussians (right). These centers will lie in the low-dimensional manifold, defined by the mapping $y(\mathbf{x}; \mathbf{W})$, embedded in the potentially high-dimensional data space”. (b) Magnification factors maps of applied GTM clustering for increasing number of clusters. From 36 - 49 clusters and above, the shape of the manifold is caught by the algorithm; more clusters refine it but do not modify it. 72
- 2.7 GTM and posterior clustering analysis for highly heterogeneous facies classification. (a), (b) Data distribution in the GTM 2D latent space for two different reservoir units. Seven different polygons with different colors around clusters signify rock types for the two reservoir units. (c) Generated seismic facies volume. From Roy *et al.* (2014). 73
- 2.8 (a) A simple neural net structure. The parameters of the orange neuron are its input weights $w_1^{(j)}$ ($j = 1..3$) and its bias b_1 . Its output is a (nonlinear) activation function (e.g. sigmoid as represented) of the weighted sum of its inputs plus the bias. Deep learning is based on the use of a lot of hidden layers. (b) Convolutional Neural Nets structure: after a series of 2D operations (convolution, pooling), fully-connected layers allow to produce a classification result. From Deshpande (2016). (c) Extract of Figure 2 from Zeiler & Fergus (2014); for each layer, their visualization of features (gray pictures) of a deep CNN allows to understand a posteriori which parts of the input images (photos) were the most important in training the network for the given classification task. 76

2.9	Illustration of the method presented in this section. (a) One seismic section and the available prior probabilities on MTD occurrence. (b) The same section where every pixel is colored according to its GTM cluster label (a number between 1 and 49), and the posterior probabilities computed from our method. A 2D colormap is used for GTM labels to account for the 2D topographic “ranking” given by GTM. (c) Retrieval of probabilities for several sections.	81
2.10	Proposed workflow for MTD identification in seismic data.	114
2.11	Qualitative comparison of the Magnification Factor (MF) maps resulting from GTM mappings on our four seismic datasets: full-stack, near-, mid- and far-offsets.	116
2.12	Computed probabilities on MTD representativeness for the 49 clusters of the GTM-built manifold in each case of the four seismic datasets: full-stack, near-, mid- and far-offsets. Cases where $\alpha = 0.3$ or 0.8 correspond to low or high confidence in the prior annotations, respectively. False positives are less permitted for $\alpha = 0.8$ than for $\alpha = 0.3$. GTM cluster labels (numbers from 1 to 49) are displayed only once for simplicity.	117
2.13	Posterior probabilities on one inline of the seismic cube used in our study, for the four datasets. Left: seismic section; Right: posterior probabilities on all pixels of the section. (a), (b) Full-stack section. (c), (d) Near-offset section. (e), (f) Mid-offset section. (g), (h) Far-offset section. Figure continued below.	118
2.14	Posterior probabilities on one inline of the seismic cube used in our study, for the four datasets.	119
2.14	Illustration of the orientation filtering results for the 23 largest objects of the processed full-stack dataset. Vectors are normed and represent the orientation of the objects. Blue vectors correspond to MTDs, red vectors correspond to non-MTD objects, and green vectors correspond to unsure or unexpected objects. The light blue contour is a sketch of the cone used for filtering out most non-MTD objects. Note that the 3D view does not render the whole direction of vectors or cone.	122
2.15	Crossplots comparing the volume, aspect ratio, and divergence to uniform (DTU in this report), of the largest connected components retrieved by our method. (a) full-stack dataset, (b) near-offset dataset, (c) mid-offset dataset, (d) far-offset dataset.	123
2.16	One seismic section after the 3D processing, with pixels of two objects (one yellow, one blue) on top of the seismic. Note that the two objects correspond to only one MTD. The red contour is a manual delineation of the targeted MTD.	125
2.17	An example of application of the Chan-Vese algorithm (Chan & Vese (2001)) on one 2D attribute image of the seismic volume: initial (left) and final (right) state of the contour (red line). Parameters to be tuned include the initial position of the contour (here chosen as split into multiple contours for accelerating the convergence, as proposed by Lianantonakis & Petillot (2007)) and the weight for constraining the curve smoothness. Here very small objects are kept, which is the signature of a low smoothness constraint.	126

2.18	An example of application of the (supervised) iterative multiplicative filtering for data labeling by Bergmann <i>et al.</i> (2017) on a test image (a), represented by 7 textural attribute images. 20, resp. 25, class centers were picked manually on the reference image in cases (b), resp. (c). Black arrows show the area of improvement (better discrepancy) from (b) to (c). Both cases were tested for two different sizes of uniformly-weighted filters: 3x3 window (left) and 5x5 window (right). Red lines are rough contours of expected objects.	128
3.1	Example of use of the International Stratigraphic Chart to retrieve Geologic Timescale Elements: the query was the word 'Cretaceous' to be 'within the label' of the elements searched. Results include all elements of the ontology having the word Cretaceous in their label. From Linked Data API (2017): link to the webpage, last accessed Sept. 10, 2018.	135
3.2	Proposed architecture for an ontology for interpretation of major surfaces in a seismic block, modified from Verney (2009). The orange text below red blocks are the corresponding steps of our methodology.	136
3.3	Example of horizon interpretation in the ontology proposed by Verney (2009). (a) Studied horizon parts shown on a seismic image; two different parts of the image give different information shown by the two graphs below the image, and resulting in interpretation of the horizons' relative ages (right). (b) Four descriptors depicted for all considered parts of horizons: two different quantitative descriptor (left and right), two different categorical descriptors (middle); the fifth rectangle on the right is the ontology proposal. The ontology proposes to merge part E with part G, and part F with part H, here based on the similarity of their descriptors. . . .	137
3.4	Magnification factors (MF) map of the GTM manifold for the full-stack dataset. Cluster labels (numbers from 1 to 49) are indicated. High values of MF indicate a stretched region of the manifold, corresponding to 'natural' boundaries between groups of points in the data space.	139
3.5	Interpreting facies groups from the GTM-defined clusters. (a) Example for the deformed facies: seismic amplitude image (left), selection of clusters (middle), all selected clusters grouped into one facies (right). (b) Interpreted facies groups used in our study, drawn on the 2D grid of 49 cluster centers. The deformed facies, for example, is defined by clusters 4, 5, 11, 12 and 13, as visualized on (a). Note that some facies groups overlap. . . .	140
4.1	Proposed workflow joining our two contributions into a global methodology for mass transport process interpretation from seismic data.	201
4.2	Objects recovered as one or more pieces. (a) Result of the object post-processing on one seismic section as presented on Figure 2.16. (b) Result of the object post-processing, where the morphological closing uses a larger structuring element - including all pixels. (c) Result of the object post-processing, where the morphological closing uses a larger structuring element - selecting only pixels with positive probability. Black arrows indicate pixels added compared to (a).	202

4.3	Integrating facies to create facies maps and lateral proportion curves. Five seismic sections are shown with the corresponding MTD sections, colored according to cluster numbers. The red-level facies map shows the vertical proportion of one facies (as defined in section 3.2 and Figure 3.5) in each column of the MTD (integration over direction dir. 3). The curve shows the lateral proportion of the facies, in each dip-oriented section of the MTD (integration over directions dir. 2 and dir. 3).	204
4.4	Clusters corresponding to the Deformed facies (numbers 4, 5, 11, 12, 13, see also Figure 3.5) on one seismic section. Horizon H1 is a hypothetical unconformity between seismic unit (I) (ancient slope) and unit (II) with MTDs.	209
4.5	Determination of a stratigraphic pattern to use for calculating 'vertical' facies proportion curves along the geological time. From the study of a seismic cube (left) and its corresponding clustered cube (middle), we hypothesize the pattern to use (right). Here, for a first approach, iso-age surfaces are considered to be parallel to the top horizon of one layer.	209
4.6	Facies proportion curves calculated along the geological time on the clustered full-stack seismic cube, in the top-most layer (between horizon H1 and the seafloor, see Figure 4.4), given the pattern shown on Figure 4.5. Approximate positions of MTDs in time are given. The 'MTD-like' facies kind is the grouping of clusters having maximum posterior probabilities in the cluster probability assignment presented in chapter 2.	210
5.1	An application of the Ilastik software to the extraction of neuronal cell bodies and nuclei from electron microscopy image stacks. Red and green strokes, as well as arrows, are inputs by the user in the interface. From Holcomb <i>et al.</i> (2016).	218
5.2	One inline of the seismic dataset with suggested relationship between the downslope region (displayed on Figure 4.4) and the upslope region. H1 downslope hypothetical unconformity illustrated as a red solid line similarly to Figure 4.4; H1u (upslope) hypothetical corresponding unconformity illustrated as a red dashed line.	221
A.1	GTM principle. From Svensen (1998): "Points on a regular grid in the low-dimensional latent space (left) are mapped, using a parameterized, non-linear mapping $y(\mathbf{x}; \mathbf{W})$, to corresponding centers of Gaussians (right). These centers will lie in the low-dimensional manifold, defined by the mapping $y(\mathbf{x}; \mathbf{W})$, embedded in the potentially high-dimensional data space".	224
A.2	One section of the training dataset, where every pixel is colored according to its cluster label (a number from 1 to 49). On the right, the same section is shown, with a mask corresponding to the ground-truth associated to this image (see also Figure 2.9a, p. 81).	227
A.3	Mapping of the Cartesian coordinate system x^i of the L -dimensional latent space onto the curvilinear coordinate system ξ^i in the L -dimensional manifold embedded in the data space. For $L = 2$, dA is an infinitesimal area in the latent space, and dA' is the corresponding region on the manifold. From Bishop <i>et al.</i> (1997).	228

B.1	Asymmetric error function for one pixel t : the error is smaller for false positives (i.e. where $X_t < Y_t$) than for false negatives (i.e. where $X_t > Y_t$). X : original prior image; Y : modeled image; $\alpha \in [0, 1]$	229
B.2	One reference image (a) and seven synthetic images ((b) to (h)), used for testing several metrics.	231
C.1	Table Supplementary 2 of the article of section 3.3.	234
C.2	Notations for Table Supplementary 2 of the article of section 3.3.	235

List of Tables

B.1	Several metric results for the seven synthetic images of Figure B.2: metric values between one image ((b) to (h) of Figure B.2) and the Reference image (Figure B.2a). $1 - FuzzyS$: Fuzzy Sensitivity (1 - index value). EM : Error Metric (for $\alpha = 1$, here divided by the number of pixels, 512x512). $1 - FuzzyMI$: Fuzzy Mutual Information (1 - index value). $1 - HaarPSI$: Haar wavelet-based perceptual similarity index (1 - index value). MM : Mass Metric.	231
B.2	Mass Metric (MM) results for the PCA dimension reduction method, for Training Images (TI) and Validation Images (VI), with $\alpha = 1$	232

Bibliography

- Alaudah, Yazeed, & AlRegib, Ghassan. 2016. Weakly-supervised labeling of seismic volumes using reference exemplars. *Pages 4373–4377 of: IEEE International Conference on Image Processing (ICIP)*.
- Alves, Tiago M., Kurtev, Kuncho, Moore, Gregory F., & Strasser, Michael. 2014. Assessing the internal character, reservoir potential, and seal competence of mass-transport deposits using seismic texture: A geophysical and petrophysical approach. *AAPG Bulletin*, **98**(4), 793–824.
- Arthur, David, & Vassilvitskii, Sergei. 2006 (June). *k-means++: The Advantages of Careful Seeding*. Technical Report 2006-13. Stanford InfoLab.
- Bacchiana, Claude. 2008. *Fundamentals of Sequence Stratigraphy*. IFP course.
- Bahorich, Mike S., & Farmer, Steve L. 1995. 3-D seismic discontinuity for faults and stratigraphic features: The coherence cube. *Pages 93–96 of: SEG Technical Program Expanded Abstracts 1995*.
- Barnes, Arthur. 2006. Too many seismic attributes ? *In: CSEG Recorder March 2006*, vol. 31.
- Bergmann, Ronny, Fitschen, Jan Henrik, Persch, Johannes, & Steidl, Gabriele. 2017. Iterative Multiplicative Filters for Data Labeling. *International Journal of Computer Vision*, **123**(3), 435–453.
- Bernard, Olivier. 2013. *Segmentation d'images par la méthode des level-set*. Master Course. Creatis, University of Lyon, INSA, France. <https://www.creatis.insa-lyon.fr/~bernard/files/courses/> (last accessed 2018-09-01).
- Berthelot, Angélique, Solberg, Anne H.S., & Gelius, Leiv-J. 2013. Texture attributes for detection of salt. *Journal of Applied Geophysics*, **88**, 52–69.
- Berton, Fábio, & Vesely, Fernando Farias. 2016. Seismic expression of depositional elements associated with a strongly progradational shelf margin: Northern Santos Basin, southeastern Brazil. *Brazilian Journal of Geology*, **46**(4), 585–603.
- Beucher, S., & Meyer, F. 1993. The Morphological Approach to Segmentation: The Watershed Transformation. *Mathematics of Morphology in Image Processing*, 433–482.
- Bhalgat, Yash, Charléty, Jean, & Duval, Laurent. 2018. CATSEYES: Categorizing Seismic structures with tessellated scattering wavelet networks. *IEEE SigPort [Online]*.

- Bishop, Alan W. 1955. The use of the Slip Circle in the Stability Analysis of Slopes. *Géotechnique*, **5**(1), 7–17.
- Bishop, C. M., Svensen, M., & Williams, C.K.I. 1997. Magnification factors for the GTM algorithm. *Pages 64–69 of: Fifth International Conference on Artificial Neural Networks*.
- Bishop, Christopher M., Svensen, Markus, & Williams, Christopher K. I. 1998a. Developments of the Generative Topographic Mapping. *Neurocomputing*, **21**, 203–224.
- Bishop, Christopher M., Svensén, Markus, & Williams, Christopher K. I. 1998b. GTM: The Generative Topographic Mapping. *Neural Computation*, **10**(1), 215–234.
- Blondel, Ph, & Sichi, O Gómez. 2009. Textural analyses of multibeam sonar imagery from Stanton Banks, Northern Ireland continental shelf. *Applied Acoustics*, **70**(10), 1288–1297.
- Bodine, J.H. 1984. Waveform analysis with seismic attributes. *SEG - 54th Annual International Meeting, 2-6 December, Atlanta, Georgia*.
- Bodine, John H. 1986. *Response waveform characterization of geophysical data*. US patent US4633447A.
- Bouziat, Antoine, Cacas-Stentz, Marie-Christine, Colombo, Daniele, Frey, Jeremy, Guy, Nicolas, Cornu, Tristan, & Gout, Claude. 2016 (04). Geo-mechanical control on natural fracturing and overpressure location in a synthetic passive margin model. *In: AAPG Hedberg conference : The future of basin and petroleum system modeling. Santa Barbara, California, USA*.
- Bull, Suzanne, Cartwright, Joe, & Huuse, Mads. 2009. A review of kinematic indicators from mass-transport complexes using 3D seismic data. *Marine and Petroleum Geology*, **26**(7), 1132–1151.
- Busson, Jean, Teles, Vanessa, Gillet, Hervé, Bouziat, Antoine, Guy, Nicolas, Joseph, Philippe, Mulder, Thierry, Borgomano, Jean, & Poli, Emmanuelle. 2018. Large-scale carbonate slope gravity failures: from stratigraphic evolution to numerical failure prediction. Article #11126. *Search and Discovery. AAPG/Datapages, Inc*.
- Campbell, Kenneth E., Frailey, Carl David, & Romero-Pittman, Lidia. 2006. The Pan-Amazonian Ucayali Peneplain, late Neogene sedimentation in Amazonia, and the birth of the modern Amazon River system. *Palaeogeography, Palaeoclimatology, Palaeoecology*, **239**(1-2), 166–219.
- Candès, Emmanuel, Demanet, Laurent, Donoho, David, & Ying, Lexing. 2006. Fast Discrete Curvelet Transforms. *Multiscale Modeling & Simulation*, **5**(3), 861–899.
- Carrillat, Alexis, Randen, Trygve, Sonneland, Lars, & Elvebakk, Geir. 2002. Seismic stratigraphic mapping of carbonate mounds using 3D texture attributes. *Pages G–41 of: EAGE Conference and Exhibition*, vol. 64.
- Caselles, Vicent, Kimmel, Ron, & Sapiro, Guillermo. 1997. Geodesic Active Contours. *International Journal of Computer Vision*, **22**(1), 61–79.

- Catuneanu, O., Abreu, V., Bhattacharya, J. P., Blum, M. D., Dalrymple, R. W., Eriksson, P. G., Fielding, C. R., Fisher, W. L., Galloway, W. E., Gibling, M. R., Giles, K. A., Holbrook, J. M., Jordan, R., Kendall, C.G.St.C., Macurda, B., Martinsen, O. J., Miall, A. D., Neal, J. E., Nummedal, D., Pomar, L., Posamentier, H. W., Pratt, B. R., Sarg, J. F., Shanley, K. W., Steel, R. J., Strasser, A., Tucker, M. E., & Winker, C. 2009. Towards the standardization of sequence stratigraphy. *Earth-Science Reviews*, **92**(1-2), 1–33.
- Chan, T. F., & Vese, L. A. 2001. Active contours without edges. *IEEE Transactions on Image Processing*, **10**(2), 266–277.
- Chan, Tony F., Sandberg, B.Yezrielev, & Vese, Luminita A. 2000. Active Contours without Edges for Vector-Valued Images. *Journal of Visual Communication and Image Representation*, **11**(2), 130–141.
- Chemenda, A., Bois, T., Bouissou, S., & Tric, E. 2009. Numerical modelling of the gravity-induced destabilization of a slope: The example of the La Clapière landslide, southern France. *Geomorphology*, **109**, 86–93.
- Chopra, Satinder, & Marfurt, Kurt J. 2007. Seismic attributes for prospect identification and reservoir characterization. *Geophysical Developments*.
- Chopra, Satinder, & Marfurt, Kurt J. 2014. Seismic facies analysis using generative topographic mapping. *Pages 1390–1394 of: Birkelo, Brad (ed), SEG Technical Program Expanded Abstracts 2014*.
- Christiansen, Eric H., & Hamblin, W. Kenneth. 2015. *Dynamic Earth: An introduction to physical geology*. Burlington, MA: Jones & Bartlett Learning.
- Clausi, David A., & Zhao, Yongping. 2003. Grey level co-occurrence integrated algorithm (GLCIA): A superior computational method to rapidly determine co-occurrence probability texture features. *Computers & Geosciences*, **29**(7), 837–850.
- Cobbold, P. R., Mourgues, R., & Boyd, K. 2004. Mechanism of thin-skinned detachment in the Amazon Fan: Assessing the importance of fluid overpressure and hydrocarbon generation. *Marine and Petroleum Geology*, **21**(8), 1013–1025.
- Coléou, Thierry, Poupon, Manuel, & Azbel, Kostia. 2003. Unsupervised seismic facies classification: A review and comparison of techniques and implementation. *The Leading Edge*, **22**(10), 942–953.
- Cruz, Alberto M. 2018. *Integrated geological and geophysical studies applied to understanding the evolution of the Offshore Amazon Basin*. Ph.D. thesis, Sorbonne Université, Paris.
- Damuth, J.E., & Embley, R.W. 1981. Mass-transport processes on Amazon Cone: western equatorial Atlantic. *American Association of Petroleum Geologists Bulletin*, **65**(4), 629–643.
- Damuth, J.E., Flood, R. D., Kowsmann, R. O., Belderson, R. H., & Gorini, M. A. 1988. Anatomy and growth pattern of Amazon deep-sea fan as revealed by long-range side-scan sonar (GLORIA) and high-resolution seismic studies. *AAPG Bulletin*, **72**(8), 885–911.

- Darros de Matos, Renato M. 2000. Tectonic evolution of the equatorial South Atlantic. *Pages 331–354 of: Mohriak, Webster, & Taiwani, Manik (eds), Atlantic Rifts and Continental Margins*. Geophysical Monograph Series, vol. 115. Washington, D. C.: American Geophysical Union.
- De Clippele, LH, Gafeira, J, Robert, K, Hennige, S, Lavaleye, MS, Duineveld, GCA, Huvenne, VAI, & Roberts, JM. 2017. Using novel acoustic and visual mapping tools to predict the small-scale spatial distribution of live biogenic reef framework in cold-water coral habitats. *Coral Reefs*, **36**(1), 255–268.
- de Matos, Marcilio Castro, Osorio, Paulo Léo, & Johann, Paulo Roberto. 2007. Un-supervised seismic facies analysis using wavelet transform and self-organizing maps. *GEOPHYSICS*, **72**(1), P9–P21.
- Dempster, Arthur P., Laird, NaN M., & Rubin, Donald B. 1977. Maximum likelihood from incomplete data via the EM algorithm. *Journal of the royal statistical society. Series B (methodological)*, 1–38.
- Deshpande, Adit. 2016. *A Beginner's Guide To Understanding Convolutional Neural Networks*. <https://adeshpande3.github.io/A-Beginner%27s-Guide-To-Understanding-Convolutional-Neural-Networks/> (last accessed 2018-09-01).
- Drucker, Daniel Charles, & Prager, William. 1952. Soil mechanics and plastic analysis or limit design. *Quarterly of applied mathematics*, **10**(2), 157–165.
- Durand, Virginie, Le Bouteiller, Pauline, Mangeney, Anne, Koné, El Hadji, Protin, Antoine, Kowalski, Philippe, Lauret, Frédéric, Brunet, Christophe, Wegner, Kerstin, Haas, Florian, & Delorme, Arthur. 2016. Using seismic data and modelling to better constrain the dynamics of rockfalls in the Dolomieu crater, Piton de la Fournaise, La Reunion. *In: CMG 2016 : 31st IUGG Conference on Mathematical Geophysics, Paris. Geo-Physics, from Mathematics to Experiments*.
- Ebuna, Daniel R., Kluesner, Jared W., Cunningham, Kevin J., & Edwards, Joel H. 2018. Statistical approach to neural network imaging of karst systems in 3D seismic reflection data. *Interpretation*, **6**(3), B15–B35.
- Eichkitz, Christoph Georg, Davies, John, Amtmann, Johannes, Schreilechner, Marcus Gregor, & de Groot, Paul. 2015. Grey level co-occurrence matrix and its application to seismic data. *First Break*, **33**, 71–77.
- Elverhoi, Anders, Breien, Hedda, de Blasio, Fabio V., Harbitz, Carl B., & Pagliardi, Matteo. 2010. Submarine landslides and the importance of the initial sediment composition for run-out length and final deposit. *Ocean Dynamics*, **60**(4), 1027–1046.
- Espurt, Nicolas, Baby, Patrice, Brusset, Stéphane, Roddaz, Martin, Hermoza, Wilber, & Barbarand, Jocelyn. 2009. The Nazca Ridge and Uplift of the Fitzcarrald Arch: Implications for Regional Geology in Northern South America. *Pages 89–100 of: Hoorn, C., & Wesselingh, F. P. (eds), Amazonia: Landscape and Species Evolution*. Oxford, UK: Wiley-Blackwell Publishing Ltd.

- Faucon, Timothée. 2007. *Segmentation morphologique et topologique de cubes sismiques*. Ph.D. thesis, MINES ParisTech.
- Favreau, P., Mangeney, A., Lucas, A., Crosta, G., & Bouchut, F. 2010. Numerical modeling of landquakes. *Geophysical Research Letters*, **37**(15), n/a–n/a.
- Figueiredo, J., Hoorn, C., van der Ven, P., & Soares, E. 2009. Late Miocene onset of the Amazon River and the Amazon deep-sea fan: Evidence from the Foz do Amazonas Basin. *Geology*, **37**(7), 619–622.
- Figueiredo, J.J.P., Zalan, P.V., & Soares, E.F. 2007. Bacia da Foz do Amazonas. *Boletim de Geociencias da Petrobras*, **15**(2), 299–309.
- Flemings, P. B., Long, H., Dugan, B., Germaine, J., John, C. M., Behrmann, J. H., & Sawyer, D. 2008. Erratum to “Pore pressure penetrometers document high overpressure near the seafloor where multiple submarine landslides have occurred on the continental slope, offshore Louisiana, Gulf of Mexico” [Earth and Planetary Science Letters 269/3-4 (2008) 309-32]. *Earth and Planetary Science Letters*, **274**(1-2), 269–283.
- Frey-Martínez, J. 2010. 3D Seismic Interpretation of Mass Transport Deposits: Implications for Basin Analysis and Geohazard Evaluation. *Pages 553–568 of: Mosher, David C., Shipp, R. Craig, Moscardelli, Lorena, Chaytor, Jason D., Baxter, Christopher D. P., Lee, Homa J., & Urgeles, Roger (eds), Submarine Mass Movements and Their Consequences*. Dordrecht: Springer Netherlands.
- Frey-Martínez, J., Bertoni, C., Gérard, J., & Matías, H. 2011. Processes of Submarine Slope Failure and Fluid Migration on the Ebro Continental Margin: Implications for Offshore Exploration and Development. *Pages 181–198 of: Shipp, R. Craig, Weimer, Paul, & Posamentier, Henry W. (eds), Mass-Transport Deposits in Deepwater Settings*. SEPM (Society for Sedimentary Geology).
- Galerie, Bruno, Leclaire, Arthur, & Rabin, Julien. 2018. A Texture Synthesis Model Based on Semi-discrete Optimal Transport in Patch Space. <https://hal.archives-ouvertes.fr/hal-01726443>.
- Gao, Dengliang. 2003. Volume texture extraction for 3D seismic visualization and interpretation. *GEOPHYSICS*, **68**(4), 1294–1302.
- Gao, Dengliang. 2008. Application of seismic texture model regression to seismic facies characterization and interpretation. *The Leading Edge*, **27**(3), 394–397.
- Gatys, L.A., Ecker, A.S., & Bethge, M. 2015. Texture Synthesis Using Convolutional Neural Networks. In: *Advances in Neural Information Processing Systems*.
- Gauthier, Quentin, & Gorini, Christian. 2018. *Filling and erosion of submarine canyons: autocyclic or allocyclic?* Internship poster. IStEP, Sorbonne-Université.
- GeoTeric. 2018. *GeoTeric website*. <https://www.geoteric.com> (last accessed 2018-09-01).
- Goodfellow, Ian, Pouget-Abadie, Jean, Mirza, Mehdi, Xu, Bing, Warde-Farley, David, Ozair, Sherjil, Courville, Aaron, & Bengio, Yoshua. 2014. Generative adversarial nets. *Pages 2672–2680 of: Advances in neural information processing systems*.

- Gorini, Christian, Haq, Bilal U., dos Reis, Antonio Tadeu, Silva, Cleverson Guizan, Cruz, Alberto, Soares, Emilson, & Grangeon, Didier. 2014. Late Neogene sequence stratigraphic evolution of the Foz do Amazonas Basin, Brazil. *Terra Nova*, **26**(3), 179–185.
- Goujon, Céline, Dalloz-Dubrujeaud, Blanche, & Thomas, Nathalie. 2007. Bidisperse Granular Flow on Inclined Rough Planes. *Pages 147–156 of: Schadschneider, Andreas, Pöschel, Thorsten, Kühne, Reinhart, Schreckenberg, Michael, & Wolf, Dietrich E. (eds), Traffic and Granular Flow'05*. Berlin, Heidelberg: Springer Berlin Heidelberg.
- Gramstad, O., & Nickel, M. 2018. Automated Top Salt Interpretation Using a Deep Convolutional Net. *In: 80th EAGE Conference and Exhibition 2018*.
- Gray, J. M. N. T., & Kokelaar, B. P. 2010. Large particle segregation, transport and accumulation in granular free-surface flows. *Journal of Fluid Mechanics*, **652**, 105–137.
- Gruber, Thomas R. 1993. A translation approach to portable ontology specifications. *Knowledge Acquisition*, **5**(2), 199–220.
- Hampton, Monty A., Lee, Homa J., & Locat, Jacques. 1996. Submarine landslides. *Reviews of Geophysics*, **34**(1), 33–59.
- Haralick, Robert M., Shanmugam, K., & Dinstein, Its'Hak. 1973. Textural Features for Image Classification. *IEEE Transactions on Systems, Man, and Cybernetics*, **3**(6), 610–621.
- Hashemi, H., de Beukelaar, P., Beiranvand, B., & Seiedali, M. 2017. Clustering Seismic Datasets for Optimized Facies Analysis Using a SSCSOM Technique. *In: 79th EAGE Conference and Exhibition 2017*. Proceedings. EAGE Publications BV/Netherlands.
- Haukås, J., Roaltdotter Ravndal, O., Fotland, B. H., Bounaim, A., & Sonneland, L. 2013. Automated salt body extraction from seismic data using the level set method. *First Break*, **31**(1971).
- Holcomb, Paul S., Morehead, Michael, Doretto, Gianfranco, Chen, Peter, Berg, Stuart, Plaza, Stephen, & Spirou, George. 2016. Rapid and Semi-automated Extraction of Neuronal Cell Bodies and Nuclei from Electron Microscopy Image Stacks. *Methods in molecular biology (Clifton, N.J.)*, **1427**, 277–290.
- Holmgren, Peter. 1994. Multiple flow direction algorithms for runoff modelling in grid based elevation models: An empirical evaluation. *Hydrological Processes*, **8**(4), 327–334.
- Hoorn, C., Wesselingh, F. P., ter Steege, H., Bermudez, M. A., Mora, A., Sevink, J., Sanmartin, I., Sanchez-Meseguer, A., Anderson, C. L., Figueiredo, J. P., Jaramillo, C., Riff, D., Negri, F. R., Hooghiemstra, H., Lundberg, J., Stadler, T., Sarkinen, T., & Antonelli, A. 2010. Amazonia through time: Andean uplift, climate change, landscape evolution, and biodiversity. *Science (New York, N.Y.)*, **330**(6006), 927–931.
- Horton, P., Jaboyedoff, M., Rudaz, B., & Zimmermann, M. 2013. Flow-R, a model for susceptibility mapping of debris flows and other gravitational hazards at a regional scale. *Natural Hazards and Earth System Sciences*, **13**(4), 869–885.

- Hühnerbach, V., & Masson, D. G. 2004. Landslides in the North Atlantic and its adjacent seas: An analysis of their morphology, setting and behaviour. *Marine Geology*, **213**(1-4), 343–362.
- Ismail, Khaira, Huvenne, Veerle AI, & Masson, Douglas G. 2015. Objective automated classification technique for marine landscape mapping in submarine canyons. *Marine Geology*, **362**, 17–32.
- Itasca. 2018. *FLAC3D, Explicit continuum modeling of non-linear material behavior in 3D*. <https://www.itascacg.com/software/flac3d> (last accessed 2018-09-01).
- Jain, A. K., & Farrokhnia, F. 1990. Unsupervised texture segmentation using Gabor filters. *Pages 14–19 of: 1990 IEEE International Conference on Systems, Man, and Cybernetics Conference*.
- Jetchev, Nikolay, Bergmann, Urs, & Vollgraf, Roland. 2016. Texture synthesis with spatial generative adversarial networks. *arXiv preprint arXiv:1611.08207*.
- Julesz, B., Gilbert, E. N., Shepp, L. A., & Frisch, H. L. 1973. Inability of humans to discriminate between visual textures that agree in second-order statistics – revisited. *Perception*, **2**(4), 391–405.
- Julesz, B., Gilbert, E. N., & Victor, J. D. 1978. Visual discrimination of textures with identical third-order statistics. *Biological Cybernetics*, **31**(3), 137–140.
- Justice, J. H., Hawkins, D. J., & Wong, G. 1985. Multidimensional attribute analysis and pattern recognition for seismic interpretation. *Pattern Recognition*, **18**(6), 391–399.
- Kadu, Ajinkya, van Leeuwen, Tristan, & Mulder, Wim A. 2017. Salt Reconstruction in Full-Waveform Inversion With a Parametric Level-Set Method. *IEEE Transactions on Computational Imaging*, **3**(2), 305–315.
- Kappes, M. S., Gruber, K., Frigerio, S., Bell, R., Keiler, M., & Glade, T. 2012. The MultiRISK platform: The technical concept and application of a regional-scale multihazard exposure analysis tool. *Geomorphology*, **151–152**, 139–155.
- Kass, Michael, Witkin, Andrew, & Terzopoulos, Demetri. 1988. Snakes: Active contour models. *International Journal of Computer Vision*, **1**(4), 321–331.
- Kervrann, Charles. 2010. *Modeles statistiques pour l'analyse d'images, algorithmes et applications en imagerie bio-cellulaire et moleculaire*. Ph.D. thesis.
- Kingma, Diederik P., & Welling, Max. 2014. Auto-encoding variational Bayes. *In: Proceedings of The International Conference on Learning Representations*.
- Kohonen, Teuvo. 1986. *Learning Vector Quantization for Pattern Recognition: Technical Report TKK-F- A601*. Helsinki University of Technology.
- Krizhevsky, Alex, Sutskever, Ilya, & Hinton, Geoffrey E. 2012. Imagenet classification with deep convolutional neural networks. *Pages 1097–1105 of: Advances in neural information processing systems*.
- Kubichek, R. F., & Quincy, E. A. 1985. Statistical modeling and feature selection for seismic pattern recognition. *Pattern Recognition*, **18**(6), 441–448.

- Lacoste, Aurélien, Vendeville, Bruno C., Mourgues, Régis, Loncke, Lies, & Lebacqz, Maxime. 2012. Gravitational instabilities triggered by fluid overpressure and downslope incision – Insights from analytical and analogue modelling. *Journal of Structural Geology*, **42**, 151–162.
- Le Bouteiller, Pauline, & Charléty, Jean. 2018. *Procédé pour la détection d'objets géologiques dans une image sismique (Patent pending)*.
- Le Bouteiller, Pauline, Charléty, Jean, Delprat-Jannaud, Florence, Granjeon, Didier, & Gorini, Christian. 2018. Mixing unsupervised and knowledge-based analysis for heterogeneous object delineation in Seismic Data. *In: 80th EAGE Conference and Exhibition 2018*.
- Le Guen, Vincent. 2014. Cartoon + Texture Image Decomposition by the TV-L1 Model. *Image Processing On Line*, **4**, 204–219.
- LeCun, Y., Bottou, L., Bengio, Y., & Haffner, P. 1998. Gradient-based learning applied to document recognition. *Proceedings of the IEEE*, **86**(11), 2278–2324.
- LeCun, Yann, Bengio, Yoshua, & Hinton, Geoffrey. 2015. Deep learning. *Nature*, **521**(7553), 436.
- Lewis, Winston, & Vigh, Denes. 2017. Deep learning prior models from seismic images for full-waveform inversion. *Pages 1512–1517 of: SEG Technical Program Expanded Abstracts 2017*. Society of Exploration Geophysicists.
- Leynaud, D., Mienert, J., & Vanneste, M. 2009. Submarine mass movements on glaciated and non-glaciated European continental margins: A review of triggering mechanisms and preconditions to failure. *Marine and Petroleum Geology*, **26**(5), 618–632.
- Lianantonakis, Maria, & Petillot, Yvan R. 2007. Sidescan Sonar Segmentation Using Texture Descriptors and Active Contours. *IEEE Journal of Oceanic Engineering*, **32**(3), 744–752.
- Lin, Tsung-Yi, Dollar, Piotr, Girshick, Ross, He, Kaiming, Hariharan, Bharath, & Belongie, Serge. 2017. Feature Pyramid Networks for Object Detection. *Pages 936–944 of: 2017 IEEE Conference on Computer Vision and Pattern Recognition (CVPR)*.
- Linked Data API. 2017. *International Chronostratigraphic Chart*. <http://resource.geosciml.org/classifier/ics/ischart/> (last accessed 2018-09-01).
- Lipton, Zachary C. 2016. The mythos of model interpretability. *arXiv preprint arXiv:1606.03490*.
- Lisboa, Douglas, Lafuerza, Sara, Gorini, Christian, Cauquil, Eric, & Contet, Julien. 2017. *Submarine canyons morphology and failure processes along the continental slope of the North Western Foz Do Amazonas basin, Brazil*. International Meeting of Sedimentology.
- Liu, Li, Long, Yunli, Fieguth, Paul W., Lao, Songyang, & Zhao, Guoying. 2014. BRINT: binary rotation invariant and noise tolerant texture classification. *IEEE transactions on image processing : a publication of the IEEE Signal Processing Society*, **23**(7), 3071–3084.

- Liu, Zhoufeng, Li, Chunlei, Zhao, Quanjun, Liao, Liang, & Dong, Yan. 2015. A fabric defect detection algorithm via context-based local texture saliency analysis. *International Journal of Clothing Science and Technology*, **27**(5), 738–750.
- Long, Zhiling, Alaudah, Yazeed, Qureshi, Muhammad Ali, Farraj, Motaz Al, Wang, Zhen, Amin, Asjad, Deriche, Mohamed, & AlRegib, Ghassan. 2015a. Characterization of migrated seismic volumes using texture attributes: a comparative study. *Pages 1744–1748 of: Schneider, Robert Vincent (ed), SEG Technical Program Expanded Abstracts 2015*.
- Long, Zhiling, Wang, Zhen, & AlRegib, Ghassan. 2015b. Seisim: structural similarity evaluation for seismic data retrieval. *In: Presented at the 2015 IEEE ICCSPA*.
- Love, P. L., & Simaan, M. 1985. Segmentation of a seismic section using image processing and artificial intelligence techniques. *Pattern Recognition*, **18**(6), 409–419.
- Lu, Yijuan, Cohen, Ira, Zhou, Xiang Sean, & Tian, Qi. 2007. Feature selection using principal feature analysis. *Page 301 of: Lienhart, Rainer, Prasad, Anand R., Hanjalic, Alan, Choi, Sunghyun, Bailey, Brian, & Sebe, Nicu (eds), the 15th international conference*.
- MacQueen, J. 1967. Some methods for classification and analysis of multivariate observations. *Pages 281–297 of: Proceedings of the fifth Berkeley Symposium on mathematical statistics and probability*, vol. 14.
- Malik, Zaki, Rezgui, Abdelmounaam, Medjahed, Brahim, Ouzzani, Mourad, & Krishna Sinha, A. 2010. Semantic integration in Geosciences. *International Journal of Semantic Computing*, **04**(03), 301–330.
- Mallat, Stéphane. 2012. Group Invariant Scattering. *Communications on Pure and Applied Mathematics*, **65**(10), 1331–1398.
- Mangeney, A., Bouchut, F., Thomas, N., Vilotte, J. P., & Bristeau, M. O. 2007. Numerical modeling of self-channeling granular flows and of their levee-channel deposits. *Journal of Geophysical Research*, **112**(F2), 2050.
- Mangeney-Castelnau, A., Bouchut, F., Vilotte, J. P., Lajeunesse, E., Aubertin, A., & Pirulli, M. 2005. On the use of Saint Venant equations to simulate the spreading of a granular mass. *Journal of Geophysical Research: Solid Earth*, **110**(B9).
- Marfurt, Kurt J. 2015. Seismic attributes and the road ahead. *Pages 4421–4426 of: Birkelo, Brad (ed), SEG Technical Program Expanded Abstracts 2014*.
- Marfurt, Kurt J., Kirlin, R. Lynn, Farmer, Steven L., & Bahorich, Michael S. 1998. 3-D seismic attributes using a semblance-based coherency algorithm. *GEOPHYSICS*, **63**(4), 1150–1165.
- Marroquín, Iván Dimitri, Brault, Jean-Jules, & Hart, Bruce S. 2009. A visual data-mining methodology for seismic facies analysis: Part 1 — Testing and comparison with other unsupervised clustering methods. *GEOPHYSICS*, **74**(1), P1–P11.
- Maslin, Mark, Vilela, Claudia, Mikkelsen, Naja, & Grootes, Pieter. 2005. Causes of catastrophic sediment failures of the Amazon Fan. *Quaternary Science Reviews*, **24**(20–21), 2180–2193.

- Masson, D. G., Harbitz, C. B., Wynn, R. B., Pedersen, G., & Løvholt, F. 2006. Submarine landslides: processes, triggers and hazard prediction. *Philosophical transactions. Series A, Mathematical, physical, and engineering sciences*, **364**(1845), 2009–2039.
- Mienert, J. 2009. Methane Hydrate and Submarine Slides. *Pages 790–798 of: Encyclopedia of Ocean Sciences*. Elsevier.
- Migeon, Sébastien, Cattaneo, Antonio, Hassoun, Virginie, Larroque, Christophe, Corradi, Nicola, Fanucci, Francesco, Dano, Alexandre, Mercier de Lepinay, Bernard, Sage, Françoise, & Gorini, Christian. 2011. Morphology, distribution and origin of recent submarine landslides of the Ligurian Margin (North-western Mediterranean): Some insights into geohazard assessment. *Marine Geophysical Research*, **32**(1-2), 225–243.
- Miramontes, Elda, Cattaneo, Antonio, Jouet, Gwenael, & Garziglia, Sebastien. 2016. Implications of Sediment Dynamics in Mass Transport along the Pianosa Ridge (Northern Tyrrhenian Sea). *Pages 301–309 of: Lamarche, Geoffroy, Mountjoy, Joshu, Bull, Suzanne, Hubble, Tom, Krastel, Sebastian, Lane, Emily, Micallef, Aaron, Moscardelli, Lorena, Mueller, Christof, Pecher, Ingo, & Woelz, Susanne (eds), Submarine Mass Movements and their Consequences. Advances in Natural and Technological Hazards Research*, vol. 41. Cham: Springer International Publishing.
- Mitchum Jr, Rober M., Vail, Peter R., & Sangree, John B. 1977. Seismic stratigraphy and global changes of sea level: Part 6. Stratigraphic interpretation of seismic reflection patterns in depositional sequences: Section 2. Application of seismic reflection configuration to stratigraphic interpretation.
- Moore, Zachary T., & Sawyer, Derek E. 2016. Assessing post-failure mobility of submarine landslides from seismic geomorphology and physical properties of mass transport deposits: An example from seaward of the Kumano Basin, Nankai Trough, offshore Japan. *Marine Geology*, **374**, 73–84.
- Morgenstern, N. R., & Price, V. E. 1965. The Analysis of the Stability of General Slip Surfaces. *Géotechnique*, **15**(1), 79–93.
- Moscardelli, Lorena, & Wood, Lesli. 2008. New classification system for mass transport complexes in offshore Trinidad. *Basin Research*, **20**(1), 73–98.
- Mougeot, Mathilde. 2015. *Enjeux mathématiques et statistiques du 'Big Data'*. http://www.irem.univ-paris-diderot.fr/videos/enjeux_mathematiques_et_statistiques_du_big_data/ (last accessed 2018-09-01).
- Moulin, Maryline, Aslanian, Daniel, & Unternehr, Patrick. 2010. A new starting point for the South and Equatorial Atlantic Ocean. *Earth-Science Reviews*, **98**(1-2), 1–37.
- Mourgues, R., & Cobbold, P. R. 2006. Sandbox experiments on gravitational spreading and gliding in the presence of fluid overpressures. *Journal of Structural Geology*, **28**(5), 887–901.
- Mourgues, R., Lecomte, E., Vendeville, B., & Raillard, S. 2009. An experimental investigation of gravity-driven shale tectonics in progradational delta. *Tectonophysics*, **474**(3-4), 643–656.

- Mourgues, R., Lacoste, A., & Garibaldi, C. 2014. The Coulomb critical taper theory applied to gravitational instabilities. *Journal of Geophysical Research: Solid Earth*, **119**(1), 754–765.
- Mulder, Thierry, & Alexander, Jan. 2001. The physical character of subaqueous sedimentary density flows and their deposits. *Sedimentology*, **48**(2), 269–299.
- Mumford, David, & Shah, Jayant. 1989. Optimal approximations by piecewise smooth functions and associated variational problems. *Communications on Pure and Applied Mathematics*, **42**(5), 577–685.
- Musen, Mark A. 2015. The Protégé Project: A Look Back and a Look Forward. *AI matters*, **1**(4), 4–12.
- Nabney, Ian T., & Bishop, Christopher M. 2002. *Netlab Neural Network Software*, webpage. <http://www.aston.ac.uk/eas/research/groups/ncrg/resources/netlab/> (last accessed 2018-09-01).
- Nailon, William Henry. 2010. Texture Analysis Methods for Medical Image Characterisation. In: Mao, Youxin (ed), *Biomedical Imaging*. InTech.
- Nair, Vinod, & Hinton, Geoffrey E. 2010. Rectified linear units improve restricted boltzmann machines. *Pages 807–814 of: Proceedings of the 27th international conference on machine learning (ICML-10)*.
- Nelson, C. Hans, Escutia, Carlota, Damuth, John E., & Twichell, David C. 2011. Interplay of Mass-Transport and Turbidite-System Deposits in Different Active Tectonic and Passive Continental Margin Settings: External and Local Controlling Factors. *Pages 39–66 of: Shipp, R. Craig, Weimer, Paul, & Posamentier, Henry W. (eds), Mass-transport deposits in deepwater settings*. SEPM (Society for sedimentary geology) special publication, vol. 96. Tulsa (Okla.): SEPM (Society for Sedimentary Geology).
- Ojala, T., Pietikainen, M., & Maenpaa, T. 2002. Multiresolution gray-scale and rotation invariant texture classification with local binary patterns. *IEEE Transactions on Pattern Analysis and Machine Intelligence*, **24**(7), 971–987.
- Omosanya, Kamal'deen O., & Alves, Tiago M. 2013. Ramps and flats of mass-transport deposits (MTDs) as markers of seafloor strain on the flanks of rising diapirs (Espírito Santo Basin, SE Brazil). *Marine Geology*, **340**, 82–97.
- Optum CE. 2018. *Optum Computational Engineering, Geophysical finite element software*. <https://optumce.com/> (last accessed 2018-01-01).
- Orozco-del Castillo, M. G., Cárdenas-Soto, M., Ortiz-Alemán, C., Couder-Castañeda, C., Urrutia-Fucugauchi, J., & Trujillo-Alcántara, A. 2017. A texture-based region growing algorithm for volume extraction in seismic data. *Geophysical Prospecting*, **65**(1), 97–105.
- Ortiz-Karpf, Andrea, Hodgson, David M., Jackson, Christopher A.-L., & McCaffrey, William D. 2016. Mass-transport complexes as markers of deep-water fold-and-thrust belt evolution: Insights from the southern Magdalena fan, offshore Colombia. *Basin Research*, **57**(4), 294.

- Osypov, Konstantin, Wilkinson, David, Bandura, Laura L., & Halpert, Adam Dean. 2018. *System and method for seismic facies identification using machine learning*. US Patent US20180106917A1.
- Owen, Matthew, Day, Simon, & Maslin, Mark. 2007. Late Pleistocene submarine mass movements: Occurrence and causes. *Quaternary Science Reviews*, **26**(7-8), 958–978.
- Pachauri, Rajendra K., Allen, Myles R., Barros, Vicente R., Broome, John, Cramer, Wolfgang, Christ, Renate, Church, John A., Clarke, Leon, Dahe, Qin, & Dasgupta, Purnamita. 2014. *Climate change 2014: synthesis report. Contribution of Working Groups I, II and III to the fifth assessment report of the Intergovernmental Panel on Climate Change*. IPCC.
- Pappas, Thrasyvoulos N., Neuhoff, David L., de Ridder, Huib, & Zujovic, Jana. 2013. Image Analysis: Focus on Texture Similarity. *Proceedings of the IEEE*, **101**(9), 2044–2057.
- Partyka, Greg, Gridley, James, & Lopez, John. 1999. Interpretational applications of spectral decomposition in reservoir characterization. *The Leading Edge*, **18**(3), 353–360.
- Patruno, Stefano, & Helland-Hansen, William. 2018. Clinoforms and clinoform systems: Review and dynamic classification scheme for shorelines, subaqueous deltas, shelf edges and continental margins. *Earth-Science Reviews*, **185**, 202–233.
- Peleg, S., Werman, M., & Rom, H. 1989. A unified approach to the change of resolution: Space and gray-level. *IEEE Transactions on Pattern Analysis and Machine Intelligence*, **11**(7), 739–742.
- Perrin, Michel, Zhu, Beiting, Schneider, Sébastien, & Rainaud, Jean-François. 2009. *Ontology-driven applications for geological modeling*. Technical Report. IFP Energies nouvelles.
- Peyton, Lynn, Bottjer, Rich, & Partyka, Greg. 1998. Interpretation of incised valleys using new 3-D seismic techniques: A case history using spectral decomposition and coherency. *The Leading Edge*, **17**(9), 1294–1298.
- Pigott, John D., Kang, Moo-Hee, & Han, Hyun-Chul. 2013. First order seismic attributes for clastic seismic facies interpretation: Examples from the East China Sea. *Journal of Asian Earth Sciences*, **66**, 34–54.
- Pitas, I., & Kotropoulos, C. 1992. A texture-based approach to the segmentation of seismic images. *Pattern Recognition*, **25**(9), 929–945.
- Portilla, Javier. 2000. A parametric texture model based on joint statistics of complex wavelet coefficients. *International Journal of Computer Vision*, **40**(1), 49–70.
- Posamentier, H. W., Davies, R. J., Cartwright, J. A., & Wood, L. 2007. Seismic geomorphology - an overview. *Geological Society, London, Special Publications*, **277**(1), 1–14.

- Posamentier, Henry W., & Martinsen, Ole J. 2011. The Character and Genesis of Submarine Mass-Transport Deposits: Insights from Outcrop and 3D Seismic Data. *Pages 7–38 of: Shipp, R. Craig, Weimer, Paul, & Posamentier, Henry W. (eds), Mass-transport deposits in deepwater settings*. SEPM (Society for sedimentary geology) special publication, vol. 96. Tulsa (Okla.): SEPM (Society for Sedimentary Geology).
- Purves, Steven, Lowell, James, Norton, Dale, & Jonathon, Henderson. 2015. *Improvements in 3D object delineation*. EP patent EP2659291B1.
- Qi, Jie, Lin, Tengfei, Zhao, Tao, Li, Fangyu, & Marfurt, Kurt. 2016. Semisupervised multiattribute seismic facies analysis. *Interpretation*, **4**(1), SB91–SB106.
- Raad, Lara, Davy, Axel, Desolneux, Agnès, & Morel, Jean-Michel. 2017. A survey of exemplar-based texture synthesis. *arXiv preprint arXiv:1707.07184*.
- Reis, A. T., Perovano, R., Silva, C. G., Vendeville, B. C., Araujo, E., Gorini, C., & Oliveira, V. 2010. Two-scale gravitational collapse in the Amazon Fan: A coupled system of gravity tectonics and mass-transport processes. *Journal of the Geological Society*, **167**(3), 593–604.
- Reis, A. T., Araujo, E., Silva, C. G., Cruz, A. M., Gorini, C., Droz, L., Migeon, S., Perovano, R., King, I., & Bache, F. 2016. Effects of a regional décollement level for gravity tectonics on late Neogene-Quaternary large-scale slope instabilities in the Foz do Amazonas Basin, Brazil. *Marine and Petroleum Geology*, **75**, 29–52.
- Reisenhofer, Rafael, Bosse, Sebastian, Kutyniok, Gitta, & Wiegand, Thomas. 2018. A Haar wavelet-based perceptual similarity index for image quality assessment. *Signal Processing: Image Communication*, **61**, 33–43.
- Reitsma, Femke, Laxton, John, Ballard, Stuart, Kuhn, Werner, & Abdelmoty, Alia. 2009. Semantics, ontologies and eScience for the geosciences. *Computers & Geosciences*, **35**(4), 706–709.
- Richardson, Steve E. J., Davies, Richard J., Allen, Mark B., & Grant, Simon F. 2011. Structure and evolution of mass transport deposits in the South Caspian Basin, Azerbaijan. *Basin Research*, **23**(6), 702–719.
- Roberto, V., Peron, A., & Fumis, P. L. 1989. Low-level processing techniques in geophysical image interpretation. *Pattern Recognition Letters*, **10**(2), 111–122.
- Roddaz, Martin, Viers, Jérôme, Brusset, Stéphane, Baby, Patrice, & Hérail, Gérard. 2005. Sediment provenances and drainage evolution of the Neogene Amazonian foreland basin. *Earth and Planetary Science Letters*, **239**(1-2), 57–78.
- Ronneberger, Olaf, Fischer, Philipp, & Brox, Thomas. 2015. U-Net: Convolutional Networks for Biomedical Image Segmentation. *Pages 234–241 of: Navab, Nassir, Hornegger, Joachim, Wells, William M., & Frangi, Alejandro F. (eds), Medical Image Computing and Computer-Assisted Intervention – MICCAI 2015*. Lecture Notes in Computer Science, vol. 9351. Cham: Springer International Publishing.
- Rousselle, Jean-Jacques. 2003. *Les contours actifs, une méthode de segmentation: Application à l'imagerie médicale*. Ph.D. thesis, Université de Tours, Tours.

- Roy, Atish. 2013. *Latent space classification of seismic facies*. Ph.D. thesis, University of Oklahoma.
- Roy, Atish, Romero-Peláez, Araceli S., Kwiatkowski, Tim J., & Marfurt, Kurt J. 2014. Generative topographic mapping for seismic facies estimation of a carbonate wash, Veracruz Basin, southern Mexico. *Interpretation*, **2**(1), SA31–SA47.
- RSI. 2003. *Attributes Revisited*. <http://www.rocksolidimages.com/attributes-revisited/> (last accessed 2018-09-01).
- Sawyer, Derek E., Flemings, Peter B., Buttles, James, & Mohrig, David. 2012. Mudflow transport behavior and deposit morphology: Role of shear stress to yield strength ratio in subaqueous experiments. *Marine Geology*, **307–310**, 28–39.
- SEG. 2018. *SEG Wiki website*. <https://wiki.seg.org> (last accessed 2018-09-01).
- Shafiq, Muhammad A., Wang, Zhen, Amin, Asjad, Hegazy, Tamir, Deriche, Mohamed, & AlRegib, Ghassan. 2015. Detection of Salt-dome Boundary Surfaces in Migrated Seismic Volumes Using Gradient of Textures. *Pages 1811–1815 of: Schneider, Robert Vincent (ed), SEG Technical Program Expanded Abstracts 2015*.
- Sharma, Ojaswa, & Anton, François. 2009. CUDA based Level Set method for 3D reconstruction of fishes from large acoustic data. *Pages 153–160 of: WSCG '2009*, vol. 17.
- Shephard, G. E., Müller, R. D., Liu, L., & Gurnis, M. 2010. Miocene drainage reversal of the Amazon River driven by plate–mantle interaction. *Nature Geoscience*, **3**(12), 870–875.
- Shipp, R. Craig, Weimer, Paul, & Posamentier, Henry W. 2011. Mass-Transport Deposits in Deepwater Settings: An Introduction. *Pages 3–6 of: Shipp, R. Craig, Weimer, Paul, & Posamentier, Henry W. (eds), Mass-transport deposits in deepwater settings*. SEPM (Society for sedimentary geology) special publication, vol. 96. Tulsa (Okla.): SEPM (Society for Sedimentary Geology).
- Sifre, Laurent, & Mallat, Stéphane. 2013. Rotation, scaling and deformation invariant scattering for texture discrimination. *In: IEEE Conference on Computer Vision*.
- Silva, C. G., Araújo, E., Reis, A. T., Perovano, R., Gorini, C., Vendeville, B. C., & Albuquerque, N. 2010. Megaslides in the Foz do Amazonas Basin, Brazilian Equatorial Margin. *Pages 581–591 of: Mosher, David C., Shipp, R. Craig, Moscardelli, Lorena, Chaytor, Jason D., Baxter, Christopher D. P., Lee, Homa J., & Urgeles, Roger (eds), Submarine Mass Movements and Their Consequences*. Dordrecht: Springer Netherlands.
- Silva, Cleverson C., dos Reis, Antonio T., Perovano, Rodrigo J., Gorini, Marcus A., dos Santos, Marcos V. M., Jeck, Izabel K., Tavares, Ana Angélica A., & Gorini, Christian. 2016. Multiple Megaslide Complexes and Their Significance for the Miocene Stratigraphic Evolution of the Offshore Amazon Basin. *Pages 49–60 of: Lamarche, Geoffroy, Mountjoy, Joshu, Bull, Suzanne, Hubble, Tom, Krastel, Sebastian, Lane, Emily, Micallé, Aaron, Moscardelli, Lorena, Mueller, Christof, Pecher, Ingo, & Woelz, Susanne (eds), Submarine Mass Movements and their Consequences*. Advances in Natural and Technological Hazards Research, vol. 41. Cham: Springer International Publishing.

- Silva, S. R. P., Maciel, R. R., & Severino, M. C. G. 1998. Cenozoic tectonics of Amazon Mouth Basin. *Geo-Marine Letters*, **18**(3), 256–262.
- Simoncelli, E. P., & Freeman, W. T. 23-26 Oct. 1995. The steerable pyramid: a flexible architecture for multi-scale derivative computation. *Pages 444–447 of: International Conference on Image Processing*.
- Soares Junior, A.V., Hasui, Y., Costa, J.B.S., & Machado, F.B. 2011. Evolucao do rifteamento e paleogeografia da margem Atlantica Equatorial do Brasil: Triassico ao Holoceno. *Geociencias*, **30**(4), 669–692.
- Sommer, Christoph, Straehle, Christoph, Köthe, Ullrich, & Hamprecht, Fred A. 2011. Ilastik: Interactive learning and segmentation toolkit. *Pages 230–233 of: Biomedical Imaging: From Nano to Macro, 2011 IEEE International Symposium on*. IEEE.
- Sultan, Nabil, Cochonat, Pierre, Bourillet, Jean François, & Cayocca, Florence. 2001. Evaluation of the Risk of Marine Slope Instability: A Pseudo-3D Approach for Application to Large Areas. *Marine Georesources & Geotechnology*, **19**(2), 107–133.
- Svensen, Johan FM. 1998. *GTM: The Generative Topographic Mapping*. Ph.D. thesis, Aston University, Aston University.
- Taha, Abdel Aziz, & Hanbury, Allan. 2015. Metrics for evaluating 3D medical image segmentation: analysis, selection, and tool. *BMC medical imaging*, **15**, 29.
- Taner, M. T., Koehler, F., & Sheriff, R. E. 1979. Complex seismic trace analysis. *GEO-PHYSICS*, **44**(6), 1041–1063.
- TeleGeography. 2018. *Submarine Cable Map website*. <https://www.submarinecablemap.com/> (last accessed 2018-09-01).
- Terzaghi, Karl. 1942. *Theoretical soil mechanics*. New York: John Wiley and Sons.
- Terzaghi, Karl. 1950. Mechanism of Landslides. *Pages 83–123 of: Paige, Sidney (ed), Application of Geology to Engineering Practice*. New York, N. Y.: Geological Society of America.
- Unser, Michael. 1995. Texture classification and segmentation using wavelet frames. *IEEE Transactions on image processing*, **4**(11), 1549–1560.
- Urlaub, Morelia, Talling, Peter J., & Masson, Doug G. 2013. Timing and frequency of large submarine landslides: Implications for understanding triggers and future geohazard. *Quaternary Science Reviews*, **72**, 63–82.
- Urlaub, Morelia, Talling, Peter J., Zervos, Antonis, & Masson, Douglas. 2015. What causes large submarine landslides on low gradient ($< 2^\circ$) continental slopes with slow (< 0.15 m/kyr) sediment accumulation? *Journal of Geophysical Research: Solid Earth*, **120**(10), 6722–6739.
- Vanneste, Maarten, Sultan, Nabil, Garziglia, Sebastian, Forsberg, Carl Fredrik, & L’Heureux, Jean-Sebastien. 2014. Seafloor instabilities and sediment deformation processes: The need for integrated, multi-disciplinary investigations. *Marine Geology*, **352**, 183–214.

- Varnes, David J. 1958. Landslide Types and Processes. *Landslides and engineering practice*, **24**, 20–47.
- Veenman, C. J., Reinders, M.J.T., & Backer, E. 2002. A maximum variance cluster algorithm. *IEEE Transactions on Pattern Analysis and Machine Intelligence*, **24**(9), 1273–1280.
- Veillard, A., Morère, O., Grout, M., & Gruffeille, J. 2018. Fast 3D Seismic Interpretation with Unsupervised Deep Learning: Application to a Potash Network in the North Sea. *In: 80th EAGE Conference and Exhibition 2018*.
- Verney, Philippe. 2009. *Interprétation géologique de données sismiques par une méthode supervisée basée sur la vision cognitive*. Ph.D. thesis, Ecole Nationale Supérieure des Mines de Paris, Paris.
- VSA partnership. 2018. *Virtual Seismic Atlas*. <https://www.seismicatlas.org/> (last accessed 2018-09-01).
- W3C. 2018. *W3C website*. <https://www.w3.org/> (last accessed 2018-09-01).
- Wang, Chengbin, Ma, Xiaogang, & Chen, Jianguo. 2018. Ontology-driven data integration and visualization for exploring regional geologic time and paleontological information. *Computers & Geosciences*, **115**, 12–19.
- Wang, Z., Bovik, A. C., Sheikh, H. R., & Simoncelli, E. P. 2004. Image Quality Assessment: From Error Visibility to Structural Similarity. *IEEE Transactions on Image Processing*, **13**(4), 600–612.
- Wang, Zhen, Hegazy, Tamir, Long, Zhiling, & AlRegib, Ghassan. 2015. Noise-robust detection and tracking of salt domes in postmigrated volumes using texture, tensors, and subspace learning. *GEOPHYSICS*, **80**(6), WD101–WD116.
- West, Brian P., May, Steve R., Eastwood, John E., & Rossen, Christine. 2002. Interactive seismic facies classification using textural attributes and neural networks. *The Leading Edge*, **21**(10), 1042–1049.
- Williamson, Daniel, Goldstein, Michael, Allison, Lesley, Blaker, Adam, Challenor, Peter, Jackson, Laura, & Yamazaki, Kuniko. 2013. History matching for exploring and reducing climate model parameter space using observations and a large perturbed physics ensemble. *Climate Dynamics*, **41**(7-8), 1703–1729.
- Wolff, B., & Carozzi, A.V. 1984. Microfacies, depositional environments, and diagenesis of the Amapa carbonates (Paleocene-Middle Miocene), Foz do Amazonas basin, offshore NE Brazil. *Petrobras, Rio de Janeiro*.
- Xu, Chenyang, Pham, Dzung L., & Prince, Jerry L. 2000. Image segmentation using deformable models. *Handbook of medical imaging*, **2**, 129–174.
- Yazdi, Mehran, & Gheysari, Kazem. 2008. A new approach for the fingerprint classification based on gray-level co-occurrence matrix. *World Academy of Science, Engineering and Technology*, **47**, 313–316.

- Zeiler, Matthew D, & Fergus, Rob. 2014. Visualizing and understanding convolutional networks. *Pages 818–833 of: European conference on computer vision*. Springer.
- Zhai, Yuanhao, Neuhoff, David L., & Pappas, Thrasyvoulos N. 2013. Local radius index - a new texture similarity feature. *Pages 1434–1438 of: ICASSP 2013 - 2013 IEEE International Conference on Acoustics, Speech and Signal Processing (ICASSP)*.
- Zhao, Tao, Li, Fangyu, & Marfurt, Kurt. 2016. Advanced self-organizing map facies analysis with stratigraphic constraint. *Pages 1666–1670 of: Sicking, Charles, & Ferguson, John (eds), SEG Technical Program Expanded Abstracts 2016*.
- Zhao, Xiaonan, Reyes, Matthew G., Pappas, Thrasyvoulos N., & Neuhoff, David L. 2008. Structural texture similarity metrics for retrieval applications. *Pages 1196–1199 of: 2008 15th IEEE International Conference on Image Processing*.
- Zujovic, Jana, Pappas, Thrasyvoulos N., & Neuhoff, David L. 2013. Structural texture similarity metrics for image analysis and retrieval. *IEEE transactions on image processing : a publication of the IEEE Signal Processing Society*, **22**(7), 2545–2558.